GEOLOGY AND GEOHYDROLOGY
OF THE EAST TEXAS BASIN

A Report on the Progress of Nuclear Waste
Isolation Feasibility Studies (1980)

by

C. W. Kreitler, E. W. Collins, E. D. Davidson, Jr., O. R. Dix,
G. A. Donaldson, S. P. Dutton, G. E. Fogg, A. B. Giles, D. W. Harris,
M. P. A. Jackson, C. M. Lopez, M. K. McGowen, W. R. Muehlberger,
W. D. Pennington, S. J. Seni, D. H. Wood, and H. V. Wuerch

Bureau of Economic Geology
W. L. Fisher, Director
The University of Texas at Austin
University Station, P. O. Box X
Austin, Texas 78712

1981

NOTICE

CONTENTS

ILLUSTRATIONS

Figures

iv

viii

Tables

EAST TEXAS SALT DOME STUDIES--A SUMMARY OF THIRD-YEAR RESEARCH ACTIVITIES

Research Staff

The third year of research was highlighted by the integration of regional basinal studies with growth histories for specific domes, studies of cap-rock diagenesis and salt deformation, preliminary studies of ground-water flow and geochemistry around Oakwood Dome, and preliminary studies of microseismicity in the Mount Enterprise fault zone.

During FY1980 we significantly advanced our understanding of the hydrologic and geologic stabilities of East Texas salt domes by analyzing extensive data acquired during FY1979. Important new data sources included (1) 194 m (636 ft) of core from the calcite and anhydrite cap rock and salt section of Oakwood Dome; (2) microseismic data from a seismometer on the Mount Enterprise fault system; and (3) five hydrologic monitoring wells completed around Oakwood Dome.

The integration of formation-specific studies (that is, Cotton Valley-Hosston, Paluxy, Nacatoch, and Wilcox Formations) has permitted reconstruction of a three-phase history of the tectonic and sedimentary evolution of the basin. In the initial phase, during Late Jurassic to Early Cretaceous, the basin was dominated by fault-controlled subsidence. The middle phase, during Late Cretaceous, was marked by a rapid decline in rates of subsidence and sedimentation. During the final phase, sedimentation and subsidence effectively ceased when Tertiary and Quaternary depocenters shifted to the Gulf of Mexico. Mobilization of salt and growth of domes was most active during Late Jurassic and Early Cretaceous (initial phase), and activity subsequently declined during Late Cretaceous and Tertiary. Differential rates of sedimentation within rim synclines surrounding the domes were coincident with exponential decline in sedimentation rates and basinal subsidence rates.

This general model of dome growth in the East Texas Basin is similar to the growth history of the Oakwood Dome. Maximum growth rates for Oakwood Dome occurred in Late Jurassic to Early Cretaceous and thereafter declined exponentially.

Oakwood cap rock consists of an upper calcite zone and a lower anhydrite zone. Analysis of the cap rock from Oakwood core indicates that the anhydrite zone is the result of dissolution of salt and accumulation of insoluble anhydrite residuum. This accumulation process occurred in an environment originally high in temperature and

1

salinity, resulting in metamorphic texture to the anhydrite rock. The cap rock appears to be an effective impermeable seal that will prevent further dissolution. Lithologic analysis of salt core indicates two distinct periods of recrystallization. Deformation and recrystallization during diapir growth produced a penetrative schistosity defined by inequant halite grains. Subsequent recrystallization of the upper 2 m (6 ft) of salt in the presence of ground water under conditions of low differential stress produced a low-strain, granoblastic texture. The low-strain, recrystallized zone implies tectonic stability.

Carbon-14 dating of bicarbonate from ground waters around Oakwood Dome shows that (1) ground water increases in age downdip from the Wilcox outcrop, (2) younger ground water occurs in the uplifted Carrizo Formation surrounding Oakwood Dome, confirming that recharge is occurring over the dome, and (3) the sodium and bicarbonate concentrations are linearly related to age of the water.

Analysis of Quaternary deposits reveals no evidence of salt dome growth during Pleistocene or Recent time. Interpretation of microseismic records suggests the occurrence of small seismic events along the Mount Enterprise fault zone.

PURPOSE AND SCOPE

Research Staff

The program to investigate the feasibility of using salt domes in the East Texas Basin as long-term nuclear waste repositories addresses the suitability of specific domes for potential repositories, as well as evaluates the tectonic, geologic, and hydrogeologic stability of all the domes in the region.

East Texas Basin investigations are part of salt dome studies underway in the Gulf Coast Interior Salt Basin of Texas, Louisiana, and Mississippi, and constitute one regional element of the national Nuclear Waste Isolation Program. The U.S. Department of Energy (DOE) intends to select one salt site for site-specific evaluation as a nuclear waste repository. This report concerns the salt dome program in East Texas and presents some preliminary conclusions reached on dome suitability during FY1980.

The 1980 program to investigate the tectonic, geologic, and hydrogeologic stability of salt domes in the East Texas Basin was divided into four subprograms: (1) subsurface geology; (2) surficial geology, remote sensing, and geomorphology; (3) hydrogeology; and (4) salt dome characteristics. Integration of the results from these four subprograms will determine the general suitability of salt domes in the East Texas Basin for further evaluation as a potential nuclear waste repository and will provide information on specific candidate domes in the East Texas Basin.

The subsurface program was designed to (1) determine pre-Pleistocene growth histories of domes in the East Texas Basin; (2) explain the relationship of basin infilling and salt dome growth; (3) map detailed subsurface geology around the salt domes; and (4) delineate size and shape of salt domes, depth to cap rock, and depth to salt.

The surficial geology and geomorphology program was designed to (1) determine if the domes have grown during the Quaternary; (2) describe in detail the surface geology over the domes; and (3) evaluate the structure of the basin to discover whether structural activity has occurred during the Quaternary.

The primary purposes of the hydrogeology program were to (1) examine regional ground-water flow paths; (2) assess the potential for salt dissolution on domes; and (3) predict any radionuclide pathways if domes were ever breached. Studies included regional hydrogeology in fresh-water aquifers, regional hydrogeology in the deeper saline aquifers, hydrogeology around domes, and hydrochemistry of fluids.

3

The research on salt dome characterization included studies of (1) the lithology, chemistry, and strain history of the salt within domes, and (2) the origin and diagenesis of cap rock and its role in preventing dome dissolution and radionuclide migration.

This progress report reviews principal conclusions, illustrates methodologies, and describes types of data and illustrations generated by the program. Several topical reports, presenting details of various geological aspects of salt domes in the East Texas Basin, will be forthcoming as phases of the study are completed. The locations of shallow domes in the East Texas Basin are plotted in figure 1, and the stratigraphic section of the East Texas Basin is shown in figure 2.
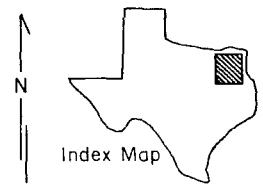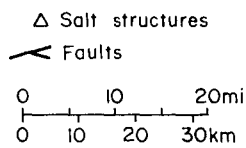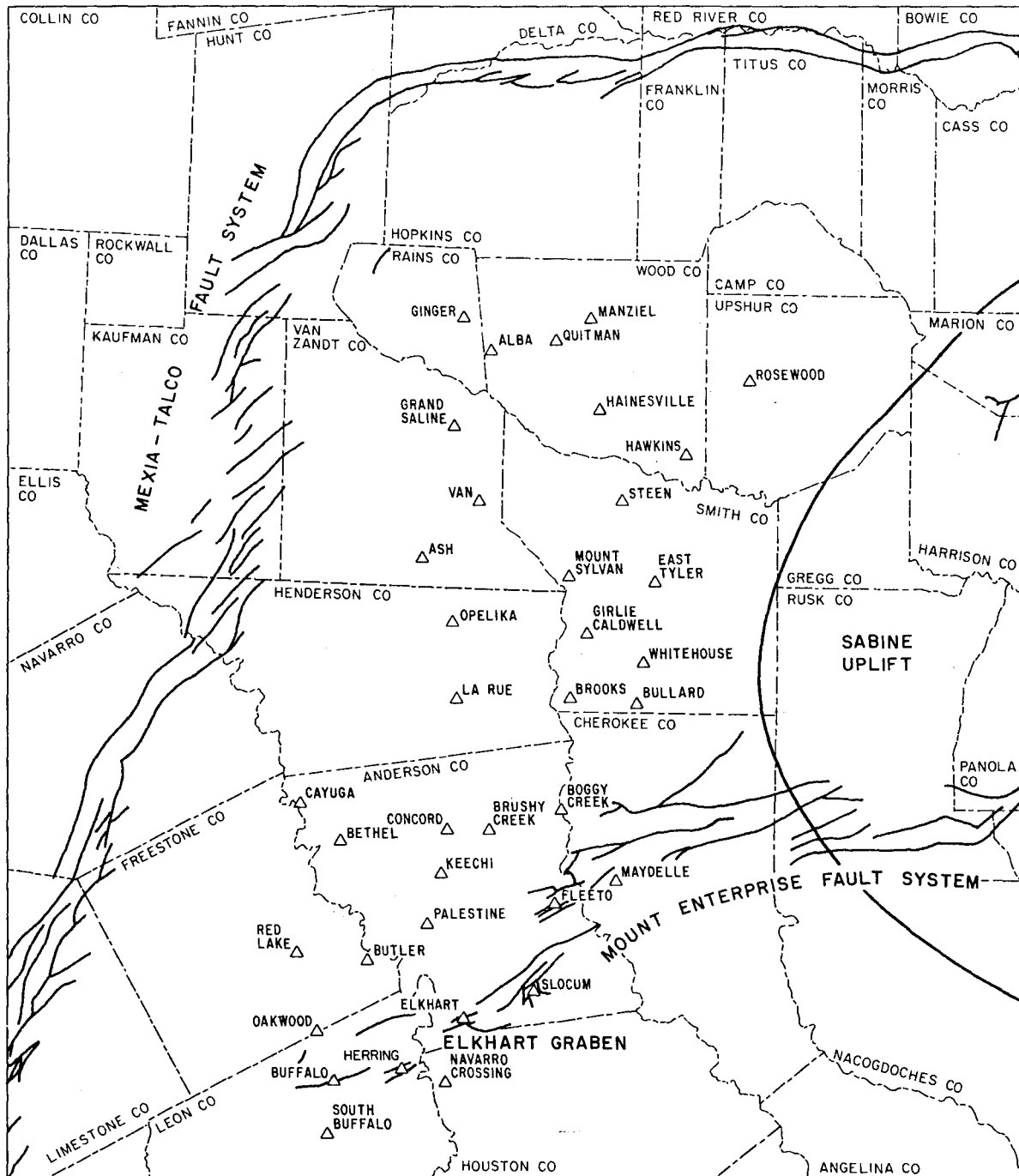
Figure 1. Location of shallow salt domes (depth to salt <3,000 ft [<1,000 m]), East Texas Basin.

5

Figure 2. Stratigraphic section, East Texas Basin.

ERA-THEM	SYSTEM	SERIES	GROUP	FORMATION
CENOZOIC	TERTIARY	EOCENE	CLAIBORNE	YEGUA / COOK MOUNTAIN / SPARTA / WECHES / QUEEN CITY / REKLAW / CARRIZO
			WILCOX	UNDIFFERENTIATED
		PALEOCENE	MIDWAY	UNDIFFERENTIATED
MESOZOIC	CRETACEOUS	UPPER CRETACEOUS	NAVARRO	UPPER NAVARRO CLAY / UPPER NAVARRO MARL / NACATOCH SAND / LOWER NAVARRO
			TAYLOR	UPPER TAYLOR / PECAN GAP CHALK / WOLFE CITY SAND / LOWER TAYLOR / OZAN ANNONA CHALK CHALK
			AUSTIN	GOBER CHALK / BROWNSTOWN / BLOSSOM SAND / BONHAM CLAY / Glauconitic Chalk Stringer / AUSTIN CHALK / Ector Chalk Mbr. / TOKIO
			EAGLE FORD	Sub Clarksville Mbr. / Coker Sand Mbr. / Harris Sand Mbr. / EAGLE FORD
			WOODBINE	WOODBINE: Lewisville Mbr. / Dexter Sand Mbr.
		LOWER CRETACEOUS	WASHITA (GEORGETOWN)	MANESS SHALE / BUDA LIMESTONE / GRAYSON SHALE / MAIN STREET LIMESTONE / WENO-PAW PAW LIMESTONE / DENTON SHALE / FORT WORTH LIMESTONE / DUCK CREEK SHALE / DUCK CREEK LIMESTONE
			FREDERICKSBURG	KIAMICHI SHALE / GOODLAND LIMESTONE
			TRINITY (GLEN ROSE / LOWER GLEN ROSE)	PALUXY / UPPER GLEN ROSE / MASSIVE ANHYDRITE / Rodessa Member / James Limestone Mbr. / Pine Island Shale Member / Pettet (Sligo) Member / TRAVIS PEAK (HOSSTON)
	JURASSIC	UPPER JURASSIC	COTTON VALLEY	SCHULER / BOSSIER
			LOUARK	GILMER LIMESTONE (COTTON VALLEY LIMESTONE) / BUCKNER / SMACKOVER
		MIDDLE JURASSIC	LOUANN	NORPHLET / LOUANN SALT / WERNER
		L. Jurassic		
		Upper Triassic		EAGLE MILLS
PALEO-ZOIC				OUACHITA

TECTONIC ENVIRONMENT DURING EARLY INFILLING OF THE EAST TEXAS BASIN

M. P. A. Jackson

The character of Mesozoic sedimentary fill in the East Texas Basin closely reflects underlying thermally induced tectonic processes characteristic of initial uplift, rifting, and thinning of Paleozoic continental crust followed by tectonic subsidence, which allowed restricted marine incursions accompanied by rift volcanism. Further subsidence resulted in the accumulation of open shallow-marine deposits followed by progradation of the continental margin by delta-dominated systems toward an oceanic spreading center in the Gulf of Mexico.

At the beginning of the Mesozoic Era, the supercontinent of Pangaea was on the verge of fragmentation and dispersal. The sedimentary record suggests that the northern Gulf Coast was entirely continental, the nearest ocean being the Pacific (Salvador and Green, 1980). Opening of the Atlantic Ocean by breakup of the lithosphere in the Early Jurassic was preceded by an episode of Triassic continental rifting, probably lasting some 40 m.y. (Burke, 1976). Reassembly of the continental fragments bordering the Atlantic indicates that the Gulf of Mexico was already partly open at the onset of Atlantic seafloor spreading (Burke, 1976; Klitgord, 1980). Rifting and subsequent seafloor spreading were probably the result of a subcrustal thermal anomaly caused by rise of asthenospheric material. Thermal anomalies, evidenced by the abundance of igneous activity and anomalously high heat flow near present-day continental rifts and midoceanic ridges, caused the overlying crust to rise owing to thermal expansion and upward migration of the pyrolite pyroxene-garnet phase boundary in the upper mantle (Ringwood, 1969). Erosion of the uplifted crust leads to thinning (Hsu, 1965; Falvey, 1974), which is augmented by listric normal faulting in the upper distended crust and ductile flow in the lower crust. A broad expanse of rifted and thinned "transitional" continental crust some 6 to 20 km (4 to 12 mi) thick beneath the Texas-Louisiana and Yucatan shelves bordering the deep Gulf of Mexico is suggested by seismic refraction data (Buffler and others, 1980); the Late Triassic sedimentary record summarized here suggests that thinned crust is also present beneath the East Texas Basin.

Rapid sedimentation of red beds in grabens during the rift phase, which was accompanied by felsic and mafic alkaline volcanism, was concentrated in grabens (fig. 3). Extensional normal faults bounding fault blocks are commonly variable in plan

because of anastomosing and branching secondary faults. Secondary faults may be at any angle to the main rift (Burke, 1976), but generally have a preferred orientation parallel to the main rift direction, which is perpendicular to the direction of maximum crustal extension (Harding and Lowell, 1979). A northeast trend for one or more Triassic rifts in Texas can be deduced from the apparent northeasterly zonation of sedimentary facies in the Eagle Mills red-bed sequence, which becomes more proximal northwestward toward the inferred rift margin (Nichols and others, 1968). This trend is also suggested by the present continental shelf break in the northern Gulf of Mexico, after allowances are made for shape modification by lateral salt flow, which formed the bulge of the Sigsbee Scarp, and progradation of clastic wedges.

Major erosion and concomitant rift sedimentation, which resulted from upward bulging of the lithosphere and its dissection by extensional block faulting, promoted levelling of the terrane. Faulting and collapse migrated laterally outward from the central graben(s) that subsided to form a topographic depression. Subsidence was an isostatic response to a number of processes including: erosional and tectonic thinning of low-density crust; increase in density of the lower crust that is due to dehydration and decarbonation metamorphic reactions caused by rise of the isotherms over the original thermal anomaly; increase in density of the attenuated crust that is due to injection of mafic dikes and extrusion of basic flows; and increase in mantle density caused by thermal contraction after cooling (Hsu, 1965; Falvey, 1974; Burke, 1976). Subsequent loading by sediments and seawater accentuated the depression.

A moderate increase in heat flow of about 33 mW/m^2 is sufficient to cause 3 km (2 mi) of subsidence below sea level; thermal blanketing and loading by sediments enabled up to 12 km (7 mi) of sediments to accumulate (Falvey, 1974). According to Kinsman's (1975) model, thinned continental crust tended to subside faster than normal continental crust, the rate of subsidence being 15 m.y. for 1 km (.6 mi) of subsidence for crust 20 km (12 mi) thick and 30 m.y. for crust 30 km (20 mi) thick: In this manner the diverging zones of maximum uplift, which migrated outward from the rift axis during the expansion phase, were followed by diverging zones of collapse, lagging by some 10 to 15 m.y. because of slow upward and outward conduction of the thermal anomaly (Falvey, 1974).

Post-rifting continental breakup was accompanied by accretion of oceanic crust in the former rift (fig. 3). Oceanic crust (seismic velocity 6.4 to 7.2 km/sec [21,000 to 22,000 ft/sec]) some 5 km (3 mi) thick is interpreted to underlie the Sigsbee Plain in the deep Gulf between the zones of thinned continental crust (Ibrahim and others,

8

1980). That this crust formed by seafloor spreading from a northeast-trending spreading center in the middle of the Gulf is suggested by several lines of evidence (Buffler and others, 1980): (1) a strikingly symmetrical distribution of salt, thinned continental crust, and basement highs on either side of the Sigsbee Plain (Buffler and others, 1980); (2) the northwestern trend of fracture zones and transform faults in the adjacent Atlantic Ocean and across the Florida Shelf (Klitgord, 1980); (3) the north-western trend of basement topographic highs in the Sigsbee Plain (Shaub and others, 1980); and (4) the northwestern trend of inferred major strike-slip faults across Mexico (Pilger, 1978; Anderson and Schmidt, 1980; Dickinson and Coney, 1980; Gose and others, 1980). At the start of seafloor spreading, migration of a spreading center away from a continental margin allowed the margin to cool and subside. Both the rate of subsidence and the heat flow decreased over a decay period of 50 to 100 m.y. to a steady state (Kinsman, 1975; Royden and others, 1980).

The character of the basin fill in East Texas appears to have been closely controlled by the tectonic evolution outlined above and to have followed a typical path from purely continental (Late Triassic) through restricted marine (Early Jurassic) to open shallow marine; there is no evidence of evolution to deep marine conditions as occurred in the central Gulf of Mexico. During the pre-rift stage, lithospheric expansion and uplift exposed the Paleozoic Ouachita Fold Belt to further erosion. Red beds of the Eagle Mills Formation were deposited unconformably on the eroded basement during the Late Triassic (fig. 3). Sedimentary environments were of the coarse bed-load-fluvial type, probably involving alluvial fans developed along fault scarps. By mid-Jurassic the East Texas Basin had subsided sufficiently to allow intermittent but increasingly frequent marine incursions along the rifts, which formed the Werner Formation, consisting of red beds and evaporites, and the evaporitic Louann Salt (fig. 3). The source of the seawater for the evaporites is more likely to have been the Pacific Ocean than the embryonic Atlantic Ocean, which had barely started to open at this time (Salvador and Green, 1980). Rift volcanism, which typically occurs in the axial zone of rifts offset by transcurrent faulting, is recorded by lava flows beneath the Werner Formation and by ash falls immediately above the Louann Salt in the largely continental Norphlet Formation (Nichols and others, 1968). The angular unconformity at the top of the Eagle Mills rift sequence may mark the onset of continental breakup, which normally follows a final uplift pulse (Falvey, 1974). The extremely planar base of nonmobilized Louann Salt in East Texas visible on seismic sections suggests that this phase of erosion was extensive. The Louann Salt of

9

East Texas is one of three salt provinces in the Gulf area; the other two are represented by separate areas of the Challenger Formation on the northern and southern continental shelves of the Gulf of Mexico.

Open shallow-marine deposits in the Upper Jurassic Smackover, Buckner, Gilmer, and Bossier Formations represent post-breakup accumulations on the subsiding continental shelf (fig. 3). The general paucity of terrigenous sediment on the shelf suggests that the rift margin, at this stage forming a rugged coastline, was still elevated above the adjoining hinterland and was diverting clastic input elsewhere. Continued cooling-induced subsidence of the continental margin eventually allowed massive progradation of terrigenous clastics represented by the Schuler and Travis Peak Formations during the Late Jurassic and Early Cretaceous (fig. 3). A rapid marine transgression allowed the accumulation of Glen Rose carbonates; the presence of massive anhydrite suggests that conditions were shallow enough to form evaporites. By the mid-Cretaceous the rate of subsidence had decreased, and rapid progradation of thick deltaic and fluvial sequences became possible, causing outbuilding of the continental shelf. Whenever a large supply of clastics was available, most of this sediment prograded over the southern rim of the East Texas Basin into the Gulf of Mexico, which received most of its detritus in the Cenozoic.

Maturation of the East Texas salt domes from low-amplitude salt pillows to diapirs was most rapid during the massive progradation of terrigenous clastics in the Early Cretaceous. Subsequent decline of halokinetic rates, determined by differential sedimentation rates in diapiric rim synclines and adjoining areas (see "Evolution of East Texas Basin"), mirrors a similar exponential decline in heat flow of passive continental margins formed by the breakup of Pangaea. The decrease in heat flow was probably responsible for a similar decline of "tectonic" subsidence rates, sedimentation rates, and halokinetic rates in a chain of cause and effect. If so, the salt domes of passive continental margins, especially those farther inland, are more likely to become stable with time, a desirable characteristic for the isolation of nuclear wastes.

10

present limits of
EAST TEXAS BASIN   present coastline   present *GULF of MEXICO*

OUACHITA FOLD BELT
                                FORELAND

PRE-RIFT
l ℞   + Paleozoic basement

EAGLE MILLS RIFT SEQUENCE
(continental red beds)   RIFT SEQUENCE

RIFT
u ℞   isotherms

LOUANN EVAPORITES   RIFT VOLCANISM   CHALLENGER EVAPORITES
(restricted marine)   (restricted marine)

RIFT
m J

SMACKOVER-BUCKNER-GILMER-BOSSIER   NORTHERN SALT   oceanic   SOUTHERN SALT
(Shallow open marine)   PROVINCE   rift   PROVINCE

BREAKUP
u J

SCHULER-TRAVIS PEAK
PROGRADATION   sea level

                                                              oceanic
                                                              rift
                                          pelagic sedimentation
PASSIVE   continental
MARGIN   crust
u J /*l*K   transitional crust   new oceanic crust

upper mantle lithosphere
                            asthenosphere

Figure 3. Schematic sections showing evolutionary stages in formation of East Texas Basin and adjoining Gulf of Mexico (not to scale). Arrows indicate thermally induced isostatic movement of the crust.

11

EVOLUTION OF THE EAST TEXAS BASIN

Steven J. Seni and Charles W. Kreitler

The tectonic and sedimentary evolution of the East Texas Basin can be divided into three phases based on patterns of sedimentation and long-term subsidence rates. The initial phase was dominated by fault-controlled subsidence. Exponential decline in rates of subsidence and sedimentation during the middle phase was probably a function of declining rates of tectonic heat flow. During the final phase, sedimentation and subsidence effectively ceased when Tertiary and Quaternary depocenters shifted toward the Gulf of Mexico, and the final accumulations in the basin were primarily nonmarine. Differential rates of sedimentation in rim synclines surrounding salt domes indicate that, in East Texas, growth of salt domes was most active during the Early Cretaceous (initial phase) and activity subsequently declined.

Salt dome stabilities and growth histories are sensitive indicators of a range of tectonic and sedimentary processes inferred to have occurred during evolution of the East Texas Basin. To understand salt dome growth histories better, and thus dome stabilities, well log data were used to analyze selected stratigraphic sequences within the East Texas Basin. The main aspects of these sequences examined were (1) depositional styles and (2) Early Cretaceous to Paleocene history of sedimentation and subsidence.

Tectonic processes active during the initial infilling of the East Texas Basin included uplift, rifting, and rapid, fault-controlled subsidence (see "Tectonic Environment During Early Infilling of the East Texas Basin"). These processes controlled deposition of very thick Triassic rift-basin fill, Jurassic evaporites, and Lower Cretaceous fluvial-deltaic deposits. The Lower Cretaceous Massive Anhydrite Formation of the Glen Rose Group was the last major evaporite unit deposited in the basin and marked the termination of the initial phase of basin infilling. The middle phase includes strata between the Massive Anhydrite and the Upper Cretaceous Navarro Group. These strata are characterized by relatively thin fluvial-deltaic deposits around the periphery of the basin. In contrast to deposits of the initial phase, middle phase fluvial-deltaic deposits do not thicken dramatically into the center of the basin, and they reflect steadily declining rates of subsidence.

During the final phase, the East Texas Basin was filled by Tertiary fluvial systems that supplied deltas that prograded to the margin of the Gulf of Mexico. Declines in the rate of sedimentation and subsidence have been successfully explained for other basins (Sleep, 1971; Sclater and Christie, 1980) and for the ocean floor

(Sleep, 1971; Kinsman, 1975; Parsons and Sclater, 1977) on the basis of a model of subsidence as a function of slow cooling of the upper part of the asthenosphere (McKenzie, 1978).

Net-sand maps of major clastic sequences deposited during each phase illustrate changes in sand-body geometry as a function of tectonic basin evolution. Based on sparse deep-well control, a net-sand map (fig. 4) of Jurassic to Lower Cretaceous terrigenous clastics deposited during the initial phase shows an increase in the thickness of coarse clastics toward the central part of the basin. Superposition of Jurassic to Lower Cretaceous depocenters over the area where Louann Salt is inferred to reach maximum thickness of 5,000 ft (1,500 m) indicates that subsidence may have been fault controlled as late as Early Cretaceous. Fault-controlled subsidence is a major characteristic of the initial period. In contrast, net-sand patterns exhibited by two younger Cretaceous clastic sequences deposited during the middle phase show the dominant influence of steady, slow subsidence and salt-related tectonics (figs. 5 and 6). For example, Paluxy and Nacatoch net-sand maps document fluvial-deltaic sedimentation around the periphery of the basin and exhibit a decrease of coarse clastics toward the center of the basin. Clastic sequences deposited during the middle phase of basin evolution are thinner, and they exhibit progressive coastal onlap, indicating that the basin was increasing in areal extent. Early in the final phase of basin development, a dendritic pattern of Wilcox streams developed in the East Texas Basin (fig. 7). Wilcox fluvial systems flowed into and down the axis of the basin and supplied deltas along the margin of the Gulf of Mexico. Except for minor episodes of thin clastic shelf deposition, the East Texas Basin ceased to be a marine basin during the Tertiary and Quaternary Periods, when major Eocene, Oligocene, Pliocene, and Pleistocene depocenters shifted toward the Gulf of Mexico.

Preliminary interpretation of depositional rates for selected sequences (fig. 8) shows that in areas unaffected by salt withdrawal, subsidence decreased exponentially from a peak in the initial phase. In the East Texas Basin, deep-water, starved-basin deposits have not been recognized, and all deposits represent shallow-water deposition in which sedimentation kept pace with subsidence. Thus, the rate of deposition is inferred to equal the subsidence rate. On the basis of an approximate maximum thickness of 5,000 ft (1,500 m) (A. Salvador, personal communication, 1981) and a duration of 5 to 7 m.y. for the Callovian Stage, a rough estimate of rates of subsidence during deposition of the Louann Salt is 700 to 1,000 ft/m.y. (0.21 to 0.30 mm/yr). Differential rates of subsidence in rim synclines surrounding salt diapirs reveal a

13

decline in the rates of salt dome growth that follow a similar decline in rates of sedimentation.

Depositional rates within salt withdrawal basins (fig. 8) were much greater than overall sedimentation rates as a result of salt migration into diapirs. Trusheim's model of salt dome growth (Trusheim, 1960) requires differential loading by thick clastic sequences to initiate dome growth. In East Texas, these conditions occurred most commonly in initial phases of basin infilling during the Early Cretaceous. Rates of dome growth diminished during the middle phases of basin evolution because of decreased sedimentation rates. The two depositional rate curves illustrate the coincidence of periods of high rates of regional sedimentation and high rates of sedimentation in salt withdrawal areas. Because the volume of sediment in salt withdrawal areas equals the volume of salt displaced, the highest rates of salt dome growth occurred during the periods of greatest sedimentation. Isolated examples of rapid thickening in rim synclines during periods of low rates of regional sedimentation (for example, the growth of Hainesville Dome during Nacatoch to Austin Chalk time; fig. 8) may indicate that dome growth was due to another mechanism involving salt core breaching and rapid extrusion or dissolution as proposed by Loocke (1978). In the final phase of basin development, dome growth was minimal because loading by thin fluvial Wilcox deposits was limited. This contrasts with the high rates of deposition and dome growth associated with the Wilcox Rockdale and Holly Spring delta systems in the Houston Embayment (Fisher and McGowen, 1967) and Mississippi Salt Basin (Galloway, 1968).

Calculations of the rates of regional deposition, subsidence, and dome growth through geologic time require a reliable numeric time scale and a statistical methodology to separate populations of regional and local (salt-influenced) thickness. This report uses the new Jurassic to Cretaceous time scale by Van Hinte (1976a, b), although it is recognized that no single time scale is universally accepted (Baldwin and others, 1974). This amended Jurassic to Cretaceous time scale integrates biostratigraphic, paleomagnetic, and radiometric data, and avoids the problems of equal duration for all twelve Cretaceous stages (for example, Casey, 1964). Thickness is the other variable used in rate calculations. The mean thickness of a given sequence was calculated by statistical analysis of basinwide populations of all isopach values. Cumulative curves were graphically analyzed to obtain statistical parameters including mean, median, standard deviation, coefficient of variance, skewness, and kurtosis. Only the regional mean thickness and the maximum salt-influenced values are graphed in figure 8.

14

Table 1 summarizes relationships among phases of basin infilling, structural and depositional styles, and rates of salt movement. Analyses of the East Texas Basin document three tectonic and sedimentary phases in the infilling of the basin. The initial phase is characterized by unstable tectonic conditions and maximum rates of dome growth, sedimentation, and subsidence. This initial phase terminated from 100 to 110 m.y. ago. Except for reactivated dome growth approximately 80 m.y. ago, rates of dome growth have declined through the Tertiary. The present tectonic-sedimentary regime indicates that East Texas Basin salt domes are more stable today than they were in the geologic past.

Table 1. Summary of relations between infilling of the East Texas Basin and structural and depositional styles, rock types, and salt withdrawal.

PHASES OF BASIN EVOLUTION	Initial	Middle	Final
Structural style	Early tectonic normal faulting associated with Triassic rift basins. Later structural deformation associated with salt movement	Dominantly salt-related deformation	Minor salt-related deformation
Depositional style	Early tectonic fan, fan deltas, rift basin evaporites, and carbonates. Characteristically very thick deltaic clastics and evaporites	Thin subequal basin margin fluvial-deltaics and inter-bedded carbonates. Minor evaporite stringers associated with Massive Anhydrite	Thin to thick fluvial deposits. Delta deposits predominantly occur downdip from East Texas Basin in Gulf of Mexico area. Thin terrigenous clastic shelf deposits. No carbonates

INCREASING THICKNESS AND RATE OF SEDIMENTATION

(Rows: Associations of rock types — Evaporites; Clastics; Carbonates; Rate of salt withdrawal --estimated)

(Time scale: TRIASSIC | JURASSIC | CRETACEOUS (Lower | Upper) | TERTIARY)

Figure 4. Net sandstone, Jurassic to Lower Cretaceous clastics, East Texas Basin (from data of M. K. McGowen). Two trends can be inferred from limited well control: (1) regional increase in net sandstone from the periphery toward basin interior and (2) local high and low net-sand values in the northwestern part of the basin associated with salt tectonics around Grand Saline Salt Dome. Regional sand trends may reflect continued basement tectonic activity.

16

Figure 5. Net sandstone, Paluxy Formation, East Texas Basin. Thick net-sandstone trends occur around northern perimeter of basin within grabens of the Mexia-Talco fault zone. Fault system formed by extension from downdip flow of Louann Salt.

17
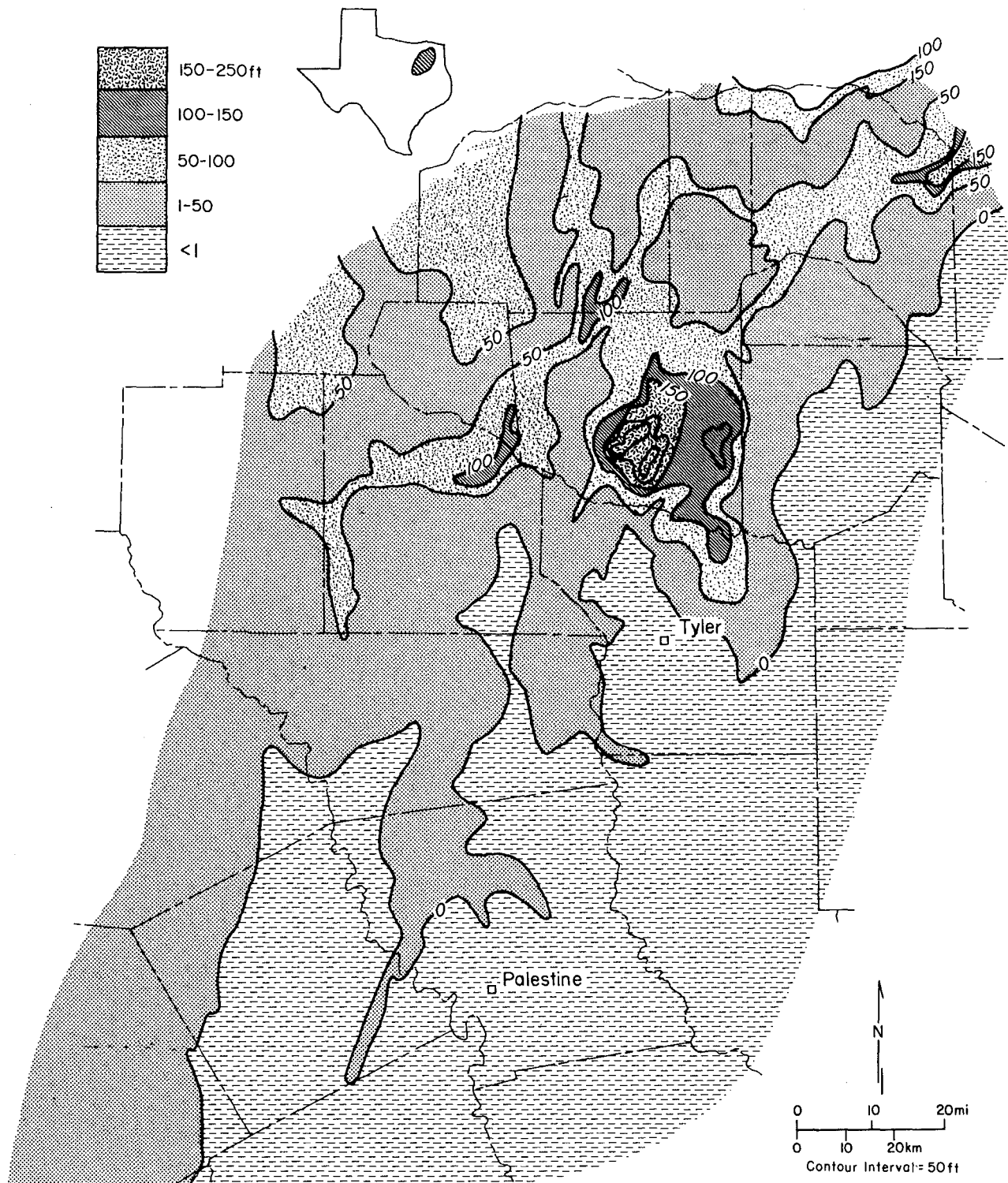
Figure 6. Net sandstone, Nacatoch Formation, East Texas Basin (from data of M. K. McGowen). Dip-oriented sand trends occur around northwestern perimeter of the basin. Sand trends become strike-oriented in central part of basin. Isolated thick net-sand areas in Wood County reflect rapid thickening around Hainesville Salt Dome.

18
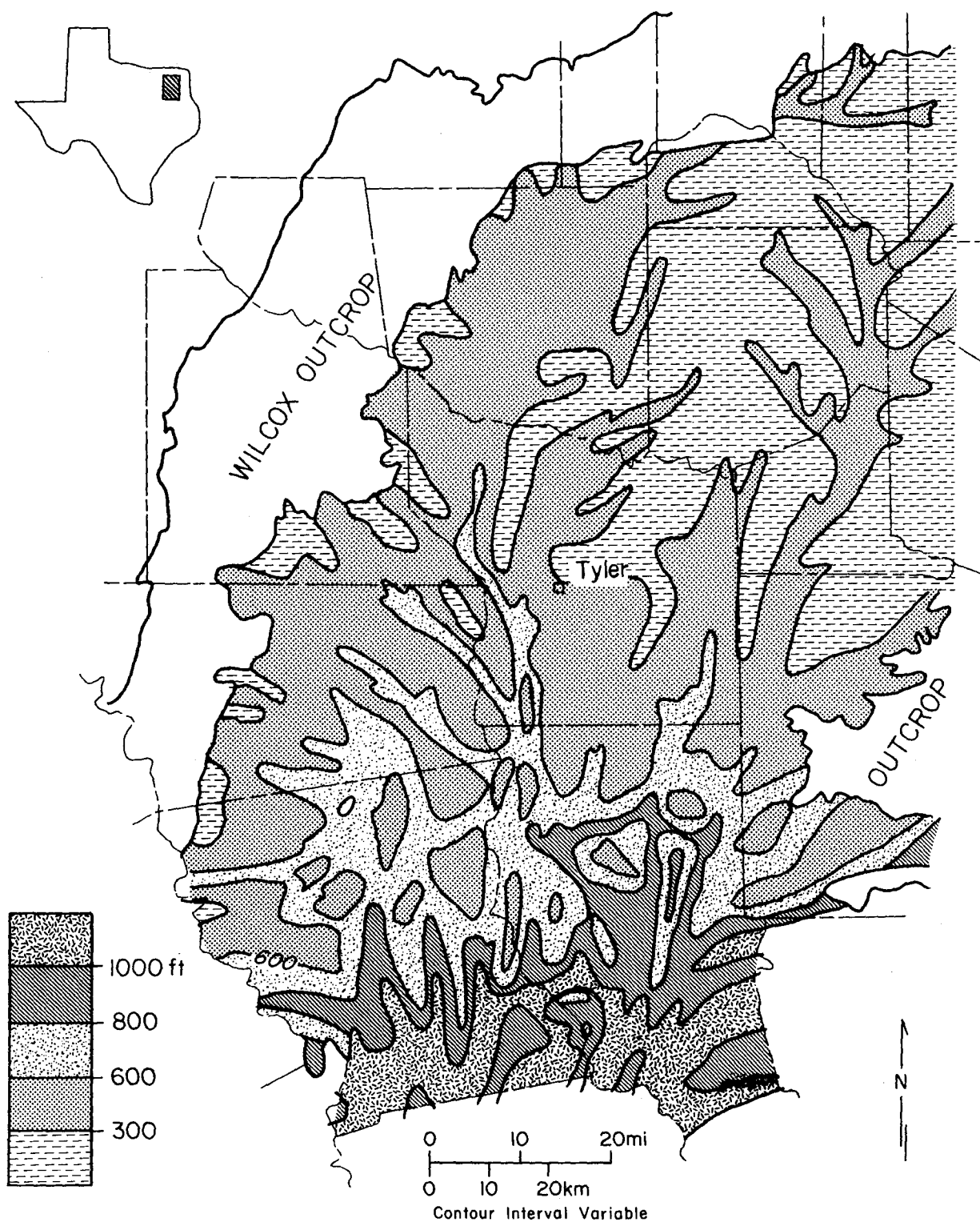
Figure 7. Net sandstone, Wilcox Formation, East Texas Basin (modified from Kaiser and others, 1978). Dendritic net-sand patterns indicate that fluvial channels extended across the East Texas Basin and supplied sediment to large deltaic systems along the Mount Enterprise-Elkhart Graben fault system in the southern part of the basin.

19

PALUXY

700

650

600

550

GLEN ROSE
TO
JAMES

500

WASHITA
GROUP

450

SEDIMENTATION RATE
IN AREAS OF SALT WITHDRAWAL

400

RATE OF DEPOSITION
FEET/MILLION YEARS

350

HIGH SEDIMENTATION RATE
DUE TO SALT WITHDRAWAL
AROUND HAINESVILLE DOME

300

PALUXY

NACATOCH SD TO
PECAN GAP

PECAN GAP
TO
BASE AUSTIN CHALK

GLEN ROSE
TO
JAMES

250

SEDIMENTATION RATE IN AREAS
UNAFFECTED BY SALT WITHDRAWAL

200

MIDWAY TO
PECAN GAP

WOODBINE

150

WASHITA
GROUP

MIDWAY TO
NACATOCH SD

WOODBINE

100

PECAN GAP
TO
BASE AUSTIN CHALK

NACATOCH SD
TO
PECAN GAP

50

MIDWAY TO PECAN GAP

0

160   150   140   130   120   110   100   90   80   70   60   50   40   30   20
MILLIONS OF YEARS AGO

200

175

150

125   METERS/MILLION YEARS

100

75

50

25

| JURASSIC | CRETACEOUS | | TERTIARY |
| | LOWER CRETACEOUS | UPPER CRETACEOUS | |

Figure 8. Rate of deposition for Cretaceous and Tertiary stratigraphic units in salt withdrawal areas and in areas unaffected by salt withdrawal, East Texas Basin. Rate of deposition was calculated by dividing average thickness of isopach interval by duration of interval. Absolute ages are from unpublished data compiled by A. B. Giles (after Martinez and others, 1976; Berryhill and others, 1968; Law Engineering Testing Company, 1978, 1980; Van Hinte, 1976a; and Gundersen and others, 1969). Curves connect average age of each isopach interval. Horizontal bar represents duration of each interval.

20

STRUCTURAL EFFECTS OF SALT MOVEMENT IN THE EAST TEXAS BASIN

Debra H. Wood

Sediments deposited in the East Texas Basin were deformed by migration of Middle Jurassic Louann Salt. Salt moved laterally, primarily in response to sediment loading, to form salt ridges and intervening withdrawal synclines. Most ridges were subdivided by subsequent loading, forming discontinuous salt anticlines. As salt movement approached vertical, many salt anticlines in the center of the basin became diapirs. Turtle-structure anticlines developed from sediment thicks deposited in original salt withdrawal synclines as their flanks collapsed because of continued withdrawal of salt. Diapirs developed primarily along the basin axis; salt anticlines remain around the basin perimeter; and turtle-structure anticlines are interspersed among the salt structures.

Evaluation of salt diapirs for nuclear waste storage is aided by an understanding of the regional salt-related structural configuration of the East Texas Basin. At least 5,500 m (18,000 ft) of Upper Jurassic, Cretaceous, and Tertiary strata in the East Texas Basin have been folded to form anticlines and synclines (Wood and Guevara, 1981). Principal folds occur in the central parts of the basin; folds diminish in amplitude updip toward the Mexia-Talco fault zone and the Sabine Uplift (figs. 9, 10, and 11). Movement of thick Middle Jurassic Louann Salt controlled most of the structural deformation in overlying strata. Consequently, pre-Louann Salt strata and the Paleozoic basement were not involved in the structural activity that produced the anticlines and synclines of the East Texas Basin.

Most structures in the central parts of the East Texas Basin conform to Trusheim's (1960) model of salt flowage (fig. 12). Salt movement was probably initiated by differential loading of overlying sediments. As salt moved away from areas of maximum loading, sediments continued to thicken in withdrawal synclines until all the salt was squeezed from beneath the depocenter. In progressively younger strata, the salt withdrawal syncline, and consequently the depocenter, migrated toward the growing salt structure. In this manner, the salt was pushed laterally into ridges that were subsequently subdivided by loading and further segmented into shorter anticlines. Loading by sands and shales of the Schuler and Travis Peak Formations, the first major post-Louann clastic deposits, probably initiated salt movement in most parts of the basin. During Schuler-Travis Peak time, salt structures may have been characterized by discontinuous salt anticlines separated by depositional basins (withdrawal synclines).

Salt anticlines are easily identified by negative gravity anomalies. Periods of active upward growth are indicated by thinning of overlying sediments. Salt anticlines

21

may deform great thicknesses of overburden; several deep-seated salt masses such as the Fleeto salt anticline (fig. 10) deformed strata as young as the (Eocene) Claiborne Group. Extensional faults are common at the crests of the anticlines. For example, the Elkhart Graben-Mount Enterprise fault system overlies a series of deep salt anticlines.

Residual salt structures are composed of salt that did not migrate (Kehle, 1971). As salt withdrew from adjacent areas, overlying sediments collapsed, creating anticlinal structures with unmobilized salt cores. Kehle (1971) identified a residual salt structure near Hainesville Dome using seismic data. These structures are not easily distinguishable from salt anticlines that developed from mobilized salt.

Salt diapirs (piercement structures) are relatively small, subcircular or elongate structures that exhibit pronounced negative gravity anomalies. They developed as salt movement became primarily vertical rather than lateral (figs. 10, 11, and 12). Salt was depleted around the base of the mature diapir, and its rim syncline migrated toward the edge of the dome. On the basis of the volume of sediments deposited in rim synclines, large volumes of salt must have been removed from some diapirs, principally by shallow salt dissolution. Associated faults include crestal grabens, radial faults, and down-to-the-dome normal faults on the diapir flanks.

As salt migrated into salt ridges, withdrawal synclines became clastic depocenters. Continued salt withdrawal caused the flanks of the depositional lens to collapse, followed by further deposition in the resultant syncline. In this manner, the thick sediment pod became the core of a turtle-shaped anticlinal structure (fig. 12) (Trusheim, 1960; Kehle, 1971). Most of these turtle-structure anticlines occur in thick Schuler-Travis Peak depocenters, but some structures, such as at the Burleson Hill field, have cores of abnormally thick Smackover carbonate sediments. Turtle-structure anticlines are characterized by relatively positive residual gravity anomalies (no salt core) and an elongate shape. These anticlines are blanketed by younger sediments rather rapidly because they are residual or passive structures that do not actively grow. Longitudinal tensional faults develop at the crests and on the flanks of turtle-structure anticlines as they collapse during salt withdrawal.

Salt diapirs occur along the axis of the East Texas Basin where overburden is thickest (fig. 13) and where the Louann Salt may have been thickest. Salt anticlines occur mainly around the outer edges of the basin. Turtle-structure anticlines are interspersed among the salt structures and are best developed among the salt diapirs in the center of the basin.
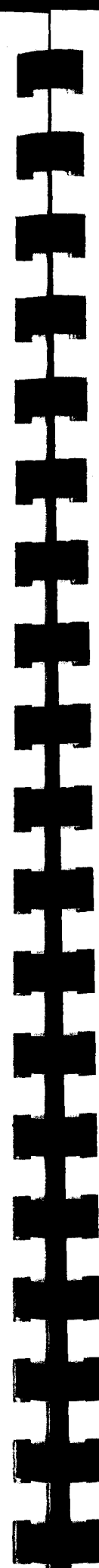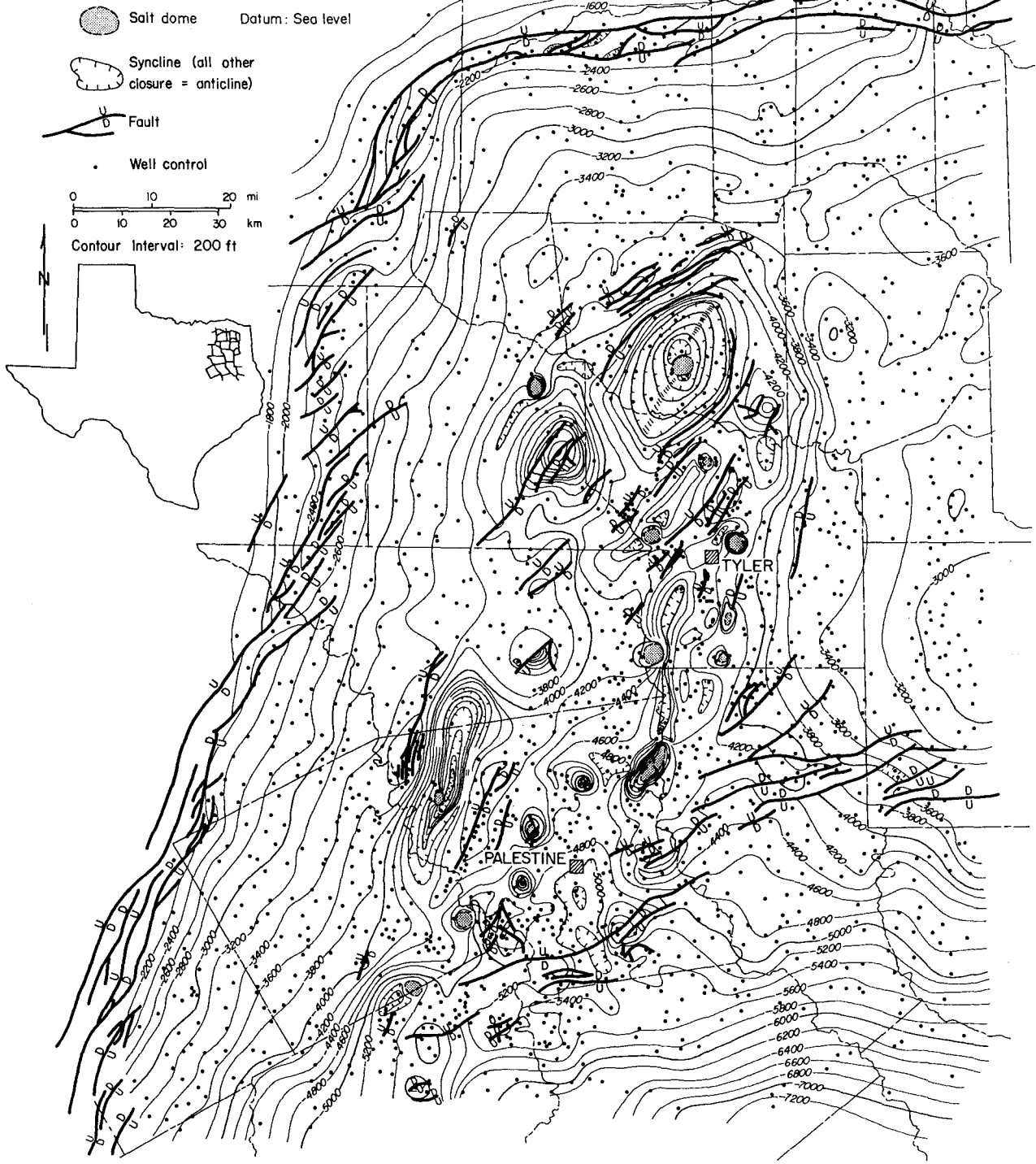
Figure 9. Structure contour map, base of Austin Chalk, East Texas Basin. Data from well logs, seismic profiles, and residual gravity data. Faults modified from Geomap Company (1980). Additional data near salt domes were interpreted by A. B. Giles.
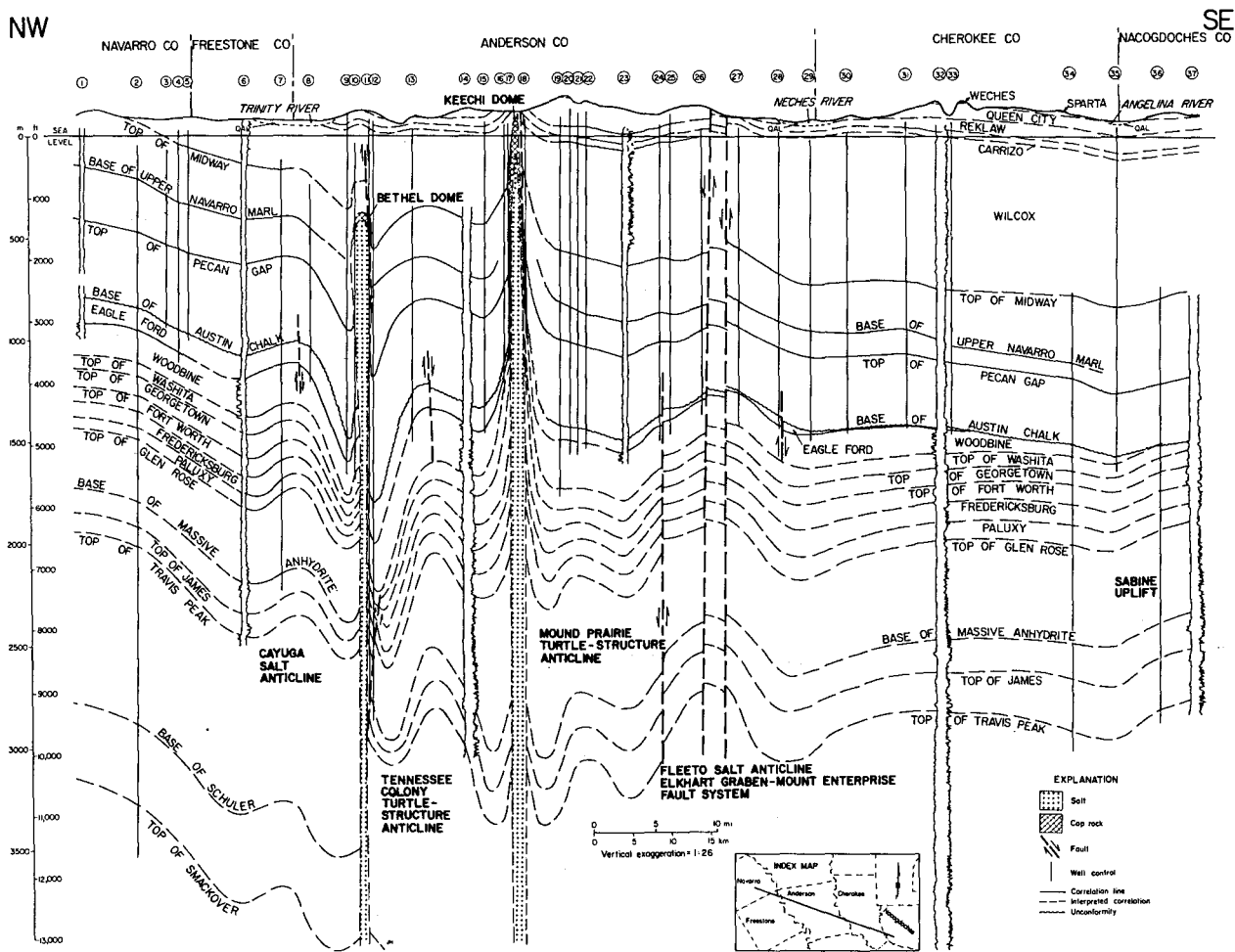
Figure 10. Regional dip cross section, East Texas Basin.
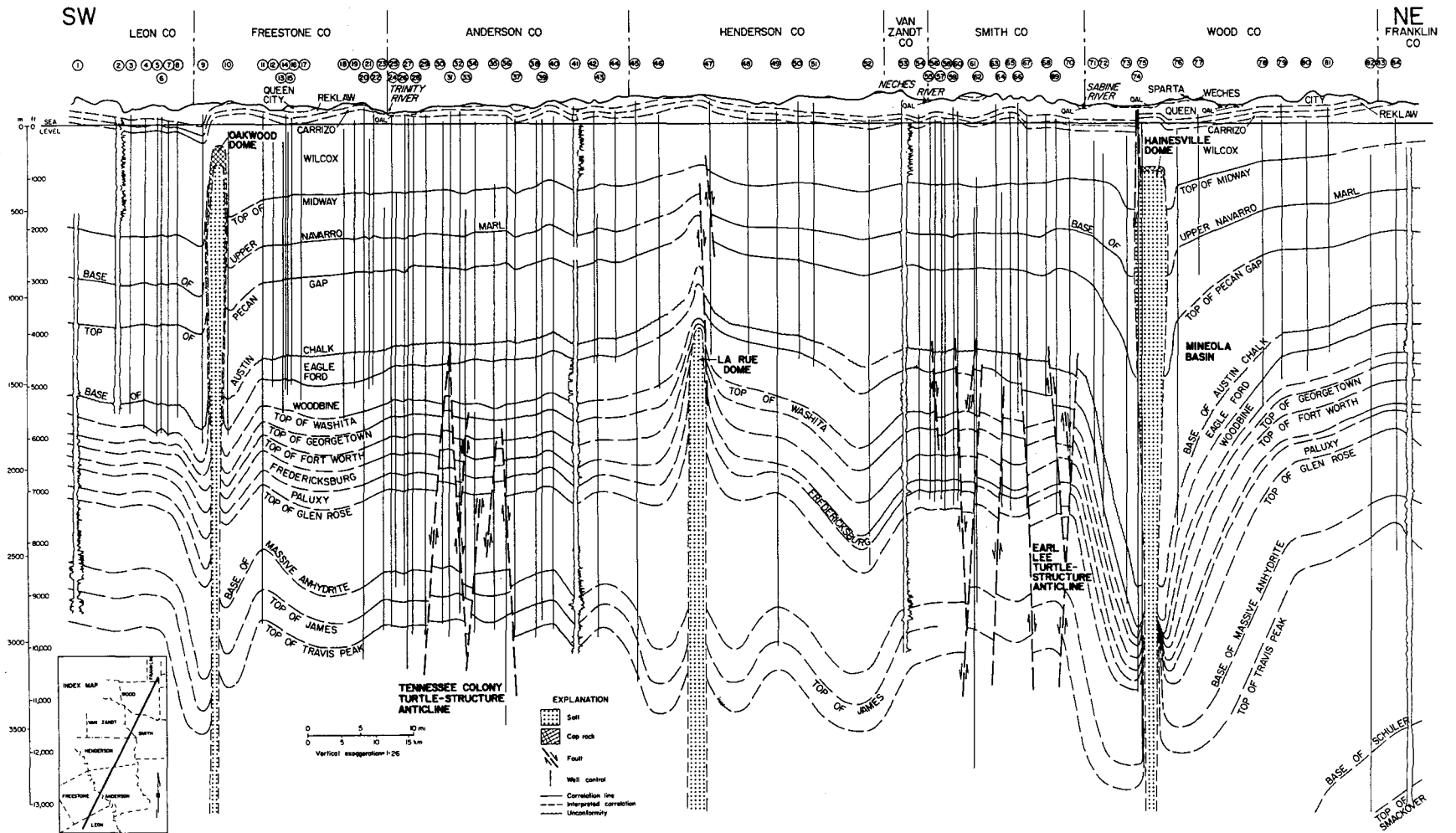
Figure 11. Regional strike cross section, East Texas Basin.

E

D

C

B

A
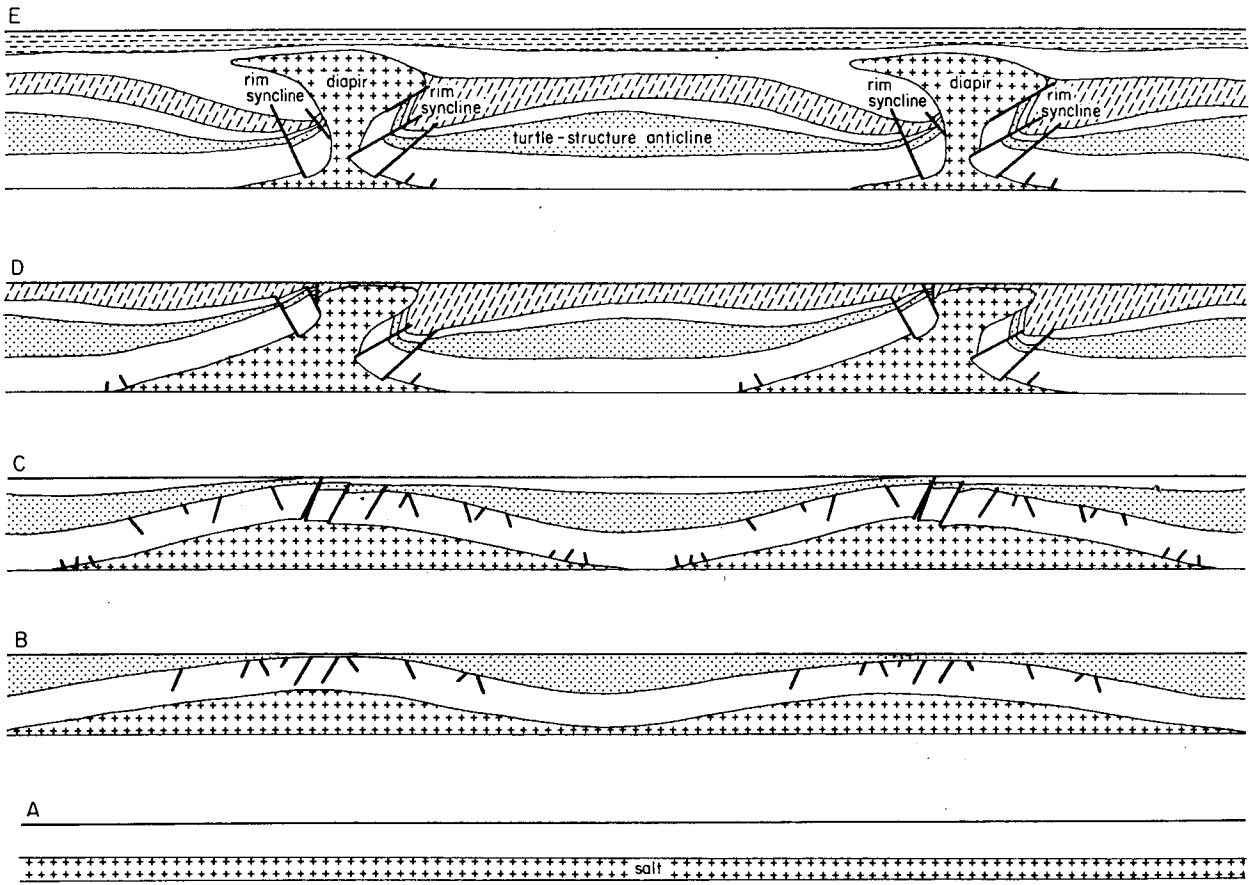
salt

Figure 12. Model of salt dome and turtle-structure anticline development (modified from Trusheim [1960]).
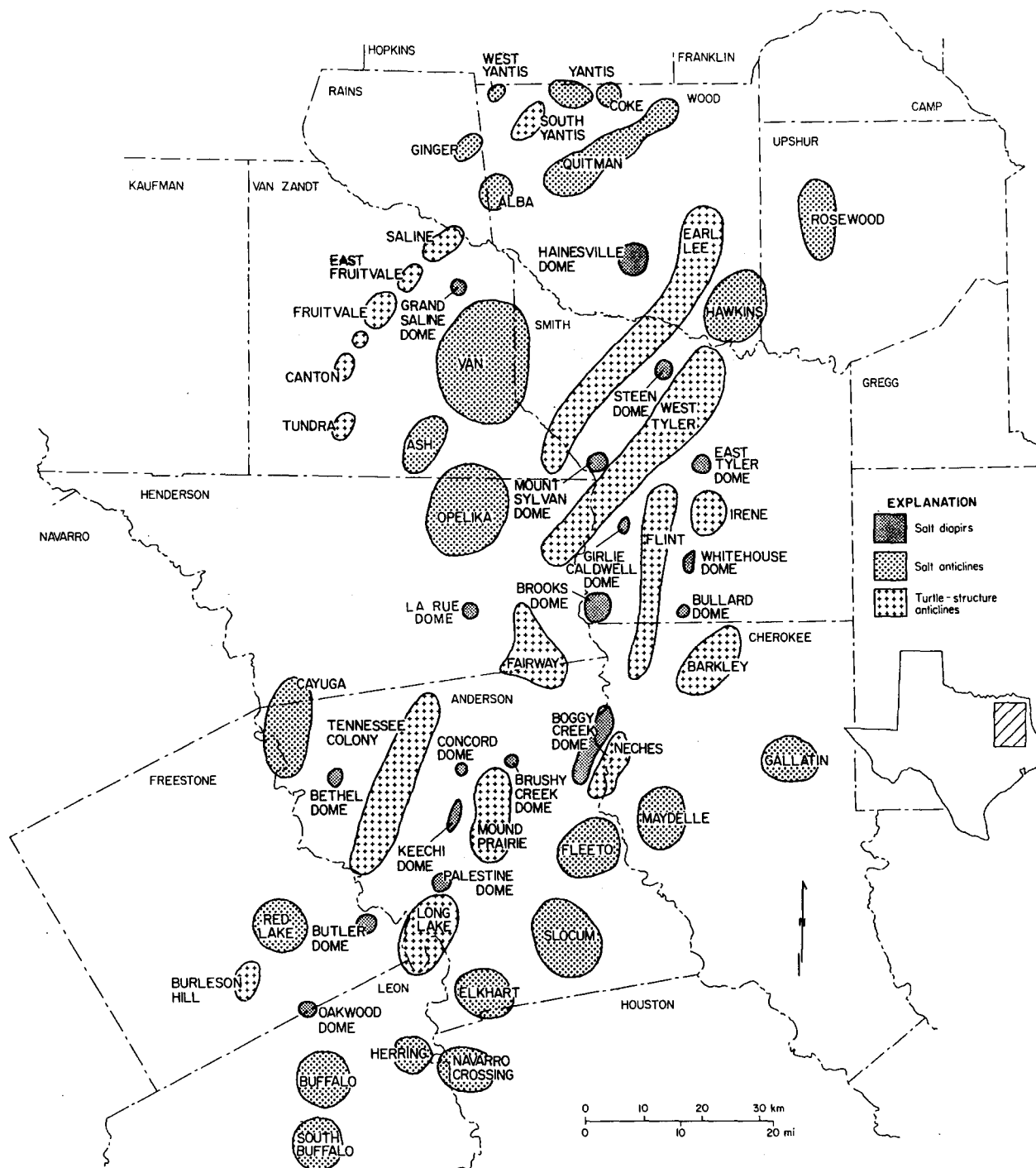
Figure 13. Turtle-structure anticlines, salt anticlines, and salt diapirs, East Texas Basin. Structures were identified using data from well logs, seismic profiles, and residual gravity data.

27

SEISMIC STRATIGRAPHY AND SALT MOBILIZATION ALONG THE NORTHWESTERN MARGIN OF THE EAST TEXAS BASIN

M. P. A. Jackson and David W. Harris

Seismic stratigraphy suggests that deformation of the Louann Salt began in the Late Jurassic at shallow depths near the basin margins. Acting as a zone of décollement, the salt allowed detachment of the folded overlying strata from the underlying planar strata.

Interpretation of two dip-oriented seismic profiles (purchased from Teledyne Exploration Company), based on sixfold common-depth-point reflection, provides information on the timing and nature of salt mobilization near the northwestern margin of the basin (fig. 14). Control is provided by electric logs from 24 deep drillholes. Eight well-defined reflections outline the subsurface configuration (table 2). Structural and stratigraphic disconformities along some of these reflections delineate four main seismic sequences, termed M1 through M4 (table 2), within the Mesozoic section. The principal features observed in the two seismic profiles are schematically illustrated in figures 15 and 16.

The Ouachita Fold Belt, which serves as a Paleozoic basement for the succession summarized in table 2, can be recognized for only a few kilometers on either side of the Mexia-Talco fault zone (fig. 15). The reflection configuration within the basement is discontinuous but shows a marked change from generally flat-lying attitudes southeast of the fault zone to moderate southeastward dips in the northwest. The dip transition zone is obscured by the overlying Mexia-Talco fault zone.

Seismic sequence M1, consisting of red beds of the Eagle Mills Formation and red beds and evaporites of the Werner Formation, onlaps the basement unconformity. The M1 sequence thickens rapidly to the southeast from zero thickness (confirmed by electric log data), suggesting that the rift sequence was deposited in a half graben whose fault-bounded margin coincides in plan view with both the underlying dip transition zone in the Paleozoic basement and the overlying Mexia-Talco fault zone.

Seismic sequence M2, represented by the Louann Salt, is characterized by prominent boundary reflections and a lack of internal reflections. Thicker zones of salt correspond to areas of gravity lows. The salt represents a zone of décollement between the extremely planar upper surface of sequence M1 below and the folded M3 sequence above. Its updip limit coincides with the Mexia-Talco fault zone (figs. 15

and 16). The salt wedge thickens downdip to form low-amplitude swells before being truncated by normal faults active during deposition of the lower M4 sequence. These faults partly coincide with the subsurface Edgewood Graben, which from the gravity residuals appears to be salt poor along the seismic lines. Salt withdrawal by downdip creep, accentuated by preferential loading in the graben, may have produced the graben. Downdip of the Edgewood Graben, the salt forms the cores of a series of moderate-amplitude anticlines; in some cases these structures are ridges extending laterally from large offline salt structures such as Van Dome (fig. 15). The seismic profiles join near the Mount Sylvan Diapir, which has pierced upward to the uppermost reflection in the M4 sequence (fig. 15).

Sequence M3 provides evidence of very early mobilization of the Louann Salt. In the region of low-amplitude folds, unit M3 shows slight but noticeable thinning in anticlines and thickening with diverging internal reflections in synclines (figs. 15 and 16), suggesting that folding of the salt started during deposition of Upper Jurassic carbonates. This contrasts with the central parts of the East Texas Basin where deformation of the salt was apparently initiated by M4 clastic sedimentation.

The lower part of unit M4, particularly the terrigenous clastic units of the Schuler and Hosston Formations below the Pettet reflection, was deposited during folding of the salt anticlines and coeval evacuation of salt from the intervening synclines, and during the rise of the salt pillow that eventually formed the Mount Sylvan Diapir. This is evident from onlapping relations shown by reflections in the synclines and turtle structures on either side of the Mount Sylvan Diapir. Piercement by Mount Sylvan Diapir started by the Early Cretaceous, as evidenced by a secondary peripheral sink defined by thickened Pettet and Buda reflections. This reflection is continuous across the fault zone (figs. 15 and 16), which indicates that early faulting associated with the Edgewood Graben ceased by Pettet time. Growth of the western moderate-amplitude salt anticline continued until the end of the Cretaceous (fig. 16), probably reflecting growth of the adjacent Van Dome, a large salt anticline.

Seismic stratigraphic analysis therefore suggests that salt movement near the northwestern margin of the East Texas Basin started in the Late Jurassic, earlier than elsewhere in the basin. The analysis also clearly demonstrates that the Mexia-Talco peripheral fault system is situated directly above the updip limit of the Louann Salt subcrop. The base of the Louann Salt is planar here so that the fault zone cannot be ascribed to crestal rupturing of an anticlinal or monoclinal warp. The Mexia-Talco

fault system appears to be a pull-apart structure formed by basement creep of the clastic overburden above the Louann décollement zone; this suggests that fault displacement was aseismic and did not involve the pre-Louann basement when it was active in the late Mesozoic and early Tertiary.

Table 2. Principal seismic reflections and seismic units near the northwestern margin of the East Texas Basin.

Series	Seismic reflection	Seismic unit
uK/Tx	Upper Navarro Marl (UNM)	
uK	Top Pecan Gap Chalk (TPGC)	
uK	Top Austin Chalk (TAC)	M4
uK/lK	Top Buda Limestone (TBL)	
lK	Top Pettet Limestone (TPL)	
uJ	Top Gilmer Limestone (TGL)	
uJ/mJ	Top Louann Salt (TLS)	M3
mJ	Base Louann Salt (BLS)	M2
Ŧ	Unconformity at base of Eagle Mills Formation	M1
Pz	Basement (Ouachita Fold Belt)	
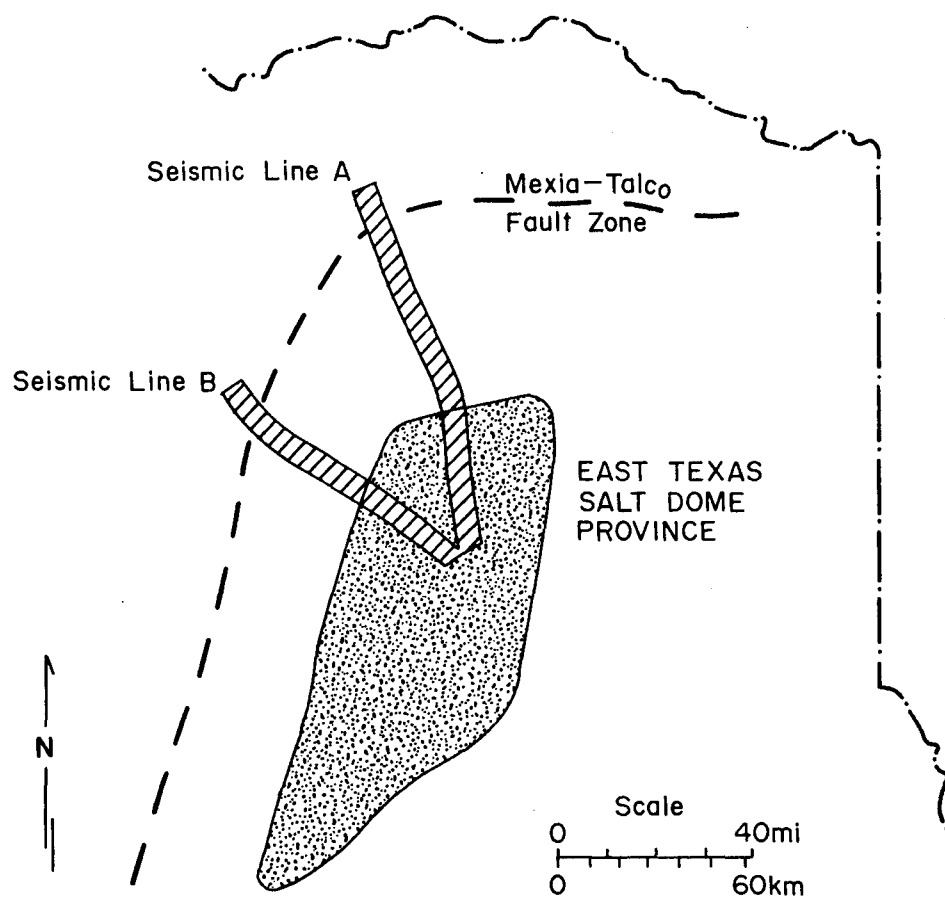
Figure 14. Locality map, seismic lines A and B, East Texas.

Figure 15

SE NW

Mexia-Talco Fault Zone

surface

UNM
TPGC
TAC
TBL

M4
M4

downthrow

Hainesville salt withdrawal

M4

M4

onlap

TCVL

TPL

M4

turtle structure

turtle structure

M3

thinning

?f Edgewood Graben

salt ridge from Quitman Dome

?f

EMI onlap
Pz

Pz

?f

EXPLANATION

TGL

M2

salt ridge from Van Dome

TLS-BLS

Mt. Sylvan Diapir

——— Moderate-strong reflection

– – – – Weak reflection

Salt

?f Inferred fault

Local depocenter

Figure 15. Schematic dip-oriented seismic section along line A from Mexia-Talco fault zone to Mount Sylvan diapir, East Texas Basin (not to scale; large vertical exaggeration). See table 2 for symbols of seismic reflections and abbreviations of units. Original seismic data courtesy of Teledyne Exploration Co.

Figure 16

SE NW

Mount Sylvan rim syncline

Van anticline

Mexia-Talco Fault Zone

surface

TPGC

M4
M4

TAC
TBL

M4

TCVL

updip limit of Louann Salt

TPL

M4

onlap

EXPLANATION

M3

——— Moderate to strong reflection

– – – – Weak reflection

Salt

TGL
TLS

M2

thickening in syncline

?f

salt ridge from Van Dome

diverging reflections in syncline

Inferred fault

?f

BLS
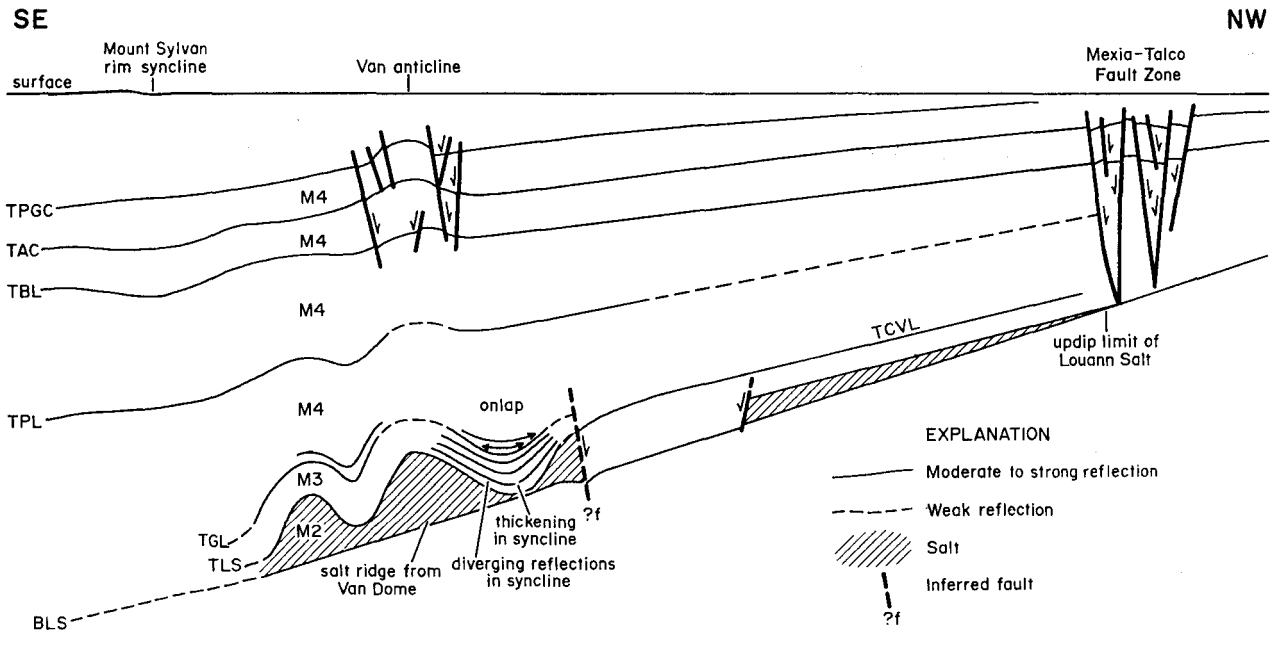
Figure 16. Schematic dip-oriented seismic section along line B from Mexia-Talco fault zone to near Mount Sylvan diapir, East Texas Basin (not to scale; large vertical exaggeration). See table 2 for symbols of seismic reflections and abbreviations of units. Original seismic data courtesy of Teledyne Exploration Co.

32

GEOMETRY OF EAST TEXAS SALT DIAPIRS

Alice B. Giles

Fifteen East Texas salt domes meet the 914 m (3,000 ft) maximum depth limit for a nuclear waste repository. Of these 15, 11 may satisfy DOE's size criterion.

Depth and size are critical factors affecting the suitability of a salt dome to isolate nuclear waste. The U.S. Department of Energy has specified a maximum depth limit for dome repositories of 914 m (3,000 ft) (Brunton and McClain, 1977). Salt domes in the East Texas Basin shallower than 914 m (3,000 ft) are listed in table 3, along with the minimum known depth to the top of these diapirs.

The minimum dome size (area) specified by DOE for a nuclear waste repository is 5.3 km^2 (1,300 acres) (Brunton and McClain, 1977). The sizes at a depth of 914 m (3,000 ft) for those domes meeting the maximum depth limit are listed in table 3. Dimensions were derived from structure contour maps on the top of salt constructed from well data and supplemented with contours from gravity models published by Netherland, Sewell and Associates, Inc. (1976) and Exploration Techniques, Inc. (1979).

Eleven domes may satisfy both size and maximum depth limit criteria for a nuclear waste repository. However, prior use precludes some of these domes from consideration as waste repository sites. For example, gas storage operations occur at East Tyler, Butler, Hainesville, and Bethel Domes. A large lake covers the Brooks Dome area. Salt mining and brining operations at Grand Saline and Palestine Domes, respectively, exclude these domes.

Four domes remain that satisfy DOE's size criterion: Keechi, Mount Sylvan, Oakwood, and Boggy Creek (figs. 17 through 20).

33

Table 3. Depth and size of East Texas salt domes.

Dome	Minimum known depth to dome from ground level, m (ft)		Source of depth data	Dome size at 914-m (3,000-ft) depth, km^2 (acre)	
Steen	23	(75)	Weeks #1 Pierce (Powers, 1926)	3.7	(914)
Palestine	37	(120)	Brine well discussed by Powers (1926)	5.9	(1,458)
Keechi	38	(125)	Navarro #2 Greenwood	6.1	(1,511)
Grand Saline	52	(171)	Morton Core Hole #2 (Peters and Dugan, 1945)	5.5	(1,359)
Brooks	59	(195)	Brooks-Saline #1 Woldert	15.3	(3,781)
Butler	95	(312)	Brine well discussed by Powers (1926)	6.6	(1,631)
Whitehouse	146	(480)	Humble #1 Van Haverburg	2.5	(618)
Bullard	161	(527)	Gulf #1 Morgan	0.9	(222)
Mount Sylvan	182	(596)	Humble #1 Reese	6.9	(1,705)
East Tyler	197	(645)	Warren #3 Kidd	9.0	(2,224)
Oakwood	214	(703)	Roxana #1 Marshall (Renick, 1928)	8.7	(2,150)
Hainesville	342	(1,123)	Pan American #1 Judge	20.5	(5,067)
Bethel	430	(1,411)	Texas Company #2 Cook	9.0	(2,224)
Boggy Creek	683	(2,242)	Humble #1 Clemons	9.7	(2,397)
Brushy Creek	889	(2,916)	Humble #B5 Royal National Bank	0.02	(5)

34
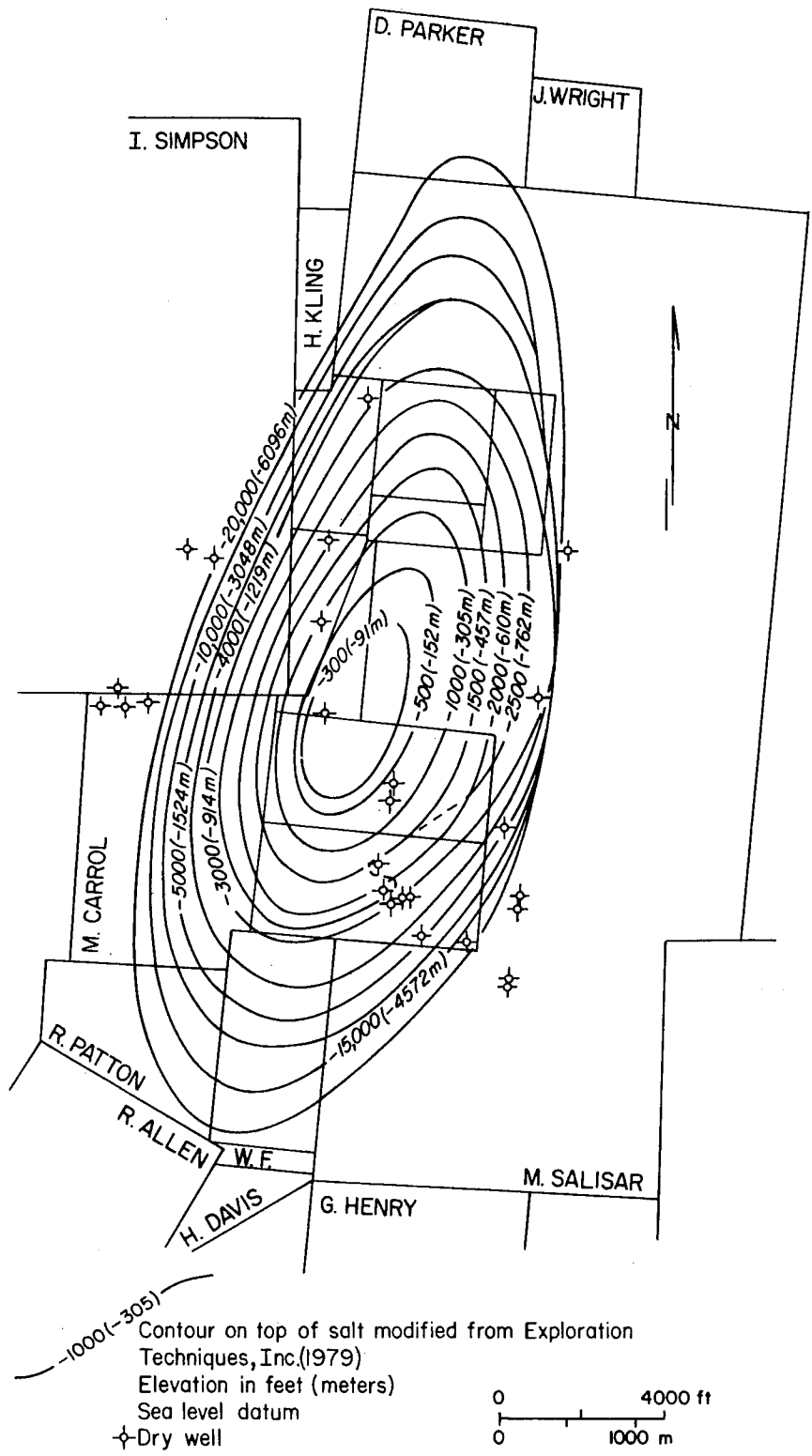
Figure 17. Structure contour map, top of salt, Keechi Dome, Anderson County, East Texas. Modified from gravity models by Exploration Techniques, Inc. (1979).

35
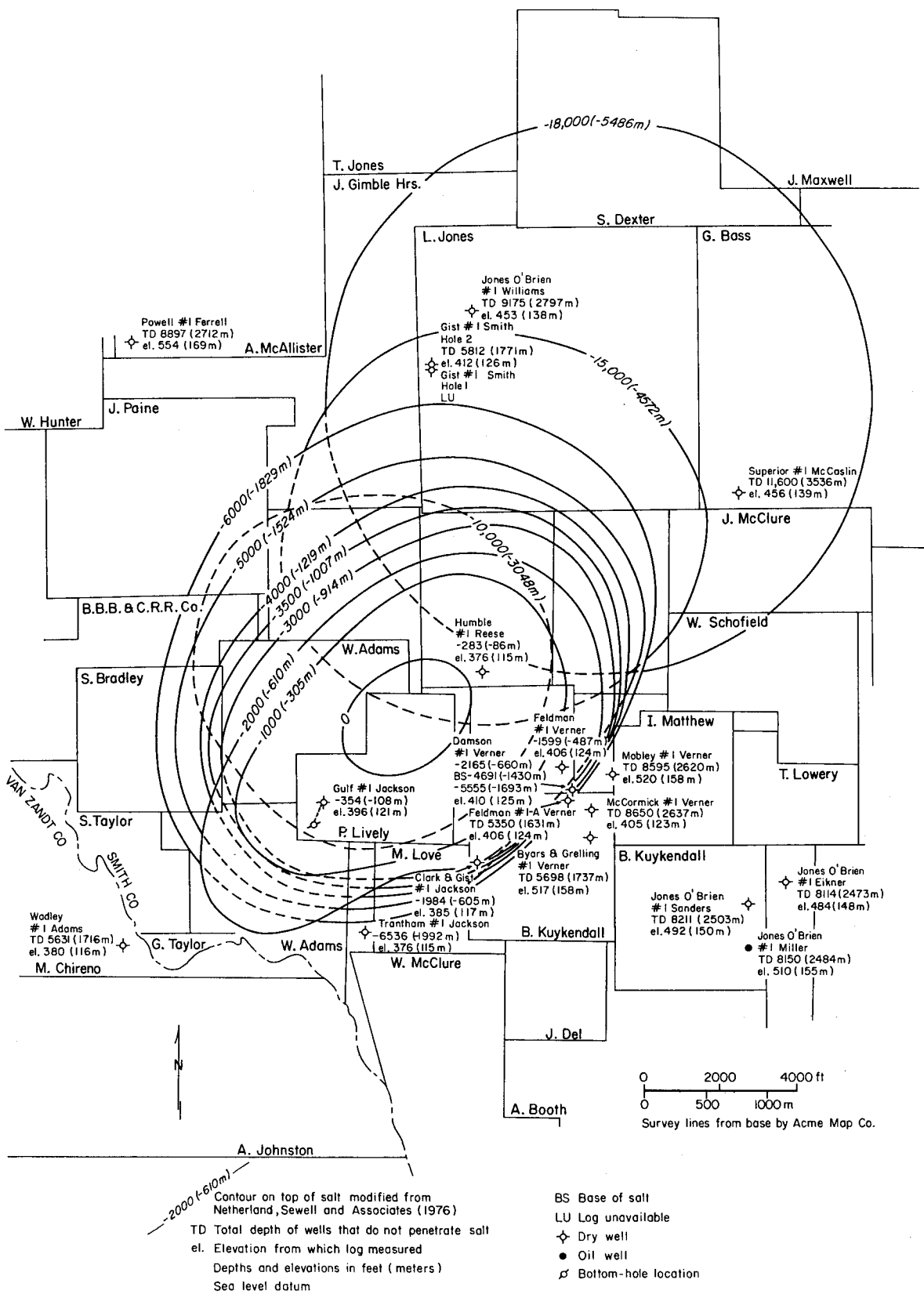
Figure 18. Structure contour map, top of salt, Mount Sylvan Dome, Smith County, East Texas. Modified from Netherland, Sewell and Associates (1976).
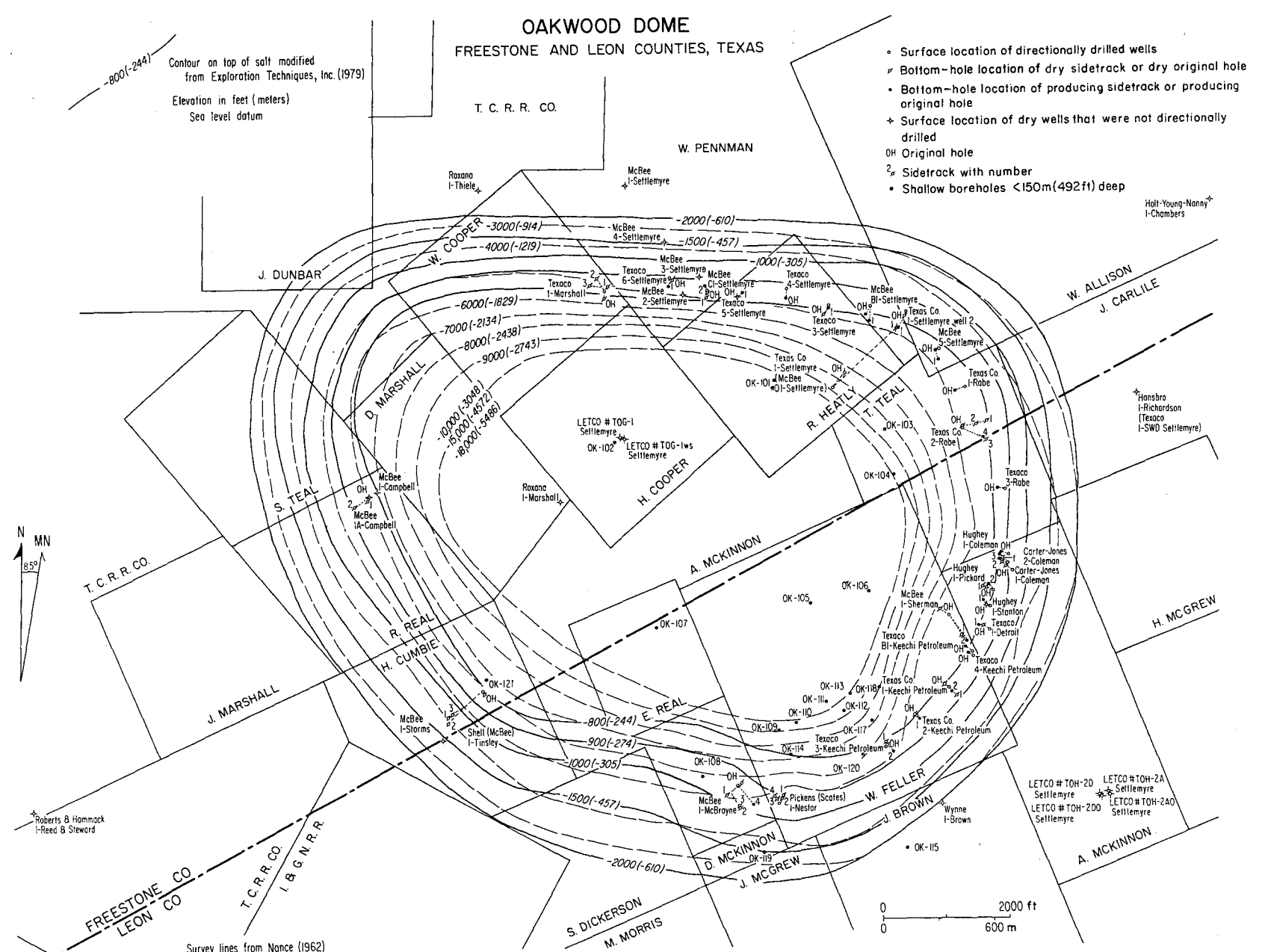
Figure 19. Structure contour map, top of salt, Oakwood Dome, Freestone and Leon Counties, East Texas. Modified from gravity models by Exploration Techniques, Inc. (1979).

W. Pool

R. Roundtree

R. Webb

J. Bell

W. Barnett

T. Trumble

T. Hays

T. East

Durrett

L. Johnson

A. Baxter

I&GNRR

-10,000(-3048m)
-9,000(-2743m)
-8,000(-2438m)
-7,000(-2134m)
-6,000(-1829m)
-5,000(-1524m)
-4,000(-1219m)
-3,000(-914m)
-2,000(-610m)

A. Oliphant

I. Durst
A. Oliphant

J. Allbright

Maverick

J. Trimble

M. Williamson
N. Johnson
P. Smith

A. Bullock
M. Kay

J. Trimble

L. Roberts

Farr & Hanks
J. Beeson

W. Lloyd

N. Sessna

S. Maverick

H. Sassamon

M. Windsor
M. Garcia

W. Roberts

M. Roberts

D. Roberts

Anderson Co
Cherokee Co

N

J. Mancha D. Clark

A. Clark H. Davis

J. Trimmer

W. Roberts N. Cannon

A. Patton
G. Tuggle

W. Wright

-3000(-914m) Contour on top of salt
Dry hole
Oil well
Gas well

Elevations in feet(meters)
Sea level datum

Survey lines and well locations
primarily from Texas Railroad
Commisson Boggy Creek Field
map.

0   4000 ft
0   1000 m

Figure 20.   Structure contour map, top of salt, Boggy Creek Dome, Anderson and Cherokee Counties, East Texas.

GROWTH HISTORY OF OAKWOOD SALT DOME, EAST TEXAS

Alice B. Giles

Mobilization of the Louann Salt in the Oakwood Dome area began in Late Jurassic (Smackover), when faulting probably caused uneven sediment loading. The dome became diapiric between deposition of the Cotton Valley Limestone and Pettet Formations. Growth continued at least until Claiborne time. Growth rates have declined from a maximum of 0.07 to 0.11 mm/yr (229 to 360 ft/m.y.) during the Early Cretaceous to 0.002 mm/yr (6.5 ft/m.y.) during post-Reklaw time.

The long-term tectonic stability of a salt dome for geologic isolation of nuclear wastes can be evaluated in part by reconstruction of the growth history of the dome. The growth history of Oakwood Salt Dome, a repository candidate, has been reconstructed by sequentially restoring major seismic reflectors to a horizontal position. Figure 21 is a palinspastic reconstruction from a seismic record section that was converted to a depth section using a single velocity function derived from an integrated sonic log. The reconstruction assumes that depositional surfaces were initially planar and that most deformation of post-Louann strata resulted from salt flowage.

Thickness variations exhibited by the Upper Jurassic Smackover Limestone in the vicinity of Oakwood Dome imply that mobilization of the Louann Salt had begun before the end of Smackover deposition. The close association of a Smackover depocenter (isopach thick) with a fault that cuts the reflector at the top of Louann Salt northwest of the dome suggests that early differential sediment loading on the salt in the area was partly fault controlled.

Oakwood Dome assumed a diapiric configuration during deposition of the Cotton Valley Limestone and pre-Pettet clastic sediments. A rim syncline that formed immediately adjacent to the west flank of the dome remained the principal source for salt that fed the diapir. Because there is no basal salt reflector on the seismic record, the amount of source salt still available for dome growth is unknown.

Southeast of the dome, salt on the downthrown side of the proposed fault appears to have lost contact with salt on the upthrown block during Cotton Valley Limestone-Pettet time, thereby restricting salt withdrawal on the southeast side of the dome to the relatively small area between the diapir and the inferred fault. Thick Cotton Valley Limestone-Pettet strata located southeast of Oakwood Dome were deposited as

salt flowed south into Buffalo Dome. Growth of Oakwood Dome continued into Claiborne time.

The small amount of stratal disruption near Oakwood Dome and the apparent absence of additional strata that would have been originally over the dome suggest that the dome remained at or near the depositional surface during most of its history. Although the model depicts a relatively thin sediment cover over the diapir, it is possible that the dome occasionally was exposed because Jurassic and Cretaceous strata have been removed from above the dome. The dome currently is covered by approximately 215 m (700 ft) of Tertiary sediments. Whether this depth of burial was typical in the past is unknown.

On the basis of the previous growth model, the maximum average vertical growth rates for different time periods were calculated. Three different approaches were used for three different time intervals because of variations in (1) the style of dome growth, (2) the response of strata to dome growth, and (3) the preservation of strata over the dome. Growth rates appear to have decreased from a maximum of 0.07 to 0.11 mm/yr (229 to 360 ft/m.y.) during Early Cretaceous to 0.002 mm/yr (6.5 ft/m.y.) during post-Reklaw time.

A maximum average vertical growth rate of the Oakwood diapir from Early Cretaceous to early Tertiary can be estimated by dividing the maximum thickness of strata in the rim syncline adjacent to the dome by the absolute time required to deposit the section (table 4). If the dome was at or near the depositional surface from post-Cotton Valley Limestone to post-Pettet Formation time, then the dome growth rate was equivalent to the sedimentation rate. Dome growth rates decline from a maximum of 0.07 to 0.11 mm/yr (229 to 360 ft/m.y.) during Early Cretaceous to 0.02 to 0.04 mm/yr (66 to 130 ft/m.y.) in early Tertiary. These statistics indicate a generally declining rate of dome growth.

The rate of dome growth during early Claiborne time is estimated at 0.01 mm/yr (33 ft/m.y.), which was determined by measuring the stratigraphic thinning of Carrizo and Reklaw strata over Oakwood Dome. This value measures uplift of the units during their deposition. By dividing the maximum amount of stratigraphic thinning over the dome by the time required to deposit the units, a maximum average vertical growth rate for that time was determined (table 5).

A more recent growth rate for Oakwood Dome can be calculated by dividing the amount of structural relief of Reklaw strata over the dome by the time since their deposition (table 6). This value (0.002 mm/yr [6.5 ft/m.y.]) represents the average

40

rate of relative uplift of the given unit from the time of deposition to the present, assuming the depositional surface was initially planar. These calculated values support the theory that vertical growth rates of Oakwood Dome have been declining. The most recent uplift cannot be determined because post-Claiborne sediments either were not deposited over the dome or have been removed by erosion.

Table 4. Maximum average vertical growth rate of Oakwood Salt Dome, East Texas, from Cotton Valley to Wilcox time.

Stratigraphic interval	Absolute time, m.y.*	Vertical rise of dome, m(ft)	Maximum average vertical growth rate	
			mm/yr	(ft/m.y.)
Top of Cotton Valley Limestone to top of Pettet Limestone	28.0 to 31.5	2,073 (6,800)	0.07	(216-243)
Top of Pettet Limestone to top of Buda Limestone	11.5 to 18.0	1,305 (4,280)	0.07-0.11	(229-360)
Top of Buda Limestone to top of Eagle Ford Shale	11.0 to 14.0	658 (2,160)	0.05-0.06	(164-196)
Top of Eagle Ford Shale to top of Upper Navarro Marl	20.5	610 (2,000)	0.03	(98)
Top of Upper Navarro Marl to top of Midway Shale	7.5 to 12.0	274 (900)	0.02-0.04	(65-130)

Table 5. Maximum average vertical growth rate of Oakwood Salt Dome, East Texas, during early Claiborne time (see fig. 21).

Stratigraphic interval	Average thickness off dome, m(ft)	Minimum thickness over dome, m(ft)	Maximum thinning over dome, m(ft)	Absolute time, m.y.*	Maximum average vertical growth rate, mm/yr (ft/m.y.)
Top of Wilcox to top of Reklaw	76 (250)	54 (177)	22 (74)	2	0.01 (33)

Table 6. Average vertical growth rate of Oakwood Salt Dome, East Texas, since Reklaw time (see fig. 29).

Stratigraphic horizon	Structural relief, m(ft)	Time since deposition, m.y.*	Average vertical growth rate, mm/yr (ft/m.y.)
Top of Reklaw Fm	76 (250)	48	.002 (65)

*Derived from Berryhill and others (1968); Nichols and others (1968); Gundersen and others (1969); Martinez and others (1976); Van Hinte (1976a); Vail and others (1977); and Law Engineering Testing Co. (1978, 1980).

41

Present

Top of Upper Navarro Marl
Top of Eagle Ford Shale
Top of Buda Limestone

Top of Pettet Limestone

Top of Cotton Valley Limestone
Top of Smackover Limestone

End of Upper Navarro Marl Time

Top of Eagle Ford Shale
Top of Buda Limestone

Top of Pettet Limestone

Top of Cotton Valley Limestone
Top of Smackover Limestone

End of Eagle Ford Time
Top of Buda Limestone

Top of Pettet Limestone

Top of Cotton Valley Limestone
Top of Smackover Limestone

End of Buda Time

Top of Pettet Limestone

Top of Cotton Valley Limestone
Top of Smackover Limestone

End of Pettet Time

Top of Cotton Valley Limestone
Top of Smackover Limestone

End of Cotton Valley Limestone Time
Top of Smackover Limestone

Louann Salt
Fault

End of Smackover Time

0   1 km
0   1 mi
No Vertical Exaggeration

Figure 21. Growth reconstruction of Oakwood Dome, East Texas. Cross section based on seismic reflection profile. Dashed line indicates where seismic reflections are indistinct or absent. Seismic profile courtesy of Law Engineering Testing Co.

PRELIMINARY STUDY OF THE UPPER JURASSIC (COTTON VALLEY) AND LOWER CRETACEOUS (HOSSTON/TRAVIS PEAK) FORMATIONS OF THE EAST TEXAS BASIN

Mary K. McGowen and David W. Harris

Early salt tectonic activity within the East Texas Basin was largely controlled by sedimentation, particularly during Late Jurassic (Cotton Valley) and Early Cretaceous (Hosston) when sedimentation was dominated by the influx of terrigenous clastics. Understanding the mechanisms responsible for early salt movement in the East Texas Basin is essential to the understanding of domal growth and stability. Determination of dome stability is critical when evaluating the suitability of salt domes as nuclear waste repositories.

The suitability of salt domes for nuclear waste repositories is contingent upon the tectonic stability of the domes. Dome-growth analysis, one approach toward evaluating stability, indicates that salt mobilization within the East Texas Basin was initiated during Late Jurassic and Early Cretaceous. Studies are underway to investigate the effects that the first major influx of terrigenous clastics into the basin had on salt mobilization. The earliest and most significant influx of terrigenous clastics into the East Texas Basin occurred during Cotton Valley (Late Jurassic) time and continued into the Early Cretaceous with deposition of the Hosston (Travis Peak) Formation (fig. 2). Before deposition of the Cotton Valley Group and the Hosston Formation, sedimentation in the basin was dominated by deposition of carbonates, evaporites, and marine shales.

Incipient salt movement began at different times in different parts of the basin. In general, the earliest movement of the salt began along the margins of the basin and was initiated by downdip gravity gliding of salt. Movement was induced by sedimentary loading of carbonate deposits combined with possible basinward tilting owing to increased subsidence toward the center of the basin. This early episode of salt movement began during deposition of the Smackover Formation and the Cotton Valley Limestone units (see "Seismic Stratigraphy and Salt Mobilization Along the Northwestern Margin of the East Texas Basin").

More extensive salt movement began with deposition of Upper Jurassic Cotton Valley clastic sediments. As can be demonstrated on a seismic section near Van Dome, no appreciable time-thickness variation can be noted between reflectors at the top of the Cotton Valley Limestone and the top of the Louann Salt (fig. 22). This is

contrary to thickness variations between reflectors at the top of the Pettet Formation and the top of the Cotton Valley Limestone (fig. 22) that indicate that in this region deposition of the Cotton Valley clastics was coeval with salt movement. Salt movement in the northwestern part of the basin appears to have been initiated by differential loading of a large fluvial-deltaic system prograding from the northwest. The density contrast between the high-percent-sand facies of the delta and subjacent salt created a mass imbalance that initiated salt movement.

Preliminary studies indicate that orientation of salt ridges is normal in relation to the axis of sedimentation because of the combined effects of gravity gliding and deltaic deposition. These salt ridges are approximately concentric with the edge of the basin as defined by the faults of the Mexia-Talco fault system.

Regional stratigraphic cross sections across the East Texas Basin document a high-percent-sand facies in the Cotton Valley Group in the northwestern part of the basin relative to the Cotton Valley Group in other areas of the East Texas Basin (figs. 23 and 24). A composite Cotton Valley-Hosston net-sand map also outlines a sand thick or depocenter northwest of Van Dome (fig. 25). It appears that Louann Salt was squeezed into a ridge downdip of the sand depocenter. Salt-ridge formation was the incipient stage in the development of Van Salt Dome. Van Dome is one of the largest of the many salt pinnacles that rise above the main salt mass constituting these ridges.
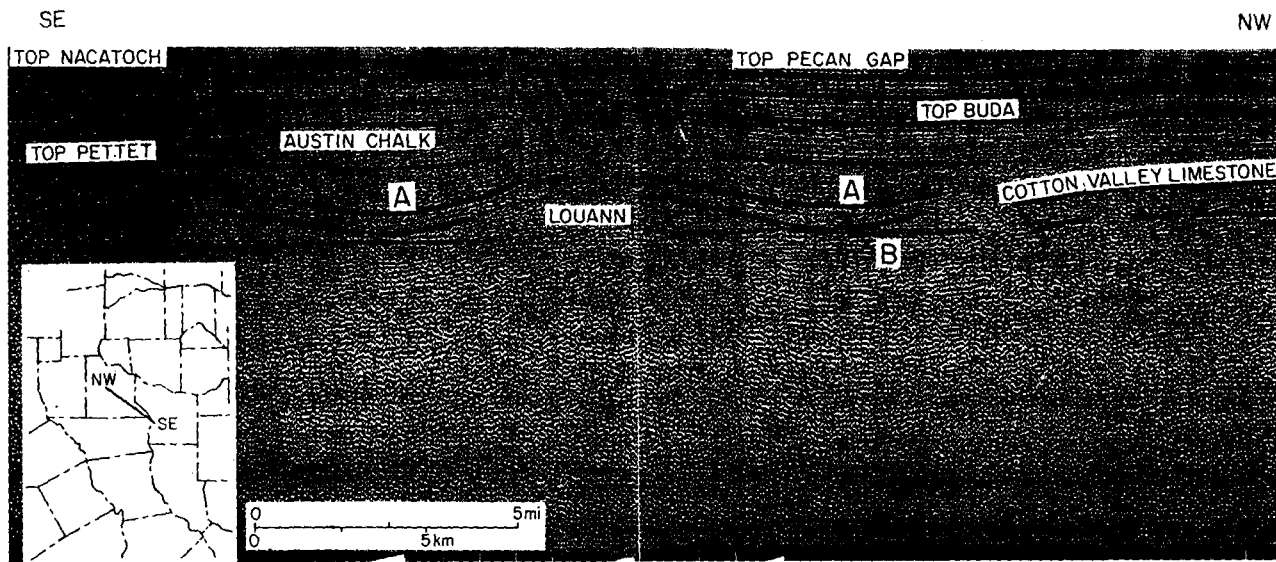
Figure 22. Seismic section through Van Zandt County, East Texas, suggests two important relations relative to salt movement. First, significant time thickness variations between reflectors at the top of Pettet Formation and Gilmer Limestone (A) suggest that deposition of the Cotton Valley clastics was coeval with salt movement. Second, no appreciable time-thickness variations exist between older reflectors (top of Gilmer Limestone and top of Louann Salt) (B). Seismic profile courtesy of Teledyne Exploration Co.
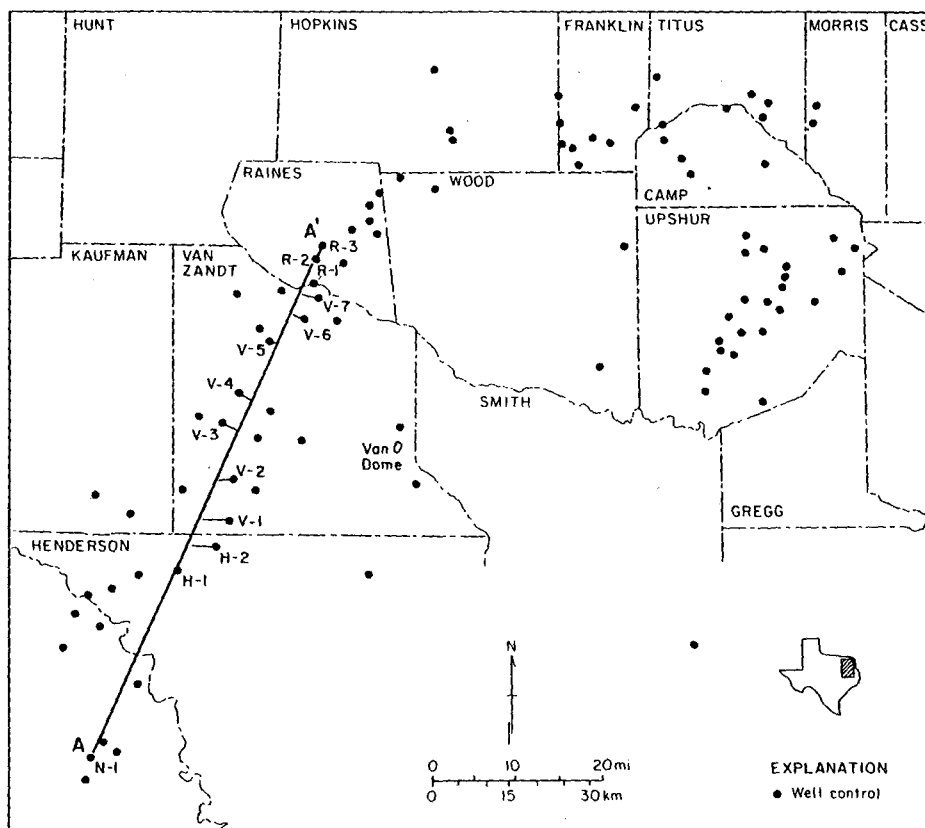
Figure 23. Location map, northwestern part, East Texas Basin, showing well control and location of regional cross section A-A'.
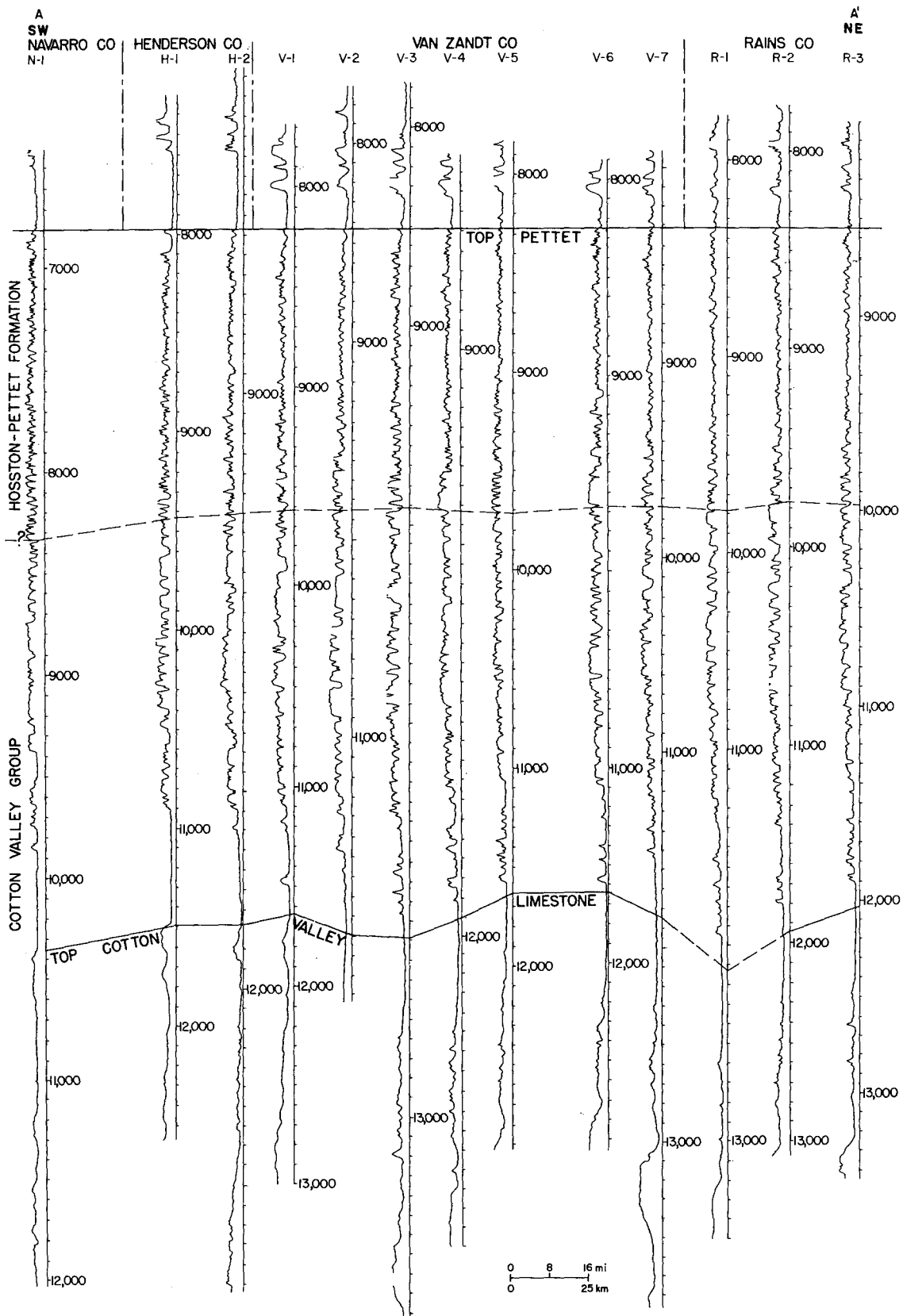
Figure 24. Northeast-southwest regional stratigraphic cross section A-A', Cotton Valley Group and Hosston Formation, East Texas Basin.

46
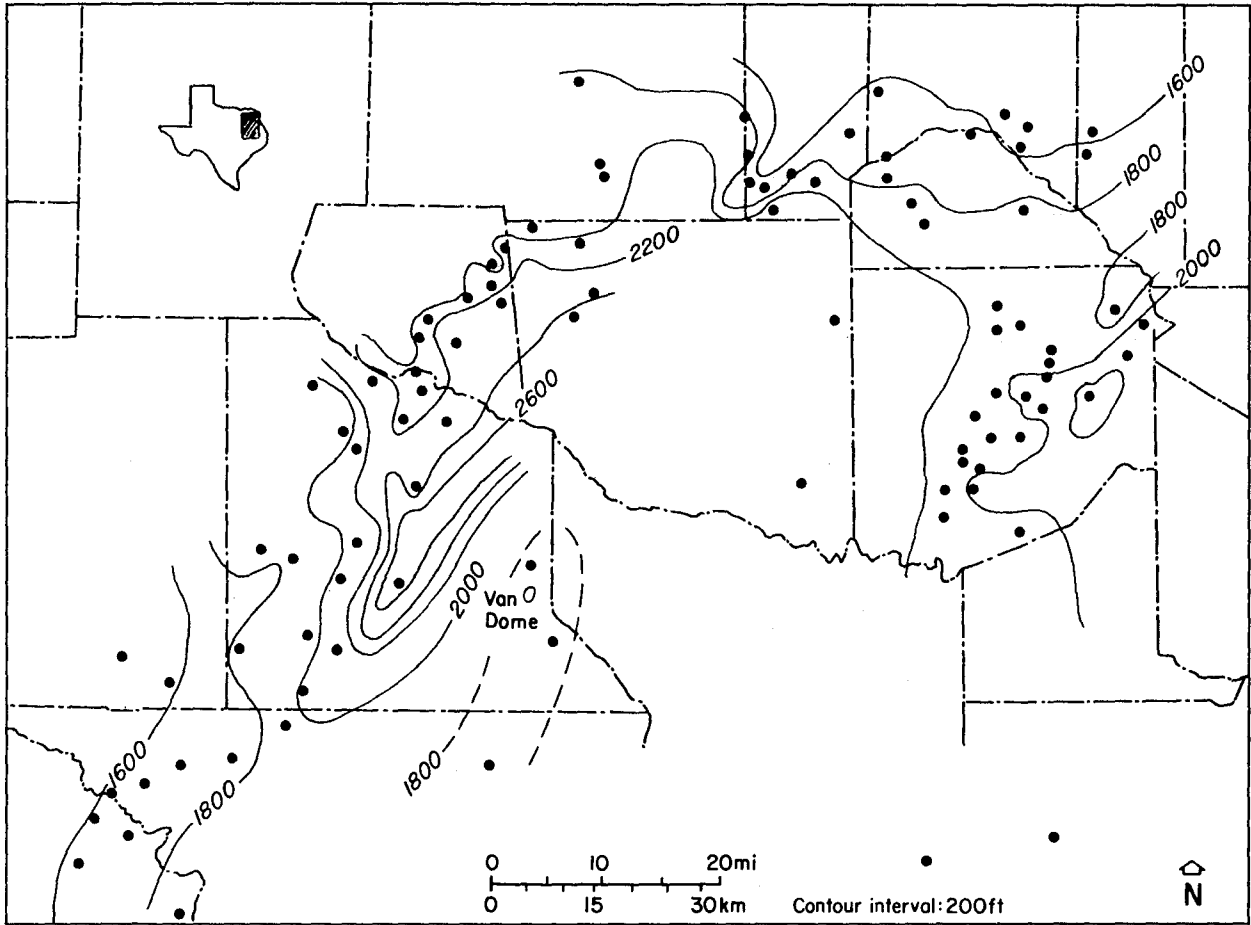
Figure 25. Composite net-sand map, Cotton Valley-Hosston (Travis Peak), East Texas Basin.

47

DEPOSITIONAL SYSTEMS OF THE LOWER CRETACEOUS PALUXY FORMATION, EAST TEXAS BASIN

Steven J. Seni

Depositional systems in the Paluxy Formation, East Texas Basin, include thick fluvial-deltaic sequences along the northern perimeter of the basin and a fine-grained terrigenous clastic-carbonate shelf in the basin center. The Arbuckle-Ouachita Mountains shed sediments that accumulated in alluvial fans and fan deltas localized along the Mexia-Talco fault system. Candidate domes (Oakwood and Keechi) for isolation of nuclear waste occur in the southern part of the basin where the Paluxy Sand grades into shelf shale and marl facies of the equivalent Walnut Formation.

During Paluxy time (Early Cretaceous), the East Texas Basin was a marine embayment that received sediments from northwestern, northern, and northeastern sources. An Arbuckle-Ouachita Mountain source area supplied sediments to braided streams and alluvial fans along the northern periphery of the basin (fig. 26). North of the 33rd parallel, the upper part of the Glen Rose Group (post-Massive Anhydrite) is predominantly a terrigenous clastic sequence that is gradational with the overlying Paluxy Formation. The two formations illustrate coastal offlap and form a facies tract that was supplied with sediment from the same source areas. The proximity (80 to 120 km [50 to 75 mi]) of mountainous source areas and the presence of blocky channel-fill log patterns (fig. 27) indicate that bed-load fluvial systems supplied fan deltas that were localized along the northern perimeter of the Mexia-Talco fault system. Destructional delta, barrier bar, and embayment facies were formed by marine reworking of fan delta lobes (fig. 28). West of the Mexia-Talco fault system, the Paluxy Formation contains strandplain facies deposited on a stable Glen Rose carbonate platform (fig. 29). Coarse-grained fluvial-deltaic deposits of the upper Glen Rose and Paluxy Formations were concentrated south of and along the Mexia-Talco fault system in grabens formed from downdip flow of the Louann Salt. Toward the center of the basin, south of Henderson, Smith, and Gregg Counties, the Paluxy Sand grades into shelf shale and marl facies (fig. 30) of the equivalent Walnut Formation.

The effect of salt tectonic activity on facies distribution decreased toward the center of the basin where clastic input diminished far from source areas. Candidate domes (Oakwood and Keechi) for isolation of nuclear waste are located in the southern part of the basin. This location favors dome stability because permeable Paluxy sands are absent around the domes.
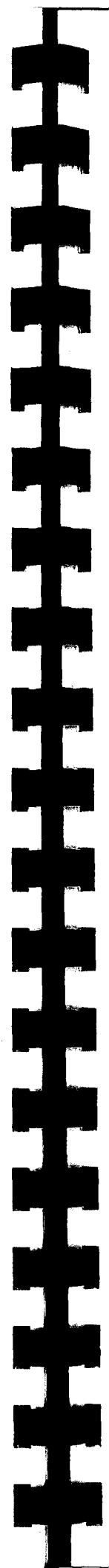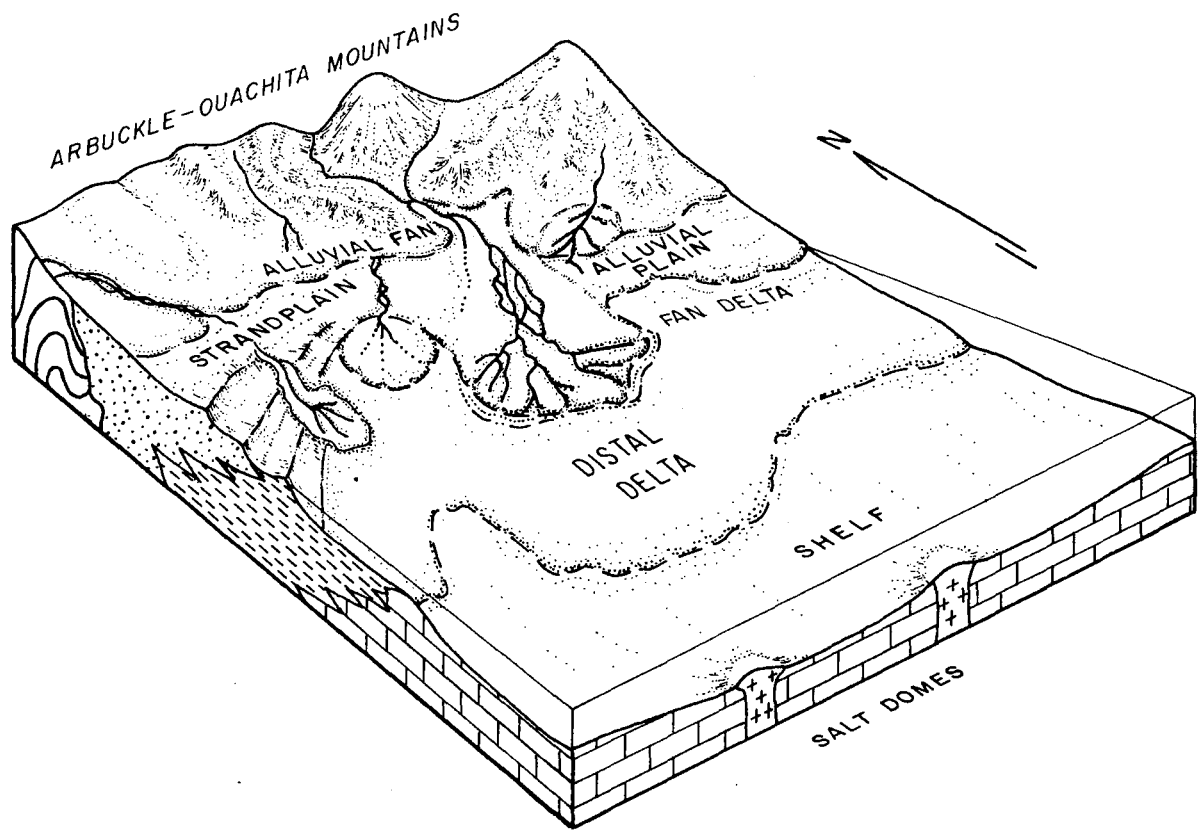
Figure 26. Schematic block diagram showing inferred Paluxy depositional systems, East Texas Basin.

49

HUGHEY OPER AND
B. ROSS
I O'Brien

GOODLAND
FM

PALUXY
FM

GLEN ROSE
FM

SP   R   ohm m²/m

5700

5800

5900

6000

6100

6200

6300

FLUVIAL FACIES
in Mexia-Talco
fault zone

EXPLANATION

Sandstone-conglomerate

Shale

Limestone and calcareous shale

5800 Depth below surface (ft)
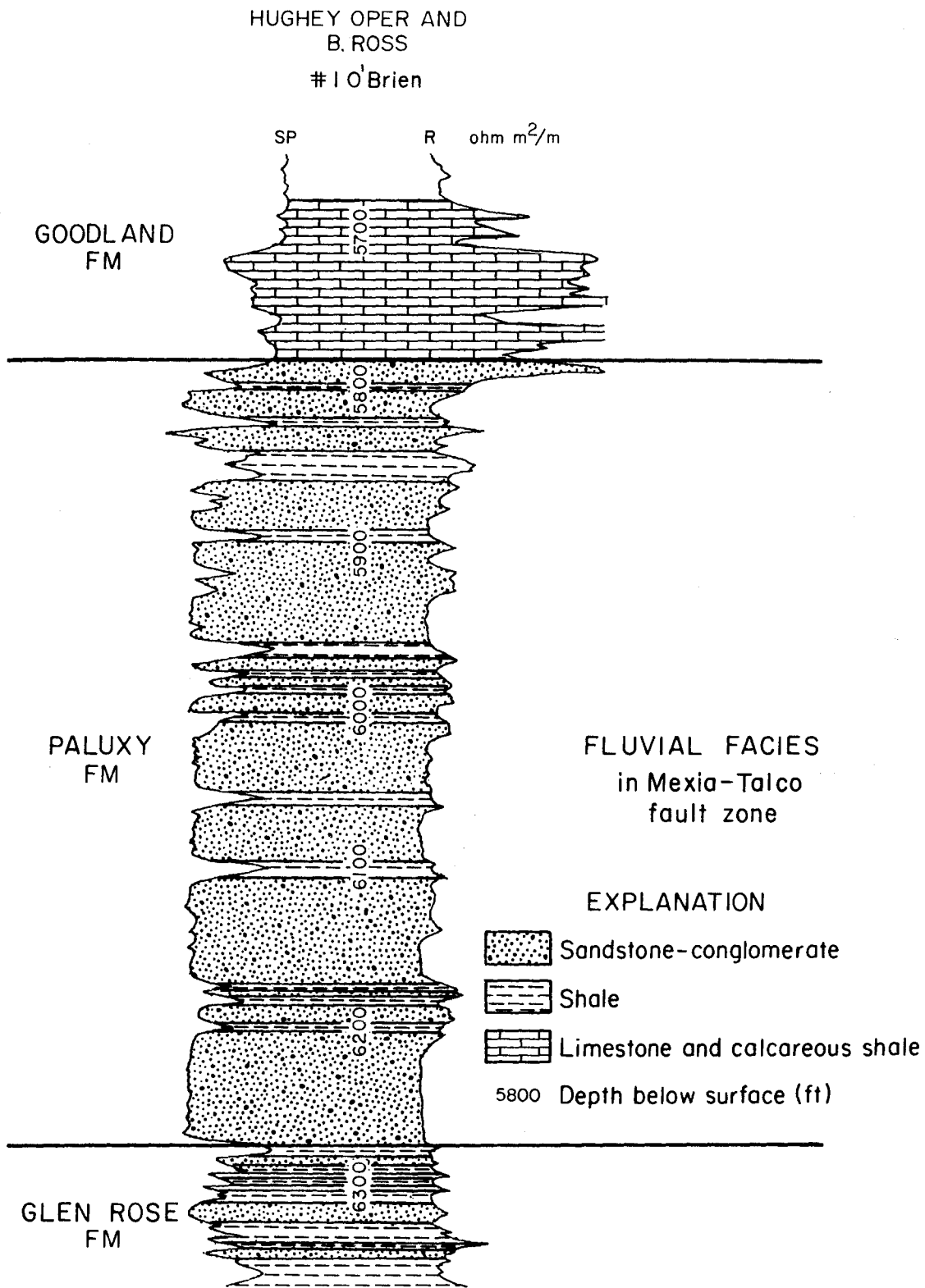
Figure 27.   Typical geophysical and lithic log of bed-load fluvial systems, Paluxy Formation, Mexia-Talco fault zone, East Texas.

CHERRYVILLE CORP.
#1 Grimes

GOODALE, BERTMAN AND CO.
#1 Brogdon Unit

HUMBLE
#1 Perryville GU

GOODLAND
FORMATION

TOP OF
PALUXY FORMATION

DELTA-DESTRUCTIONAL
EMBAYMENT FACIES

BRAIDED-
STREAM
FLUVIAL
FACIES

FAN-DELTA
PROXIMAL
FACIES

FAN-DELTA
DISTAL FACIES

GLEN ROSE
FORMATION

EXPLANATION

	Limestone and calcareous shale	Progradational sequence
	Sandstone-conglomerate	6700 Depth below surface (ft)
	Shale	

Figure 28. Cross section showing transition between sand-rich fluvial facies and fan-delta facies, Paluxy Formation, East Texas Basin. Delta abandonment (subsidence or rising sea level greater than sedimentation) caused barrier-bar and other delta-destructional facies to transgress fluvial-deltaic facies.
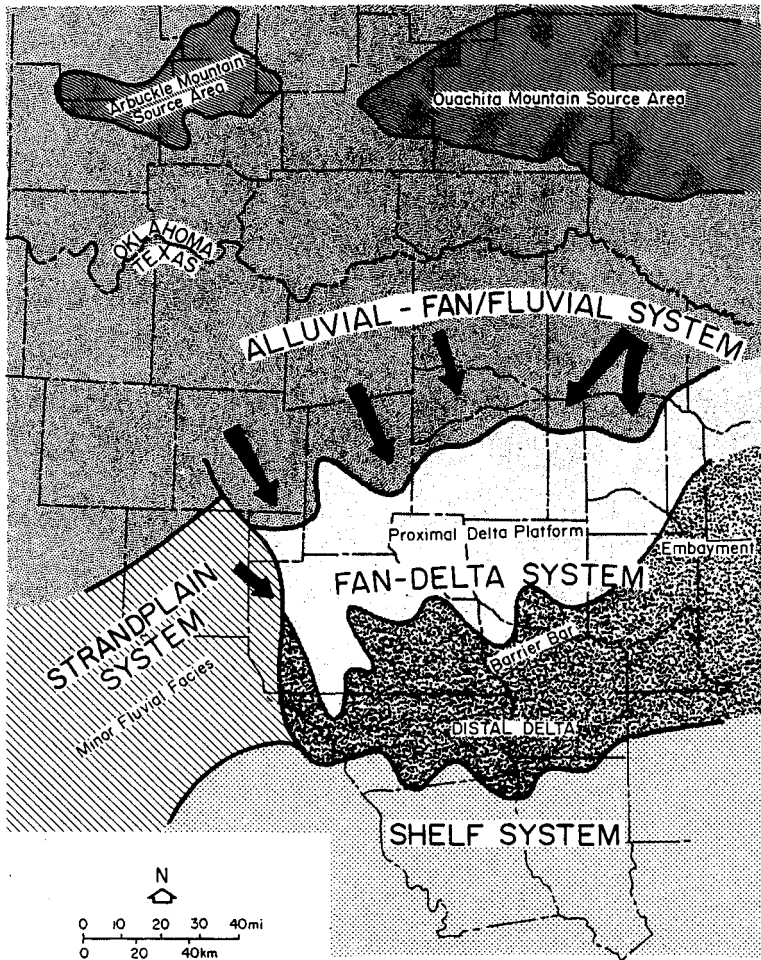
Figure 29. Depositional systems and component facies, Paluxy Formation, East Texas Basin. Interpretation based on net-sand maps, cross sections, and log data.

51
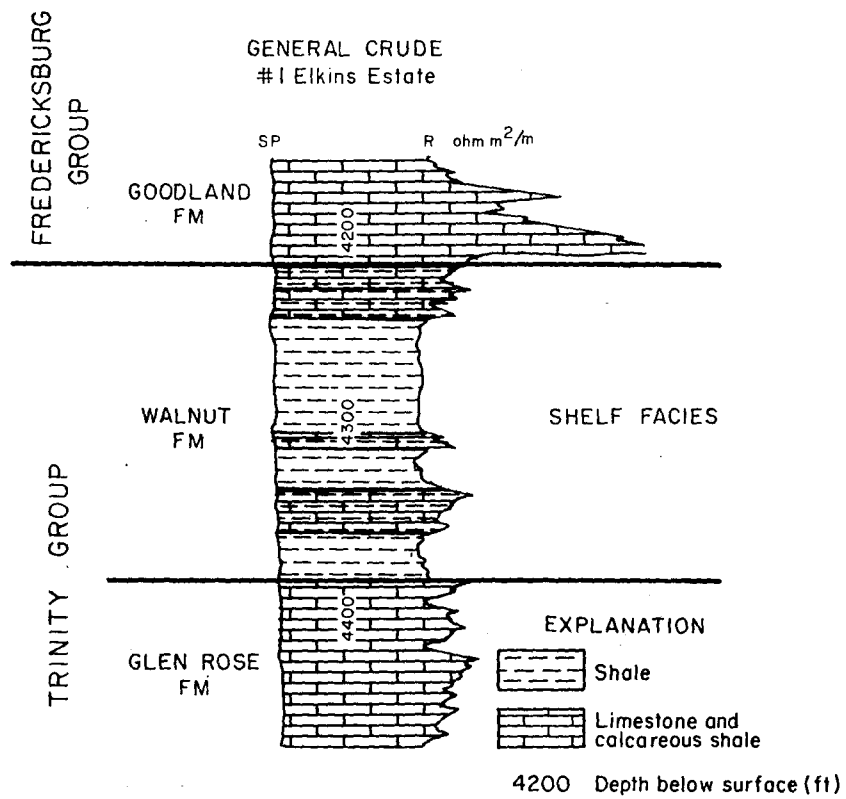
Figure 30. Typical geophysical and lithic log of fine-grained terrigenous clastic-carbonate shelf facies, Walnut Formation, East Texas Basin. Walnut shelf facies are equivalent to nearshore Paluxy facies.

52

THE EFFECT OF SALT TECTONICS ON DEPOSITION OF THE LOWER CRETACEOUS PALUXY FORMATION, EAST TEXAS

Steven J. Seni

Changes in depositional styles, facies, and thickness of the Paluxy Formation are related in part to salt tectonic activity. Regional facies and thickness variations along the northern periphery of the East Texas Basin resulted from salt flowage, contemporaneous faulting, and, locally, from uplift around salt anticlines. Local thickness changes in the center of the basin are associated with rim synclines around salt diapirs.

Salt tectonic activity was a major factor influencing variations in thickness, sand-body geometry, and depositional facies in the Lower Cretaceous Paluxy Formation. Major salt-related structures that affected Paluxy sedimentation include contemporaneous faulting along the Mexia-Talco fault zone, broad uplift associated with salt anticlines, and subsidence of rim synclines associated with active salt diapirism (fig. 31). Whether salt movement was initiated, accelerated, or maintained by Paluxy sedimentation is a critical question that remains unanswered. Paluxy sedimentation patterns can be explained by preferential (thick) deposition in areas that subsided by salt withdrawal, as well as by restricted (thin) deposition in areas uplifted by salt anticlines.

Paluxy thickness and net-sand values are greatest along the Mexia-Talco fault zone in the northern part of the East Texas Basin (figs. 32 and 33). Downdip flowage of Louann Salt created down-to-the-coast normal faults, grabens, and intervening horsts. A basement fault may have influenced salt movement and localization of the Mexia-Talco system (M. P. A. Jackson, personal communication, 1981). Alluvial fans and braided streams occupied low areas formed by contemporaneous faulting. Dip-oriented sedimentation trends were normal to the strike of the fault system.

Variations in Paluxy thickness and sedimentation patterns indicate that Van, Hainesville, and Hawkins Domes were actively growing salt anticlines (salt pillows of Trusheim, 1960) during Paluxy deposition (fig. 34). Fluvial-deltaic strata thicken, and sand percentages increase up to the margins of the salt anticline, but thin, sand-poor sequences overlie the salt structures. Major fluvial axes (5 to 10 km [8 to 16 m] wide) flank the Hainesville Dome. The axes occur 5 to 10 km (8 to 16 mi) east and 7 to 15 km (2 to 25 mi) west of the present location of the Hainesville Dome. A 40 to 200 percent increase in the thickness of Paluxy strata around the Hainesville Dome

indicates that development of Hainesville's primary peripheral sink (Trusheim, 1960) was initiated during Paluxy time because older formations do not show comparable thickening. According to Loocke (1978), Hainesville did not develop a diapiric configuration until erosion exposed the top of the salt core during Eagle Ford-Woodbine time.

Whereas subsidence associated with salt structures localized rivers and fan deltas in the northern part of the basin, in the southern part of the basin salt diapirs and associated rim synclines (secondary peripheral sinks of Trusheim, 1960) affected only the thickness of shelf facies. For example, shelf facies (Walnut Formation) thicken into the rim synclines around Palestine, Butler, Keechi, and Brushy Creek Salt Domes, but sandstone is absent (fig. 31). The thickness of the Paluxy Formation increases up to 100 percent in rim synclines associated with Brooks and East Tyler Salt Domes in Smith County in the central part of the East Texas Basin. In this region, shelf and distal deltaic facies (fig. 35) are complexly intercalated as a result of shifting shoreline positions, sediment supply, rate of subsidence, and sea-level changes.

Salt-related tectonic movement resulted in the greatest variation in Paluxy thickness and sand percentage along the Mexia-Talco fault zone and around Hainesville, Hawkins, and Van salt structures in the northern part of the East Texas Basin. In the southern part of the basin the only effect of salt tectonic activity was an increased thickness of Paluxy shelf facies in rim synclines. Sedimentary loading by a great thickness of pre-Paluxy strata initiated early development of diapirs in the southern basin area (Oakwood, Butler, Palestine, Keechi, and Brushy Creek Salt Domes). In the northern part of the basin, however, Van, Hainesville, and Hawkins were salt anticlines during Paluxy deposition, in part, because loading by post-Louann and pre-Paluxy strata was less than that required to initiate piercement.

Detailed analysis of the interrelationships between Paluxy depositional facies and contemporaneous salt tectonic activity is critical to East Texas waste isolation feasibility studies. The contrast in facies, depositional styles, and sand-body geometry between the northern salt structures and salt diapirs in the southern part of the basin supports the choice of the southern domes (Oakwood and Keechi) for further study for two reasons. First, the lack of sand facies precludes deposition of permeable Paluxy sandstones around the southern domes. Second, the relatively recent (post-Paluxy) history of diapirism and uplift is associated with salt structures in the northern area.
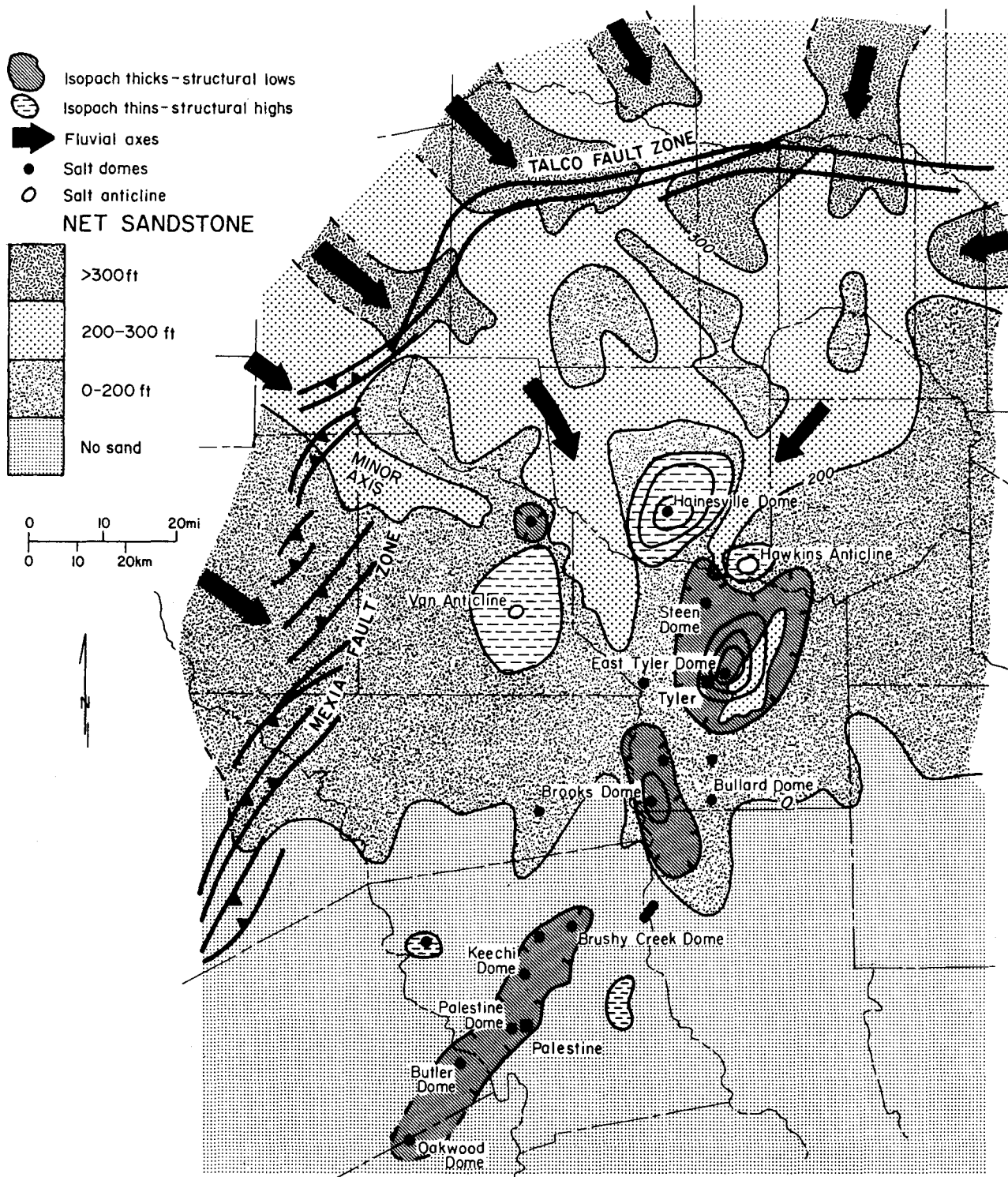
Figure 31. Net-sandstone patterns and related structural elements, Paluxy Formation, East Texas Basin. Dip-oriented net-sandstone trends become strike-oriented along northern part of Mexia-Talco fault zone. The Paluxy thickens into the basin and locally thins over contemporaneous salt anticlines. Dip-oriented sandstone (fluvial) trends bifurcate around structural highs above salt anticlines.

55
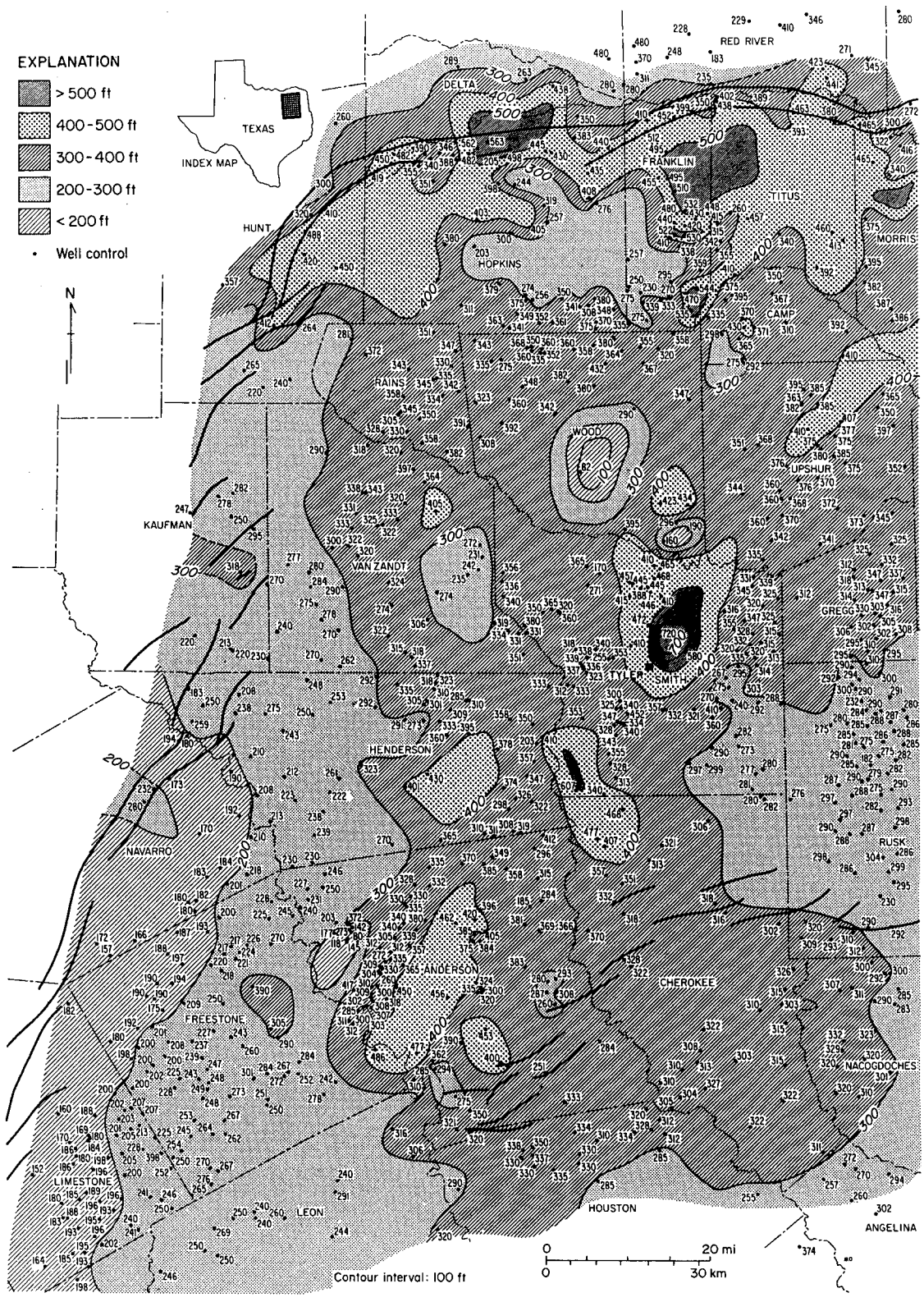
Figure 32. Isopach map, Paluxy Formation, East Texas Basin. Paluxy locally thickens in rim synclines, and thins over salt anticlines. Thickening increases regionally along northern part of Mexia-Talco fault zone; no thickness variations are evident along western part of fault zone.

56
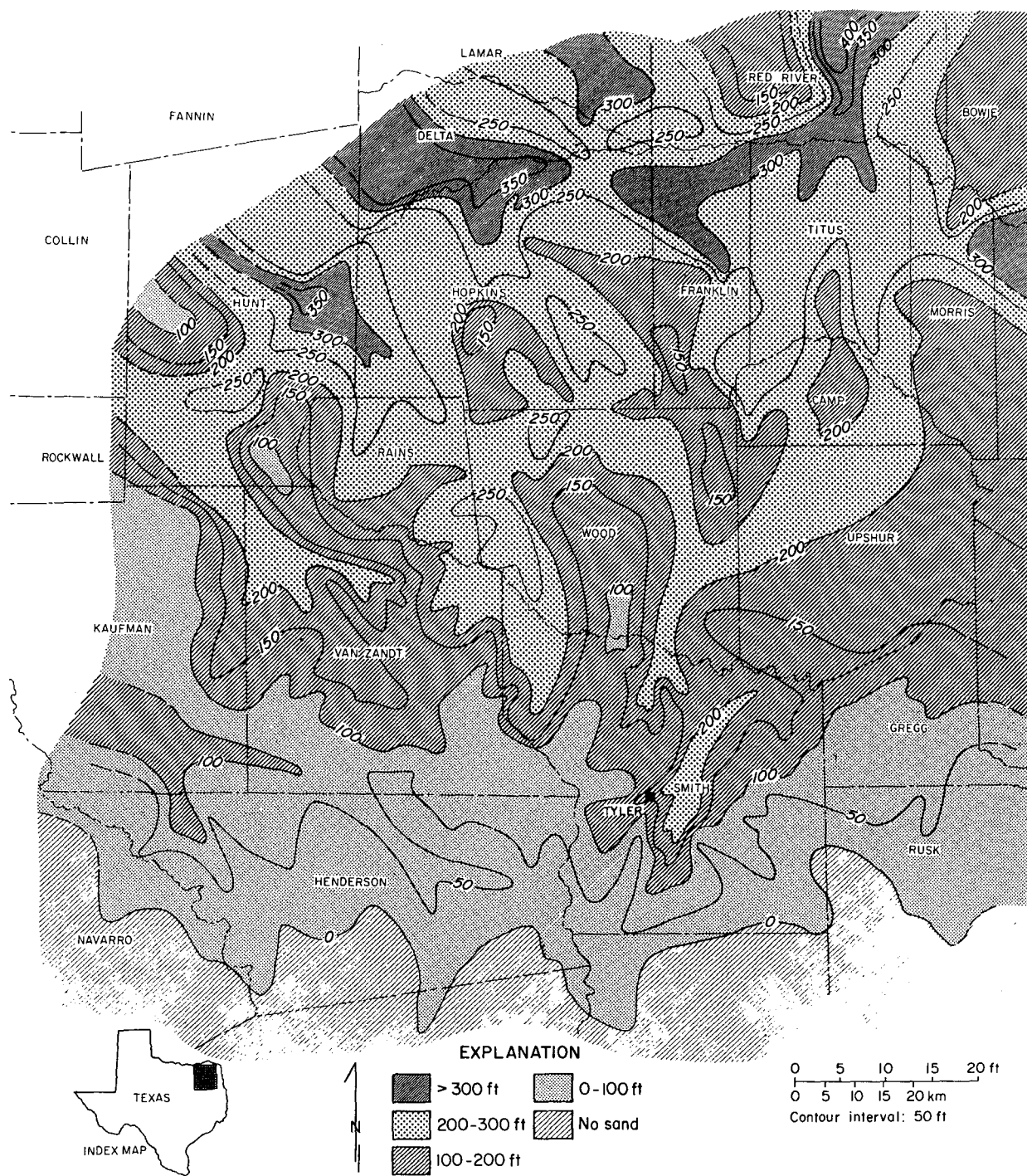
Figure 33. Net-sandstone map, Paluxy Formation, East Texas Basin. Comparison of this more detailed net-sandstone map with figure 31 illustrates the effect of structural elements on Paluxy sandstone thickness trends.

57

SEDIMENT INPUT

200 ft Net sand

Hainesville

Hawkins

Van

H

H'

Tyler

SMITH CO.

0   20 mi
0   30 km

H

CAROWAY
#1 Gilmore

UNION OIL OF CALIF.
#10 Maxfield

SUN OIL
#1 Retherford

TRICE AND JACKSON
#1 Pool

HUMBLE   HUMBLE
#1 Hawkins #15 Hawkins

H'

SANDS AND SANDS
#1 McCollum

KIAMICHI SHALE

GOODLAND LIMESTONE

Datum

PALUXY FORMATION

GLEN ROSE
FORMATION

Percent sand: 37 %

Percent sand: 51 %

Percent sand: 38 %

Percent sand: 46 %

Percent sand: 50 %

Percent sand: 54 %

Percent sand: 57 %
MINOR
FLUVIAL AXIS

MAJOR
FLUVIAL AXIS

VAN
SALT ANTICLINE

HAINESVILLE
PIERCEMENT
SALT DOME

MAJOR
FLUVIAL AXIS

HAWKINS
SALT ANTICLINE

MINOR
FLUVIAL AXIS

ft   m
800 — 240

600 — 180

400 — 120

200 — 60

0 — 0

0   10   20   30   40 mi
0 10 20   40   60 km

Figure 34. Cross section across Van, Hainesville, and Hawkins salt structures, northern part of East Texas Basin. Decreased thickness and sand percentage over each structure indicate that fluvial systems bifurcated around salt structures that were contemporaneous highs during Paluxy deposition.
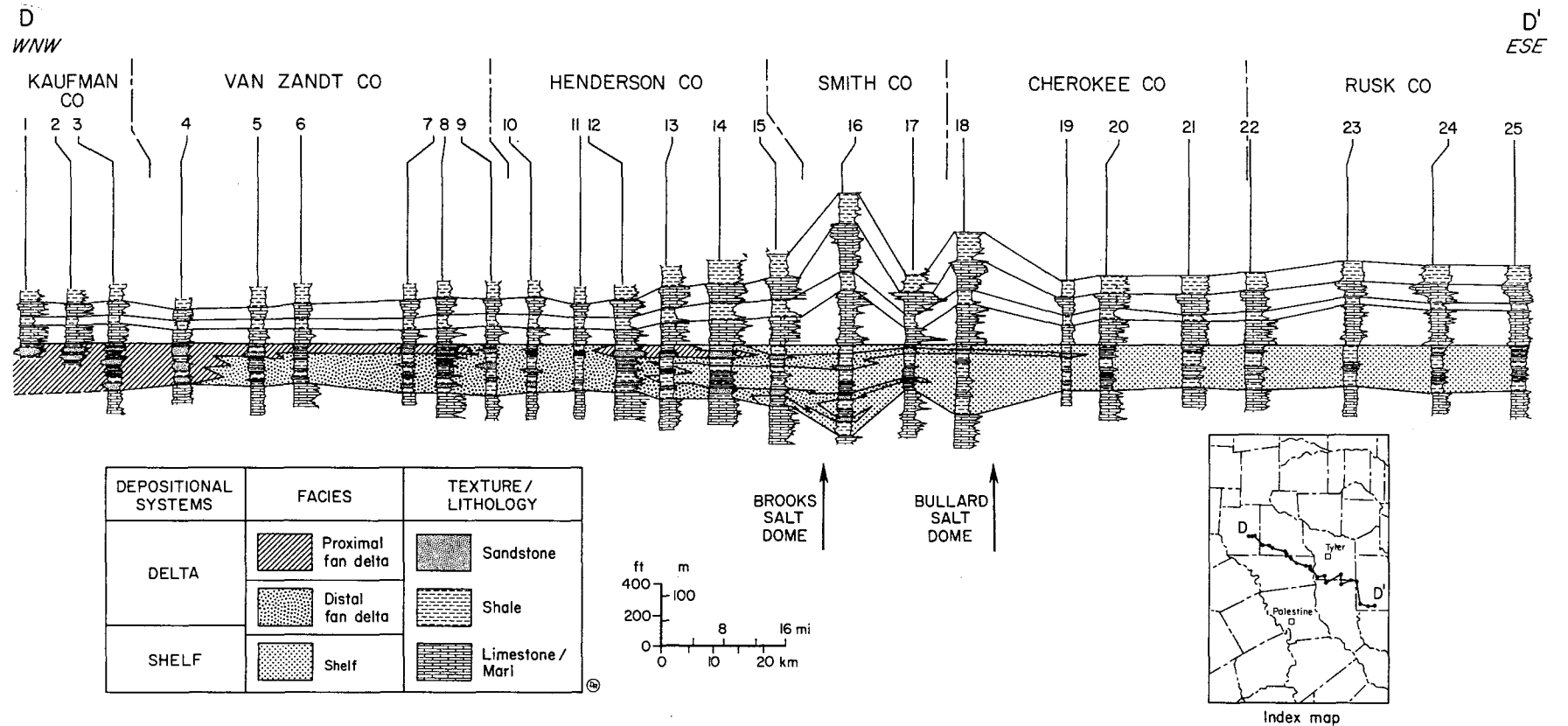
Figure 35. Cross section near Brooks and Bullard Salt Domes, East Texas Basin. Paluxy Formation thickens into rim synclines, but facies associations and sand-body geometry exhibit no variation. Preservation of delta-destructional facies (distal barrier bars) at margin of fan deltas may have been facilitated by rapid subsidence of rim synclines. For example, thicker sands occur in the rim syncline of East Tyler salt dome, central Smith County (fig. 31).

DEPOSITIONAL SYSTEMS IN THE NACATOCH FORMATION (UPPER CRETACEOUS), EAST TEXAS AND SOUTHWESTERN ARKANSAS

Mary K. McGowen and Cynthia M. Lopez

Deposition of Nacatoch sands represents a minor period of uplift of the landmass bordering the East Texas Basin to the north; the result was an influx of terrigenous clastics into the basin. Nacatoch deposition followed an extended period of deposition of shelf muds during Taylor to early Navarro time. As terrigenous clastic supply waned, the Nacatoch sands were reworked by marine processes, and deposition was again dominated by marine muds. The distribution and thickness variations of individual clastic sequences in the East Texas Basin provide pertinent information about the growth history and tectonic stability of salt domes in the basin.

The distribution patterns of individual clastic sequences within the East Texas Basin supply data essential to the assessment of domal growth and tectonic stability within the East Texas Basin. In the northern part of the basin, the distribution and thickness of sands in the Nacatoch Formation were locally controlled by actively subsiding salt withdrawal basins associated with salt domes. However, few sandstones occur in the Nacatoch Formation in the southern part of the East Texas Basin and, thus, do not pose a threat to the hydrologic integrity of those salt domes being investigated as possible nuclear waste repositories.

In the East Texas Basin, the Nacatoch Formation, the middle formation of the Navarro Group (fig. 2), consists of marine sand and mud sediment derived largely from source areas northwest, north, and northeast of the East Texas Embayment. Terrigenous clastic sediments were supplied to the Nacatoch basin by a major northeastern sediment dispersal system originating in southwestern Arkansas. Three minor fluvial-deltaic systems contributed sediment in southern Red River, Delta, and Hunt Counties, Texas.

Five facies are recognized in Nacatoch outcrops in southwestern Arkansas: tidal flat, tidal channel, tidal-inlet association, shoreface, and shelf facies. In northeastern Texas a delta sequence occurs in south-central Hunt County, and shelf sandstones and mudstones are present in Navarro and Kaufman Counties. The lateral association of deltaic deposits and tidal-flat sequences, together with the type, scale, and distribution pattern of inferred tide-produced structures, suggests that microtides (upper range: 0 to 6 ft [0 to 2 m]) or mesotides (lower range: 6 to 12 ft [2 to 4 m]) were operative in the East Texas and North Louisiana Embayments during deposition of the Nacatoch Sand.

The Nacatoch Formation in the East Texas Basin is restricted to the northern and western parts of the basin (fig. 36). The dominant trend of sandstone bodies is northeast to southwest in the northern part of the basin and north to south along the western margin. In the southern half of the basin, the Nacatoch Formation consists of mudstones.

In the subsurface of the East Texas Basin the Nacatoch Formation generally can be subdivided into nearshore and offshore deposits. Nearshore sequences include deltaic deposits in the northern and northwestern part of the basin located downdip from surface exposures of the same facies (figs. 37 and 38). Two high net-sand axes, oriented perpendicularly to the outcrop belt, extend southward into the basin. Orientation of these sand axes changes abruptly to become parallel with the dominant northeast-southwest trend, suggesting that the delta was dominated by tides and waves. It is inferred that interdeltaic areas were sites of short barrier islands, broad tidal inlets with associated tidal deltas, and tidal flats.

Offshore deposits can be arbitrarily divided into a lower and upper sandstone sequence divided by 50 to 100 ft (16.6 to 33.3 m) of marine mudstone. The elongate sandstone bodies of the lower sequence exhibit gradational lower boundaries and abrupt upper contacts, and grade laterally into muddy sandstones and mudstones (figs. 37, 38, and 39). Sandstones constituting these depositional sequences are well sorted, calcitic, glauconitic, fine- to medium-grained, and they contain shell fragments. The sandstone bodies are interpreted to be offshore bars, the geometry of which resulted primarily from tidal currents. Sandstones of the upper sequence constitute a fairly continuous sheet sand. Textures and composition are similar to sandstones of the lower sequence.

Tectonism, coincident with deposition, controlled local sandstone distribution patterns. Development of rim synclines accompanying salt dome growth considerably affected the thickness and distribution of the Nacatoch Formation; for example, thick Nacatoch sections exist around Hainesville Salt Dome in Wood County, Texas (figs. 40, 41, and 42). Other diapirs associated with salt withdrawal basins that were active during Nacatoch deposition are Steen, Mount Sylvan, East Tyler, Brook, and Bethel.

Sandstones within the Nacatoch Formation in the East Texas Basin are important shallow oil and gas reservoirs. Hydrocarbon reservoirs are restricted to the shelf/sand facies. However, hydrocarbon entrapment appears to be more a function of structural closure than of depositional facies. Hydrocarbons are produced from Nacatoch fields developed over the Van Salt Dome in Van Zandt County and along the Mexia fault system trend near the western margin of the basin (fig. 43).
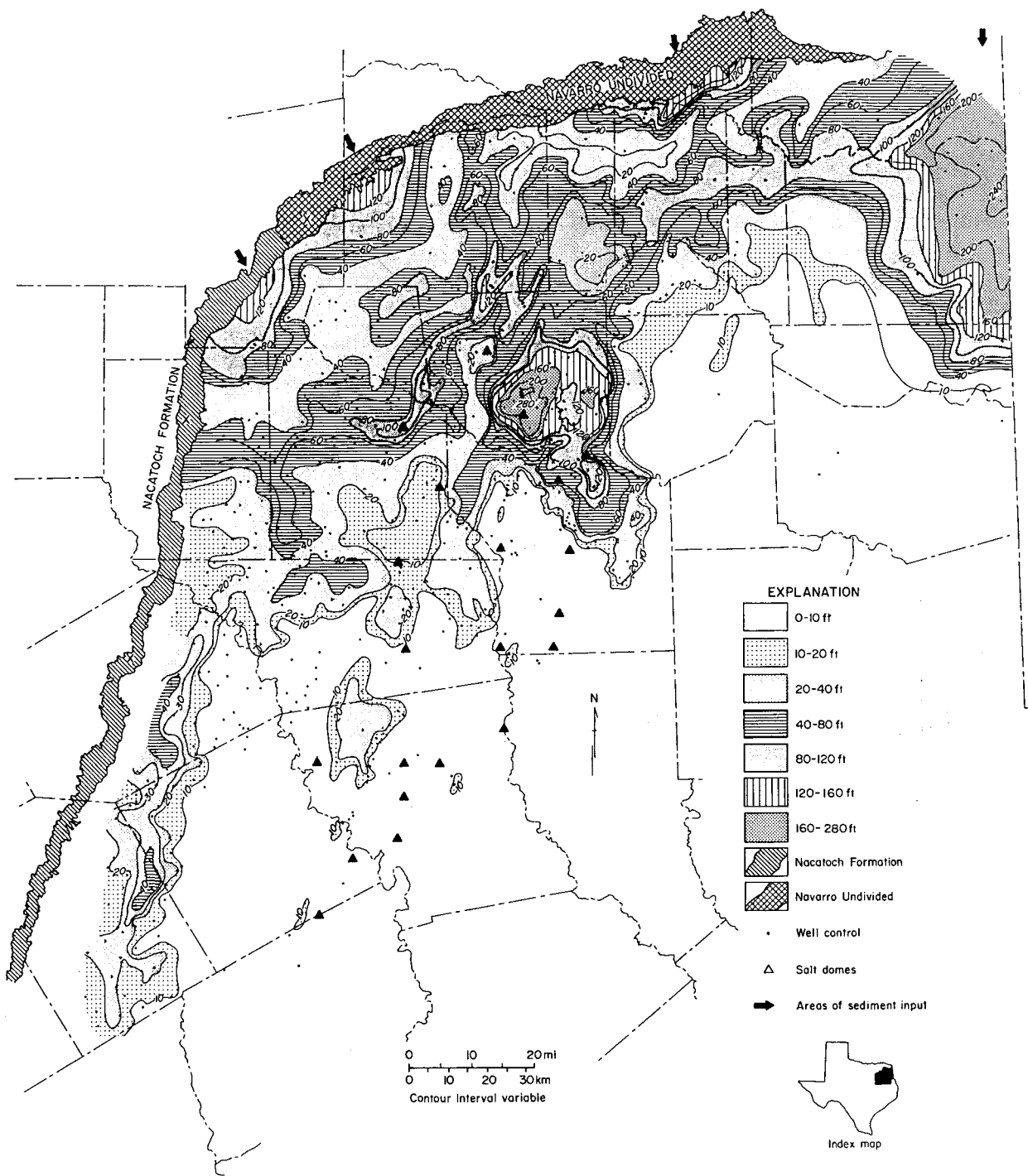
Figure 36. Net-sand map, Nacatoch Formation, East Texas Basin, showing outcrop of Nacatoch Formation and surface sample locations.

62
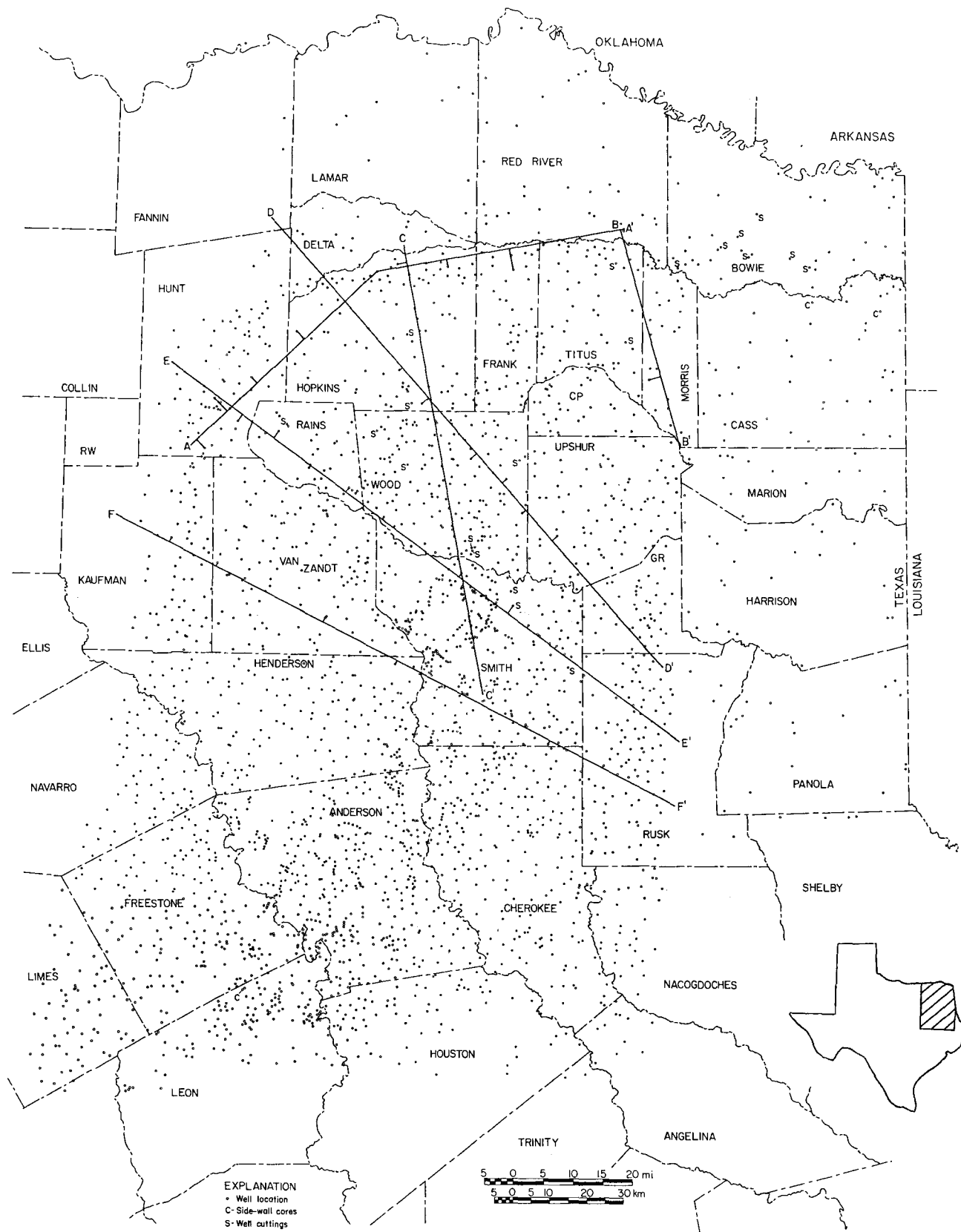
Figure 37. Index map, East Texas Basin, showing location of well control, regional cross sections, and wells from which Nacatoch sidewall cores and drill cuttings were taken.

63
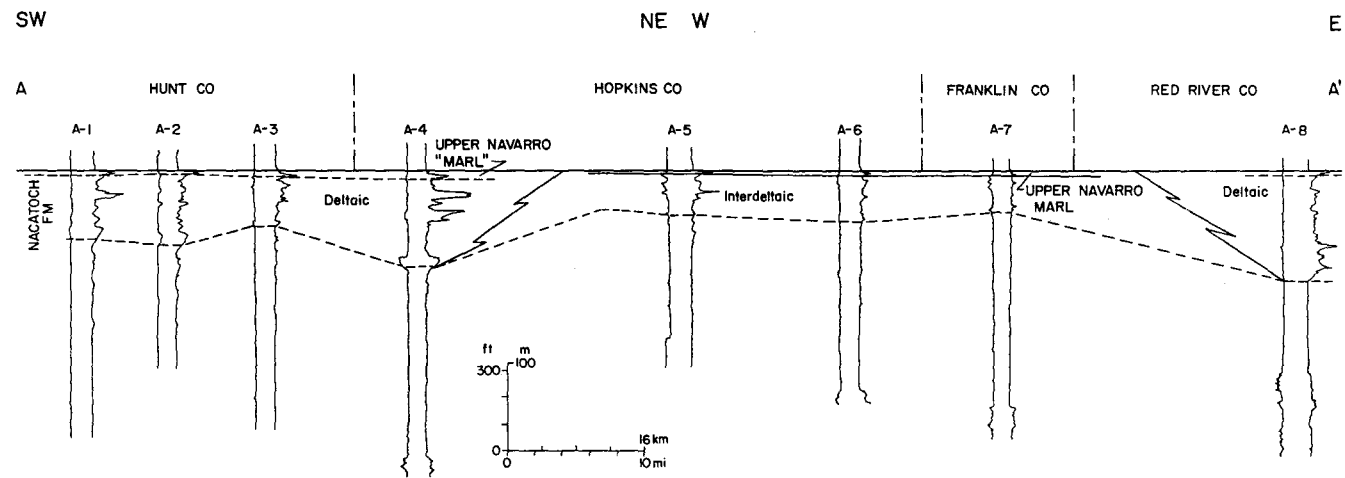
Figure 38. Regional stratigraphic section A-A', northwestern and northern part of East Texas Basin, showing deltaic and interdeltaic facies. For location, see figure 37.
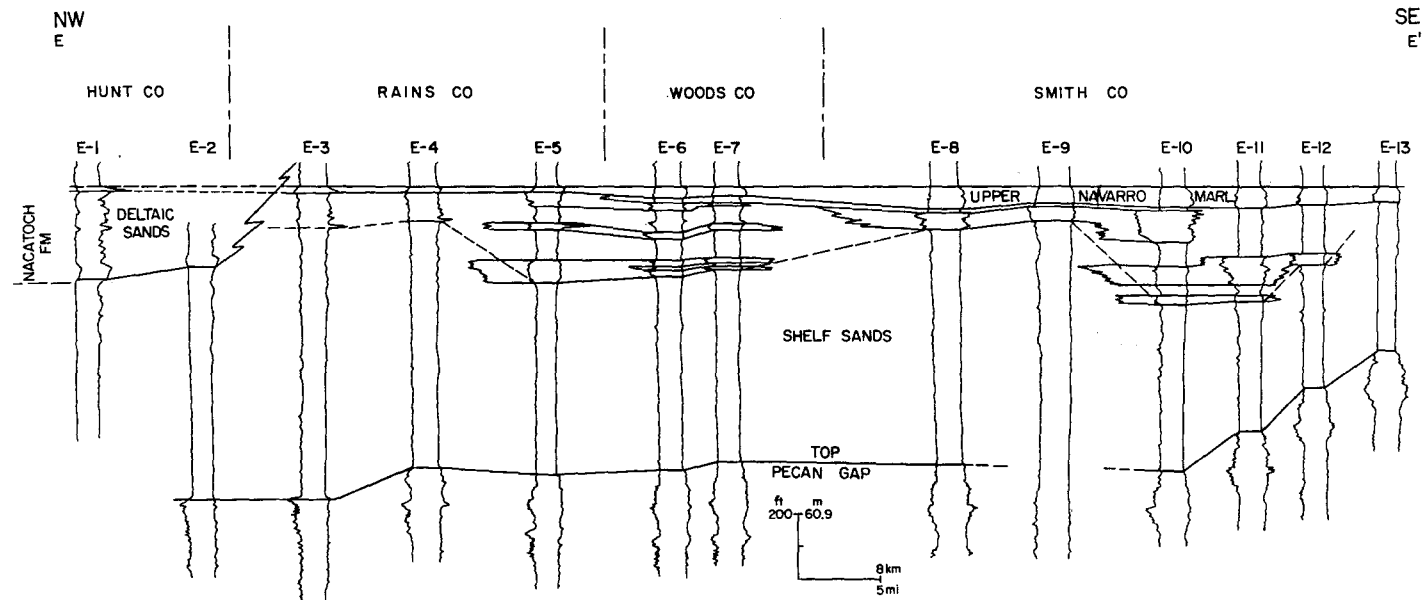
Figure 39. Regional northwest-southeast stratigraphic section E-E', part of deltaic and shelf facies, Nacatoch Formation, East Texas Basin. For location, see figure 37.
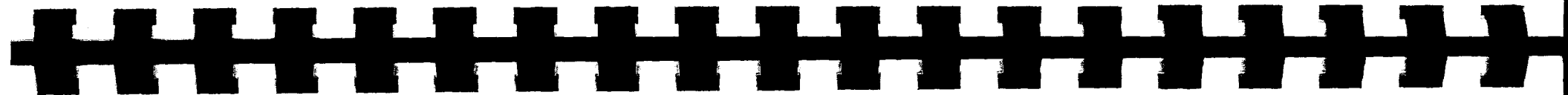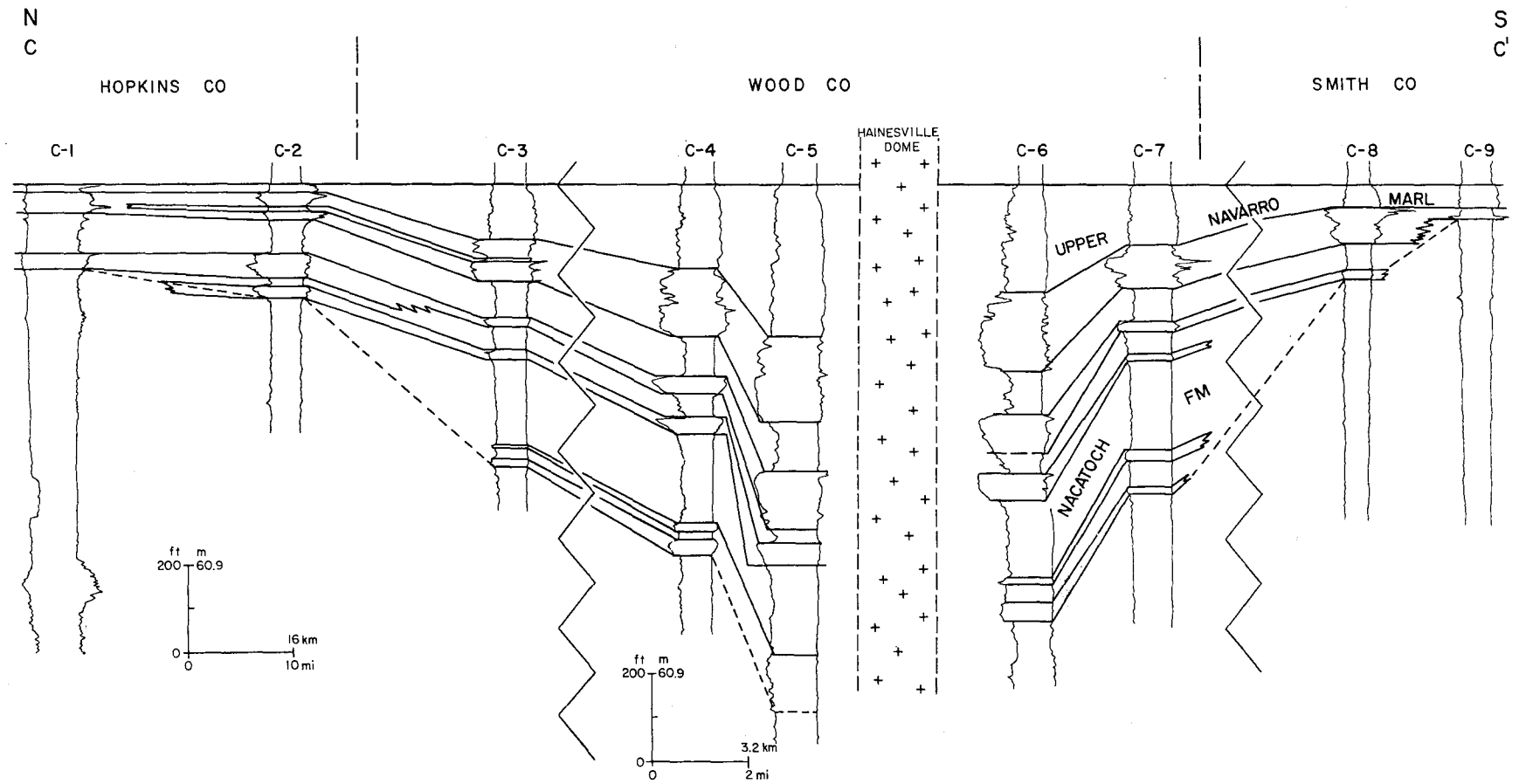
Figure 40.   Regional north-south stratigraphic section C-C' showing influence of Hainesville Dome on distribution of Nacatoch Formation, East Texas Basin.   For location, see figure 37.
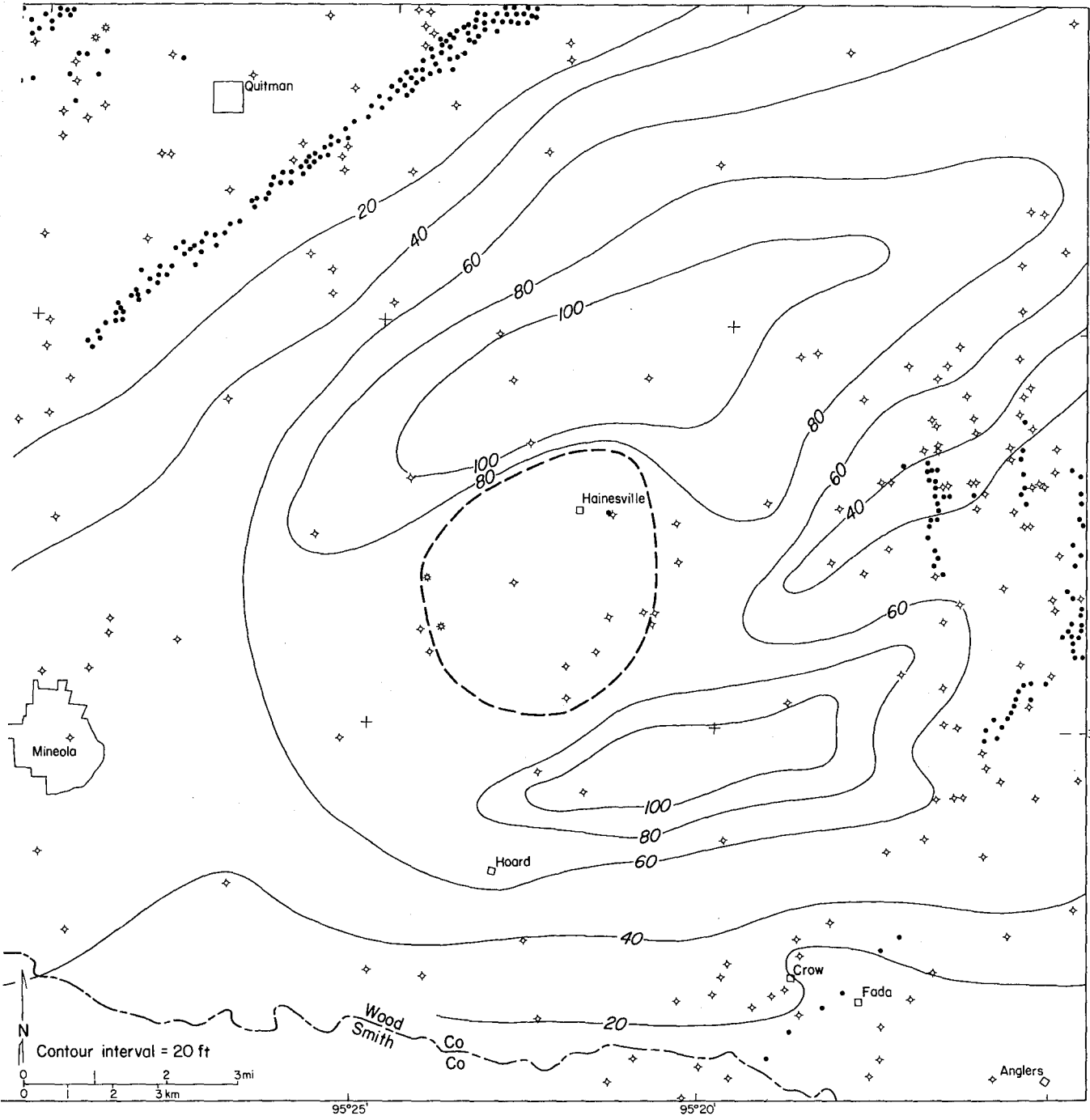
Figure 41. Net-sand map, lower Nacatoch sands, Hainesville Dome, East Texas Basin.
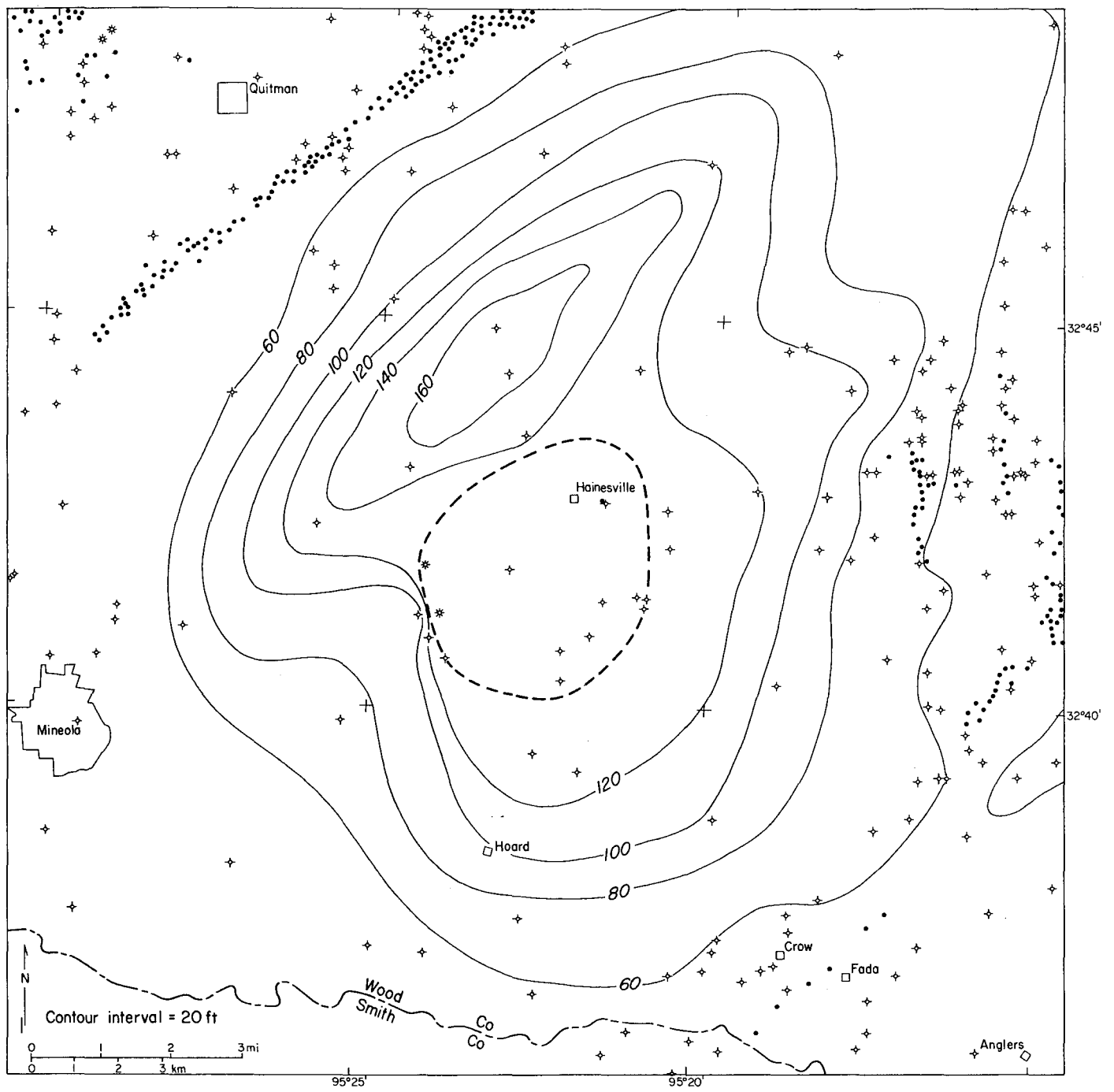
Figure 42. Net-sand map, upper Nacatoch sands, Hainesville Dome, East Texas Basin.

67
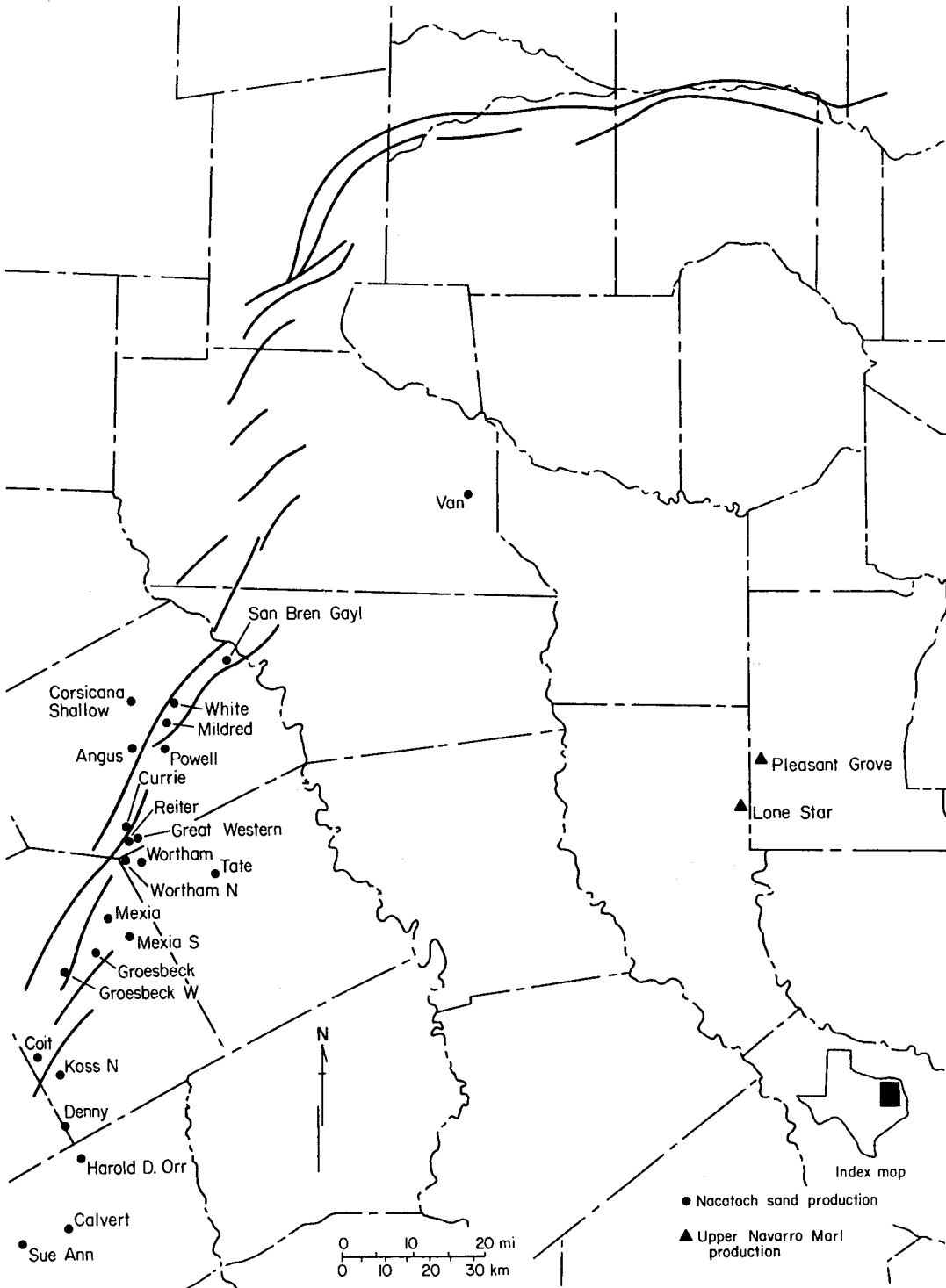
Figure 43. Oil and gas fields producing from Nacatoch Formation and Upper Navarro Marl, East Texas Basin.

68

PETROLEUM ACCUMULATION PATTERNS IN THE EAST TEXAS SALT DOME AREA

Alice B. Giles and Debra H. Wood

Petroleum production from traps associated with shallow East Texas salt diapirs is insignificant compared with that from anticlines over deep-seated salt domes and turtle-structure anticlines.

Flowage of the Louann Salt created shallow salt diapirs, deep salt domes, and turtle-structure anticlines within the East Texas Basin. Hydrocarbon fields associated with these structures account for most of the petroleum production in the central part of the basin (fig. 44).

Deep salt structures have provided the traps for most of the oil (84 percent) and gas (78 percent) produced from the central part of the basin (fig. 45). The major control on hydrocarbon entrapment was doming of strata over the salt structures (see Van Dome seismic profile, fig. 22). Faults associated with crestal grabens over deep salt structures are commonly secondary control. Because deep-seated domes elevate thick stratigraphic sections, resulting anticlines are typically multiple-zoned productive structures.

The productivity of petroleum traps associated with turtle-structure anticlines (see "Structural Effects of Salt Movement in the East Texas Basin") is lower than productivity of anticlines over deep salt domes for two reasons. (1) Turtle structures formed after the deep-seated salt anticlines, indicating that petroleum migrated to the turtle structure at a later time; and (2) thinner stratigraphic sections were uplifted over turtle structures. Anticlines and extensional faults (fig. 46, north of Mount Sylvan Dome) localized petroleum within turtle structures.

Petroleum production associated with shallow salt diapirs has been relatively minor; less than 1 percent of the oil and only 5 percent of the gas in the central part of the East Texas Basin have been produced from these structures (fig. 45). Furthermore, individual fields are small. Small closures are expected because domeward migration of the rim syncline with increasing domal maturity causes the area of hydrocarbon catchment to shrink. If large amounts of oil and gas accumulated over early salt-pillow structures, then much of it has leaked along dome flanks and faults during dome growth or from breached reservoirs uplifted and eroded from the dome crest.

Types of traps found around the shallow East Texas salt diapirs include: uplifted strata abutting the salt stock at Boggy Creek (fig. 47) and Butler Domes; traps beneath dome overhangs at Oakwood (fig. 48), Hainesville (fig. 49, northeast side), Steen, Bethel, and Brooks Domes; traps associated with local unconformities at Hainesville Dome (fig. 49, southwest side); fault traps near dome flanks at Grand Saline Dome (fig. 50); and traps formed by uplift and faulting of strata over the dome crest at Concord (fig. 51) and Brushy Creek Domes. Some dry domes such as Keechi (fig. 51), Bullard, and Whitehouse Domes have not been tested at depth.

Potential nuclear waste isolation sites such as shallow salt diapirs should not be prime targets for future petroleum exploration. In spite of early and continued exploration, production from shallow salt diapirs in the East Texas Basin has generally been of minor importance because of their unfavorable growth histories. Therefore, exploration potential of shallow salt diapirs of the East Texas Basin may not preclude their consideration as nuclear waste isolation repositories.
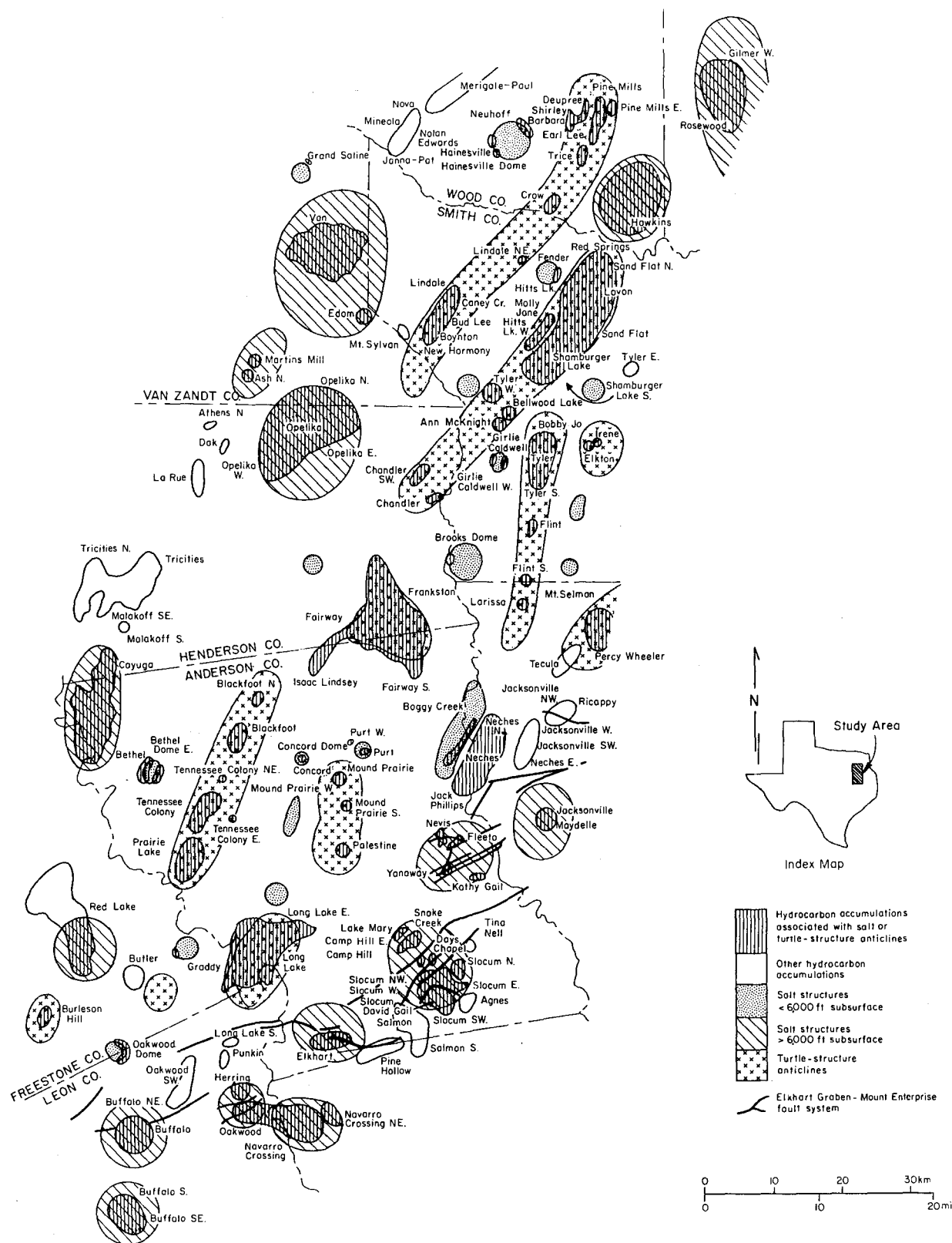
Figure 44. Salt structures, turtle-structure anticlines, and hydrocarbon fields, central East Texas Basin. Only hydrocarbon fields are named here. See figure 13 for names of salt structures and turtle-structure anticlines.

OIL

Shallow Salt Diapirs
(<6000 ft subsurface)
12,099,635 bbl
.8 %

Other Traps
24,748,659 bbl
1.6 %

Turtle-Structure
Anticlines
210,707,638 bbl
14 %

Deep Salt Domes
(>6000 ft. subsurface)
1,253,836,823 bbl
83.5 %

GAS

Other Traps
209,189,350 mcf
10%

Shallow Salt Diapirs
(<6000 ft subsurface)
112,976,254 mcf
5%

Turtle-Structure
Anticlines
150,993,971 mcf
7 %

Deep Salt Domes
(>6000 ft subsurface)
1,679,900,700 mcf
78 %
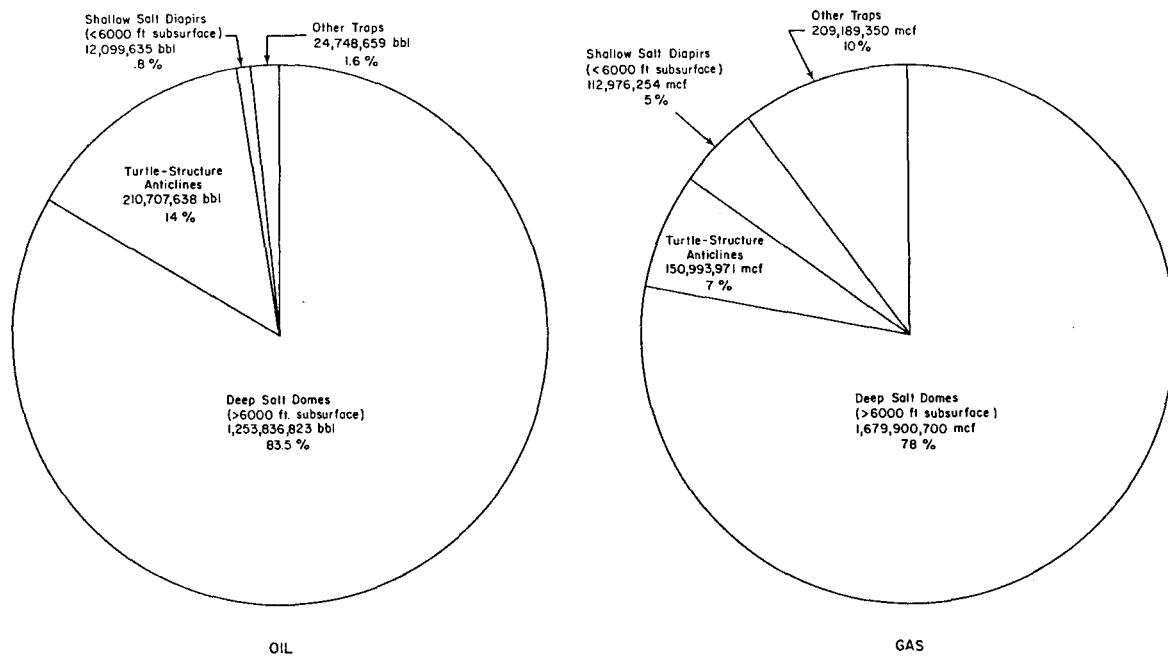
Figure 45. Relative hydrocarbon production associated with salt structures and turtle-structure anticlines, central East Texas Basin. Production data from Texas Railroad Commission (1978) and the International Oil Scouts Association (1978) are cumulative through 1978.
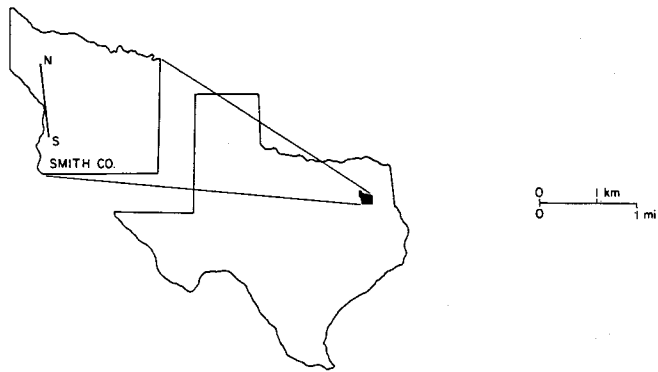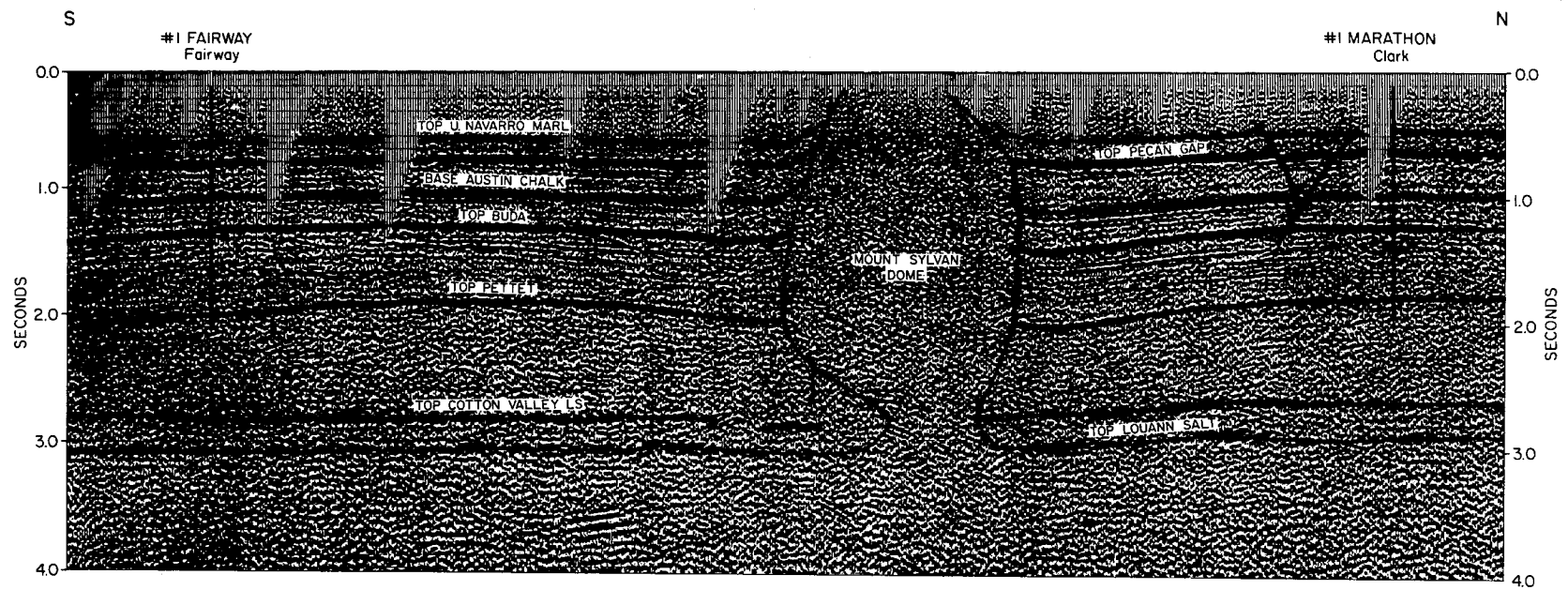
Figure 46. South-north seismic section through Mount Sylvan Dome, East Texas Basin. Pre-Pettet sediment thicks have formed turtle-structure anticlines on each side of the dome; Bud Lee and Lindale Fields are developed on the northern turtle-structure anticline. Seismic line courtesy of Teledyne Exploration Company.

74
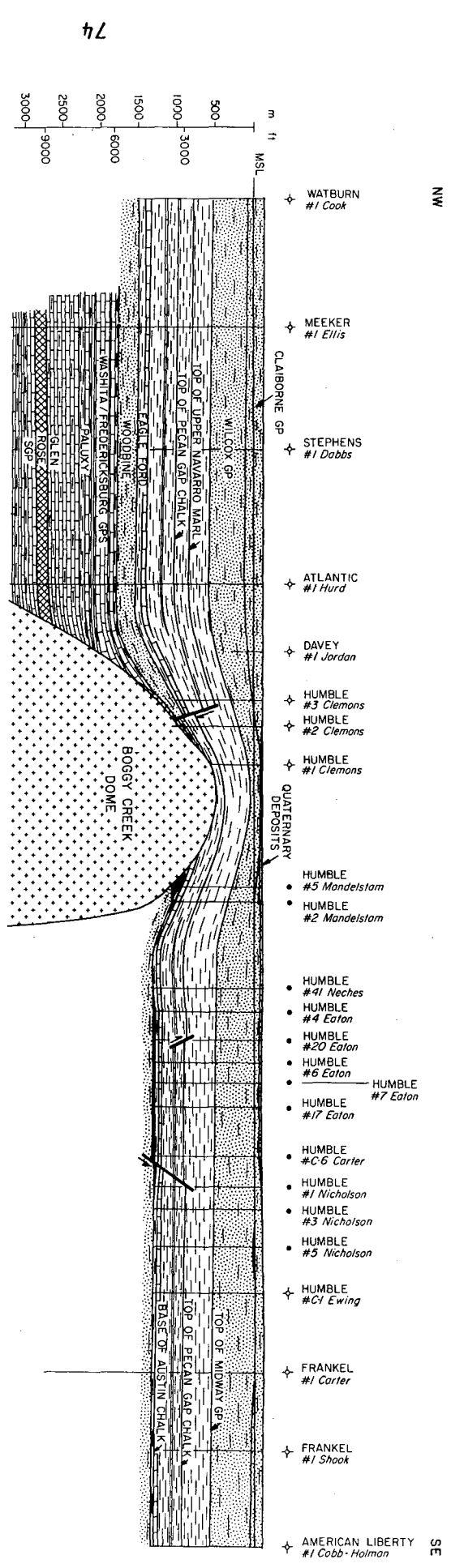
Figure 47. Northwest-southeast structure section through Boggy Creek Dome, East Texas Basin. Hydrocarbon production at Boggy Creek Field is from Woodbine sandstones that abut southeast flank of dome. Farther southeast, the Neches Field produces oil from Woodbine sandstones in a turtle-structure anticline.

NW

SE

KILLAM #1 Yeager

ROXANA #1 Thiele
McBEE #1 Settlemyre
TEXACO #1 Marshall Stk. 1
LETCO #TOG-1 Settlemyre
McBEE #1 Sherman
TEXACO #3 Keechi Petroleum Stk. 2
WYNNE #1 Brown
LETCO #2A Settlemyre
KATZ #1 Keep
TEXACO #1 Keep
STEWARD #1 Kells
McCORMICK #1 Recknor
RIDLEY #1 Longley
FISHER #1 Coats

m   ft

MSL

500

1000 — 3000

1500 — 6000

2000

2500 — 9000

3000

3500 — 12,000

4000

4500 — 15,000

5000

5500 — 18,000

6000 — 21,000

CLAIBORNE GP

WILCOX GP
TOP OF MIDWAY GP
TOP OF UPPER NAVARRO MARL
TOP OF PECAN GAP CHALK

OAKWOOD DOME

BASE OF AUSTIN CHALK
EAGLE FORD
WOODBINE
WASHITA & FREDERICKSBURG
GPS
PALUXY
GLEN
ROSE
SGP

TRAVIS PEAK FM

SCHULER FM

BOSSIER FM

COTTON VALLEY LIMESTONE
SMACKOVER FM

LOUANN SALT

NORPHLET FM

0   1000 m
0   3000 ft.

⊹ Dry well

● Oil well

Normal fault

Hydrocarbons

Anhydrite or cap rock

Salt

Shale or mudstone

Sandstone

Limestone or chalk

Dolomite

Dome shape modified from Exploration Techniques, Inc. (1979)

Figure 48. Northwest-southeast structure section across Oakwood Dome, East Texas Basin. Oakwood Dome Field is developed within Woodbine sandstones beneath dome overhang. Dome shape modified from Exploration Techniques, Inc. (1979).
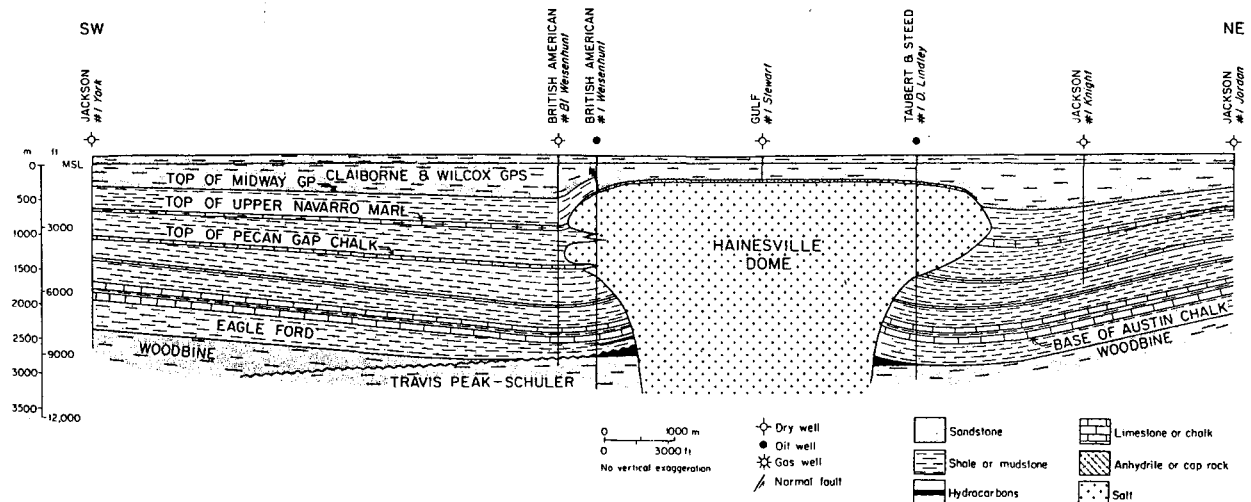
Figure 49. Southwest-northeast structure section across Hainesville Dome, Wood County, East Texas. At Hainesville Dome Field, an unconformity has trapped hydrocarbons in Travis Peak sandstones beneath overhang on east side of dome. Production from Hainesville Field from Sub-Clarksville sandstone on east side of dome. Neuhoff Field beneath west overhang has produced from Woodbine and Paluxy sandstones.
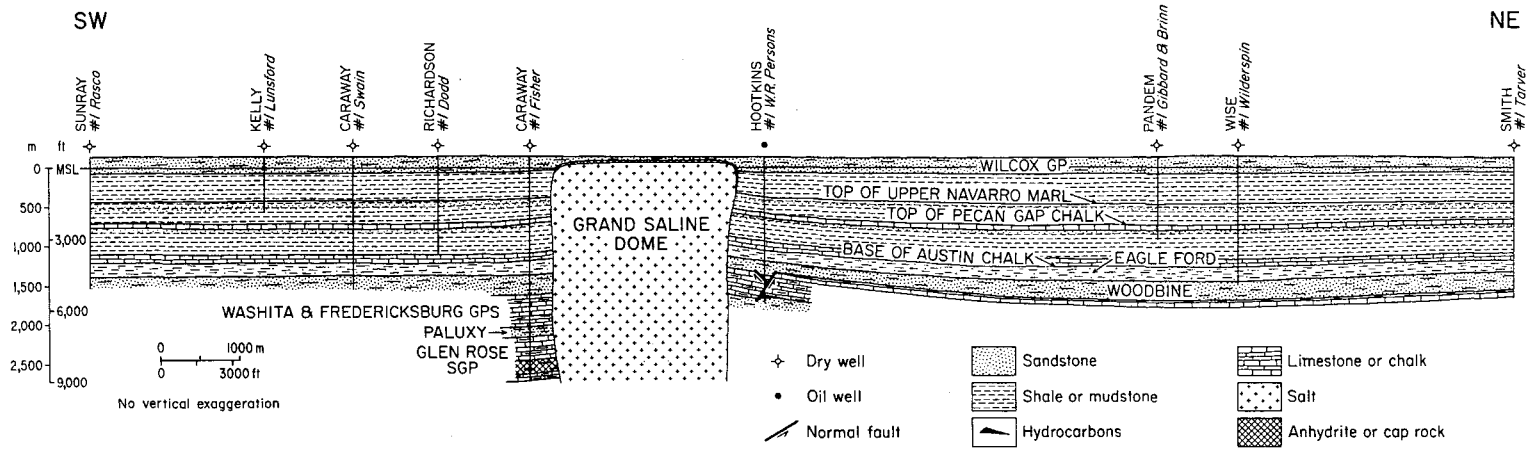
Figure 50. Southwest-northeast structure section across Grand Saline Dome, East Texas Basin. Oil is produced from faulted Paluxy sandstones off northeast flank of dome and is part of the Grand Saline Field.
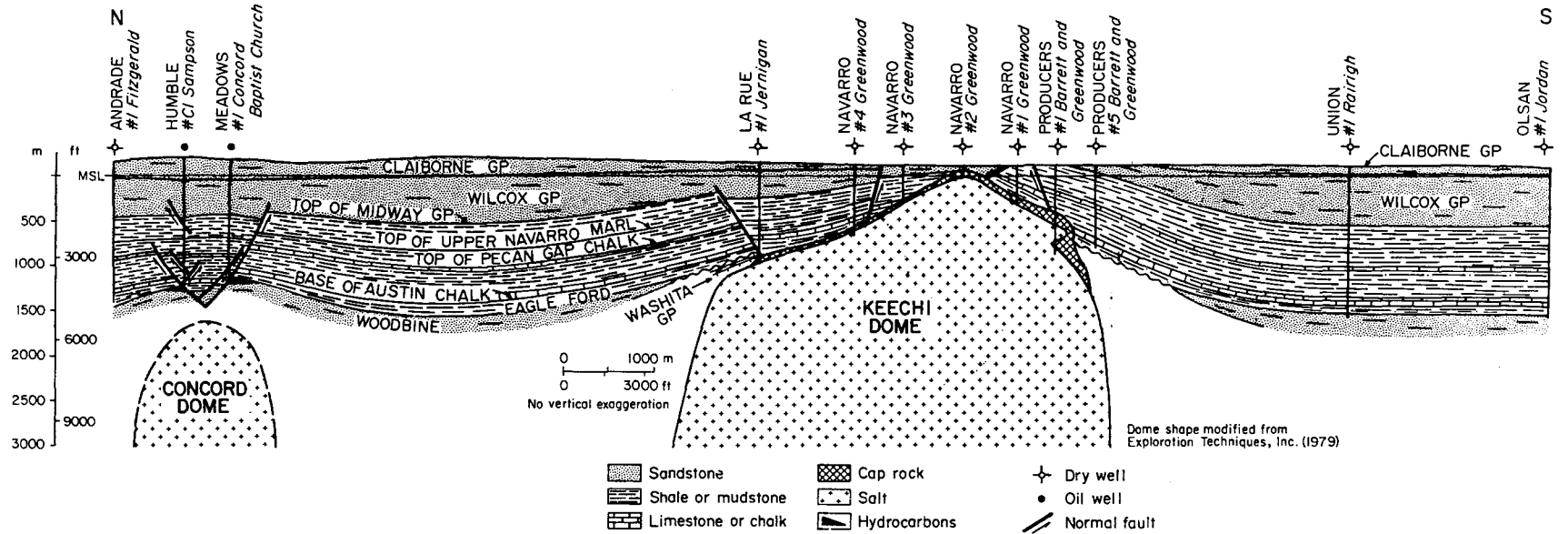
Figure 51. North-south structure section across Concord and Keechi Domes, Anderson County, East Texas. Concord and Concord Dome Fields produce from Woodbine sandstones. Dome shape modified from Exploration Techniques, Inc. (1979).

77

TRINITY RIVER TERRACES NEAR PALESTINE SALT DOME, EAST TEXAS

Edward W. Collins

On the western flank of Palestine Salt Dome are Trinity River terrace deposits of Quaternary age. Palestine Dome is one of the few domes in East Texas that is overlain by Quaternary deposits. Topographic profiles of the terrace surface over and adjacent to the dome do not indicate deformation of the Quaternary terraces.

Palestine Dome is partially overlain by Trinity River terrace deposits of Quaternary age (fig. 52). Four terraces (T-1a, T-1b, T-2, and T-3) are recognized along the Trinity River and their heights above the floodplain define them as follows (figs. 53 and 54):

T-1a	1 to 3 m	(3 to 10 ft)
T-1b	4.5 to 9 m	(15 to 30 ft)
T-2	15 to 21 m	(50 to 70 ft)
T-3	27.5 to 36.5 m	(90 to 120 ft)

These terrace levels appear to correlate with the Pleistocene Montgomery and Beaumont Formations, and the Upper Pleistocene or Holocene (?) Deweyville Formation (fig. 54). Although specific ages have not been determined, T-1a and T-1b appear to be associated with Deweyville time; T-2 corresponds to Beaumont time; and T-3 appears to be related to Montgomery time (fig. 54). At Palestine Dome, T-3 overlies the western flank of the dome, and small erosional remnants may occur over other parts of the dome (fig. 52). A topographic profile of the T-3 terrace surface on the western flank of the dome does not differ from profiles of the same terrace surface to the north and south, away from the dome (figs. 52 and 55). Similarly, there is no apparent change in the regional topographic gradient of the four terrace levels in the vicinity of Palestine Dome (location 10, figs. 53 and 54). This suggests that no dome growth has occurred since deposition of these terrace deposits, although this assumption relies greatly on the idea that the terrace surface has not been "leveled" by erosion.

Although Palestine Dome is not a potential candidate site for the disposal of nuclear waste, knowledge of its stability during Quaternary time is essential for evaluation of other domes in the East Texas region for repository sites. Palestine Dome is one of the few domes in East Texas that is overlain by Quaternary deposits, and these terraces display no apparent evidence of warping as a result of dome growth.

EXPLANATION

QUATERNARY	▦	MODERN ALLUVIUM
	⬚	TRINITY RIVER TERRACE DEPOSIT
	▒	UPLAND TERRACE DEPOSIT
TERTIARY	▦	QUEEN CITY FM
	⧄	REKLAW FM
	⧄	CARRIZO FM
	▤	WILCOX GROUP
	▦	MIDWAY GROUP
CRETACEOUS	⬚	TAYLOR & NAVARRO GROUPS
	▒	AUSTIN CHALK
	⧄	WOODBINE & EAGLE FORD GROUPS
	■	BUDA LIMESTONE

U/D FAULT − − INFERRED OR COVERED
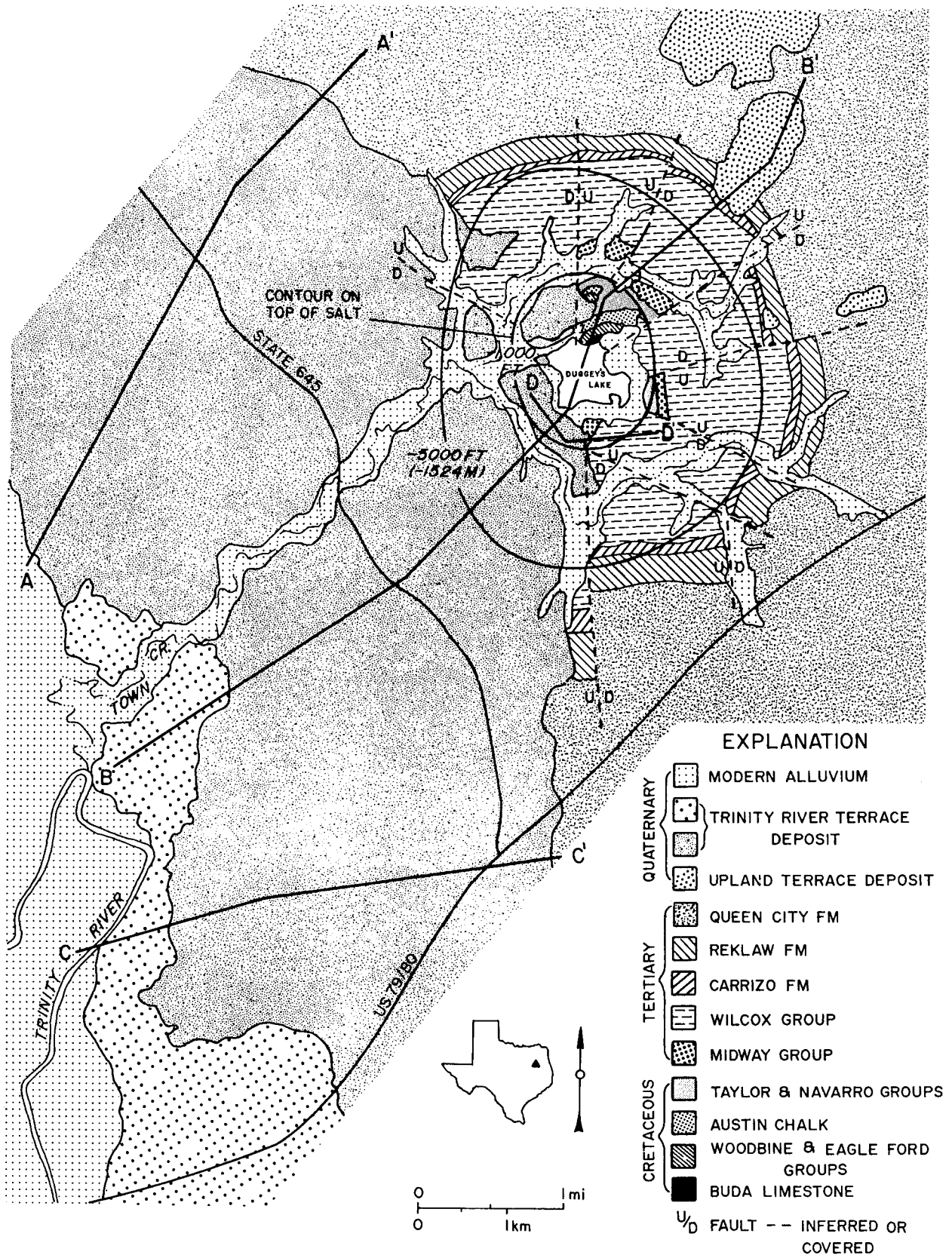
Figure 52. Geologic map, Palestine Dome area, East Texas. Modified from Hightower (1958).

79
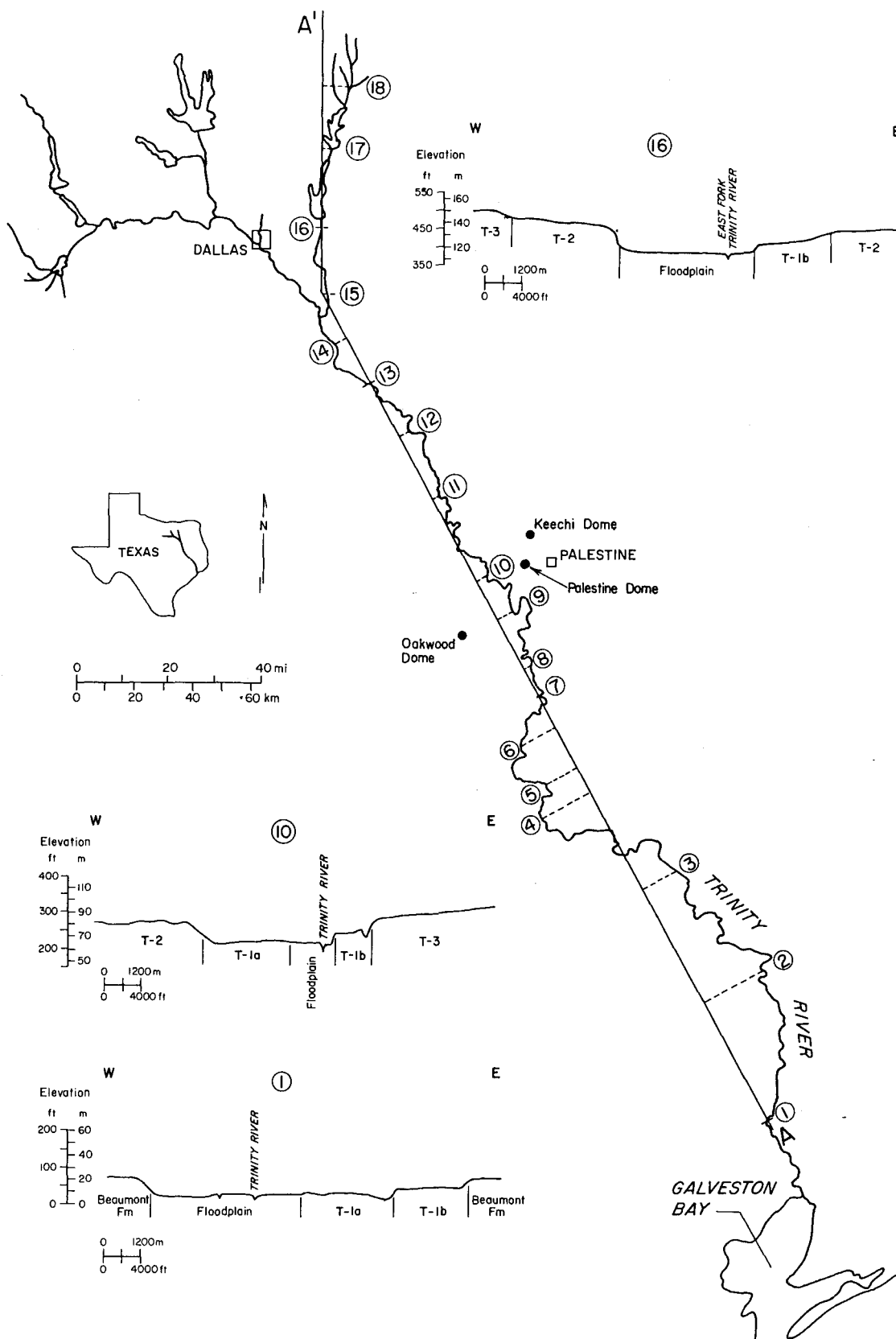
Figure 53. Location of terrace deposits along Trinity River, East Texas.
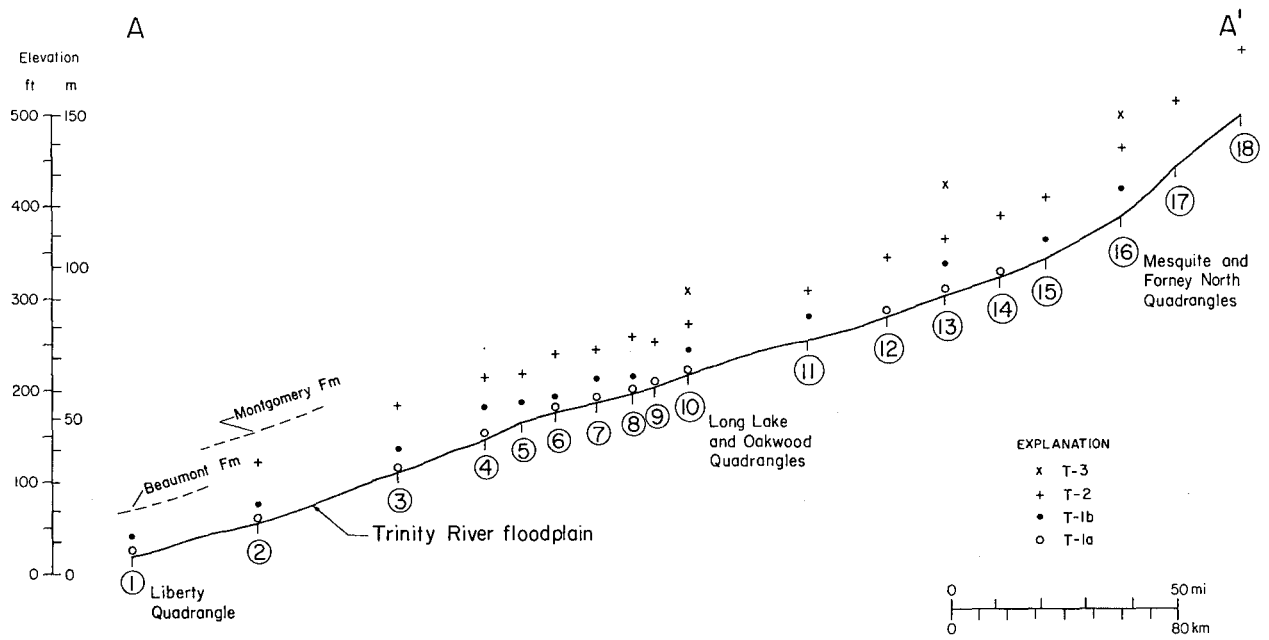
Figure 54. Profile of Trinity River terrace deposits, East Texas.
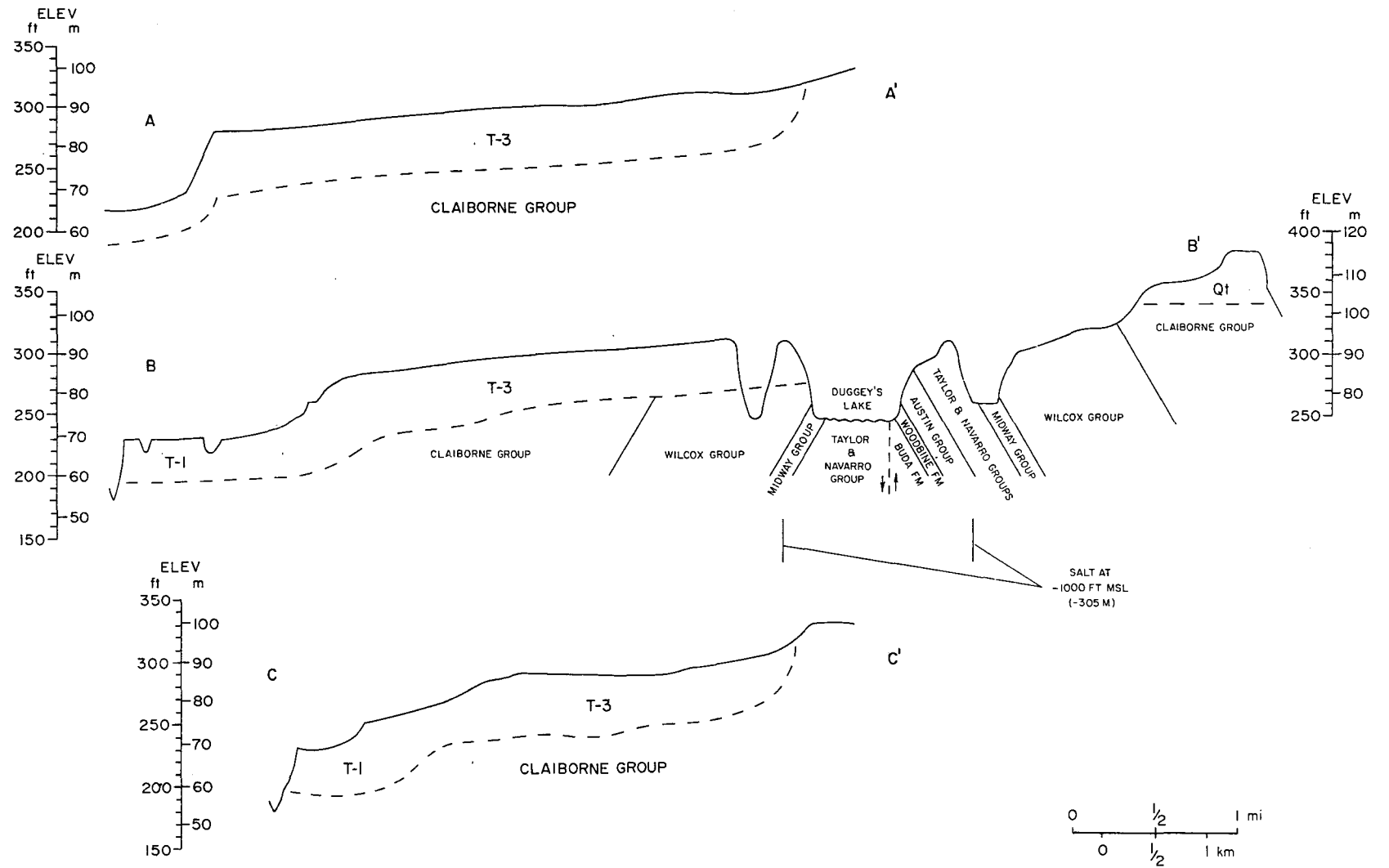
Figure 55. Topographic profiles of terrace surface on and adjacent to the western flank of Palestine Dome, East Texas.

82

STATISTICAL ANALYSIS OF LINEAMENTS ON AERIAL PHOTOGRAPHS AND LANDSAT IMAGERY OF THE EAST TEXAS BASIN AND THEIR RELATION TO REGIONAL STRUCTURE

Owen R. Dix and M. P. A. Jackson

A sequence of mathematical and statistical operations was used in the analysis of lineaments in East Texas. The study indicates that well-defined northwest and northeast trends are present throughout the basin. Shallower salt domes in the southern part of the basin are associated with higher densities and more random orientation of lineaments, probably reflecting greater amounts of radial or concentric fracturing of their overburdens.

The distribution of lineaments in the East Texas Basin was examined to establish the relation between lineament trends and the regional tectonic framework. If Holocene faulting or movement of salt domes has occurred, the effects might be detectable in the regional lineament pattern.

Study area I is documented by black-and-white aerial photographs ranging in scale from 1:17,400 to 1:25,500 and is 15,400 km^2 (6,000 mi^2) in area (center of fig. 56). Study area II is depicted by 1:250,000 Landsat imagery and has an area of 70,700 km^2 (30,000 mi^2) (entire area of fig. 56). More than 8,300 lineaments were identified on the aerial photographs; their total length is 7,660 km (5,000 mi) and have a mean length of 900 m (2,900 ft). More than 260 Landsat lineaments were identified that range in length from 3 km to 75 km (2 mi to 48 mi) and have a mean length of 10 km (6 mi).

The lengths and orientations of lineaments from each study area were processed to identify preferred orientations (peaks) and to test whether these peaks are statistically significant and, therefore, geologically meaningful. The data were initially plotted on polar graphs using relative lengths (fig. 57) and the square root of length-weighted frequencies. Further processing of the data involved vector summation and statistical analyses using Bernshtein accuracy criteria (fig. 58) and correlation coefficients.

The following conclusions may be drawn:

(1) A well-defined and consistent lineament pattern comprising trends of 320° and 050° is present throughout the East Texas Basin. Statistical analysis indicates that each of these trends is bimodal, comprising two preferred orientations 15° to 20°

apart. Study area I may be divided into structural domains on the basis of the dominance of each component of the bimodal peak.

(2) The northeast-trending set is parallel to the individual faults making up the Mexia-Talco fault system, to subsurface faults in the center of the basin, and, in some places, to stratigraphic contacts.

(3) The northwest-trending set is apparently not related to any particular structural elements of the basin, but like the northeast-trending set, is thought to reflect preferential directions of fracture induced by interference folding at depth. This folding is caused by halokinesis and is reflected in the regional gravity field.

(4) Lineaments show increased dispersion and density over shallow domes in the south, probably as a result of fracturing and faulting of overburden above the domes.

(5) The Elkhart-Mount Enterprise fault zone has had no dramatic effect on the regional lineament pattern, partly because of data processing and the orientation of the fault zone with respect to the regional pattern. Regional fractures, rather than the fault zone itself, are probably the main cause of the lineament pattern.

(6) Because most of the lineaments are defined by straight segments of drainage channels, their recognition has been only slightly masked by cultivation. However, areas covered by floodplain deposits have a significantly lower number of lineaments.

(7) Study of lineament distributions generated artificially by random processes indicates that orthogonal sets are almost invariably present, and suggests that the geologic significance of orthogonal pairsets has been exaggerated in the literature.

(8) The artificial data sets also show that confidence levels of 90 percent or 95 percent, commonly employed in the literature, are insufficiently rigorous to reject nonsignificant peaks formed by random ordering; a confidence level of 99 percent is required, particularly if the samples contain fewer than 200 lineaments.

One purpose of this investigation was to determine if the regional lineament pattern suggests recent halokinesis, an important factor in assessing the suitability of salt domes as nuclear waste repositories. Results have shown that the southern salt domes are associated with higher densities of lineaments of more random orientations, strongly indicative of increased fracturing or faulting in the domal overburdens. The maximum age of these lineaments is that of the youngest stratigraphic unit in which they have formed. Their minimum age cannot be established because, although lineaments have propagated upward from bedrock into modern drainage systems and surficial deposits, this provides no clue to the age of the deformation event responsible for their structural control. Accordingly, this study has not been able to confirm or deny the occurrence of Holocene deformation in the East Texas Basin.

84
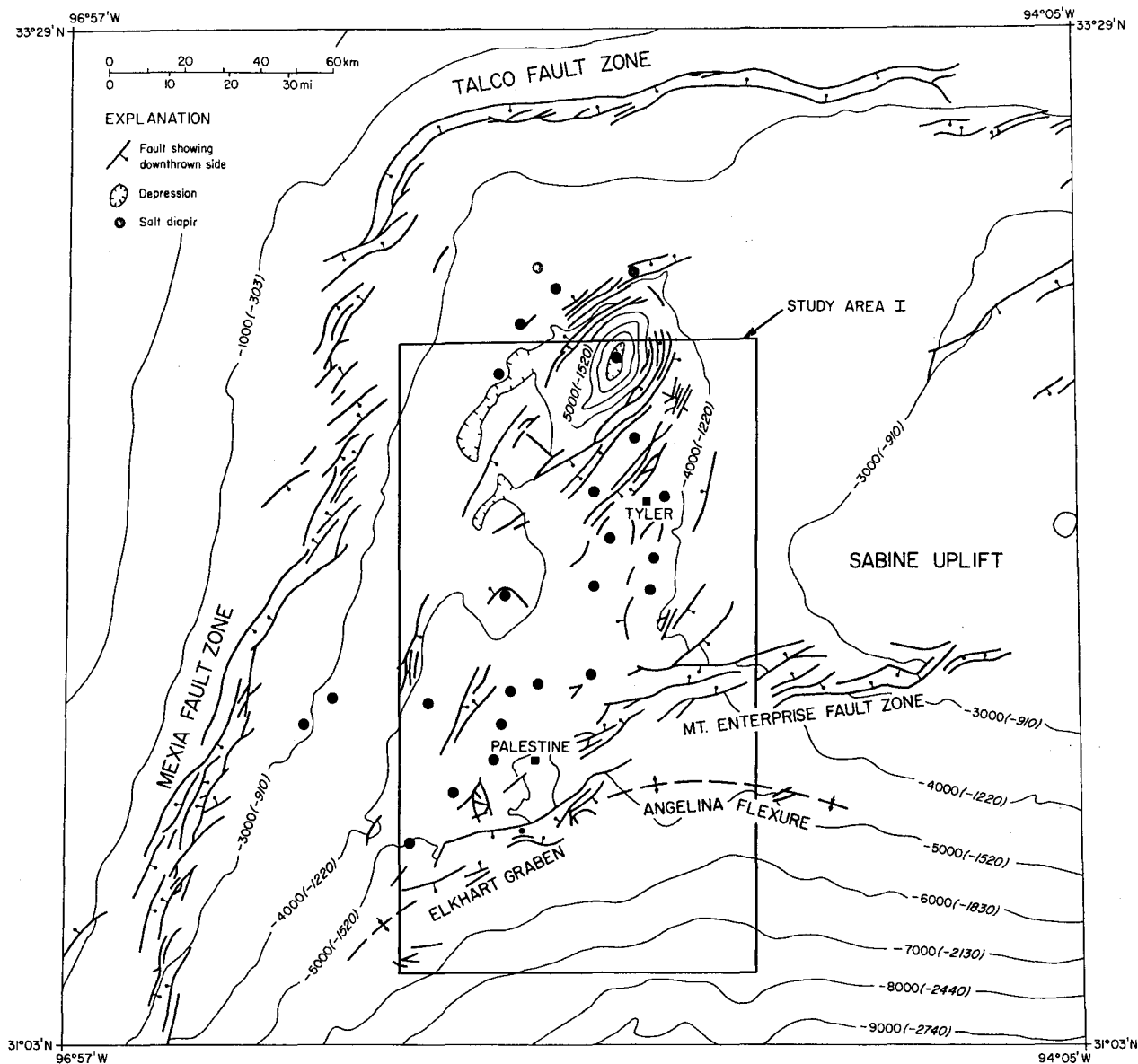
Figure 56. Study area I (in small block) and study area II (entire map area) superimposed on subsurface structural framework of East Texas Basin showing fault traces and structure contours (in feet and meters below sea level) on base of Austin Chalk (modified from Geomap [1980]).
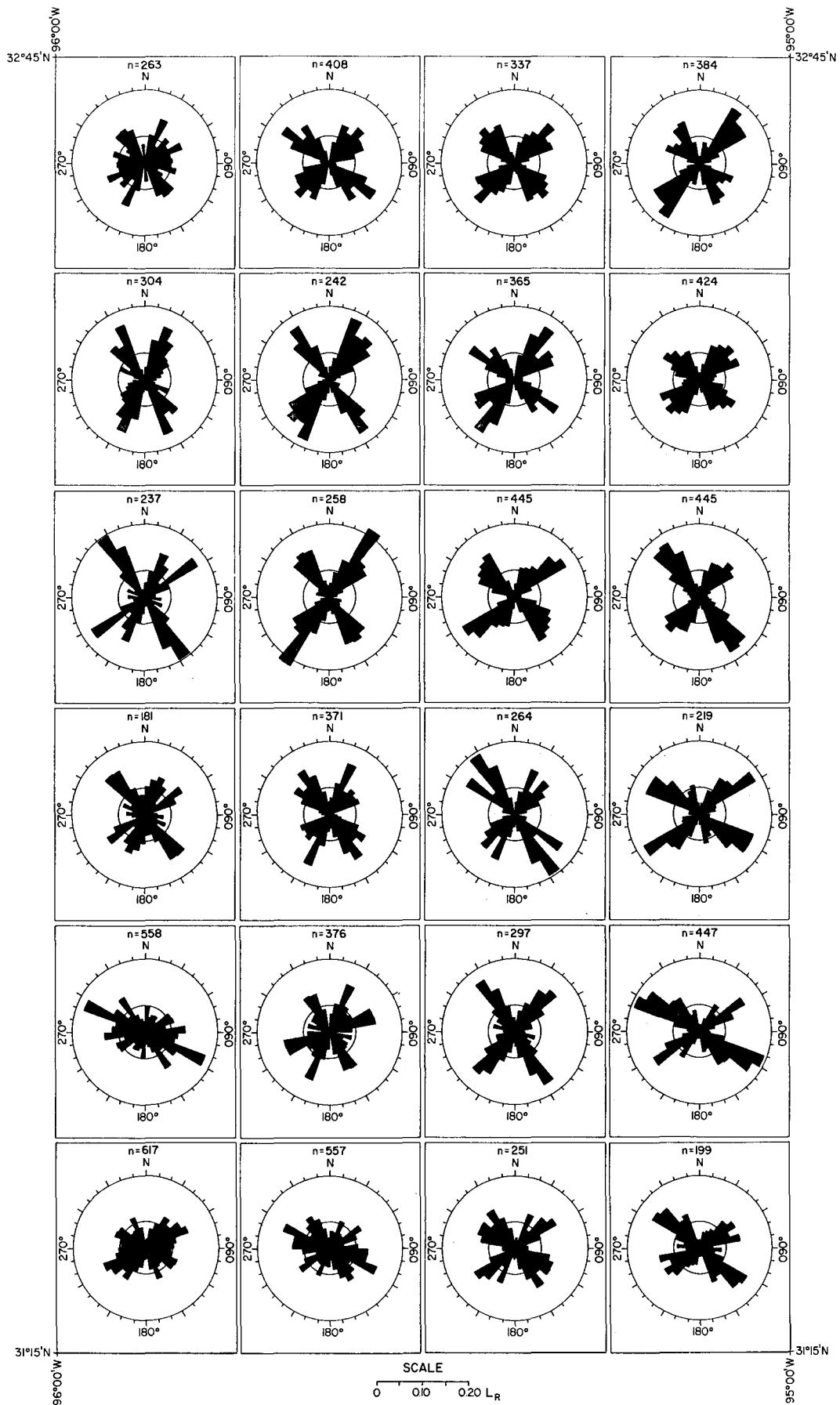
Figure 57. Polar graphs showing relative lengths of lineaments (L$_R$) in each 15-minute quadrangle of study area I, East Texas. Inner circle represents arithmetic mean.
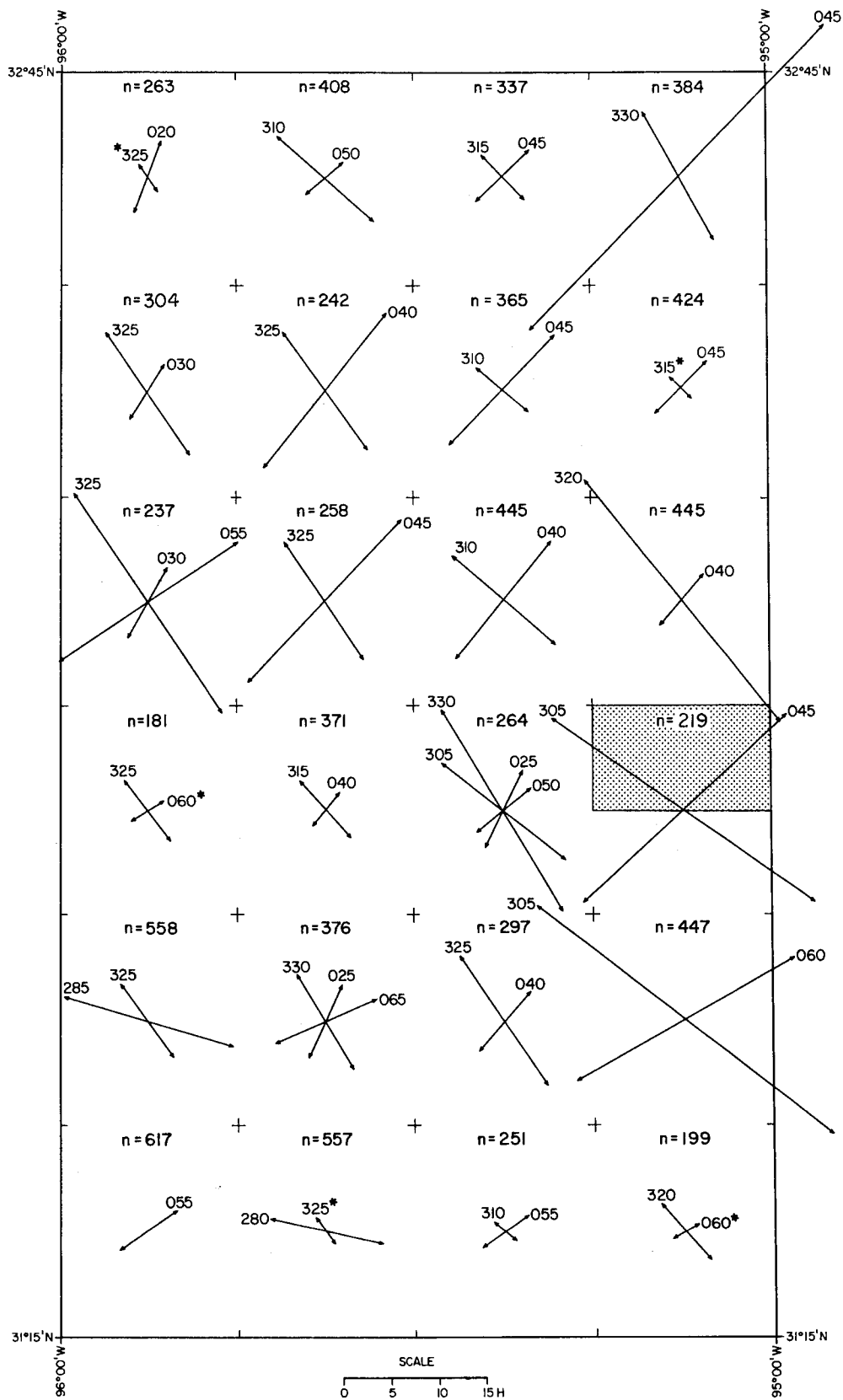
Figure 58. Polar graphs showing Bernshtein accuracy criteria (H) for greater-than-average peaks in each 15-minute quadrangle, East Texas. Photographic coverage in stippled area was unavailable. Asterisks denote peaks significant only at 95-percent level; all other peaks also significant at 99-percent level.

87

DENUDATION RATES IN EAST TEXAS

Edward W. Collins

Denudation rates in East Texas were determined to be 8.85 cm/1,000 yr according to suspended-sediment-load data of East Texas rivers, and 16.8 cm/1,000 yr on the basis of sedimentation-resurvey data of East Texas reservoirs. Rates of recent denudation appear sufficiently low so that there is no threat of breachment to the East Texas salt domes. Studies of incision by the Trinity River during the last glacial period will provide further insight on denudation rates in the region.

The initial investigation of possible breachment of East Texas salt domes involved evaluation of present denudation rates in the East Texas salt basin. The area receives an average rainfall of 75 to 130 cm (30 to 50 inches) and is drained by the Trinity, Neches, and Sabine Rivers and their tributaries. The region is heavily vegetated, and land use ranges from crop and pasture land to densely forested areas.

Both Oakwood and Keechi Salt Domes underlie the Trinity River Basin. Oakwood Dome is covered by approximately 80 percent forest land and 20 percent pasture land. Vegetation at Keechi Dome consists of 80 percent pasture land and 20 percent woodlands. Surface morphology of Oakwood Dome is more rugged than Keechi Dome, exhibiting greater relief and steeper hill slopes.

In East Texas, sediment is removed from drainage basins primarily by rivers or streams. Rates of denudation were computed using suspended-sediment-load data of rivers (fig. 59; table 7) and data from sedimentation resurveys of East Texas reservoirs (fig. 60; table 8). The following equations are used for these computations:

Denudation from suspended-sediment-load data is calculated by

$$\frac{S + B}{A} = Ds ; \qquad\qquad Ds + Dc = D_T \qquad\qquad (1)$$

where A = net drainage area;
        S = suspended-sediment load (avg per yr);
        B = bed load (est per yr);
      Ds = denudation from suspended sediment (per yr);
      Dc = chemical denudation (per yr);
      D_T = total denudation (per yr)

88

Denudation from sedimentation-resurvey data is calculated by

$$\frac{d}{A} = D_T$$ (2)

where A = net drainage area;

  d = average annual deposition (per yr);

  D_T = total denudation (per yr)

An average denudation rate for East Texas using suspended-sediment-load data is estimated to be 8.85 cm/1,000 yr (3.4 inches/1,000 yr). Average rates computed for the Trinity, Neches, and Sabine River basins are 11.45 cm/1,000 yr, 8.16 cm/1,000 yr, and 6.95 cm/1,000 yr (4.6 inches/1,000 yr, 3.3 inches/1,000 yr, 2.7 inches/1,000 yr), respectively (fig. 59; table 7). Suspended-sediment-load data were collected for periods ranging from 7 to 36 years at 10 recording stations maintained by the Texas Department of Water Resources. Consequently, computation of a modern denudation rate is probably accurate despite the necessity of estimating the bed load and chemical denudation. Bed-load values were calculated to be 10 percent of the suspended load (Fisk and others, 1954), and the chemical denudation for the western Gulf region is estimated at 0.037 mm/yr (Livingstone, 1963). Sedimentation resurvey data from four reservoirs in East Texas were used to compute an average denudation rate of 16.8 cm/1,000 yr (6.5 inches/1,000 yr) (fig. 60; table 8). This value is close to the denudation rate computed using suspended-load data and helps to verify the accuracy of these modern denudation values.

Whether recent denudation rates may be projected into the future is questionable. However, these values compare moderately well with Pleistocene rates of denudation along the Texas Gulf Coast calculated by Winker (1979), who determined that Late Pleistocene denudation rates ranged from 3 cm/1,000 yr to 10 cm/1,000 yr (1.2 inches/1,000 yr to 4 inches/1,000 yr). Recent denudation in East Texas appears sufficiently slow so that there is no threat of breachment to potential candidate salt domes, since Oakwood and Keechi Domes are 214 m and 38 m (700 ft and 125 ft) below the surface, respectively. Projection of the modern denudation rate for the next 250,000 years indicates only 23 m (75 ft) of denudation. Predicting future denudation rates to determine the potential for dome breachment requires consideration of future climatic conditions. Results of continuing studies to estimate the incision rate of the Trinity River during the last glacial period should provide more relevant conclusions concerning possible breachment of East Texas salt domes.

89

Table 7. Denudation rates determined in East Texas from suspended-sediment-load data.[a]

Sampling station location	Record period (yr)	Net drainage area km²	Streamflow (avg) m³	Suspended-sediment load (avg)			Bed load[b] (est. 10% susp.-sed. load) m³	Denudation from suspended sediment mm/yr	Estimated[c] chemical denudation for western Gulf region, mm/yr	Total denudation, cm/1,000 yr	Average denudation of basin, cm/1,000 yr
				kg	kg/km²	m³					
TRINITY RIVER BASIN											
1. Trinity River near Rosser	22 (1938-1940)(1953-1975)	21,098	2.24x10⁹	9.19x10⁸	43,788	819,945	81,994.5	0.042	0.037	7.9	
2. Chambers Creek near Corsicana	12 (1963-1975)	2,497	4.19x10⁸	4.32x10⁸	135,216	300,852	30,085.2	0.132	0.037	16.9	
3. Trinity River near Crockett	7 (1968-1975)	36,030	5.83x10⁹	1.58x10⁹	43,788	1,405,620	140,562	0.043	0.037	8	
4. Trinity River at Romayor	29 (1936-1965)	44,512	6.63x10⁹	4.26x10⁹	95,982	3,801,339	380,133	0.093	0.037	13	11.45
NECHES RIVER BASIN											
5. Neches River near Diboll	9 (1966-1975)	7,055	1.39x10⁹	3.35x10⁴	7,356	45,621	4,562	0.007	0.037	4.4	
6. Bayou La Nana at Nacogdoches	10 (1965-1975)	81	2.75x10⁷	3.6x10³	73,213	4,932	493	0.067	0.037	10.4	
7. Neches River near Rockland	35 (1930-1966)	9,166	2.0x10⁹	6.68x10⁸	-----	595,539	59,553	0.071	0.037	10.8	
8. Angelina River near Zavalla	8 (1945-1952)	7,260	3.0x10⁹	5.02x10⁸	-----	447,579	44,757	0.067	0.037	10.4	
	8 (1953-1960)	8,897	1.64x10⁹	1.03x10⁸	-----	91,242	9,124	0.011	0.037	4.8	8.16
SABINE RIVER BASIN											
9. Sabine River near Tatum	7 (1968-1975)	9,047	2.67x10⁹	1.24x10⁸	13,661	110,970	11,097	0.013	0.037	5	
10. Sabine River near Logansport, La.	36 (1932-1933)(1935-1968)	12,533	2.92x10⁹	6.68x10⁸	53,247	595,539	59,553	0.052	0.037	8.9	6.95

[a] Derived from Stout and others (1961); Adey and Cook (1964); Cook (1970); Mirabal (1974); Dougherty (1979)
[b] From Fisk and others (1954)
[c] From Livingstone (1963)

Table 8. Denudation rates in East Texas determined from sedimentation resurvey data.

Reservoir	Stream	Date of survey	Drainage area (km²)	Average annual deposition per yr (m³)	Denudation (cm/yr)	Denudation (cm/1,000 yr)
Wolf Creek	Wolf Creek	1919 to Apr. 1939 (20 yr)	6.6	1.446×10^3	2.19×10^3	21.9
Grand Saline	Simons Branch	Feb. 1925 to Apr. 1938 (13.25 yr)	5.5	2.143×10^3	3.89×10^{-2}	38.9
Dam B (Steinhagen)	Neches River	1951 to Feb. 1960 (8.83 yr)	19,614	2.39×10^5	1.18×10^{-3}	1.18
Lake Cherokee	Sabine River	Oct. 1948 to Apr. 1960 (11.5 yr)	440	2.87×10^5	5.28×10^{-3}	5.28

Source: Evans and Bramblett (1960); U.S. Army Corps of Engineers (1960); Sedimentation Committee of Water Resources Council (1975).
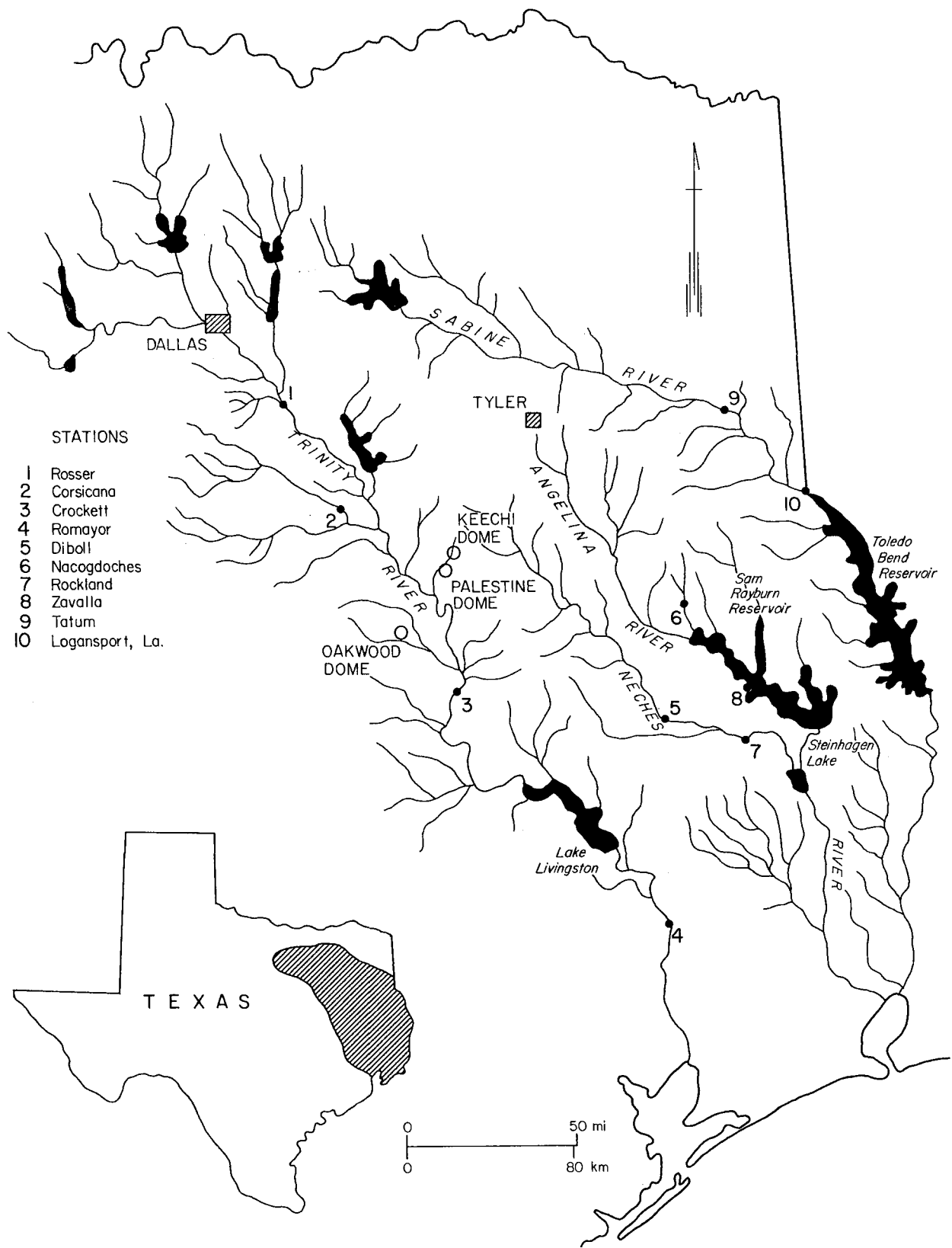
Figure 59. Location of sampling stations for suspended-sediment-load data, East Texas.
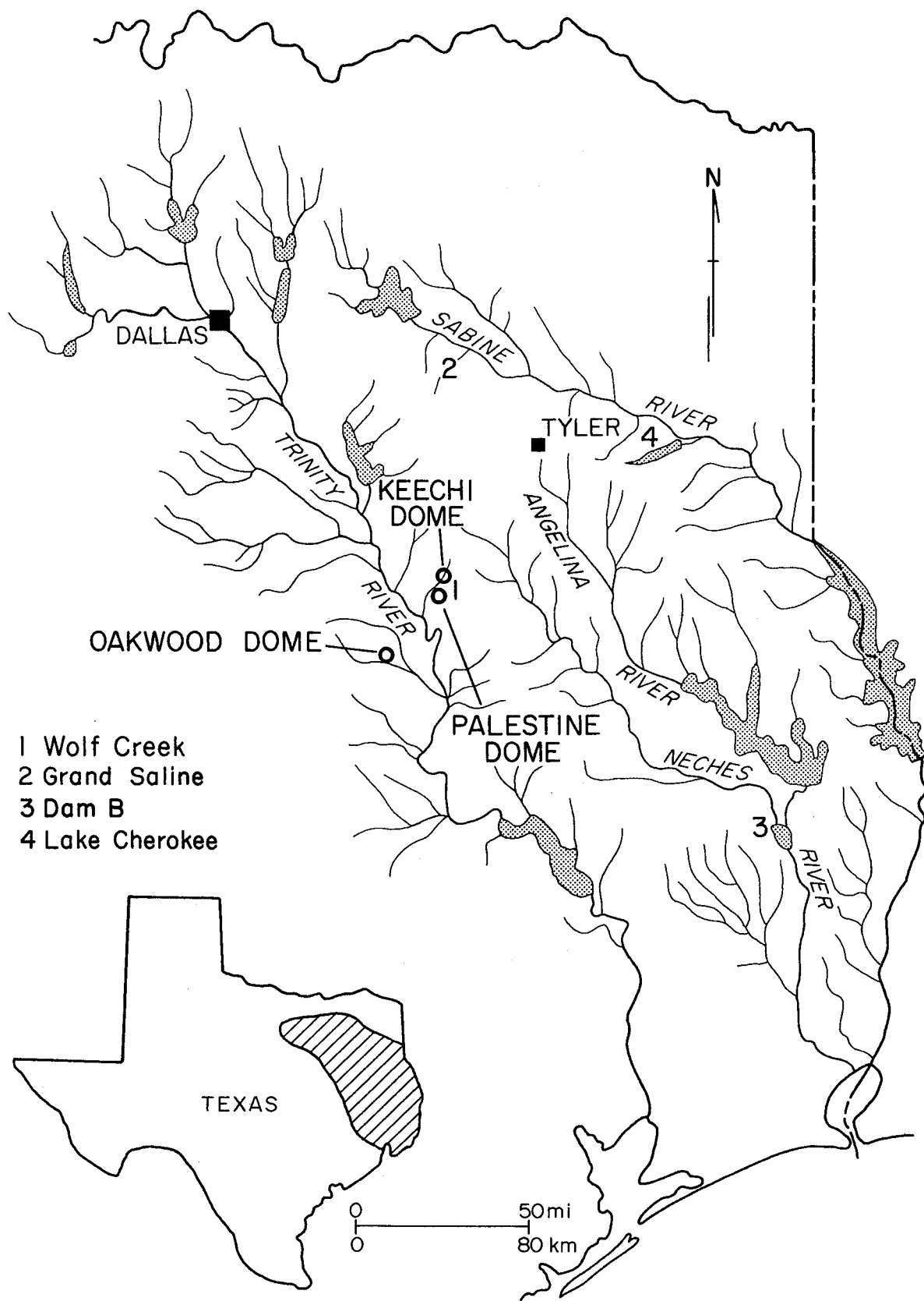
Figure 60.   Location of sedimentation resurvey data for selected East Texas reservoirs.

POTENTIAL MICROSEISMICITY IN EAST TEXAS

Wayne D. Pennington,* Charles W. Kreitler, and Edward W. Collins

A number of impulsive events have been recorded on a single-channel smoked-paper seismograph located near Rusk, Texas. These recorded events may be microseismic events from the Mount Enterprise fault system.

A single-channel smoked-paper seismograph was installed near Rusk, Texas, by Law Engineering Testing Company and the Bureau of Economic Geology on February 5, 1980. A filter setting was changed on March 24, 1980, and most of the high quality seismograms were recorded after that date.

The seismograph, as currently installed, is operating with a peak magnification of about 35,000 times at 10 Hz; the response diminishes sharply at both higher and lower frequencies. This is not very sensitive; similar seismographs operated for local microearthquake detection may peak at 30 Hz with magnification of over 1,000,000 times. The instrument will not satisfactorily record events of $M_L \leq 2$ at distances greater than 20 km (12 mi) nor events of $M_L \leq 3$ beyond about 50 km (30 mi), where M_L equals the local Richter magnitude. The detection capabilities of the current installation are poor. This report is based on the analysis of data recorded March 24, 1980, through July 13, 1980.

A number of impulsive events were recorded, many of which occurred within 6 to 40 km (4 to 25 mi) of the station (fig. 61a to e). Some of the events are explosions (fig. 61a), exhibiting typical characteristics such as daytime occurrence, compressional (up) first motions, and poor shear-wave generation. These events are probably associated with seismic-reflection exploration surveys in the general area. Other events may be less readily classified as explosions or earthquakes. Such events may occur day or night, may exhibit varying first motions, and may sometimes show good shear-wave generation. Many of these events (figs. 61b to e) resemble microearthquakes (of $M_L = 0.0$ to 1.5) rather than explosions, but no definite conclusion can be made at this time. Recordings of known small earthquakes made during an aftershock sequence in Pakistan in 1975 are shown in figures 61f and g. There is a strong similarity between the known Pakistan earthquakes and the events of East Texas.

---

*Department of Geological Sciences, The University of Texas at Austin.

93

However, non-earthquake sources such as quarries, nearby falling rocks, or atmospheric disturbances, given the right set of circumstances, can yield seismograms such as those presented for East Texas.

On March 19, 1957, a series of four earthquakes shook the area of Rusk, Texas (U.S. Coast and Geodetic Survey, 1957). These events were not instrumentally located, but they presumably lie within the isoseismal line enclosing the area of intensity V (see fig. 62). The currently installed seismograph is operating near the center of this isoseismal area and is presumably near the epicenters of the 1957 events. Some of the events recorded by the seismograph may be microearthquakes associated with the feature responsible for the 1957 events, which would most likely be the Mount Enterprise fault system. Collins and others (1980) have shown that parts of the Mount Enterprise fault system have been active in recent times and may be active today, as indicated by offsetting Quaternary gravels and elevation anomalies following first-order releveling. Because the areas described in their study are 20 and 60 km (10 and 40 mi) from the seismic station, only the maximum events from those regions would be recorded at the Rusk station. Additional station coverage with increased sensitivity will be necessary before confirmation can be made of the presence or absence of seismic activity along the Mount Enterprise fault system or any other features in the area. Data from additional station coverage will also be necessary to reveal whether this seismicity could threaten the integrity of a nuclear waste repository in a nearby salt dome.

Figure 61 (right). Events recorded by seismograph near Rusk, East Texas (a to e); known earthquakes recorded on a similar instrument in Pakistan, 1975 (f to g).

    (a)   Probable nearby explosion: 21:42 u.t. (3:42 p.m. c.s.t.) April 21, 1980

    (b)   Nighttime event, probably 30 km away: 09:17 u.t. (4:17 a.m. c.d.t.) June 29, 1980

    (c)   Daytime event, dilational first motion, 6 km distant: 17:16 u.t. (11:16 a.m. c.s.t.) April 22, 1980

    (d)   Nighttime event, one of many in a series, 20 to 40 km distant: 06:00 u.t. (1:00 a.m. c.d.t.) June 6, 1980

    (e)   Early morning event, compressional first motion, 14 km distant: 11:06 u.t. (6:06 a.m. c.d.t.) May 15, 1980

    (f)   Typical small earthquake recorded at a site with alluvial cover, on an instrument with severe filtering, 14 km distant

    (g)   Typical small earthquake recorded at a good site, with broad bandpass, 21 km distant
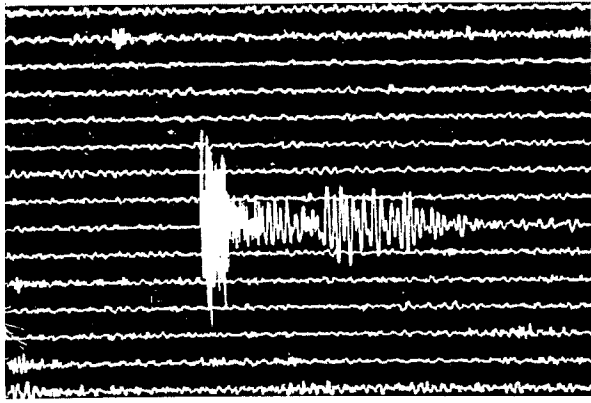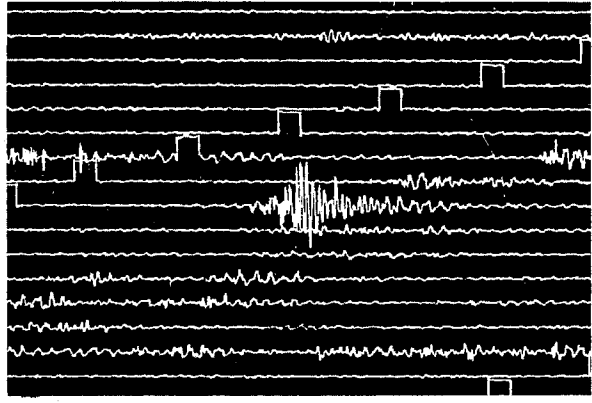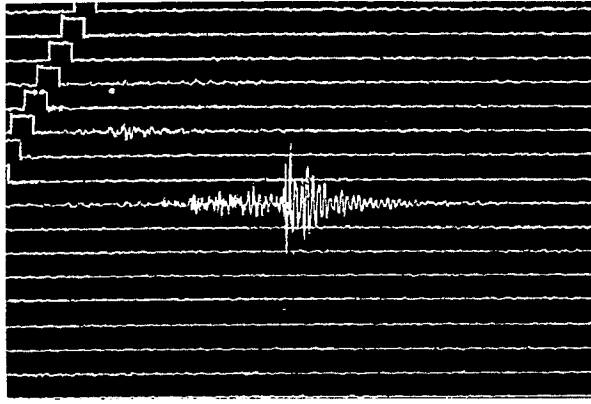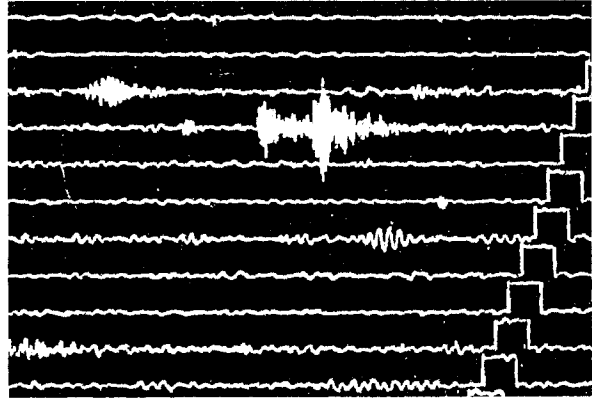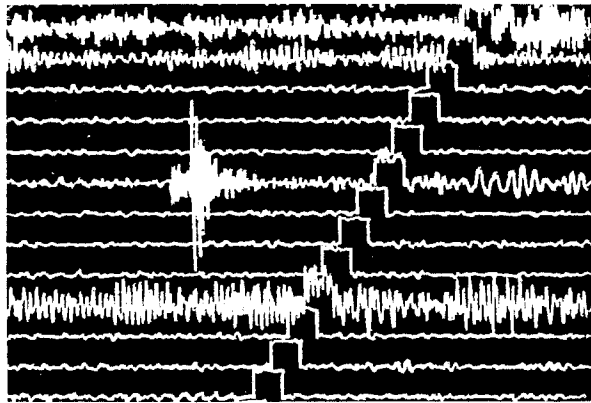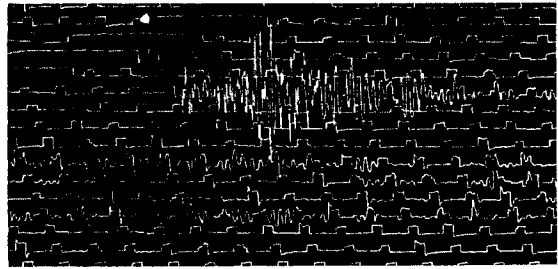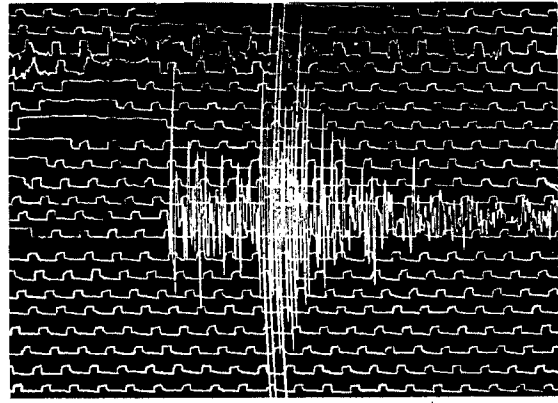
Figure 61 (a-g).
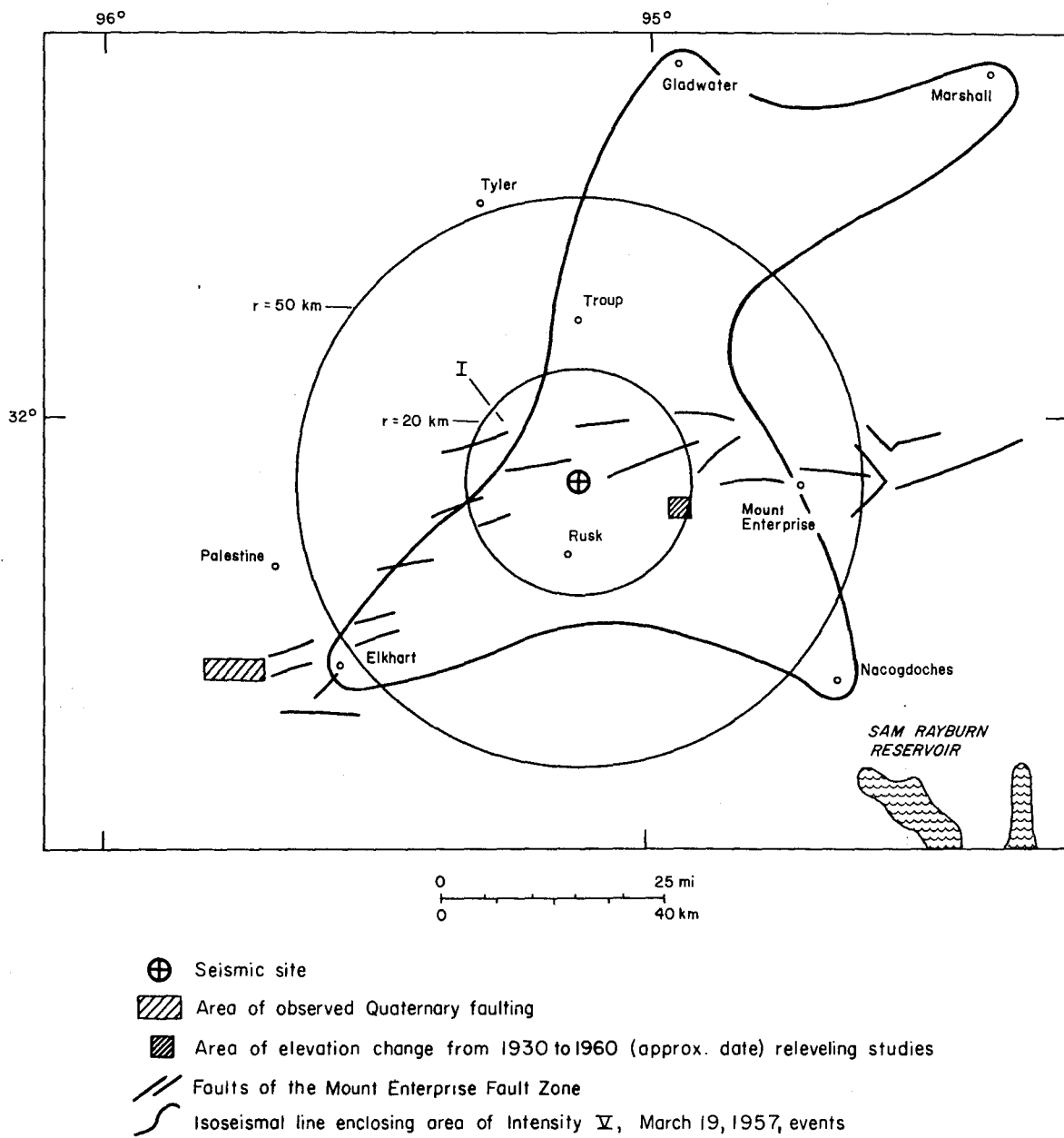
Figure 62. Location map of seismograph recording site and nearby geographic features near Rusk, East Texas.

96

HOLOCENE ALLUVIAL DEPOSITS AT OAKWOOD DOME, EAST TEXAS

Edward W. Collins and Owen R. Dix

Holocene floodplain deposits occupy a topographic depression over the Oakwood Dome. The floodplain extends from the central area of the dome, across the southern flank of the dome, and then away from the dome. Drilling of shallow boreholes revealed that floodplain deposits over the dome are twice as thick as the deposits away from the dome. Subsidence over the dome may account for the thickening of this Holocene unit.

To better understand the "central depressions" commonly observed over shallow salt domes, detailed investigations of the central drainage system and floodplain deposits over Oakwood Dome were made. The drainage network is characterized by a number of well-defined valleys confining moderately to deeply incised channels of intermittent streams. The streams generally commence as shallow, vegetated rills that grade into steep-sided channels 1 to 4 m (3 to 12 ft) deep with width to depth ratios ranging from 0.7 to 4.0. In their headwaters the channels are now being incised in bedrock and contain little Holocene alluvium; however, in the south-central part of the dome area, the streams have deposited a floodplain with an average width of 300 m (980 ft). Maximum depth of incision (6 m [19.8 ft]) generally occurs near the center of the dome (fig. 63).

Many tributaries of the main channels have discordant junctions with elevation differences of up to 2 m (6 ft). Nickpoints are also abundant within the channels; some are capped by resistant, ferruginous sandstones, whereas others exhibit no lithologic control. Presence of nickpoints with no lithologic control indicates that the channels have not attained equilibrium and are youthful (Heede, 1974) compared with the characteristically mature patterns of adjacent non-dome areas.

Ten shallow boreholes were drilled into the Holocene floodplain deposits on the south side of Oakwood Dome to determine thickness variations over and away from the dome (figs. 64 and 65). Floodplain deposits consist of a thin (10 to 40 cm) basal gravel unit composed of subrounded to subangular ironstone pebbles and coarse- to medium-grained sand. Overlying this basal unit are medium- to fine-grained sand and silty clay units. The deposits over the dome are consistently 8 to 11 m (26 to 36 ft) thick, whereas away from the dome they are 4 m (12 ft) thick; the change in thickness occurs at or near the salt dome boundary (fig. 65). At the center of the dome, 200 m (650 ft)

north of a well-developed floodplain, intermittent streams are incising bedrock. These variations in thickness of the Holocene deposits suggest that subsidence occurred during deposition, resulting in thicker sediment accumulation over the dome than south of the dome. This subsidence may result from loss of volume created by ground-water interactions with salt or cap rock, although this has yet to be established.

This investigation is developing new data on the origin of the "central depressions" that are common over the East Texas salt domes. If subsidence is occurring over Oakwood Dome, ongoing cap-rock and hydrologic investigations may determine the mechanism for subsidence and provide further insight into the dome's stability.
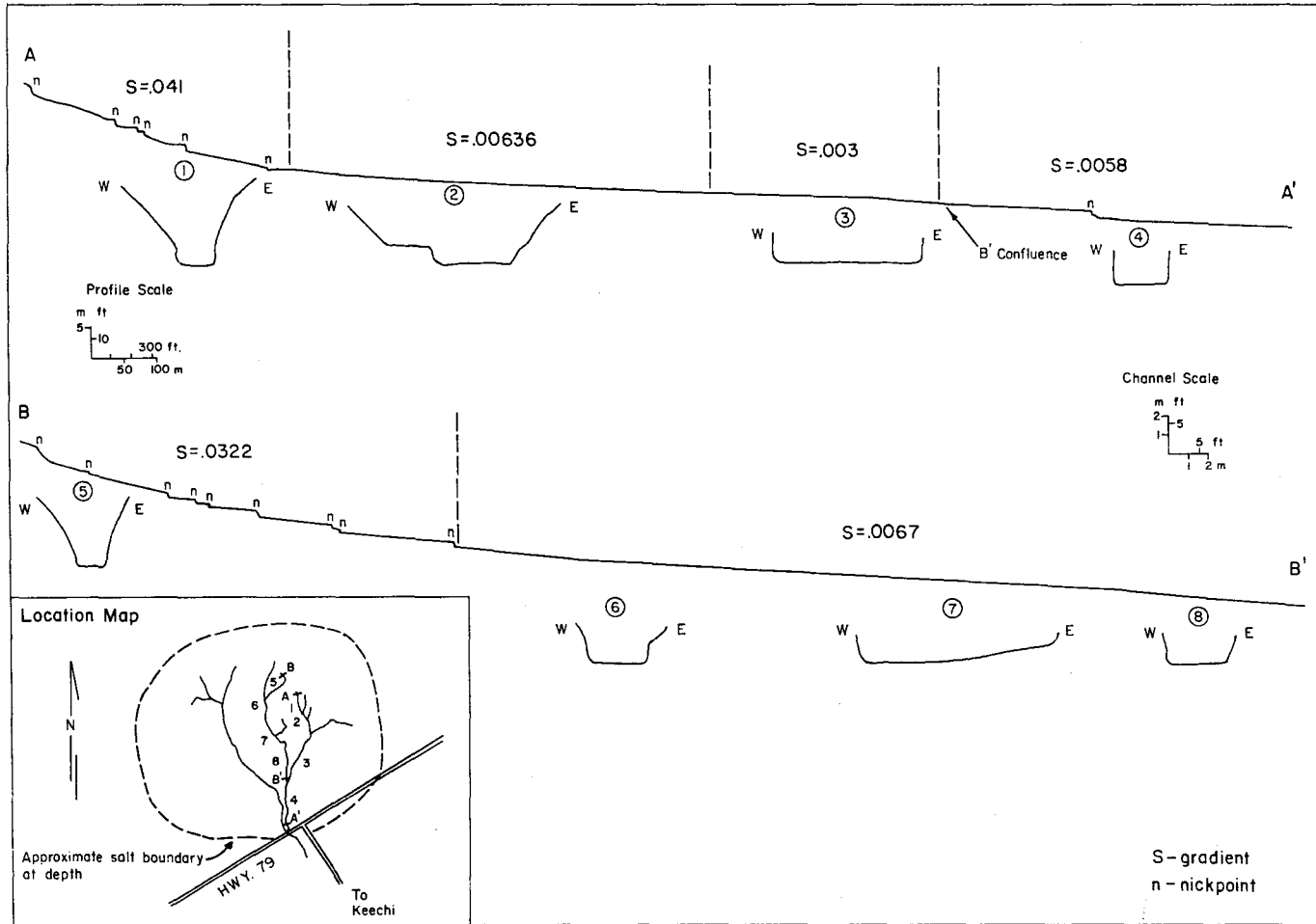
Figure 63. Stream profiles and channel cross sections of streams over central Oakwood Dome area, East Texas.

Figure 64. Geologic map, Oakwood Dome, East Texas.
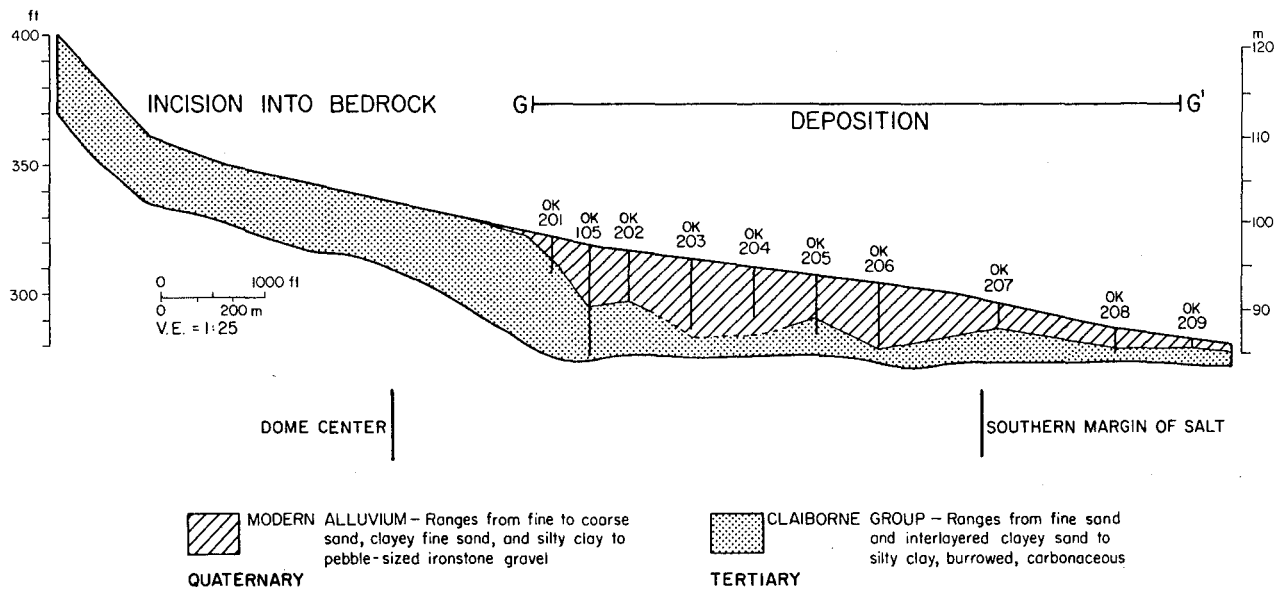
Figure 65. Cross section G-G' of floodplain deposits over Oakwood Dome, East Texas.

MORPHOLOGIC MAPPING OF OAKWOOD, PALESTINE, AND KEECHI SALT DOMES, EAST TEXAS

Edward W. Collins

Oakwood and Palestine Domes display an annular drainage pattern around the perimeter of the dome as well as developing subdendritic and centripetal patterns over the central dome areas. Drainage of the Keechi Dome area is subdendritic with a creek flowing over the center of the dome. Morphologic mapping of the three domes has determined that hillside slopes at Oakwood Dome are steeper slopes than at other domes, but all three dome areas display central topographic low areas where modern sediment deposition is occurring.

The surficial expression and stream drainage over salt domes can provide data on the present nature of the dome, and such data are necessary to evaluate any recent movement that may have occurred. Dix (1979) has shown from quantitative analyses of stream drainage that Oakwood Dome may be in a less mature geomorphic stage than are Palestine and Keechi Domes. Geomorphic studies of the domes support this theory as well as document features common to all three domes.

Drainage at Oakwood Dome displays an annular pattern around the perimeter of the dome and a subdendritic pattern flowing toward a topographic low at the south-central side of the dome (figs. 66 and 67). Palestine Dome is encircled by annular drainage, whereas intermittent streams in a centripetal pattern feed a man-made lake in the central topographic depression above the dome (figs. 68 and 69). At Keechi Dome, Keechi Creek flows north to south within a slight topographic low over the center of the dome (figs. 70 and 71).

Morphologic maps of Oakwood, Palestine, and Keechi Domes (figs. 72, 73, and 74) contrast the difference in slopes that have resulted from erosional processes and slopes that have resulted from depositional processes. Slopes were determined from U.S. Geological Survey topographic maps at a scale of 1:24,000. These maps enable a comparison of erosional slopes, depositional slopes, and drainage patterns at the three domes.

At Oakwood Dome, erosional slopes are predominantly steeper than the slopes at Keechi and Palestine Domes. Approximately 50 percent of the surface expression of Oakwood Dome has slopes within a range from 5° to 15°; at Keechi Dome, greater than 95 percent of the area has slopes ranging from 0° to 5°. At Palestine Dome, hillsides with slopes ranging from 0° to 5° compose approximately 65 percent of the

area. Erosional slopes over Oakwood and Palestine Domes are steeper than hillside slopes away from the dome; at Keechi Dome, however, this relationship between steepness of slope and proximity to the dome does not persist.

Although steepness of erosional slopes varies for each dome, all three domes display depositional slopes commonly occurring in a central topographic depression. In the central area over Keechi Dome the floodplain of Keechi Creek is approximately three times as wide as the floodplain upstream and downstream from the dome. At Palestine Dome, a man-made lake is located over the central dome area. A relatively large floodplain occurs in the south-central part of Oakwood Dome; drilling in this area has revealed that the modern floodplain alluvium is twice as thick over the dome than away from it. This may indicate subsidence over Oakwood Dome, possibly because of the interaction of ground water with cap rock or salt.
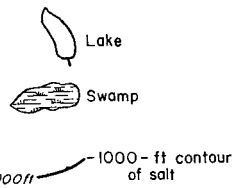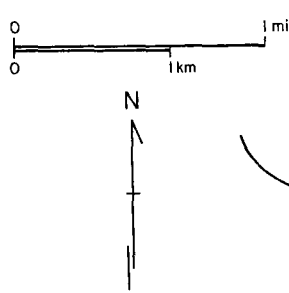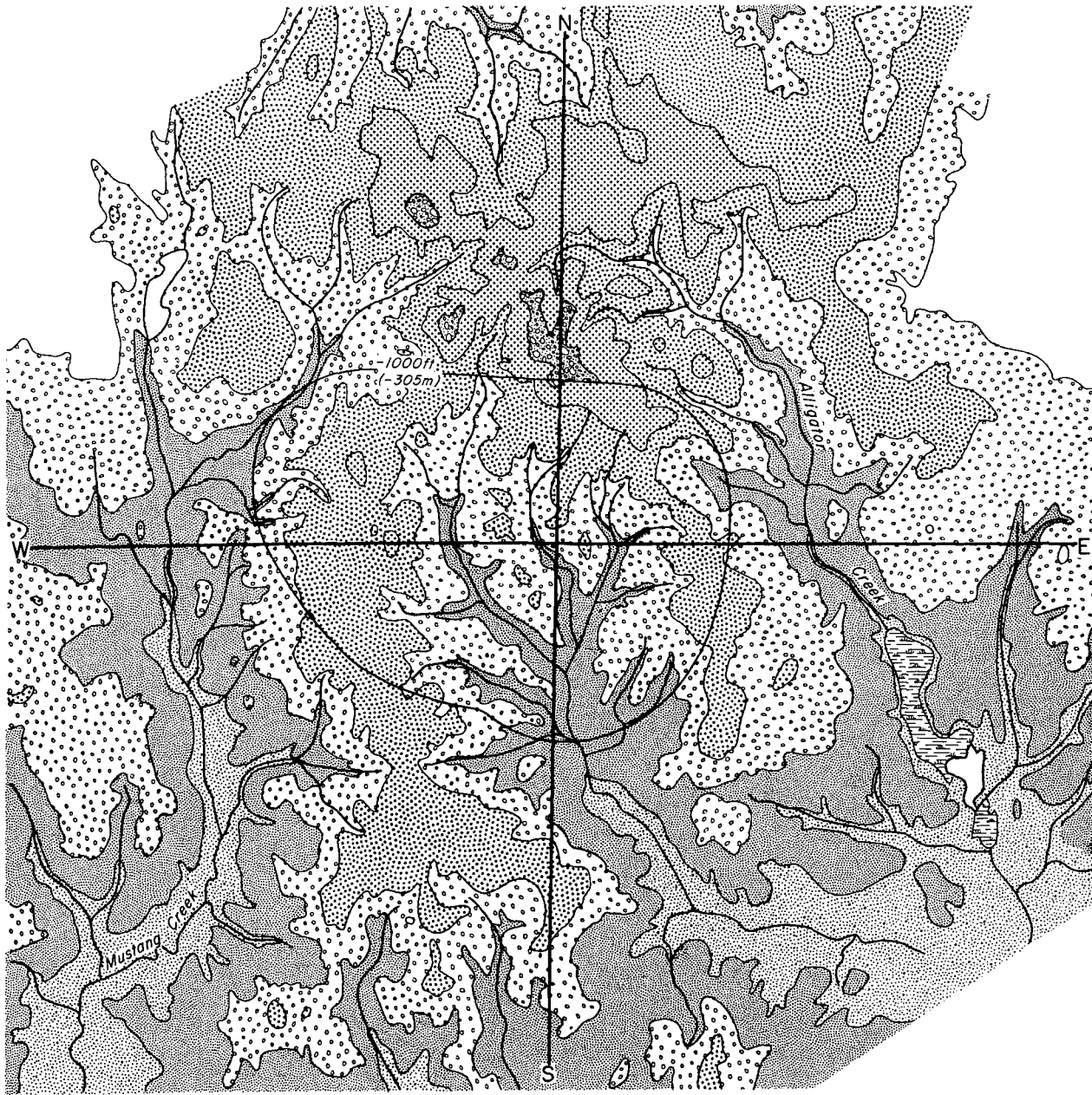
Figure 66. Elevation map, Oakwood Dome area, East Texas.
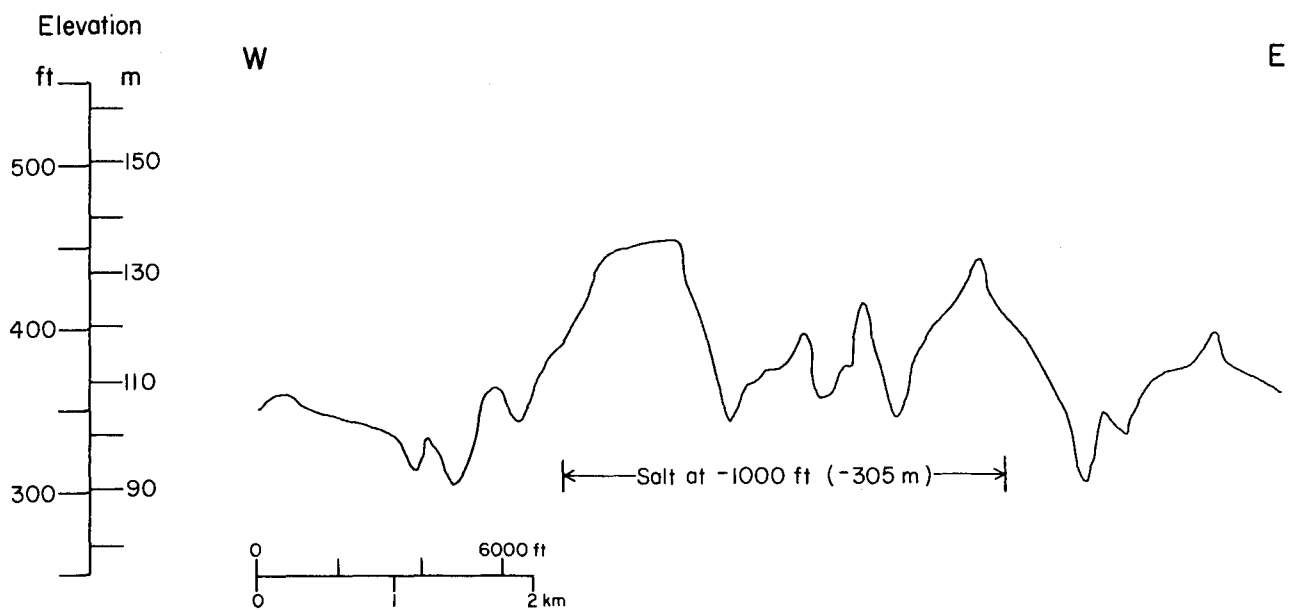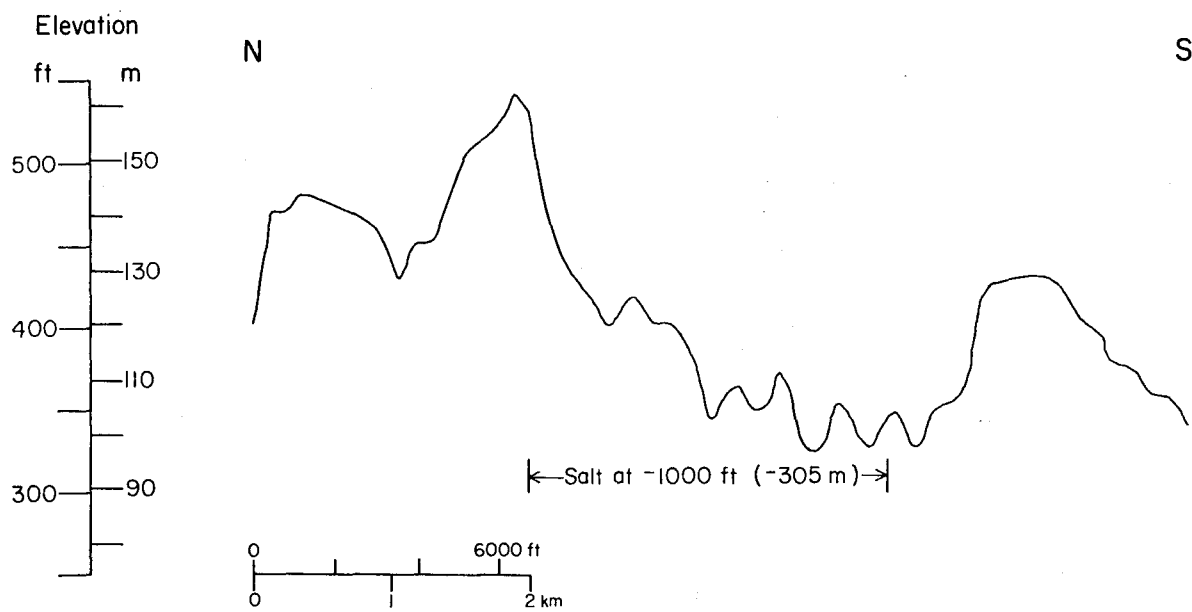
Figure 67. North-south and east-west topographic profiles over Oakwood Dome, East Texas, displaying topographic lows over the dome.

105
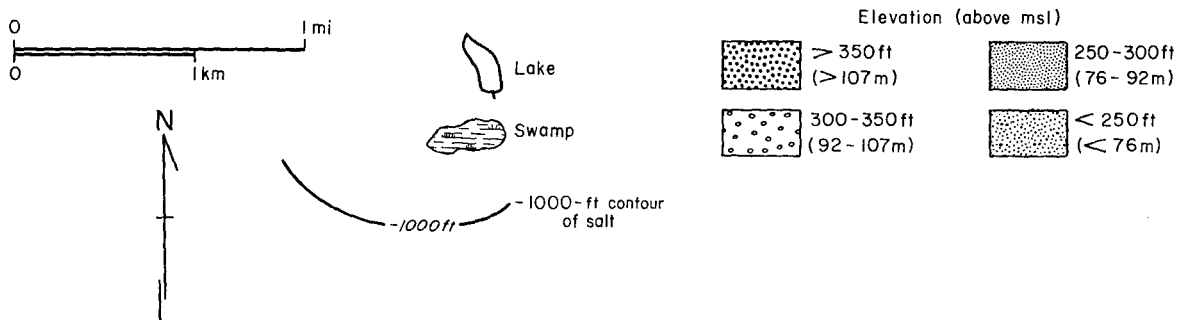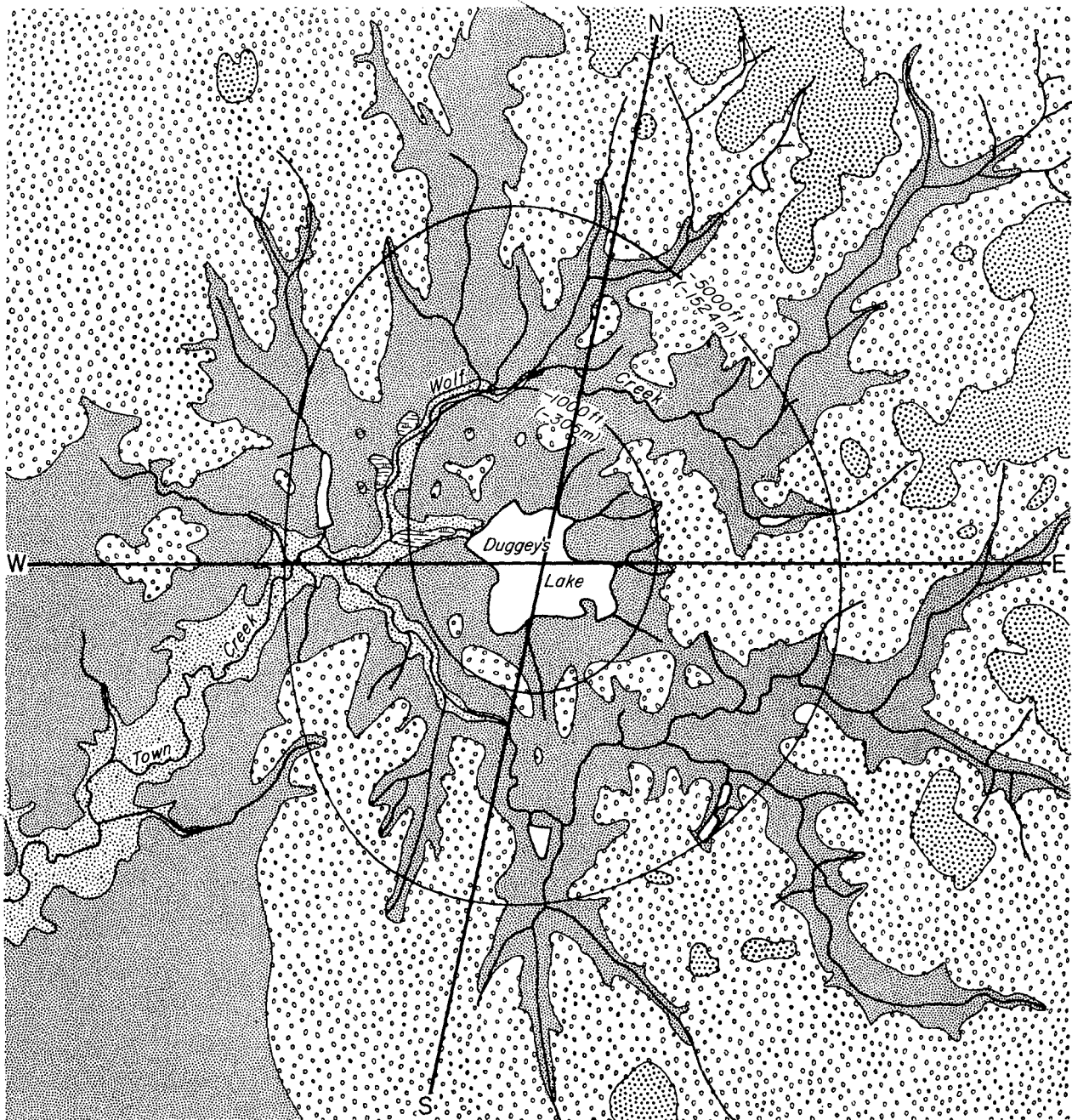
Figure 68. Elevation map, Palestine Dome area, East Texas.
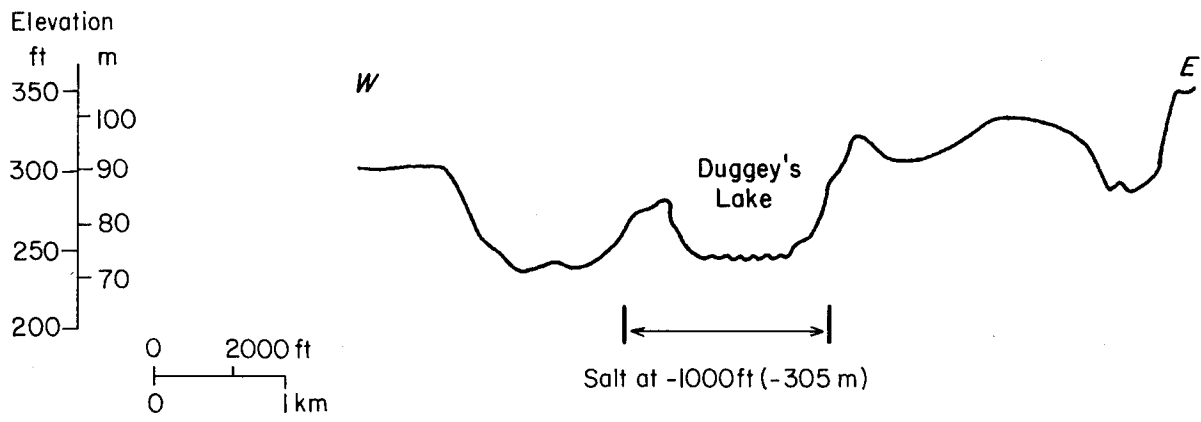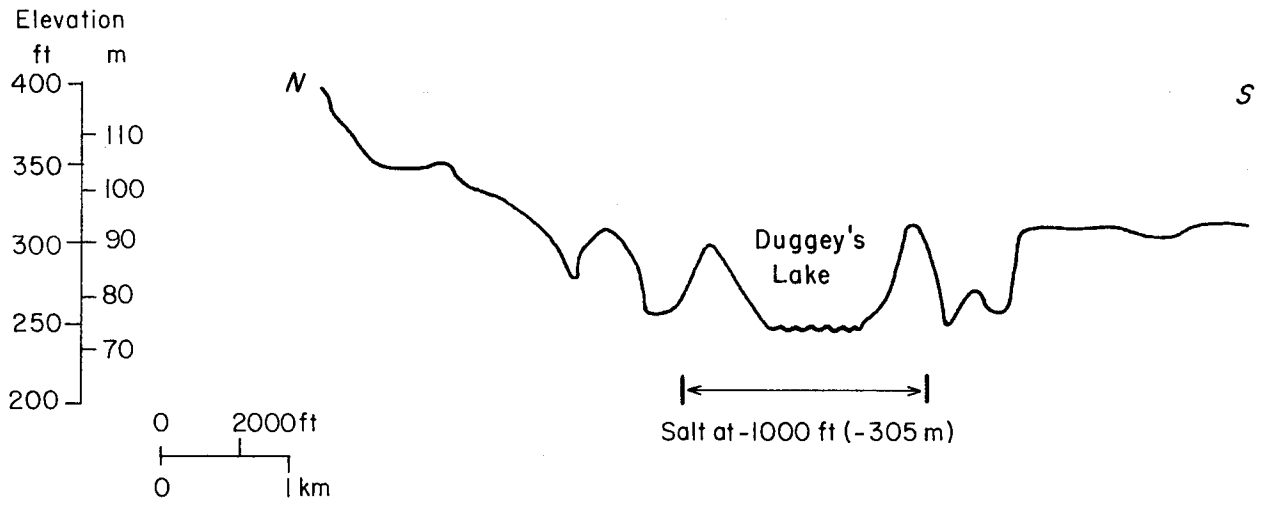
Figure 69. North-south and east-west topographic profiles over Palestine Dome, East Texas, showing topographic depression over the dome.
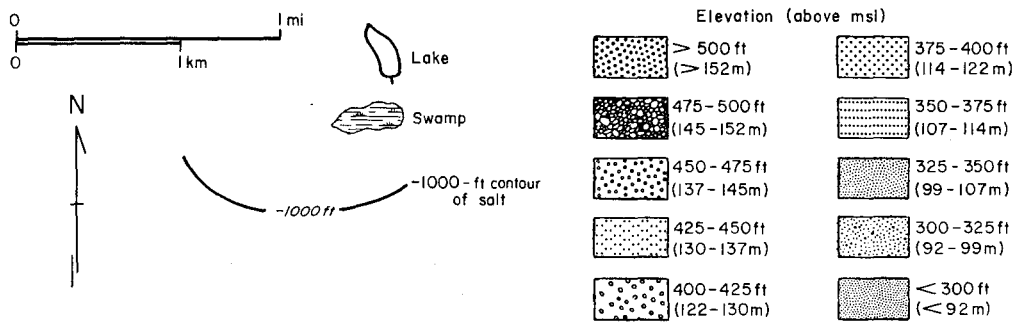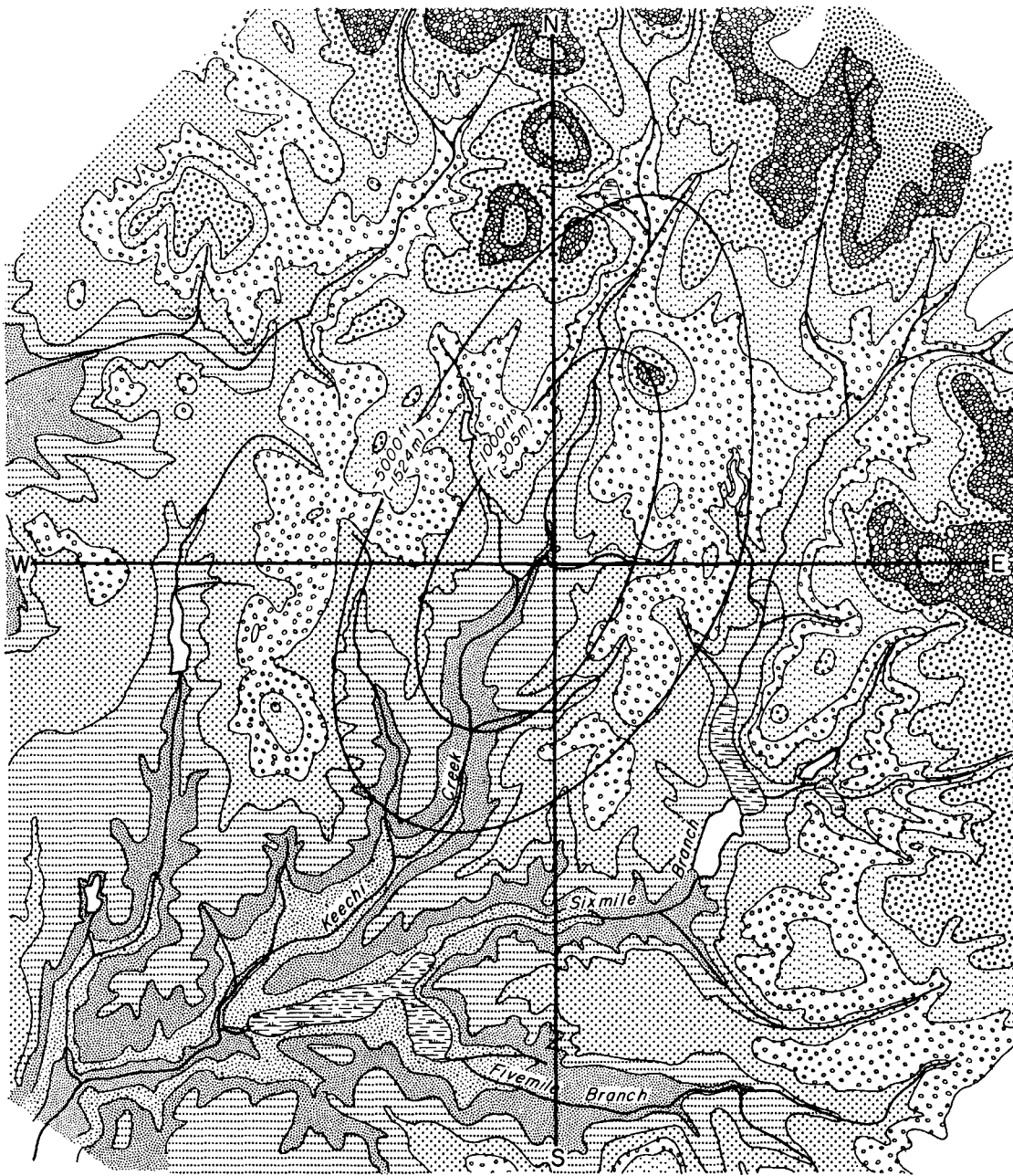
Figure 70. Elevation map, Keechi Dome area, East Texas.
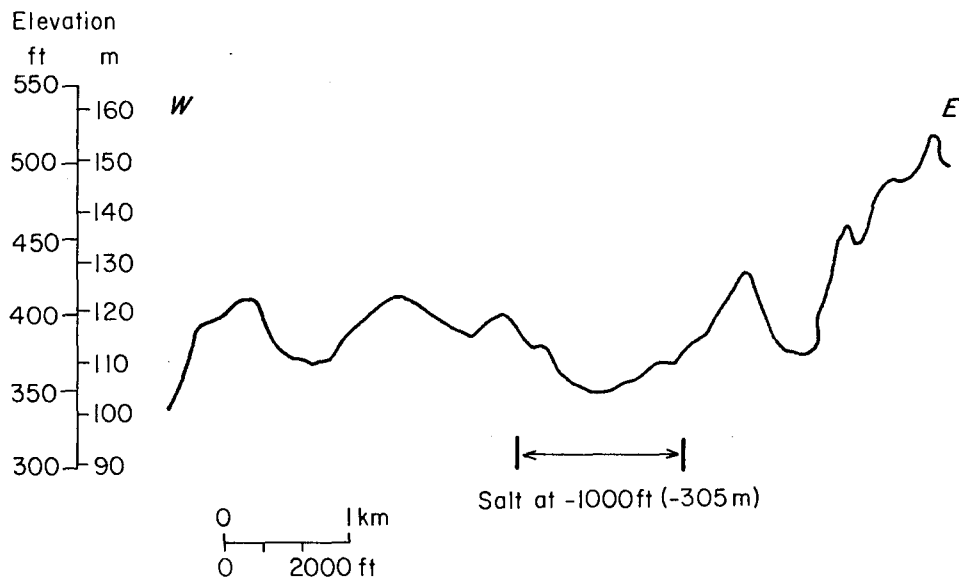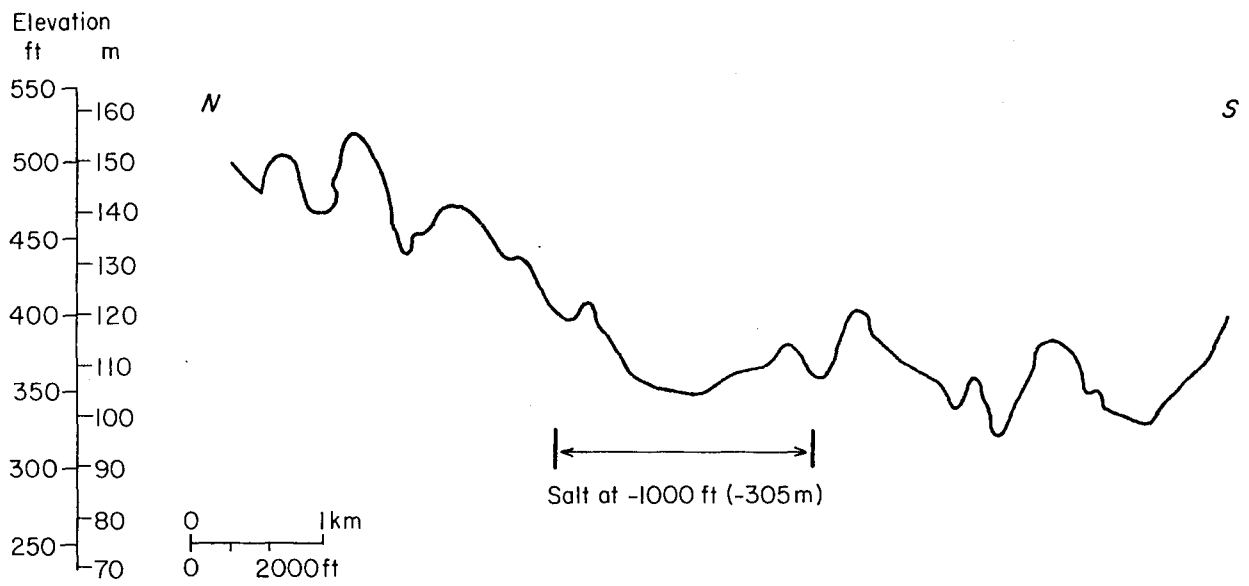
Figure 71. North-south and east-west topographic profiles over Keechi Dome, East Texas.
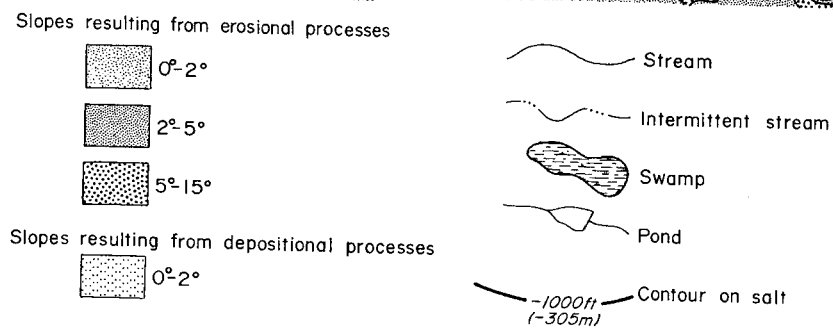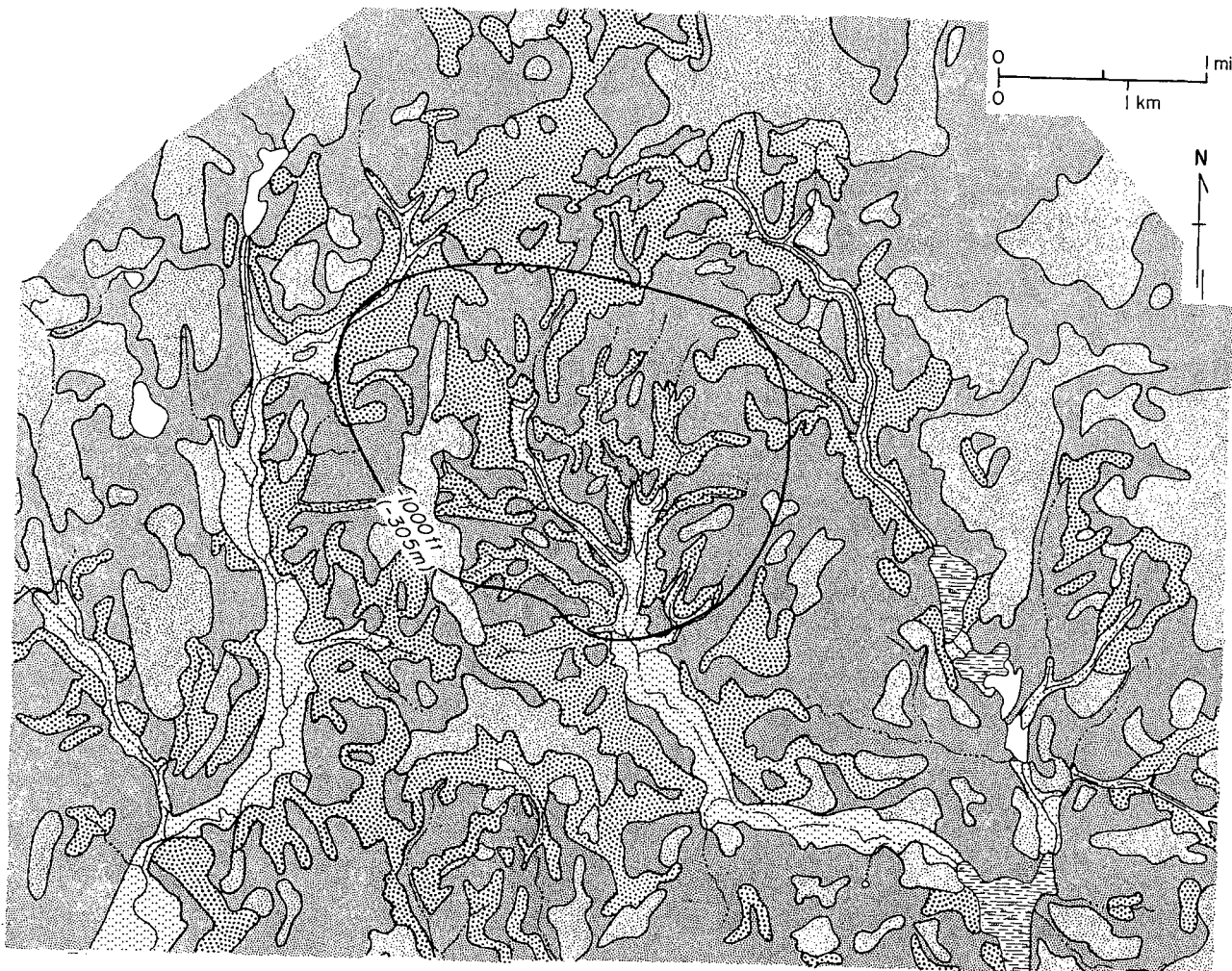
Figure 72. Morphologic map, Oakwood Dome, East Texas.

110
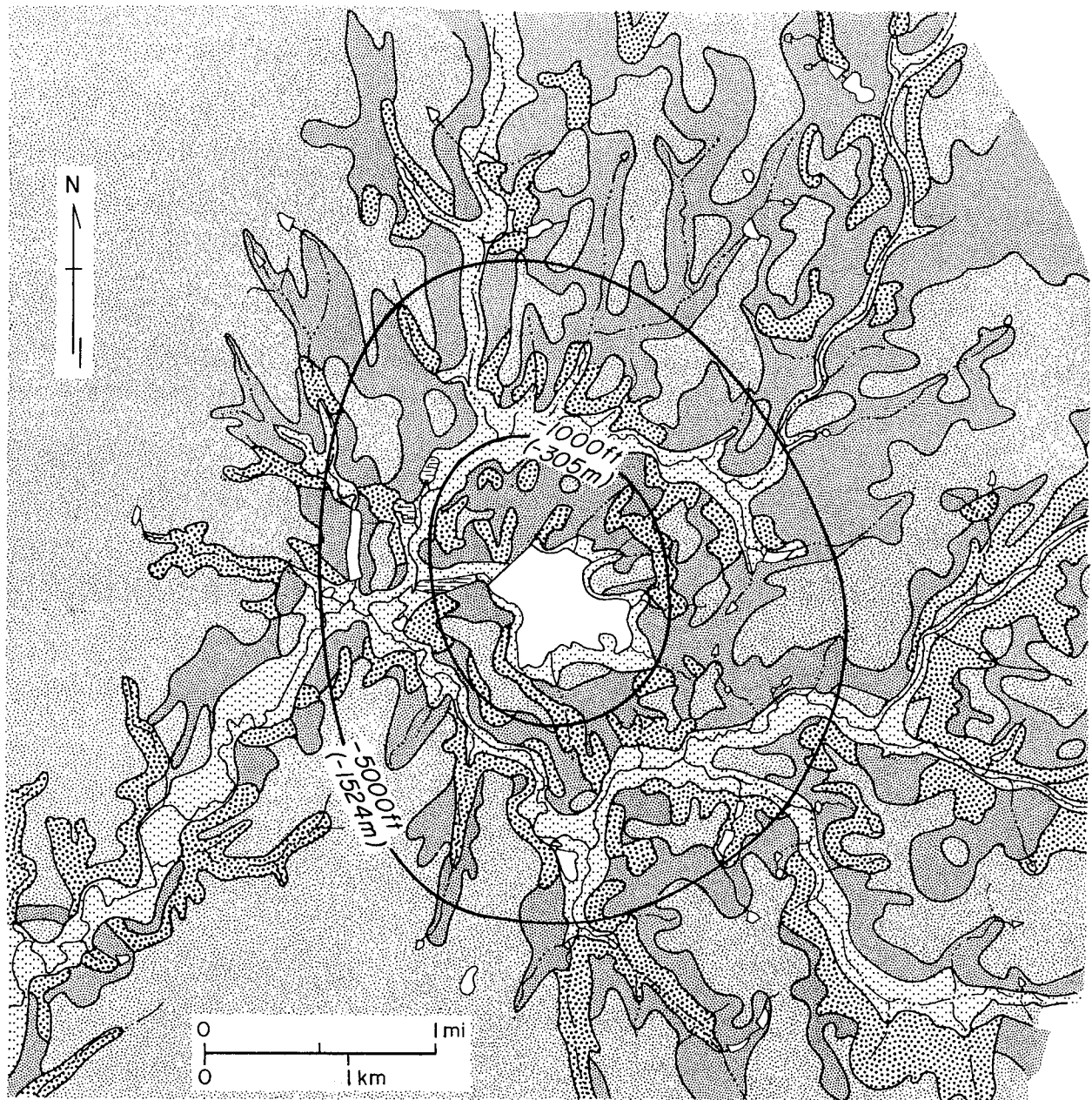
Slopes resulting from erosional processes

▦	0°-2°
▦	2°-5°
▦	5°-15°
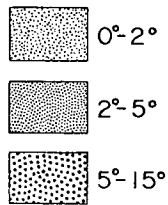
Slopes resulting from depositional processes

▦	0°-2°
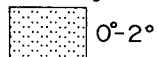
Stream

Intermittent stream

Swamp

Pond

Contour on salt
-1000ft
(-305m)

Figure 73. Morphologic map, Palestine Dome, East Texas.

111
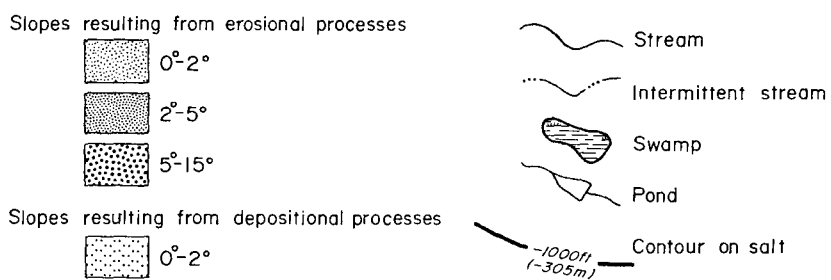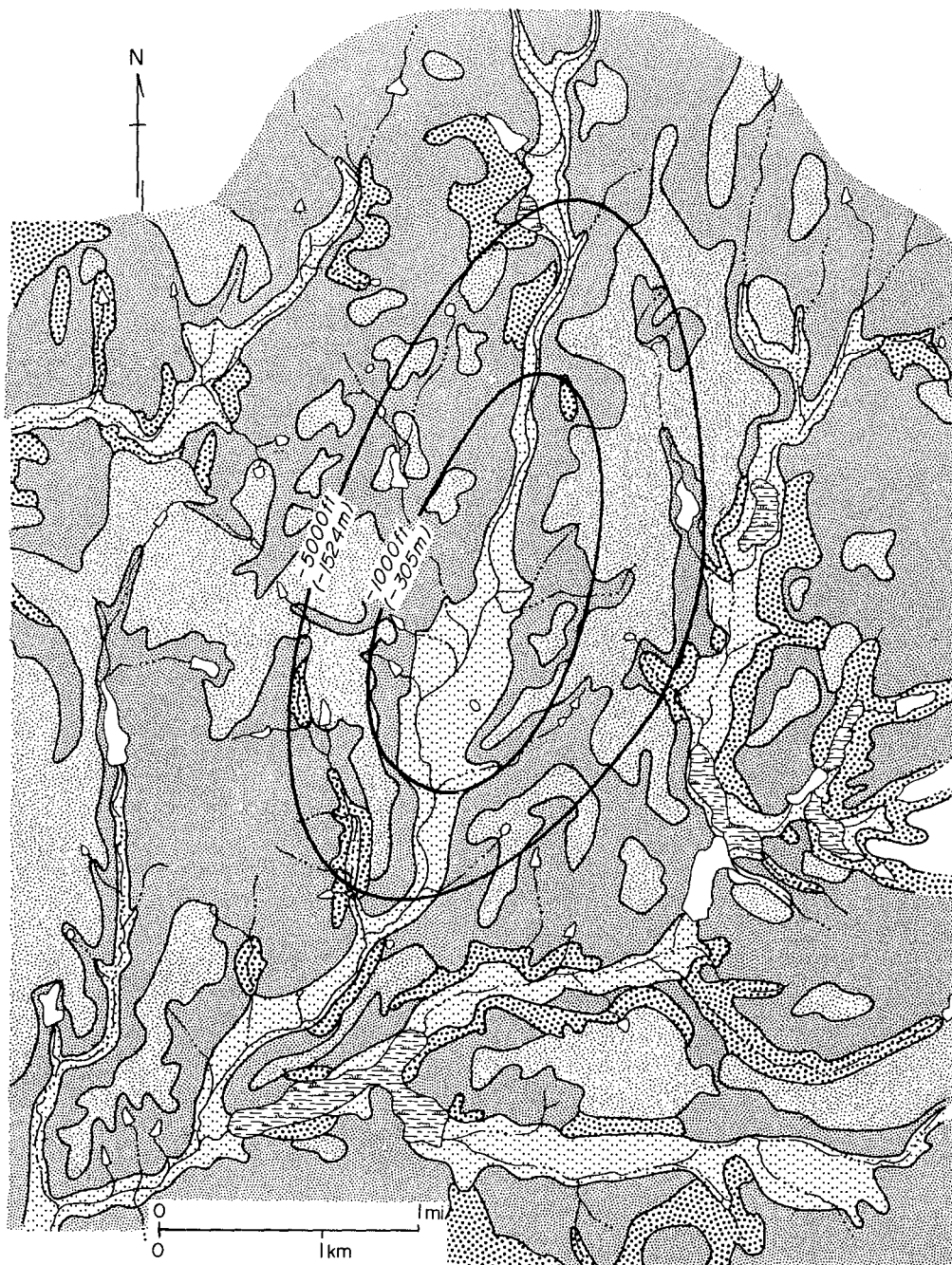
Figure 74. Morphologic map, Keechi Dome, East Texas.

TENSION CRACKS ON KEECHI SALT DOME, EAST TEXAS

Edward W. Collins

Two cracks, 30 m and 12 m (100 ft and 40 ft) long and up to 3.5 cm (1.5 inches) wide, were observed at Keechi Dome. During a five-month period, the cracks were gradually filled by slumping and soil erosion. The cracks are probably tension fractures because no vertical or horizontal offsets were observed.

At Keechi Salt Dome, two unusual cracks, or fissures (fig. 75), were observed during November 1979. A landowner at Keechi Dome reported that the cracks were first discovered during the spring of 1978. Observations showed that slumping and soil erosion gradually filled the cracks with sand and leaves. By May 1980, the cracks were filled.

These fractures developed along a southeastern extension of an inferred fault mapped near the dome center by Ebanks (1965). The inferred fault trends northwest to southeast, although the fractures display trends of N. 7° E. and N. 67° W. When first observed in November 1979, these cracks appeared to be nearly vertical and were 30 m and 12 m (100 ft and 40 ft) long; maximum width for the larger fracture was about 3.5 cm (1.5 inches). Exact depth of the cracks is unknown, but the base of the larger crack was deeper than 1 m (3 ft). Landowners reported an approximate depth of 4 m (12 ft) measured in the spring of 1978, but this has not been documented. The upper meter of soil cover is composed of 50 cm (20 inches) of slightly clayey sand above 20 cm (8 inches) of red to yellow mottled clay and 30 cm (12 inches) of silty clay.

Any relationship between the fractures and the inferred fault is speculative. Although the mechanism that produced the fractures is unknown, the cracks are probably tension fractures rather than shear fractures since no offset was observed. The significance of the cracks to the stability of Keechi Dome cannot be determined until further geologic investigations are initiated at the dome.

Figure 75. Tensional crack on Keechi Dome, East Texas. Photographed November 14, 1979. Measuring rod is 1 meter long.

FLUID-PRESSURE VERSUS DEPTH RELATIONSHIPS IN THE WILCOX-CARRIZO AQUIFER SYSTEM, EAST TEXAS

Graham E. Fogg

A significant control on transport of radionuclides, should they enter the Wilcox-Carrizo aquifer system, would be vertical ground-water flow. Would contaminants be transported up or down in the system? Fluid-pressure versus depth relationships show that in the artesian section of the Wilcox-Carrizo the vertical component of hydraulic gradient is generally downward everywhere except beneath the Trinity River; here, the component is upward. Thus, beneath the Trinity River there is potential for movement of fluids into the upper parts of the Wilcox-Carrizo aquifer.

Fogg (1980b) and Fogg and Kreitler (in preparation) demonstrate that the Reklaw aquitard, which confines the Wilcox-Carrizo aquifer system over much of the East Texas Basin, is leaky and allows an undetermined amount of ground water to discharge along the Trinity and Sabine Rivers. This leakage, or vertical movement, may also induce vertical movement within the Wilcox-Carrizo system itself. Determining and characterizing any such movement and depths to which it may penetrate is necessary in order to predict potential radionuclide transport in the Wilcox-Carrizo. Radionuclides leaking from a salt dome in the East Texas Basin would, at worst, enter the artesian section of the Wilcox-Carrizo aquifer system. Because of the great thickness of this section (approximately 1,200 to 3,000 ft [365 to 915 m]), downward flow into lower parts of the system could cause contaminants to be effectively isolated from upper parts of the system, where all the water supply wells are located. In areas of upward flow, the potential for contamination of the biosphere would be greatest.

Fluid-pressure versus depth (p-d) relationships in the Wilcox-Carrizo were used to help locate areas of upward or downward fluid movement. The slope (m) of the p-d line can be interpreted as follows (where p is in units of ft of fresh water, and d is in ft below land surface): (1) when $m < 1$, the vertical flow component is downward; (2) when $m > 1$, the vertical flow component is upward; and (3) when $m = 1$, flow is perfectly horizontal. A value of $m \neq 1$ only indicates that a vertical component of flow exists. It does not indicate whether this component is significant relative to horizontal components. Additional details on use of p-d relationships can be found in Tóth (1978) and Fogg and Kreitler (in preparation).

Pressures in the Wilcox-Carrizo system were estimated using well-screen depths and measured depths to water levels, as described in figure 76. In figure 77, the plot

115

of all available data (598 points) yields m = 0.84 and excellent correlation (R) of depth to pressure head of 0.97 (table 9). As mentioned by Fogg (1980b), this slope indicates that, on the average, vertical fluid movement in the system is downward. This downward movement is presumably caused by flow down the structural dip and by widespread occurrence of downward leakage into the Wilcox-Carrizo from the Queen City aquifer. Broad scatter in the data between depths of 400 and 900 ft (120 and 274 m) (fig. 77) is caused by excessive drawdowns resulting from pumpage in several wells. The value of m < 1 is not an artifact of such drawdowns, because when the points most affected by pumpage are removed from the data, the regression results remain essentially the same (fig. 77; table 9).

Fluid-pressure versus depth plots of data located within 2 mi (3.2 km) of major streams were constructed because ground-water discharge is most likely to occur in these areas (fig. 78a, b, and c; table 9). Only the section of the Trinity River that traverses the artesian section of the Wilcox-Carrizo aquifer yielded m > 1 (in this case, m = 1.10), indicating a certain amount of upward movement. Because the data in figure 78a were recorded from a maximum depth of about 1,200 ft (365 m), the upward component of flow apparently persists at least to this depth. The base of the Wilcox aquifer occurs as deep as about 3,800 ft (1,160 m) in the area.

The value of m = 0.97 along the Trinity River where it traverses the unconfined aquifer (table 9) indicates recharge rather than discharge. This relationship appears to be an artifact of the distances of wells from the stream and the nature of ground-water discharge from unconfined systems. Modeling studies have demonstrated that upward discharge beneath streams is much more localized for unconfined aquifers than it is for confined aquifers (compare figures 6.2a and 6.4b in Freeze and Cherry [1979]). Thus, it appears that the wells in the unconfined section are still in a recharge zone and are not close enough to the Trinity River to register a value of m > 1.

Fluid-pressure versus depth data along the Sabine River (fig. 78c) have been divided into four groups, each reflecting a different hydrologic regime (Fogg and Kreitler, in preparation). Because all values of m computed for the Sabine are less than 1, it appears that any upward leakage across the Reklaw aquitard (Fogg, 1980b; Fogg and Kreitler, in preparation) occurs at a rate too slow to induce upward flow within the Wilcox-Carrizo.

Fluid-pressure versus depth relationships have helped confirm that the Trinity River is a potentially important ground-water discharge area. Furthermore, the data

116
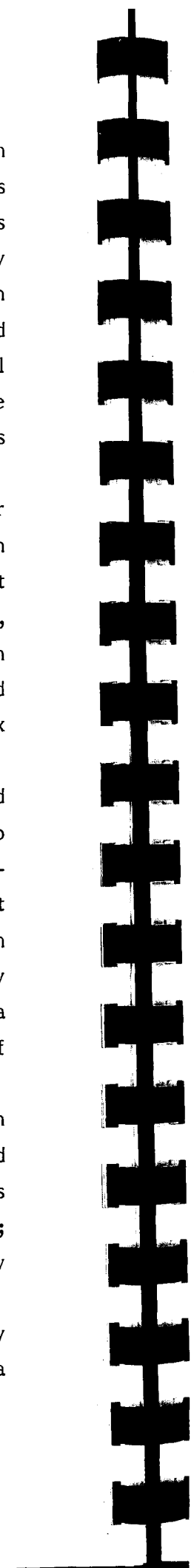
suggest that vertical leakage may significantly affect vertical flow within the Wilcox-Carrizo system itself. Fluid-pressure versus depth data have limitations: (1) They only indicate the direction of the vertical hydraulic gradient. (2) Vertical hydraulic conductivity in horizontally stratified systems such as the Wilcox-Carrizo may be much lower than the horizontal conductivity, thus rendering insignificant the vertical components of hydraulic gradient. One goal of numerical modeling (see "Aquifer Modeling of the Oakwood Salt Dome Area") is to simulate in three dimensions all the hydrologic factors that could affect Wilcox-Carrizo ground-water flow.

Fogg (1980b) showed that beneath the Neches River the direction of leakage is downward. Accordingly, p-d data along the Neches River (fig. 78b) indicate a downward component of flow within the Wilcox-Carrizo.

Table 9. Summary of fluid-pressure versus depth (p-d) relationships,
Wilcox-Carrizo aquifer, East Texas.

Data group	No. of points	Correlation (R)	Slope (m)
All	598	0.97	0.84
All*	513	0.99	0.88
Trinity River			
confined	10	0.98	1.10
unconfined	11	0.99	0.97
Neches River	15	0.99	0.93
Angelina River	13	0.92	0.61
Sabine River			
confined - west	9	0.99	0.95
confined - east	9	0.98	0.99
unconfined - west	7	0.99	0.97
unconfined - east	4	0.98	0.90

*Excluding circled data on figure 77

117
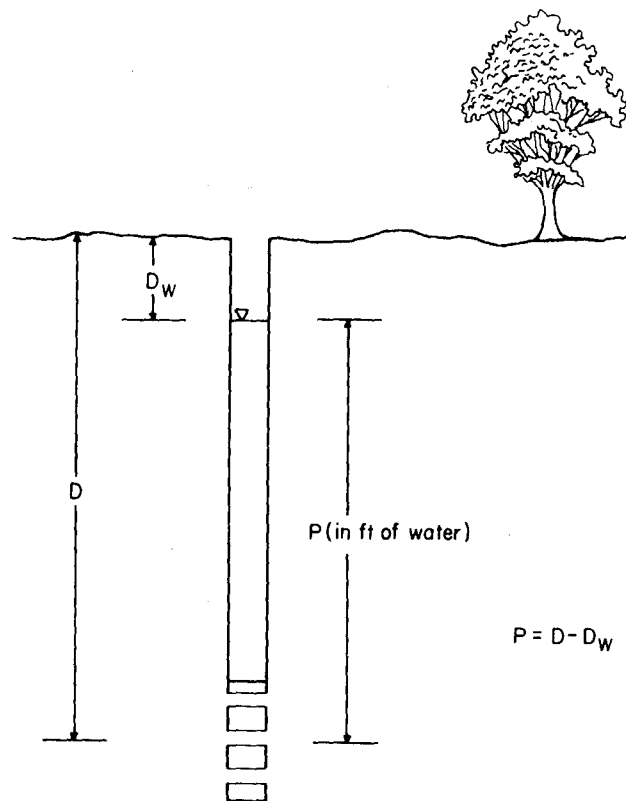
Figure 76. Method of computing pressure (p) from water-well information.
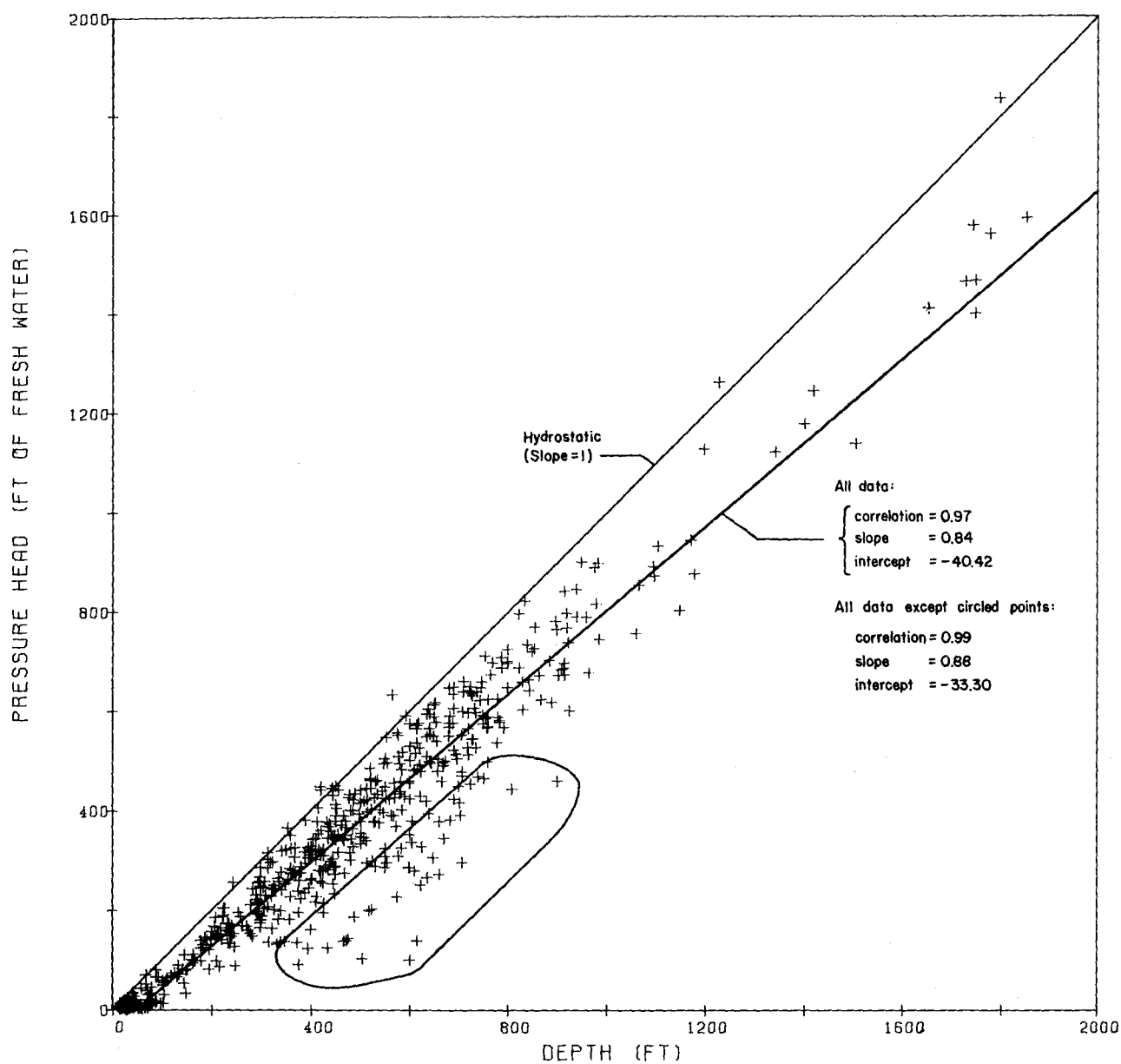
Figure 77. Plots of fluid-pressure versus depth (p-d) for all data from the Wilcox-Carrizo aquifer, East Texas. Vertical component of flow is downward when m < 1, upward when m > 1, and nonexistent when m = 1. Data representing excessive drawdowns caused by pumpage (see circled points) do not significantly affect results.
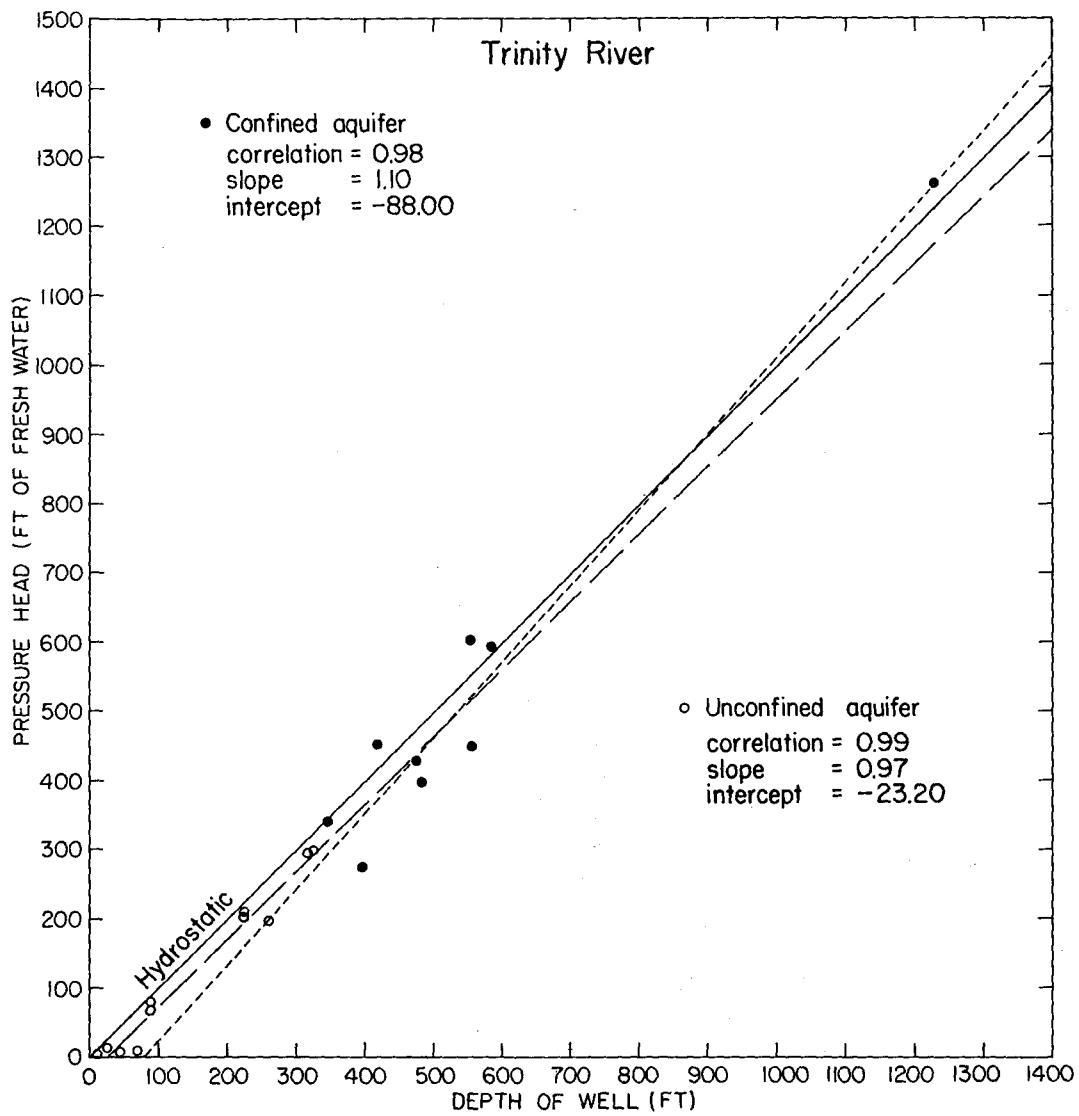
Figure 78a. Plots of fluid-pressure versus depth (p-d) data located within 2 mi (3.2 km) of the Trinity River, East Texas.

120
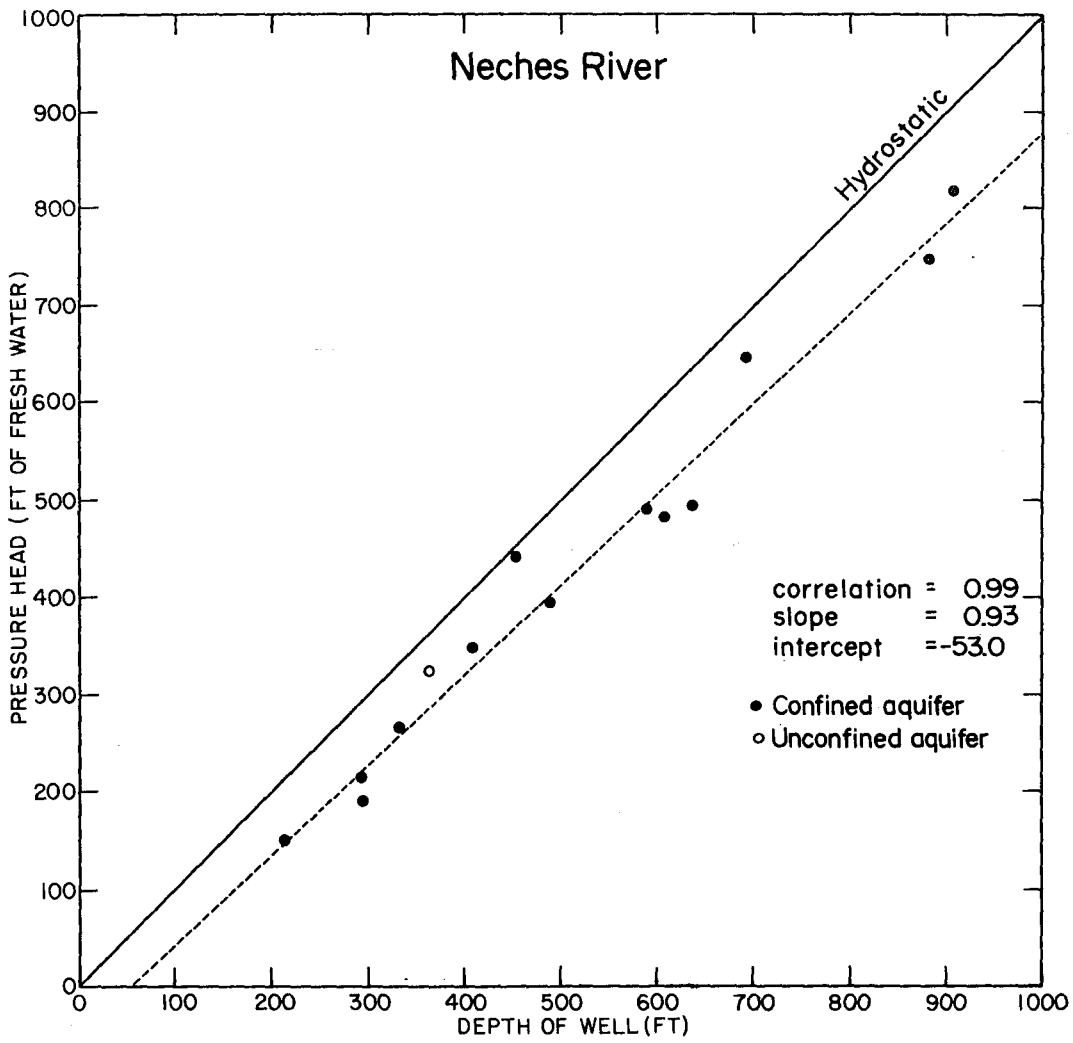
Figure 78b. Plots of fluid-pressure versus depth (p-d) data located within 2 mi (3.2 km) of the Neches River, East Texas.

121
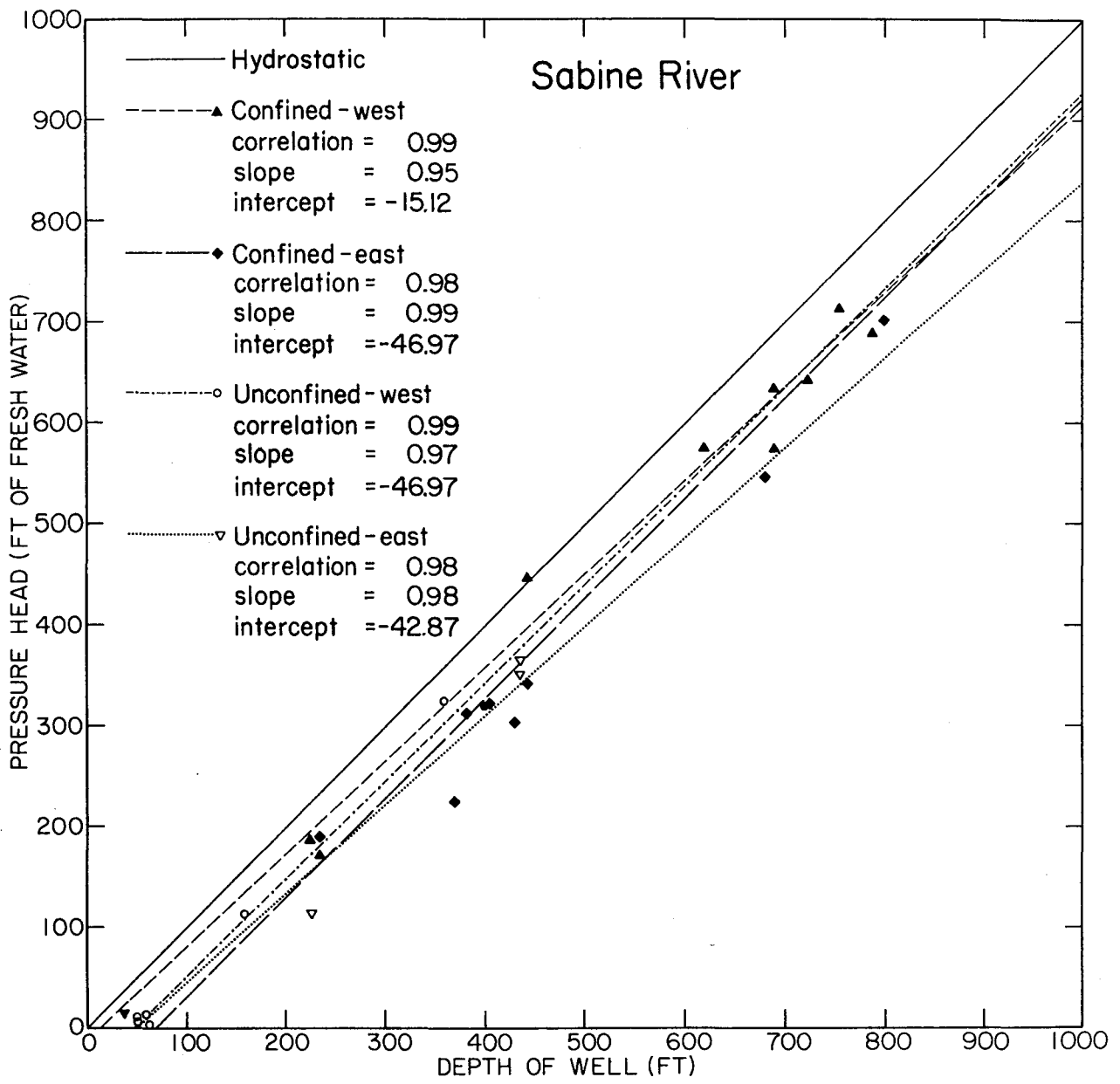
Figure 78c. Plots of fluid-pressure versus depth (p-d) data located within 2 mi (3.2 km) of the Sabine River, East Texas.

TOTAL DISSOLVED SOLIDS IN THE EOCENE WILCOX-CARRIZO AQUIFER AROUND KEECHI SALT DOME, EAST TEXAS

Graham E. Fogg

Concentrations of total dissolved solids (TDS) in waters of the Wilcox-Carrizo aquifer around Keechi Salt Dome were estimated from electrical resistivity logs. All the estimates imply that salt dissolution at Keechi Dome is proceeding extremely slowly or not at all. The most obvious reason for the low TDS values is that the flanks of the dome are surrounded by relatively impermeable Midway clay, and only a small area on top of the dome is in contact with Wilcox-Carrizo ground water.

Concentrations of total dissolved solids (TDS) of waters in the Wilcox-Carrizo (Wx-Cz) aquifer system near Keechi Salt Dome have been estimated from electrical resistivity logs using the same method employed around Oakwood Salt Dome (Fogg, 1980c; Fogg and Kreitler, in preparation). The purpose is to detect evidence of salt dome dissolution and to learn more about the local hydrologic system. Results are shown in figure 79, where estimated TDS values for the Carrizo Formation and three sands in the Wilcox Group are plotted in hundreds of mg/L. Three sands from the Wilcox that were selected for study are generally thick (100 ft [30 m]), clean sands distributed in the upper, middle, and lower thirds of the aquifer. If salt dome dissolution is occurring, it should be evident in these sands.

Like most salt domes in the East Texas Basin, Keechi Dome is entirely surrounded by fresh and moderately brackish water in the Wilcox-Carrizo aquifer. Waters in the Carrizo and upper two-thirds of the Wilcox rarely contain more than 500 mg/L TDS (fig. 79). In every case the highest TDS value occurs at the bottom of the aquifer. The highest TDS value estimated in the Wilcox-Carrizo aquifer is 6,000 mg/L for three wells located about 2 mi (3.6 km) east of the dome (fig. 79). Ground water may flow eastward from the dome because of recharge through the outcrop of Wilcox-Carrizo over Keechi Dome (Fogg, 1980b). The anomalous TDS values may therefore originate from dissolution of the dome or upward leakage of deep saline waters along dome flanks. Data are insufficient to show a direct connection between the anomalous TDS values and the dome. Wells drilled directly over the dome contain primarily fresh water. If sands of the Wilcox-Carrizo were in direct hydraulic communication with the salt of Keechi Dome, one would expect TDS values near the dome to be much higher than the values shown in figure 79 since TDS values at the aquifer-salt interface would be around 300,000 mg/L (approximately saturated with

123

respect to halite). It can therefore be inferred from estimates of TDS in figure 79 that either salt dissolution at Keechi Dome is proceeding at a very slow rate or there is no dissolution.

There are three possible explanations for the apparently slow rate of dissolution: (1) the dome is surrounded on all flanks by uplifted clay of the Midway Group so that salt is in contact with the Wilcox aquifer only over a rather small area directly above the dome (Giles, 1980); (2) salt-dome cap-rock may protect the salt from circulating ground water (Fogg and others, 1980; Kreitler and others, 1980); and (3) any high TDS water originating from the dome may be diluted to much lower concentrations by mixing with recharge waters that enter the system through outcrops directly over the dome. The first explanation has been verified as a viable hypothesis by Giles (1980), who mapped the Midway clay in the subsurface around the dome. The second and third explanations are currently being investigated by the cap-rock research and ground-water modeling programs.

Cz 7/2.4
10/7.2
13/10
18/12

Cz 8/3.3
12/5.6
15/5.2
16/10

Cz 7/3.6
12/7.2
14/7.2
16/15

Cz 4/7.2
6/10
9/20
14/18

Cz 3/3.9
6/4.4
9/4.8
12/6.3

7/7.2
10/3.1
13/10

Cz 7/2.8
10/7.2
12/5.6
16/11

Cz 8/2.6
10/4.8
16/7.2
20/15

Cz 8/5.7
11/10
15/7.2
20/11

Cz 3/4.3
5/4.3
8/8.2
12/10

7/7.2
10/7.2
14/8.0

Cz 4/5.2
8/12
11/10

Cz 7/1.9
12/5.6
15/7.2
18/18

Cz 7/4.2
9/10
14/7.2
16/10

Cz 7/4.3
9/7.2
13/7.2
15/10

Cz 6/2.0
11/5.6
15/7.2
18/13

Cz 6/3.0
8/12
13/7.2
18/13

Cz 6/2.6
10/10
14/10
18/10

Cz 5/5.6
10/10
15/10
18/17

□ Montalba

Cz 7/2.2
10/7.2
15/5.6
19/30

Cz 6/1.7
12/4.8
15/4.8
19/11

Cz 5/3.3
7/9.8
14/5.6
17/9.8

7/5.6
11/5.6

Cz 3/4.2
5/7.2
9/7.2
15/25

5/7.2
9/8.2

Cz 7/1.7
10/4.8
13/7.2
20/60

Cz 5/2.5
7/10
15/7.2
19/12

Cz 5/4.8
8/9.8
14/5.6
19/7.2

3/7.2
9/5.6

6/7.2
11/5.6

5/7.2
8/7.2

Cz 7/3.7
9/7.2
15/5.6
19/44

6/4.8
9/7.2
12/12

4/4.2
10/6.6

31°50'

3/12

31°50'

Cz 7/2.8
9/10
15/3.3
20/60

8/7.2
11/4.2

6/5.6

7/5.6

95°45'

95°40'

Cz 3/3.6
8/4.7
12/6.3
14/12

Cz 7/3.0
11/5.6
17/1.8
22/60

Cz 6/2.4
8/4.2
15/4.8
21/35

5/11
11/7.2
15/25

Cz 3/2.6
8/8.2
12/6.3
14/12

Cz 7/1.2
9/4.2
16/4.8
22/10

Cz 2/2.7
7/4.8
11/3.6
15/17

8/4.8
13/7.2
17/35

Cz 4/1.6
8/3.3
15/2.2
19/10

Cz 6/1.2
9/4.8
16/5.6
21/44

Cz 7/1.8
12/7.2
16/7.2
20/4.2

9/4.8
14/7.2

Cz 5/4.2
9/7.2
13/7.2
16/29

10/7.2
13/3.0
18/10

Cz 7/1.8
11/4.8
17/1.8
22/44

Cz 7/1.6
12/7.2
16/3.3
22/15

Cz 7/1.8
8/7.2
16/4.2
22/20

6/12
13/3.6
18/13

7/10
14/4.8
19/15

11/3.6
17/3.0
20/10

City of
Palestine

3/10
11/5.6
16/20

7/3.6
12/3.0
19/17

5/10
11/4.8
13/17

6/5.6
12/12

EXPLANATION

DEPTH / TDS in 100's of ft and 100's of mg/L, respectively.
● Cz 5 / 4.2 ← Carrizo
9 /7.2
13 /7.2 } Sands of the Wilcox
16 / 29

Outcrop area of Wilcox - Carrizo and Cretaceous units
over Keechi Salt Dome

-N-

0   1   2   3 mi

0   1   2   3   4   5 km
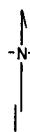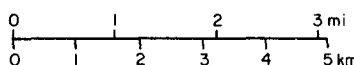
Figure 79. Estimates of total dissolved solids (TDS plotted in hundreds of mg/L) in the Wilcox-Carrizo aquifer around Keechi Salt Dome, East Texas, using data from electric logs.

125

AQUIFER TESTING AND MONITORING AROUND OAKWOOD SALT DOME, EAST TEXAS

Graham E. Fogg

Results of pumping tests conducted around Oakwood Dome have been used to calculate hydraulic properties of aquifers and to infer general hydrologic conditions. Distribution of water levels in wells directly over the dome delineates a recharge area in the vicinity of the Carrizo outcrop and correlates with water-chemistry data from the same wells. Water levels in the Carrizo aquifer around the dome fluctuate in response to seasonal variations in rainfall. Monitoring of water levels and local weather conditions is continuing in order to help detect individual recharge events occurring over the dome. The aquifer testing and monitoring is providing basic data necessary to understand and to model hydrologic conditions around the dome.

In 1979 and 1980, 14 pumping tests were conducted around Oakwood Salt Dome. Tests were carried out in five production wells (TOH-2A, TOH-2AO, TOH-2D2, TOH-5D, and TOG-1WS; fig. 80) and in nine PVC-cased monitoring wells (OK-102, OK-103, OK-104, OK-105, OK-106, OK-107, OK-108, OK-115, and OK-119; fig. 80). Details of well construction are shown in figure 81a and b. All wells were screened in the Carrizo Formation except for TOH-2A and TOH-2AO, where sands are screened in the Wilcox Group, and OK-119, where the Newby Sand Member of the Reklaw Formation is screened. Each pumping test lasted 24 hours, except for the test of OK-115, which lasted 8 hours.

Values of transmissivity (T), hydraulic conductivity (K), and storativity obtained from analysis of test data from the production wells (identified by prefix "TO") are shown in table 10. The graphical methods of Theis (1935) and Cooper and Jacob (1946) were used in analyzing both drawdown and recovery data. Alternate methods that can account for the effects of barrier boundaries and leakage across confining beds were not applied if either hydrologic conditions or data necessary to apply these methods were lacking. Effects of partially penetrating wells did not bias data because each "TO" well was screened along the total thickness of sand in which the well was completed. Test results (table 10) appear to be reliable estimates of aquifer parameters, except for one or two cases where response of the aquifer to pumping was complex and difficult to analyze.

Figures 82 and 83 illustrate how the pumping-test data were analyzed. Figure 82 shows a Cooper-Jacob drawdown plot of drawdown versus time for observation well TOH-2DO during pumping of TOH-2D2. The assumptions of the Theis and Cooper-

The water levels of the Carrizo aquifer measured on May 15, 1980, are contoured in figure 80. The contour patterns clearly indicate the presence of a recharge area near the Carrizo and Reklaw outcrops, which is consistent with the water-chemistry data for Oakwood Dome (see data in "Water Chemistry, Oakwood Salt Dome"). Faults mapped in the eastern half of the area apparently act as partial barriers to flow, causing the steeper hydraulic gradients (fig. 80). There is a general correlation between precipitation and water-level rises in the monitoring wells, confirming that the area over Oakwood Dome is a recharge area.

Typical long- and short-term water-level fluctuations are plotted together with barometric pressure and rainfall in figures 84 and 85. Annual water-level fluctuations in the Carrizo aquifer are generally about 0.5 ft (0.15 m); maximum levels occur in winter and early spring when rainfall is greatest. The period of record is too short (8 months) to determine whether the two deepest wells, TOH-2A and TOH-2AO, respond to wet and dry periods. Short-term water-level fluctuations in all the wells reflect barometric pressure effects and artesian conditions (see fig. 85). Some daily fluctuations in water levels and barometric pressure have been used to calculate storativity coefficients that are approximately 10^{-4}, which is consistent with data from aquifer tests (table 10). At this point, no correlations can be drawn between individual rainfall events and water-level changes because drought conditions have prevailed since the rainfall gage was installed.

Table 10. Well completion data and results of pumping tests from drilling program, Oakwood Dome, East Texas.

Well	Unit, screened interval (m)	Aquifer interval, thickness (m)	Transmissivity (m²/d)		Hydraulic conductivity (m/d)		Storativity		Remarks
			Cooper/Jacob[c] drawdown/ recovery	Theis[d] drawdown/ recovery	Cooper/Jacob[c] drawdown/ recovery	Theis[d] drawdown/ recovery	Cooper/Jacob[c] drawdown/ recovery	Theis[d] drawdown/ recovery	
TOG-1WS	Carrizo	23.8-51.5	76.0	75.	2.7	2.7	--	--	1. Barrier boundary detected.
	30.8-49.4	27.7	80.0	75.	2.9	2.7	--	--	2. Head in 1WS dropped below bottom of upper aquitard during test.
Obs. well	Carrizo	27.4-48.8	--a	32.?	--a	1.5?	--a	8.2×10^{-5}?	
OK-102	42.1-45.1	21.4	--	--	--	--	--	--	
TOH-5D	Carrizo	142.3-154.5, 157.0-183.5	270.0	220.	7.0	5.7	--	--	1. The observation well results are questionable owing to their great distances from TOH-5D, small drawdown responses, and sparsity of measurements.
	144.5-150.6, 158.2-182.6	38.7	270.0	240.0	7.0	6.2	--	--	
Obs. well	Carrizo	60.4-79.9	--a	440.?	--a	23.?	--a	1.4×10^{-4}?	
OK-103	70.1-73.2	19.5	--	440.?	--	23.?	--	1.2×10^{-4}?	2. Observation well data was corrected for barometric effects.
Obs. well	Carrizo	39.6-57.9	--a	680.?	--a	37.?	--a	3.3×10^{-4}?	
OK-104	51.8-54.9	18.3	--	--b	--	--b	--	--b	
TOH-2D2	Carrizo	155.8-176.2	170.0	200.0	8.3	9.8	--	--	1. Values of T and K from 2DO are lower because of poor connection to aquifer.
	157.3-175.9	20.4	160.0	150.0	7.8	7.4	--	--	
Obs. well	Carrizo	155.8-176.2	140.0	140.0	6.5	6.9	1.1×10^{-4}	1.3×10^{-4}	2. During pumping, water levels rose 6.7 cm in TOH-2AO and 45.7 cm in TOH-2A.
TOH-2DO	158.2-176.8	20.4	140.0	140.0	6.9	6.9	2.2×10^{-4}	1.7×10^{-3}	
TOH-2A	Wilcox	579.0-586.0	1.4	1.4	0.21	0.21	--	--	1. Incomplete recovery.
	579.0-585.0	6.7	1.8	1.6	0.27	0.24	--	--	
TOH-2AO	Wilcox	253.9-285	190.0	170.0	6.1	5.5	--	--	1. Early data used. 2. Barrier boundary detected.
		31.1	195.0	200.0	6.3	6.4	--	--	3. During pumping, water level rose 345.0 cm in TOH-2A.

[a] Jacob method of analysis inappropriate because u too large.

[b] Recovery measurements were too sparse to use.

[c] From Cooper and Jacob (1946)

[d] From Theis (1935)
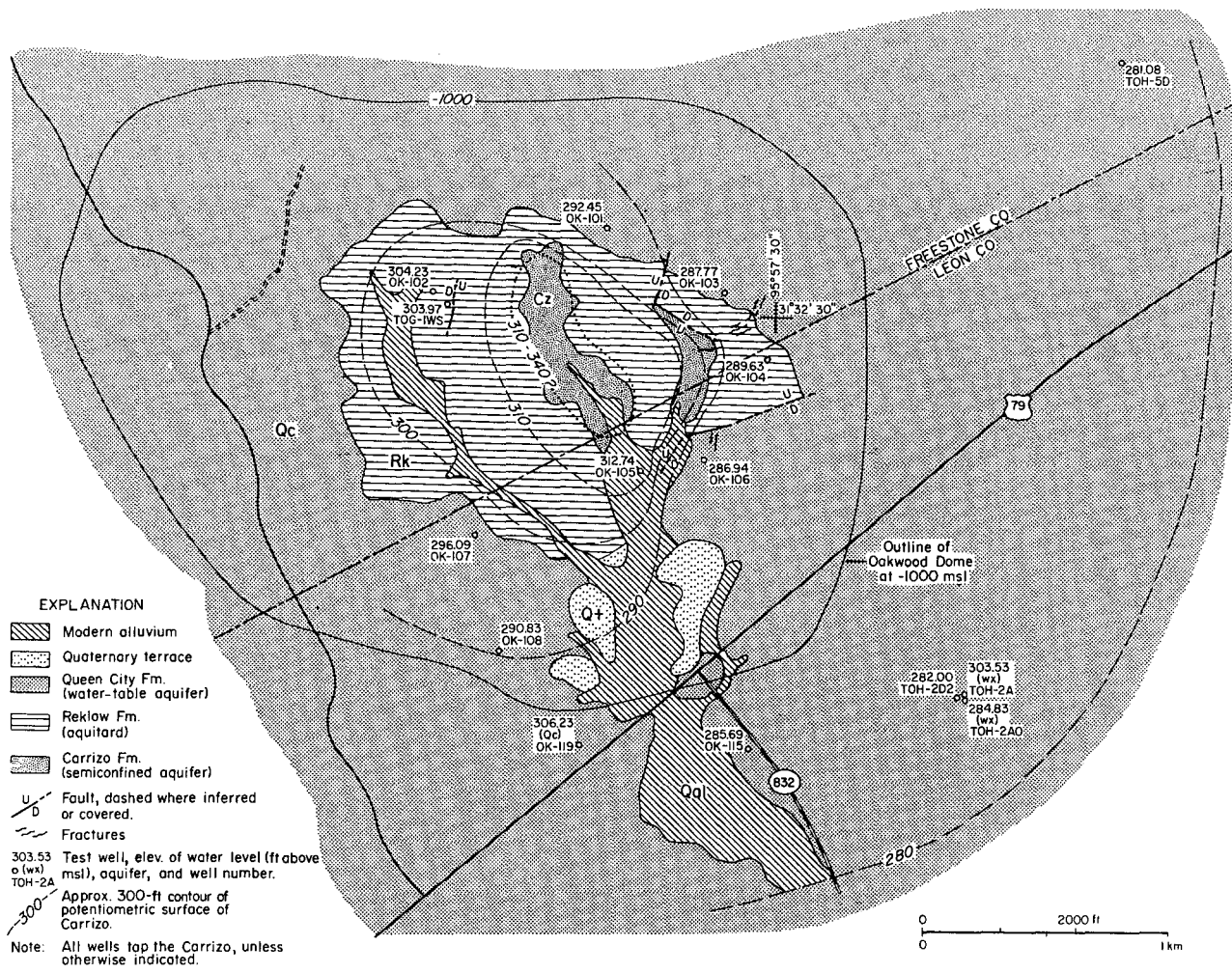
Figure 80. Potentiometric surface of Carrizo aquifer over Oakwood Salt Dome, East Texas (geology from Collins and Hobday, 1980). Also shown are locations of production and monitoring wells.
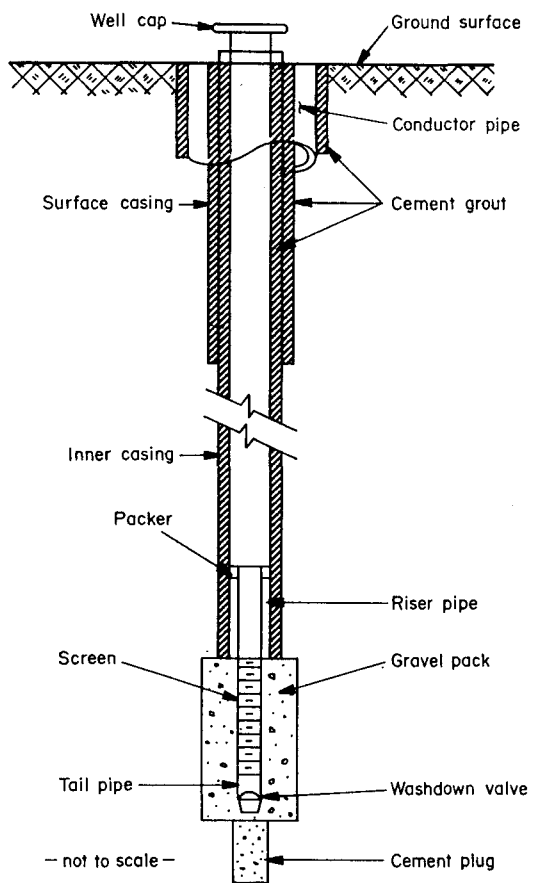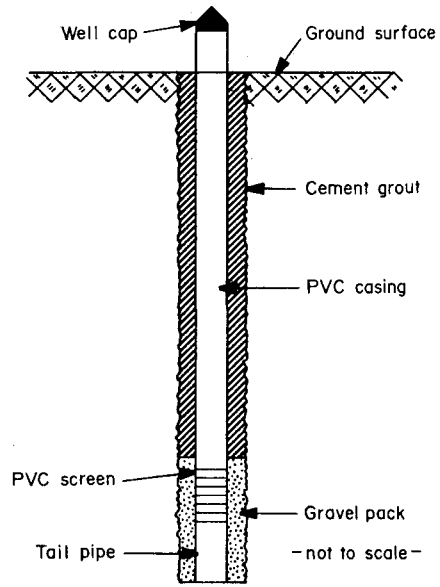
Figure 81. Schematics of well construction: (a) production wells ("TO" wells) and (b) PVC monitoring wells ("OK" wells).

131

Drawdown in TOH-2D2 (ft)

40

35

30

25

20

15

10

5

10^{-1} 10^0 10^1 10^2 10^3 10^4

Time since pumping began (min)

Q = 313.5 gal/min (1.98×10^{-2} m^3/s)

Δh = 7.5 ft (2.29 m)

Sand thickness, b = 67 ft (20.4 m)

r = 20 ft (6.1 m)

t_0 = 1.36×10^{-5} d

Due to decline in pumping rate, Q

$T = \dfrac{264\,Q}{\Delta h} \cong 11{,}000 \text{ gal/d/ft} \cong 1470 \text{ ft}^2/\text{d} \cong 140 \text{ m}^2/\text{d}$

$K = \dfrac{T}{b} \cong 160 \text{ gal/d/ft}^2 = 21 \text{ ft/d} = 6.5 \text{ m/d}$

$S = \dfrac{.3\,T t_0}{r^2} = 1.1 \times 10^{-4}$
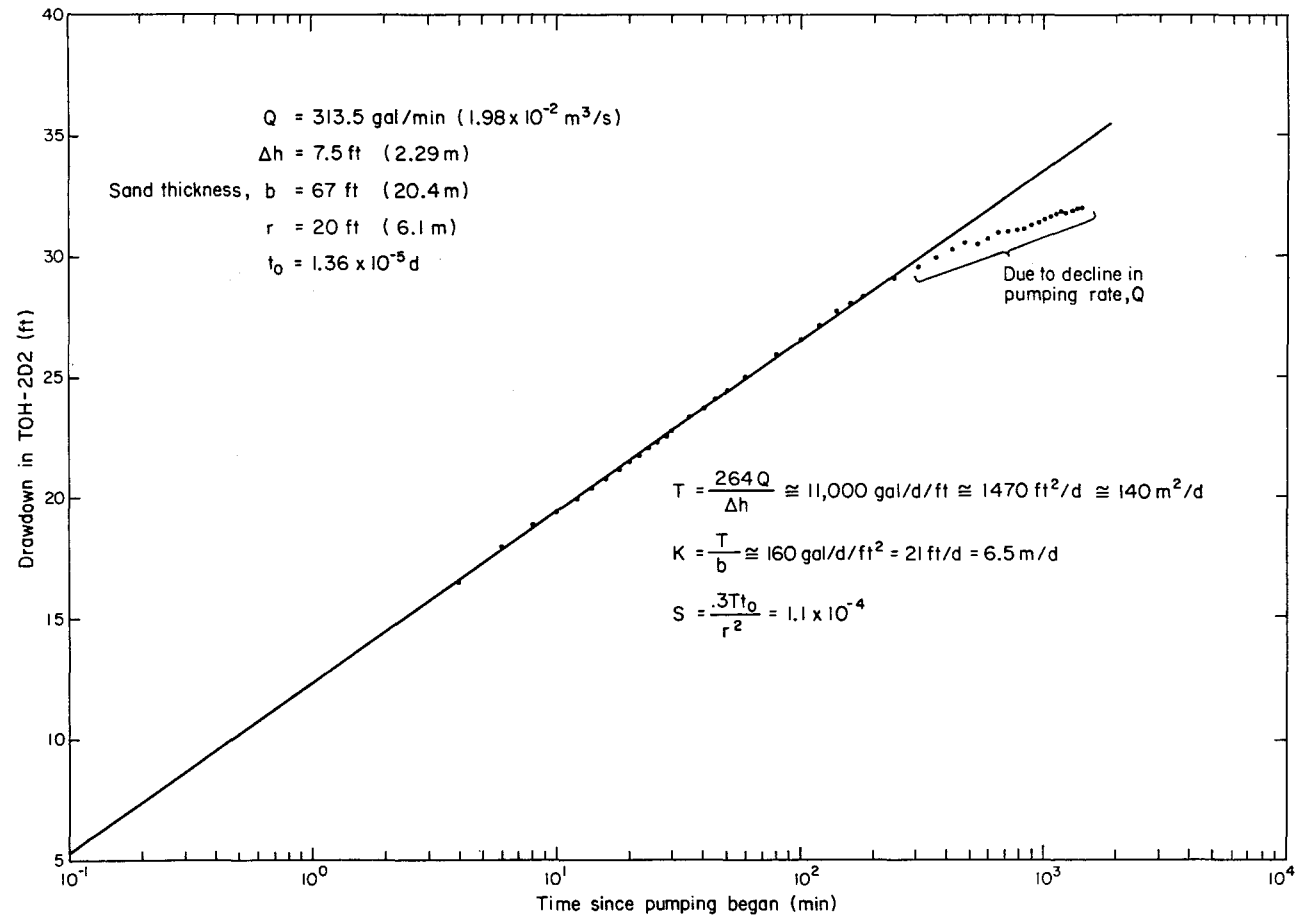
Figure 82. Cooper-Jacob analysis of drawdown in well TOH-2DO during pumping of TOH-2D2, Oakwood Dome area, East Texas.

Q = 46.0 gal/min (2.90 x 10 m³/S)

Sand thickness , b = 91 ft (27.7 m)

$T = \dfrac{264Q}{\Delta h} \cong 6900 \, gal/d/ft \cong 930 \, ft^2/d \cong 90 \, m^2/d$

$K = \dfrac{T}{b} \cong 76 \, gal/d/ft^2 = 10 \, ft/d \cong 3.1$

Δh = 1.75

Δh = 2.00

$T \cong 6100 \, gal/d/ft \cong 800 \, ft^2/d \cong 75 \, m^2/d$

$K \cong 67 \, gal/d/ft^2 \cong 9.0 \, ft/d \cong 2.7 \, m/d$

Drawdown in TOG-1WS (ft)

Time since pumping began (min)
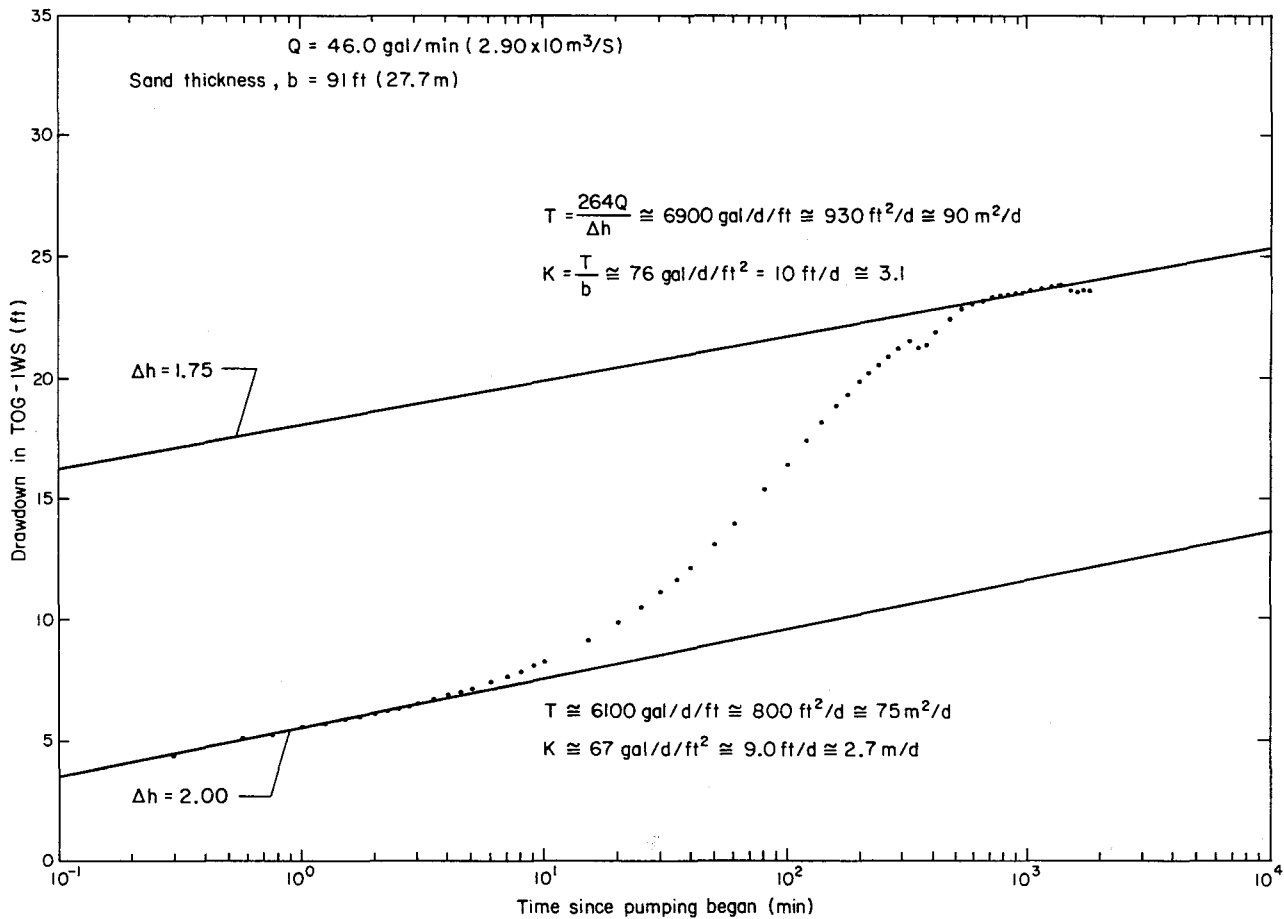
Figure 83. Cooper-Jacob analysis of drawdown in well TOG-1WS during pumping of TOG-1WS, Oakwood Dome area, East Texas. Increase in rate of drawdown around t = 5 min may be due to effects of a barrier boundary; decrease in the rate of drawdown around t = 400 min may be due to drainage from overlying Reklaw aquitard as water level in well nears top of aquifer.
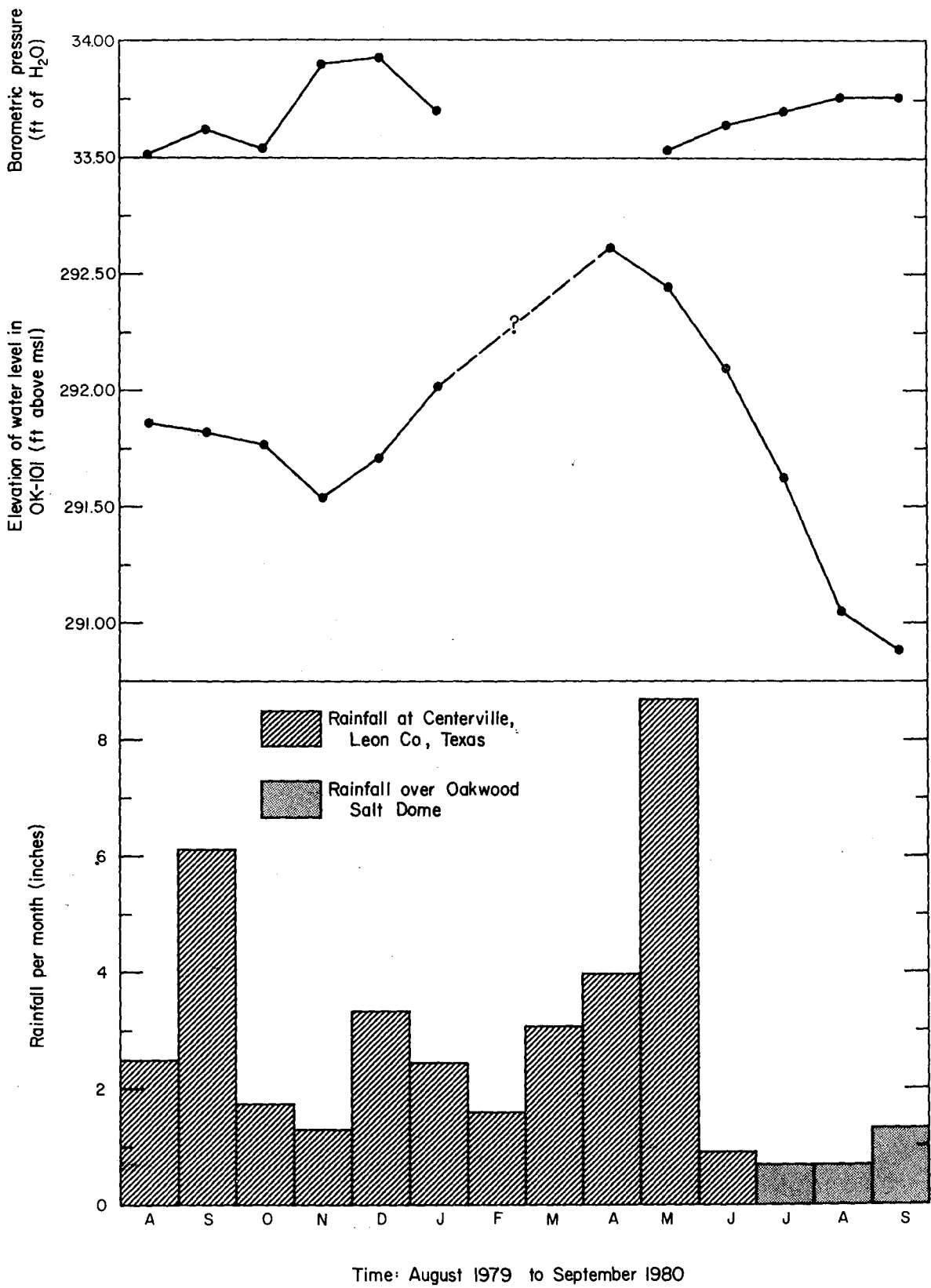
Figure 84. Graph of long-term water-level fluctuations in Carrizo aquifer (well OK-101), rainfall, and barometric pressure variations over Oakwood Dome, East Texas. There is a general correlation between precipitation and water-level rises, confirming that the outcrop over Oakwood Dome is a recharge area.

134
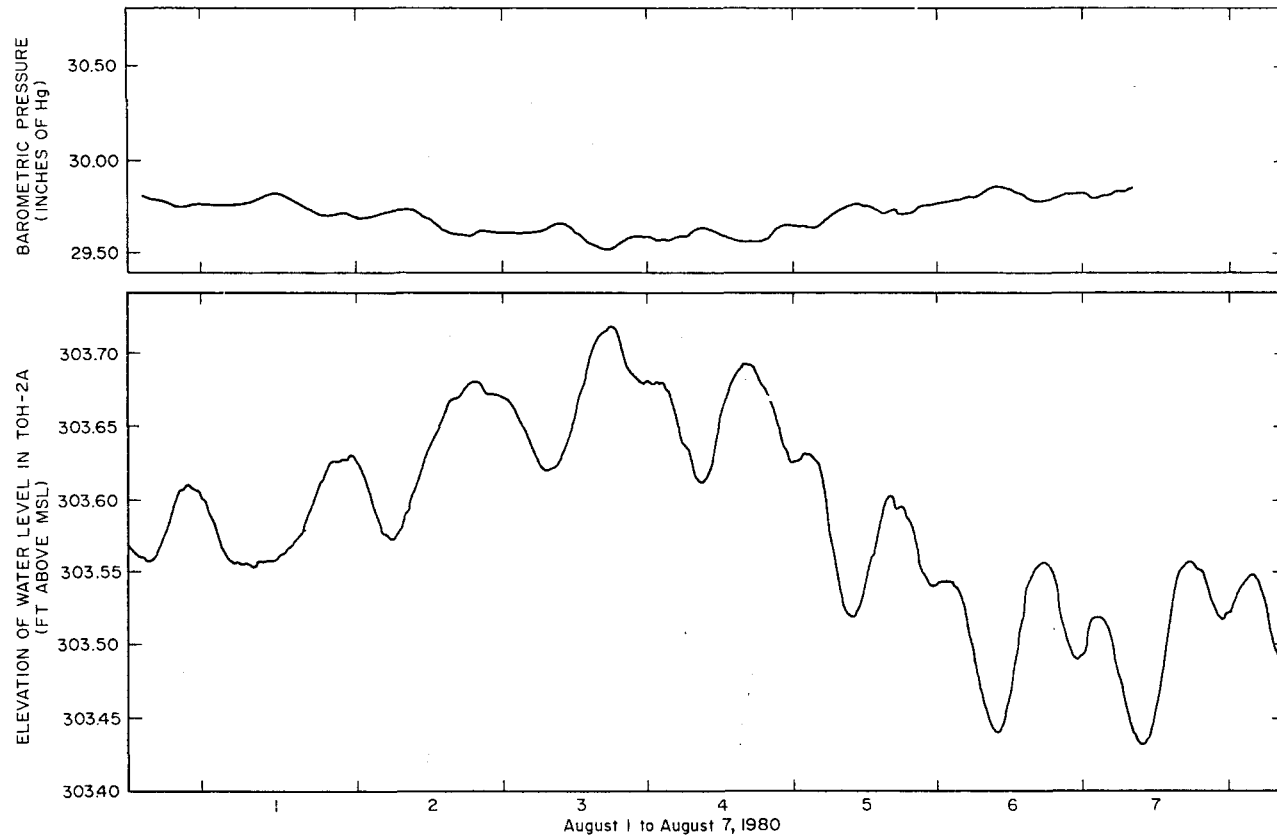
Figure 85. Graph of short-term water-level fluctuations in Wilcox aquifer (well TOH-2AO) and barometric-pressure variations, Oakwood Dome, East Texas. Correlation between barometric pressure and water level indicates artesian conditions. All other wells monitored in the area exhibit similar, short-term fluctuations in response to barometric pressure.

CORE ANALYSIS OF HYDROLOGIC PARAMETERS, EOCENE WILCOX AQUIFER, EAST TEXAS

Graham E. Fogg, Steven J. Seni, and Shirley P. Dutton

A total of 46 plug samples of core from various Wilcox sands near Oakwood Dome were tested in the laboratory for permeability. Results of tests for depths shallower than 1,000 ft (305 m) appear unreliable owing to the difficulty of obtaining undisturbed samples in that interval. In contrast, results of tests for samples obtained below 1,000 ft (305 m) compare favorably with results of one pumping test. Results of permeability tests done both in the laboratory and field together with ongoing analysis of Wilcox core will yield more accurate estimates of permeability, which will allow more realistic ground-water-flow models to be built for the Oakwood Dome area.

Estimating hydraulic conductivity of a thick, heterogeneous aquifer like the Wilcox is difficult because the aquifer contains many more sand bodies than can practically be analyzed by pumping tests. Therefore, 46 plug samples of core from various Wilcox sands in a well near Oakwood Dome were tested for porosity and permeability by Core Laboratories, Inc. The core was drilled in well TOH-2AO (fig. 80) during the fall of 1979. Permeability was measured using a laboratory permeameter apparatus, and reported values represent horizontal permeabilities in the aquifer. Plug dimensions were 1 inch (2.5 cm) in diameter by 2 inches (5 cm) in length. Care was taken to minimize disturbance of the core and plug samples during every phase of sample preparation. Above a depth of 1,000 ft (305 m), the cored sediments were fairly non-cohesive, and therefore, plugs from this interval were the most modified (Core Laboratories, Inc., personal communication, 1980). Each plug was encased in a lead sleeve to minimize flow along the side of the plug. In order to simulate overburden pressures during testing, each plug was subjected to a pressure calculated to represent in situ pressure.

Hydraulic conductivity values obtained from laboratory testing range from 3.35×10^{-5} to 2.02 m/d (fig. 86). The wide range of conductivity values is to be expected in fluvial and deltaic sediments such as the Wilcox Group. Laboratory values were compared to conductivity values obtained from pumping (field) tests conducted at wells TOH-2AO and TOH-2A (fig. 86). Laboratory values agree with pumping test results for TOH-2A, but do not agree with pumping results from TOH-2AO. Well TOH-2AO was constructed in the Wilcox core hole, and well TOH-2A was constructed at a distance of about 50 ft (15 m) from TOH-2AO.

The sand tapped by TOH-2AO is in the interval above a depth of 1,000 ft (305 m), where the cored sands are loose and difficult to test in the lab without significantly disturbing the in situ conditions (Core Laboratories Inc., personal communication, 1980). Thus, the lack of agreement between results of laboratory and field testing in well TOH-2AO can be attributed to disturbed core-plug samples. In contrast, the mean of the three laboratory-derived conductivity values obtained from the sand screened by well TOH-2A (0.25 m/d) differs negligibly from the value of 0.24 m/d obtained from the field tests (fig. 86; table 10). As plotted in figure 86 in the interval tapped by TOH-2A, two of the laboratory-derived conductivity values lie well to the left of the field-derived conductivity value and only the third laboratory-derived conductivity value lies to the right of it. Inspection of the core and the geophysical logs (fig. 86) reveals that grain size of the section represented by the third laboratory-derived conductivity sample is relatively coarse, thus explaining its higher conductivity. Although the aquifer zone represented by the third sample may make up a small percentage of the interval screened by well TOH-2A, it probably transmits most of the water produced from the well, owing to its higher conductivity.

Testing for permeability in the laboratory can only approximate natural conditions and may produce erroneous results. Nevertheless, laboratory data (fig. 86) can be useful if they are carefully analyzed and compared with other types of permeability measurements and geologic interpretation. Analyses completed to date represent the first step in hydrologic analysis of the Wilcox core. Additional work will include statistical analysis of permeability data (fig. 86), study of depositional controls on permeability, and measurements of grain-size distribution. Masch and Denny (1966) successfully estimated permeabilities within the Carrizo Sand in the East Texas Basin by analyzing grain-size distribution. Such an analysis may provide another means of performing laboratory measurements of permeability for the fairly unconsolidated sands of the Wilcox Group.
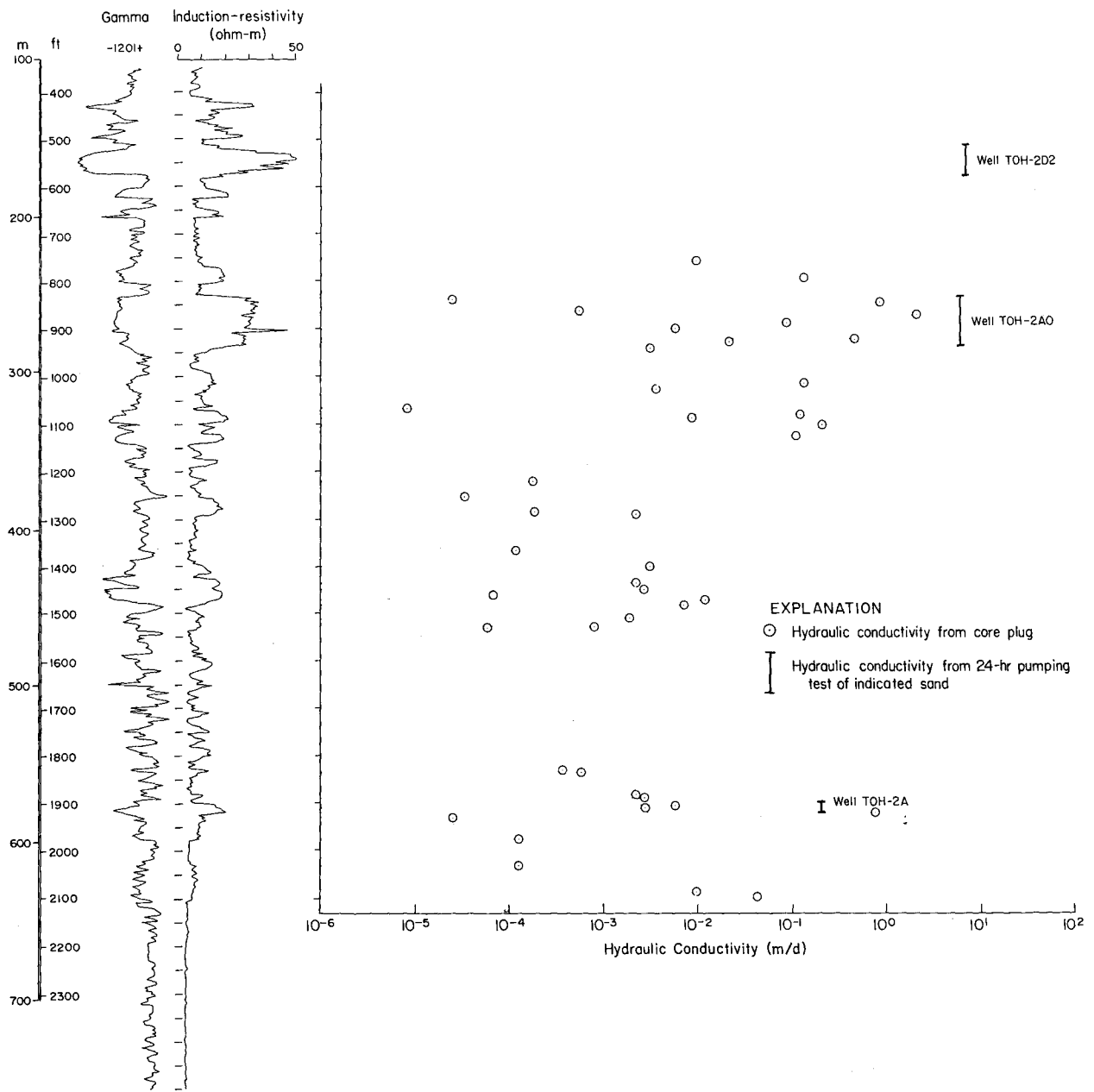
Figure 86. Results of hydraulic conductivity tests conducted on Wilcox core and in adjacent pumped wells, East Texas. Above a depth of 1,000 ft (305 m) core-conductivity values are believed inaccurate because of disturbance of loose, unconsolidated sediment. Average measured porosity of all core samples is 33.5 percent; there appears to be no porosity trend with depth.

138

AQUIFER MODELING OF THE OAKWOOD SALT DOME AREA

Graham E. Fogg

A three-dimensional ground-water-flow model of the Oakwood Dome area has been constructed, and preliminary test simulations have been completed. Currently, the model demonstrates the effects of the dome uplift and regional structure. In successive simulations, additional complexities such as vertical leakage and aquifer heterogeneities will be built into the model. Results are expected to include (1) a better understanding of salt-dome hydrology in general; (2) better estimates of salt dissolution rates; (3) prediction of how contaminants would move through the aquifer systems; and (4) prediction of how future perturbations in climate or ground-water temperature would affect the system hydrology.

A three-dimensional ground-water-flow model of the Wilcox-Carrizo aquifer in the Oakwood Dome area has been constructed, and preliminary test simulations have been made using the model. The computer program TERZAGI, which implements the model, employs the integrated finite difference (IFD) method and a mixed explicit-implicit solution technique. A brief description of TERZAGI and a list of references on its theory and use can be found in Fogg (1980a).

The goal of the modeling effort is to characterize ground-water flow near the dome and the surrounding region in as much detail as possible. Once this is accomplished, salt-dissolution rates can be calculated more accurately, probable destinations of any contaminants entering the system can be determined, and possible effects of future perturbations in the system hydrology (that is, changes in either sea level or climate, or increases in ground-water temperatures owing to cooling of nuclear waste) can be predicted.

The surface geology and potentiometric surface for the study area are shown in figure 87. Important factors include recharge over Oakwood Dome and potential for discharge to the Trinity River and Upper Keechi and Buffalo Creeks. A plan view of the IFD mesh is superimposed on the surface geology in figure 88. The mesh was generated with the computer program OGRE (Weres and Shroeder, 1978), which automatically constructs an IFD mesh, given coordinates of nodal points in two-space or three-space. The southern and eastern boundaries of the model were placed along the southern boundary of the Upper Keechi Creek watershed and the Trinity River, respectively (fig. 88). From our regional studies, these boundaries generally appear to be no-flow boundaries (that is, flow roughly parallels these boundaries in most areas).

139

This arrangement of boundaries is also convenient for water-budget analysis of the system because all precipitation that falls on the area of the model must leave the area either by way of surface runoff, evapotranspiration, ground-water discharge from the model, or ground-water pumpage from wells. The rates of ground-water pumpage in the area are negligible. The western boundary of the model was placed approximately along the boundary between outcrop belts of the Carrizo and the Reklaw Formations. The Reklaw is a leaky aquitard that overlies the Wilcox-Carrizo aquifer. Node spacing is densest near the dome where the system is most complex. Upper Keechi Creek and Buffalo Creek are both areas of potential ground-water discharge from the Wilcox-Carrizo aquifer (by way of upward leakage), and thus care was taken to place nodes along these stream courses. A cross-sectional view of the area being modeled is shown in figure 89.

Using structure contour maps of the immediate dome area (fig. 90a and b) and structure maps for the entire model area, the three-dimensional IFD mesh (figs. 88, 91, and 92) was generated using the computer program OGRE. The presence of the domal uplift is marked by abrupt vertical variations in the mesh; abrupt vertical changes in the mesh also occur in areas of faults or rather steep dips. The mesh consists of three layers to allow simulation of vertical fluid movement. The upper and lower surfaces conform to the top of the Carrizo Formation and bottom of the Wilcox Formation, respectively. The dome is treated as an impermeable plug. Total number of nodes in the system is 425.

The modeling strategy has been to begin by simulating general flow conditions in the system and then gradually to build more complexity into the model in successive simulations. The first simulation included the essential aspects of the system: (1) geologic structure (as imposed by the three-dimensional mesh); (2) recharge occurring over the dome; (3) lateral flow into the model inward along the western boundary; (4) lateral flow out of the model along a short reach of the southern boundary; and (5) upward discharge to the Trinity River. Each in-flow and out-flow boundary is treated as a prescribed head boundary, using heads measured in nearby water wells. Hydraulic conductivity was uniformly set at a value of 3.0 m/d, on the basis of estimated pumping-test data and sand-to-mud ratios in the system.

In a preliminary simulation, the model computed the distribution of hydraulic head (fig. 93) for the uppermost layer of the mesh. The downstream bulge in the hydraulic head contours at Oakwood Dome reflects recharge occurring over the dome. Most other variations in head are caused by boundary conditions rather than factors

140

within the system. The gradual, downstream decrease in hydraulic gradient is due to the downstream increase in aquifer thickness (fig. 92).

Heads in the lower two layers of the model are not shown because they are similar to those in figure 93. This lack of obvious vertical change in head is not caused by uniformly horizontal flow, since beneath the Trinity River, flow is directed straight up in the model.* Rather, it is caused by the large cross-sectional area through which vertical flow can take place compared with that for horizontal flow. Darcy's equation states that, for a given flow rate, the hydraulic gradient varies inversely with the product of hydraulic conductivity (K) and cross-sectional area of flow (A). Thus, if the horizontal area of the aquifer is much greater than its cross section (as generally occurs), and if vertical and horizontal values of K do not differ significantly, the vertical hydraulic gradients will be minute even where flow is perfectly vertical. In the system being modeled, the cross-sectional area for vertical flow is about 100 times greater than that for horizontal flow.

In reality, vertical hydraulic gradients generally must be greater than those computed by the model, because of horizontal stratification in the aquifer and consequently lower vertical hydraulic conductivity compared with horizontal hydraulic conductivity. These preliminary results, nevertheless, serve as a warning that in local areas within the Wilcox where vertical continuity of sands is good, vertical flow may be taking place even if the heads imply horizontal flow.

How and where vertical flow takes place in the system will be better understood when such factors as vertical leakage from above, aquifer heterogeneity, and anisotropy are added to the model. The leakage boundary condition will be applied over the entire upper surface of the model by using Darcy's equation to describe vertical flow across the Reklaw aquitard between the Queen City water-table system and the Wilcox-Carrizo aquifer. Data needed for this boundary condition include head in the Queen City aquifer, and thickness and vertical hydraulic conductivity (K_v) of the Reklaw aquitard. Hydraulic conductivity of the Reklaw can be estimated only with an accuracy of a few orders of magnitude. The sensitivity of the model to errors in such estimates will be determined by repeated simulations with different K_v values. Hydraulic conductivity values for the model will be derived from the results of pumping tests and continuing studies of Wilcox core and geophysical logs.

---

*In addition to computing hydraulic head, the model computes the fluxes at each node, thus allowing direct verification of flow direction.
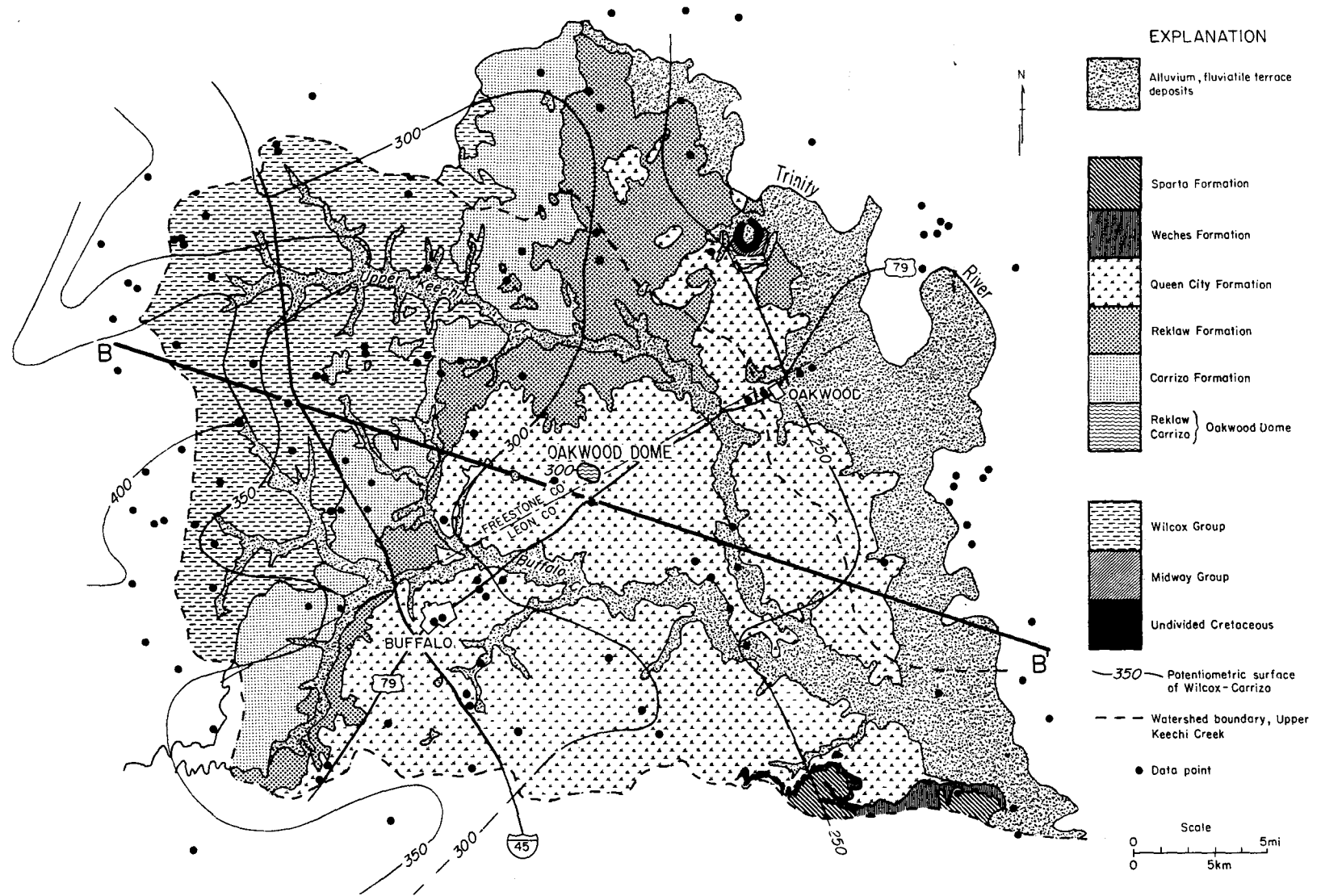
Figure 87. Geologic map, Oakwood Dome area (Upper Keechi Creek watershed), East Texas, showing regional potentiometric surface of Wilcox-Carrizo aquifer system (geology from Barnes, 1967, 1979). Important factors include recharge over Oakwood Dome and potential for discharge to Trinity River, and Upper Keechi and Buffalo Creeks.
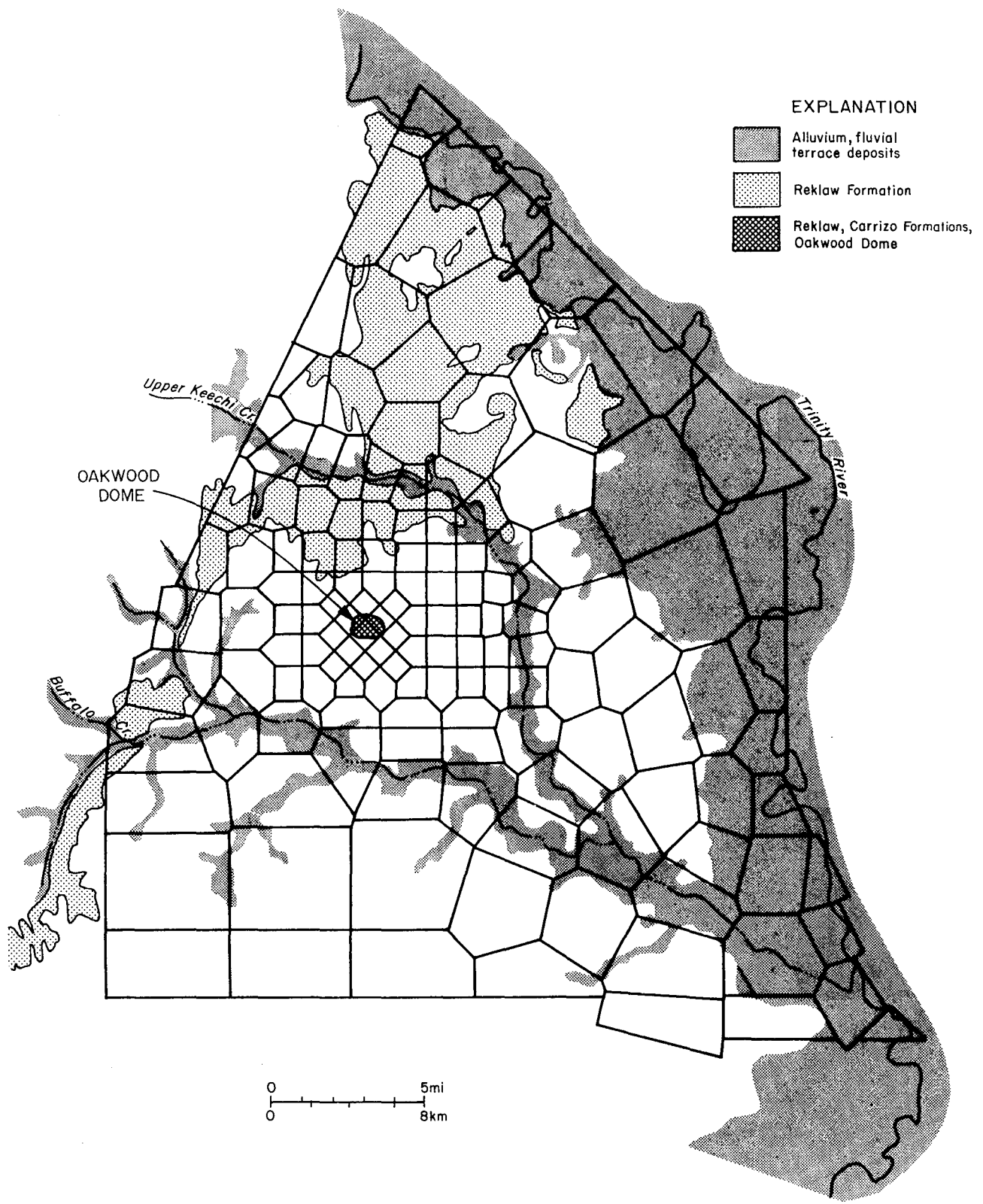
Figure 88. Plan view of integrated finite difference (IFD) mesh, Oakwood Dome area, East Texas. Each polygon represents a finite volume of Wilcox-Carrizo (Wx-Cz) aquifer system.

143
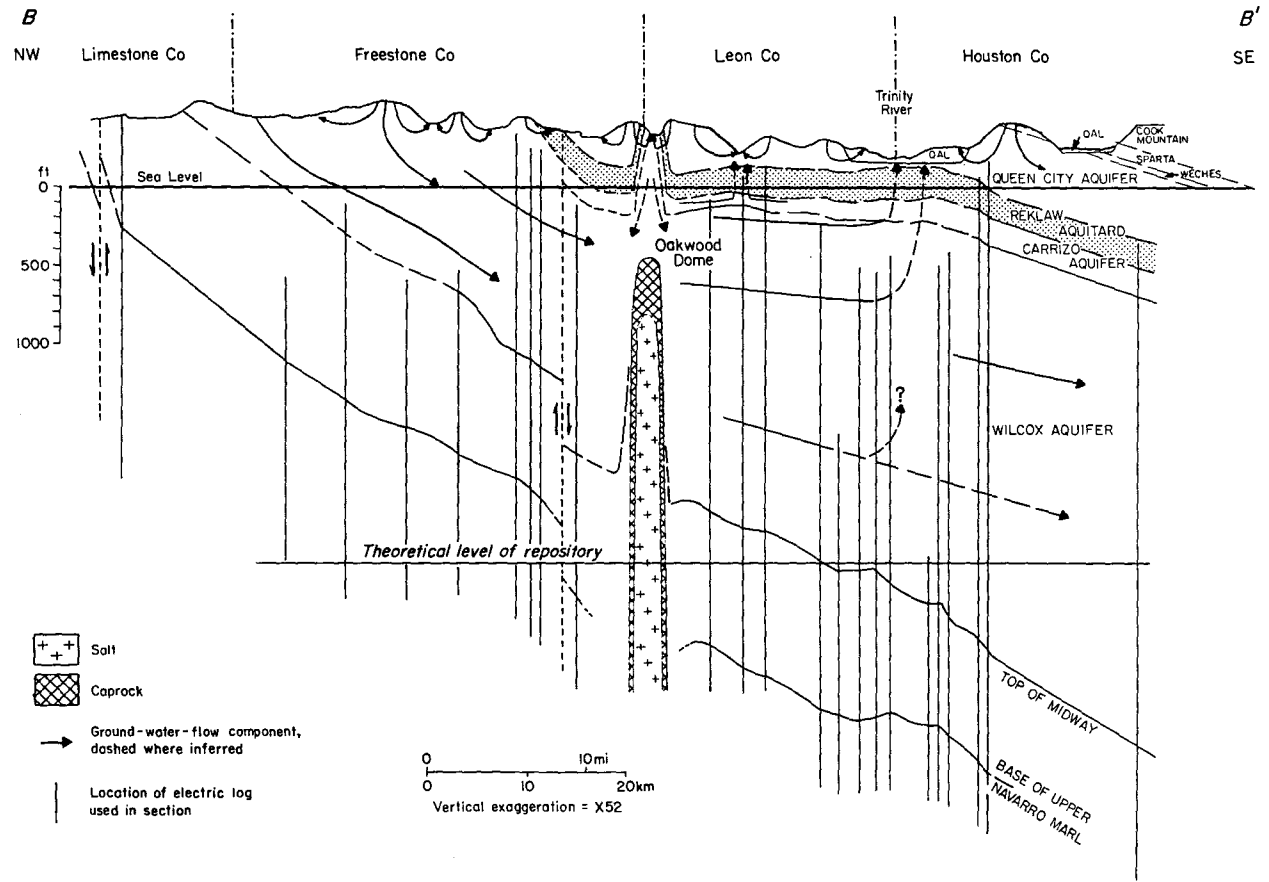
Figure 89. Northwest-southeast geologic cross section through model area, Oakwood Dome, East Texas (adapted from Wood and Guevara, 1981). Ground-water flow lines are based on regional studies (Fogg, 1980b).
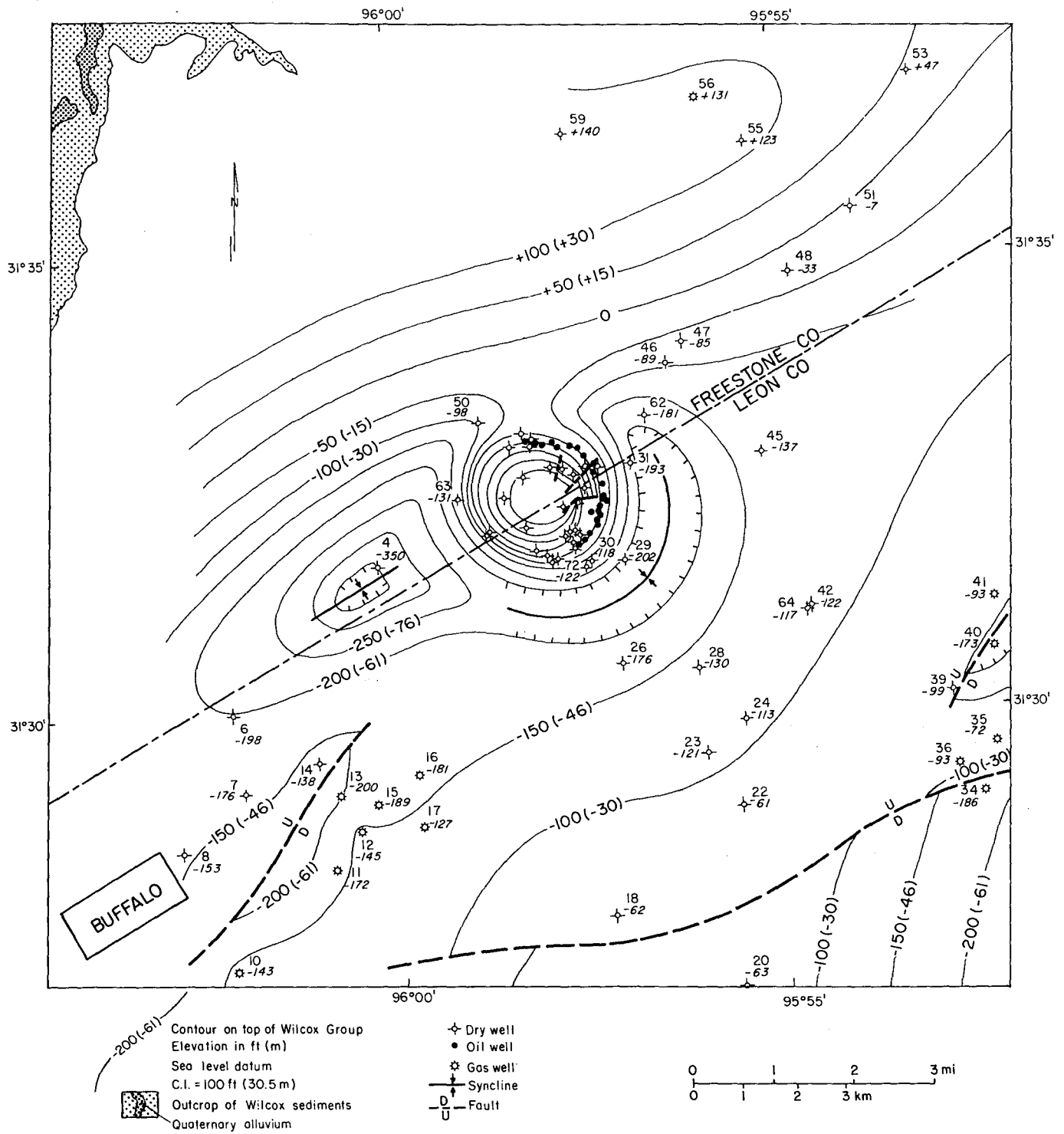
Figure 90a. Structural configuration of Oakwood Dome area, East Texas. Structure map, top of Wilcox Group (from Giles and Wood, in preparation).

145
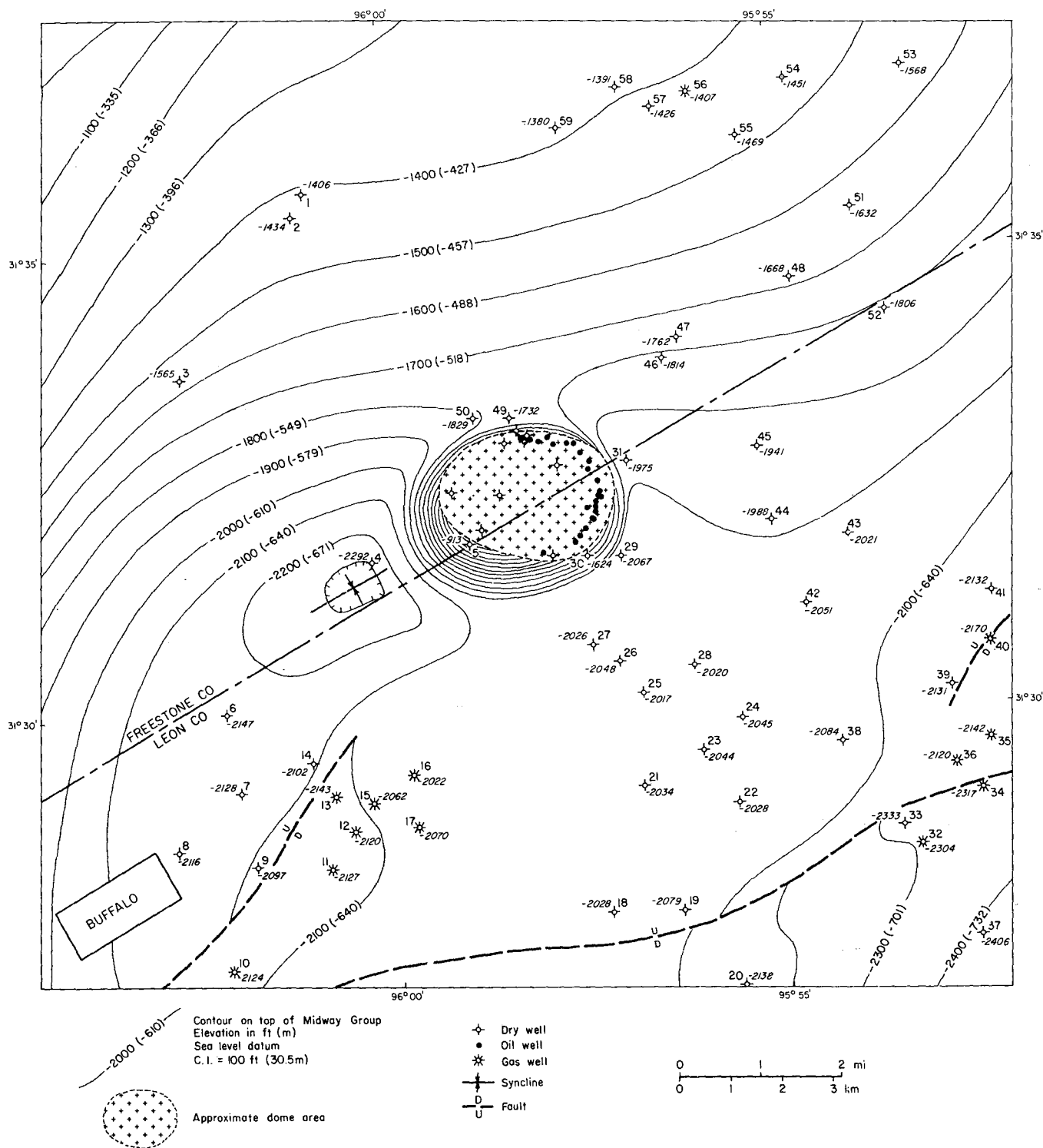
Figure 90b. Structural configuration of Oakwood Dome area, East Texas. Structure map, top of Midway Group (from Giles and Wood, in preparation).

146
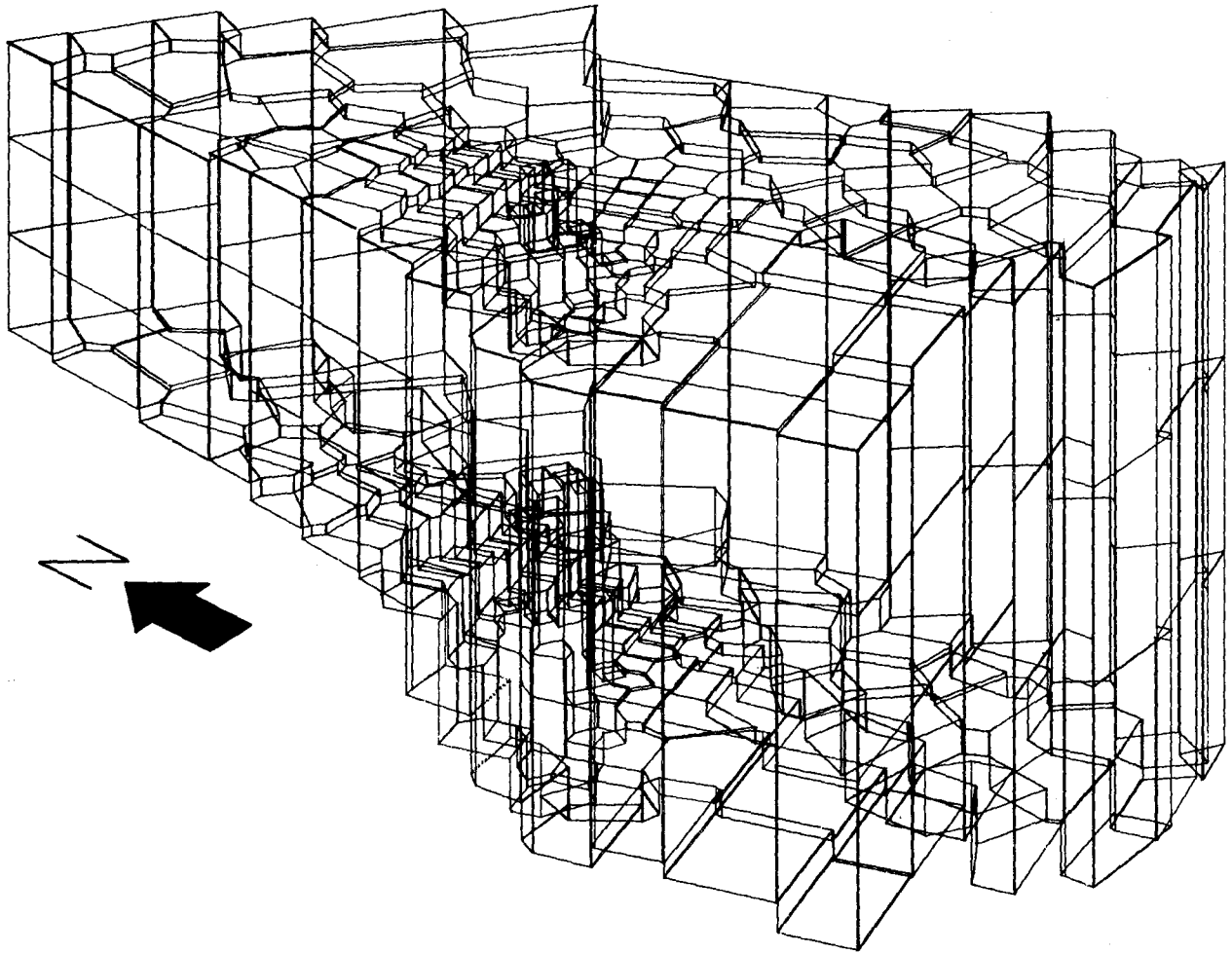
Figure 91. Three-dimensional view from southwest of integrated finite difference (IFD) mesh, Oakwood Dome area, East Texas. Interior framework of mesh is not plotted. Upper and lower surfaces of mesh conform directly to geologic structural configuration, which was obtained from maps such as those shown in figure 90a and b.

147

Figure 92. Three-dimensional view from southeast of upper surface (top of Wilcox-Carrizo aquifer) of integrated finite difference (IFD) mesh, Oakwood Dome area, East Texas.

148

Contour of hydraulic head,
upper layer of the Oakwood model
(ft above m.s.l.)
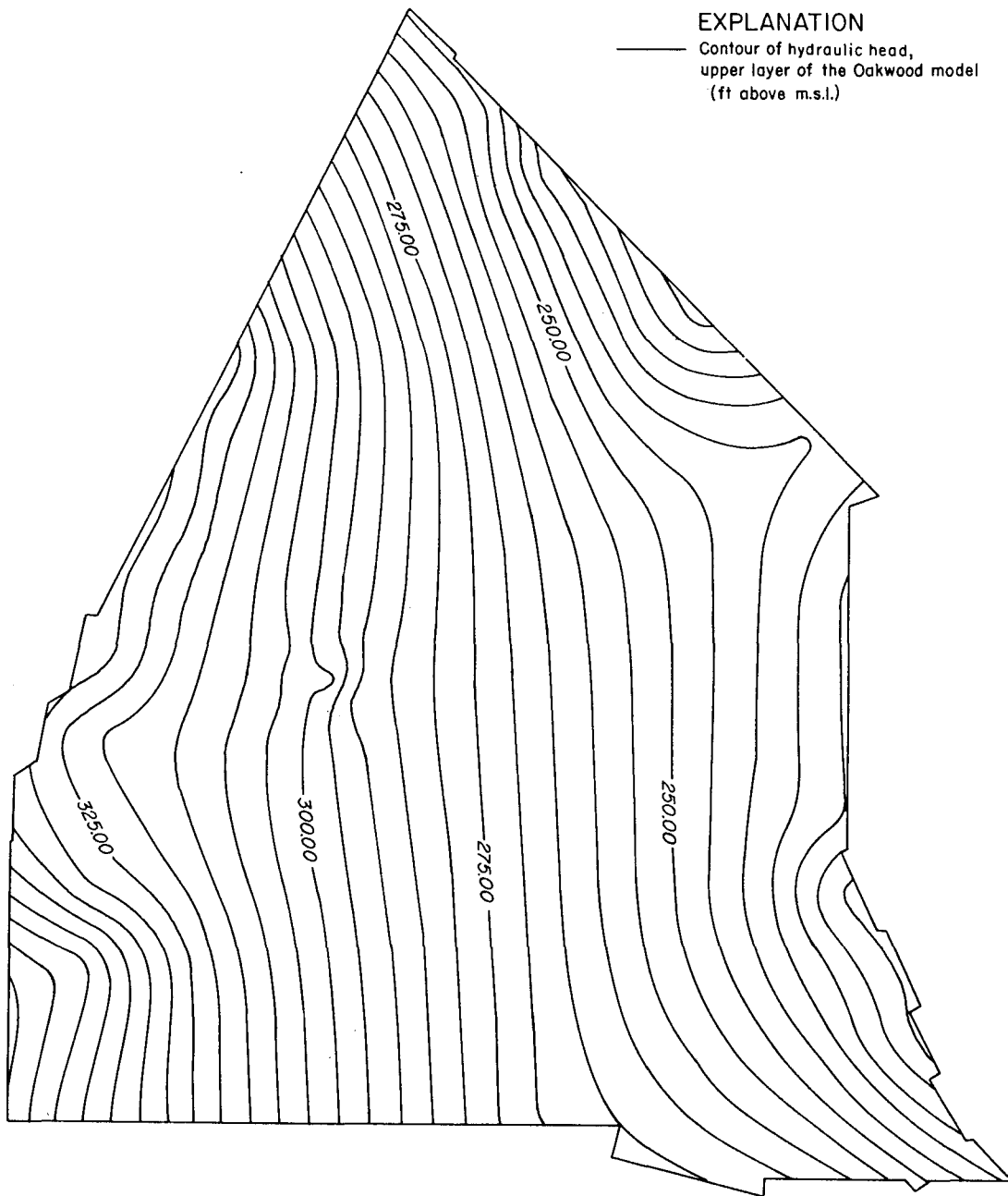
Figure 93. Contours of hydraulic head computed in upper layer of model of Oakwood Dome area, East Texas, during first simulation. Bulge at Oakwood Dome is due to recharge occurring over dome. Gradual downstream decrease in hydaulic gradient is due to corresponding increase in aquifer thickness.

149

WATER CHEMISTRY, OAKWOOD SALT DOME

Charles W. Kreitler and H. Victor Wuerch

Composition of ground waters indicates that recharge is occurring in the dome area, but there is little evidence that salt dissolution of Oakwood Dome is occurring.

Continued growth of the Oakwood Dome during Claiborne time uplifted the Carrizo and Wilcox aquifers (see "Growth History of Oakwood Salt Dome, East Texas"). The Carrizo aquifer now crops out over the dome and has become a recharge zone (see "Fluid-Pressure Versus Depth Relationships in the Wilcox-Carrizo Aquifer System, East Texas"). Recharge waters in East Texas Tertiary aquifers are typically oxidizing and acidic (Kreitler and others, 1980). Retardation of radionuclides is, however, most effective under basic, reducing conditions (Relyea and others, 1978). It therefore becomes important to measure how deeply the recharge waters penetrate into the Carrizo and Wilcox aquifers in the vicinity of Oakwood Dome.

Twelve monitoring wells drilled near Oakwood Salt Dome (fig. 80) provided samples for chemical and isotopic analyses to determine the hydrology near the salt dome (table 11). Analyses included major anions and cations, and δC^{13} and C^{14} of bicarbonate. The C^{14} ages were corrected using a δC^{13} correction factor (Ingerson and Pearson, 1964) (see "Carbon-14 Dating of Ground Water near Oakwood Dome, East Texas").

Composition of water samples from these recently constructed monitoring wells may not represent true aquifer conditions because drilling muds were not completely flushed from the formation surrounding the well bore. The amount of error of an analysis is dependent upon the concentration of the measured constituent and the sensitivity of the particular analysis. Results from two monitoring wells drilled at Oakwood Dome illustrate the problem.

At well TOH-5, the nontoxic fluorocarbon, chlorobromodifluoromethane, was injected into the drilling mud during drilling. Water was sampled four times during a pump test (at elapsed times 0.0 hr, 0.5 hr, 13.25 hr, and 23.75 hr), and Dr. Glen Thompson, University of Arizona, tested the samples for the presence of the fluorocarbon. All samples still contained the tracer at levels of 1 to 10 parts per trillion ($1 \text{ ppt} = 10^{-12}$ g/mL) (fig. 94). The results from water-chemistry analyses of these

samples, however, remained constant during the time of the pump test and are typical for Carrizo Formation waters.

The persistence of the tracer through the duration of the pump test suggests that its presence either may be controlled by desorption from the aquifer or may be attributed to contamination of sample-collection equipment. Tracer concentrations remaining between 1 to 10 parts per trillion after 24 hr of pumping could easily result from a desorption phenomenon if the aquifer material had been initially exposed to high tracer concentrations during drilling.

Similar sorption-related problems were evident in the studies of fluorocarbon tracers by Bassett and others (1981). The chromatograms from the tracer analysis clearly show a reduction in concentration of unidentified trace organic compounds as pumping continued (fig. 94). For example, the peak at 1.77 min (0.0 hr) is reduced to two smaller peaks appearing at 1.47 min after 0.5 hr of pumping. (The smaller of the two appears as a shoulder on the peak of the chromatogram at 1.47 min.) These two peaks continue to decline as pumping progresses, eventually reaching the point where there is baseline separation between them at 23.75 hr. Other peaks in the chromatogram show similar behavior, giving additional evidence that the organic composition of the formation water is gradually changing as the pump test continues.

A second example of sampling-derived error occurred at monitor well TOH-2A (table 11) where a carbon-14 date for bicarbonate was obtained. (The date is considered unreliable and therefore not included in table 11.) A plot of uncorrected carbon-14 ages versus bicarbonate (fig. 95) shows a general trend of increasing HCO_3 with increasing uncorrected age. The carbon-14 age of bicarbonate from TOH-2A is considerably younger than ages determined from samples from other wells with high bicarbonate concentrations and is therefore considered incorrect. Results of chemical analyses of water samples taken from TOH-2A three times during a 24-hr pump test remained constant, and appear to represent true ground-water chemistry. The anomalous carbon-14 ages may be related to the use of drilling mud containing an organic polymer. The organic polymer is designed to decay for easy well cleanup. Decay of the organic polymer, which is composed of modern cellulose, to carbon dioxide possibly enriched the C^{14} content of the bicarbonate in the formation water. This could account for a very young carbon-14 date without measurably affecting the general water chemistry.

Water chemistry of shallow ground waters in the Carrizo and Queen City aquifers around Oakwood Dome (table 11) characteristically displays low pH and low

151

anion and cation concentrations that are typical of Carrizo recharge waters in the East Texas Basin (Fogg and Kreitler, in preparation). The light δC^{13} values range from -14 to -21 $^o/_{oo}$ and confirm that these waters are recharge waters, assuming that the δC^{13} of soil carbon dioxide is approximately -20 $^o/_{oo}$ (see "Carbon-14 Dating of Ground Water near Oakwood Dome, East Texas").

Test wells TOH-2A and TOH 2AO, producing from the Wilcox around Oakwood Dome have water chemistry typical of artesian Wilcox samples (Fogg and Kreitler, in preparation), with high pH values, high Na and HCO_3 concentrations, and heavier δC^{13} values. It is expected that radionuclides would be retarded more effectively in the high pH, reducing Wilcox aquifer than in the low pH, oxidizing Carrizo.

Well TOH-2A is the only Wilcox well containing water with high chloride concentrations. Whether this increased chloride concentration is the result of salt dome dissolution or other hydrogeologic phenomena is not known (see Fogg and Kreitler, in preparation).

Table 11. Chemical and isotopic values of water samples from water wells near Oakwood Dome, East Texas.*

Well no.	Sample tests	Depth (ft)	Screened interval (ft)	Aquifer	C^{13}/C^{12}	C^{14} age	Corrected C^{14} age	Temp. (°C)	Conductivity (µMHOS)	Salinity	pH	HCO_3^-	Ca^{+2}	Na^+	Cl^-	SO_4^{-2}	K^+	Br^-	Mg^{+2}	F^-	SiO_2	Fe	NO_3^-	Date	Elapsed pumping time (h)
TOH-5	Init. cap. 24-h	600	474 - 600	Carrizo	-19.0	4,300 ± 60	3,910	24.7	590	0.2	6.0	82.4	40.9	68.6	133.5	100.3	11.8	0.82	9.75	0.32	14.8	1.35	<0.01	11/1/79	<6
	1							24.1	300	0.0	5.5	28.1	22.3	31.5	53.1	76.1	8.1	1.82	5.53	0.23	16.1	0.15	0.04	11/2/79	0.5
	2							24.0	235	0.0	4.9	10.1	18.5	28.8	50.2	79.7	7.6	2.86	5.27	0.22	18.8	0.17	0.06	11/2/79	13.25
	3							24.1	235	0.0	5.2	12.1	18.3	28.6	43.8	82.0	7.6	2.68	5.59	0.23	17.5	0.17	0.05	11/3/79	23.75
OK-119	1	216	206 - 216	Queen City				21.8	1,290	0.7	5.9	72.4	120.5	69.7	115.5	324.6	16.0	10.3	49.9	0.63	99.6	27.3	0.46	11/8/79	0.75
	2				-17.8	4,290 ± 70	3,970	22.0	1,280	0.6	5.8	54.3	106.3	69.1	172.2	318.6	16.3	15.8	51.4	0.82	100.0	30.3	0.54	11/9/79	23.0
TOG-IWS	1	160	80 - 160	Carrizo				21.8	130	0.0	4.5	6.0	6.1	19.4	49.5	38.8	3.9	0.06	1.43	0.06	23.0	0.12	0.04	11/13/79	1.0
	2				-19.3	2,980 ± 60	2,650	21.4	150	0.0	4.2	4.0	3.9	19.8	71.8	40.8	3.9	0.01	1.56	<0.01	25.1	0.12	0.02	11/14/79	22.0
TOH-2A	1	1,920	1,900 - 1,920	Wilcox				28.9	1,495	0.8	8.9	711.5	6.5	343	138.0	30.6	3.8	0.63	0.7	0.83	18.7	0.76	0.36	1/21/80	1.0
	2				-9.2	11,520 ± 190[3]		31.8	1,600	0.8	8.9	715.6	5.9	347	127.0	34.7	3.5	0.63	0.9	0.86	25.4	0.26	0.12	1/21/80	8.5
	3							33.8	1,625	0.7	8.7	713.6	2.9	344	130.0	35.5	3.5	0.38	0.7	0.79	25.1	0.15	<0.1	1/22/80	22.0
TOH-2AO	Init. cap. 24-h	945	835 - 945	Wilcox	-14.9	10,540 ± 120	7,836	26.8	460	0.0	9.3	266.0	12.2	98.7	25.5	25.0	6.1	0.38	1.5	0.22	21.6	0.05	<0.1	1/18/80	<6
	1							26.2	450	0.0	9.1	266.0	11.4	97.5	21.8	19.4	5.0	0.13	1.5	0.28	21.5	0.14	<0.1	1/24/80	2.5
	2				-12.5	11,690 ± 120	7,940	26.8	455	0.0	8.9	256.0	11.4	97.5	25.5	19.8	4.7	0.63	1.8	0.21	20.8	0.10	<0.1	1/24/80	9.0
	3							26.8	448	0.0	8.6	256.0	10.7	98.0	21.8	19.4	4.2	0.13	1.8	0.22	21.6	0.28	<0.1	1/25/80	22.0
TOH-2D2	1	575	515 - 575	Carrizo				24.8	450	0.2	6.3	62.3	28.8	36.2	27.4	156	9.7	<0.01	9.8	0.12	13.5	0.67	<0.1	2/7/80	2.0
	2							24.0	458	0.1	6.2	60.3	28.8	36.1	31.0	159	9.7	0.25	9.3	0.13	14.6	3.95	<0.1	2/7/80	10.0
	3				-17.1	ND	ND	24.2	462	0.1	6.2	64.3	28.0	36.2	29.2	158	9.7	1.4	9.6	0.12	13.0	3.45	0.31	2/8/80	22.5
OK-103	1	240	230 - 240	Carrizo				22.2	72	0.0	6.8	42.2	11.2	2.2	8.8	26.0	4.1	0.68	0.8	0.08	13.0	0.46	<0.1	2/12/80	1.5
	2							22.3	69	0.0	6.7	40.2	10.3	2.8	13.5	28.7	4.3	0.48	0.9	0.07	13.3	0.43	<0.1	2/12/80	9.0
	3				-18.5	3,470 ± 100	2,710	22.2	72	0.0	6.6	38.2	10.1	2.1	10.2	48.3	4.9	0.59	0.8	0.06	13.7	0.90	0.38	2/13/80	22.0
OK-104	1	180	170 - 180	Carrizo	-20.4	1,100 ± 100	1,100	21.9	270	0.0	5.9	24.1	19.6	9.5	33.9	55.5	6.4	0.70	6.7	0.13	17.3	0.02	<0.1	2/14/80	0.5
	2							21.5	297	0.0	5.4	16.1	20.3	10.9	39.1	71.7	6.7	0.77	8.7	0.13	16.6	0.07	0.30	2/14/80	7.0
	3							21.3	308	0.0	4.8	8.0	20.4	12.8	42.0	96.2	7.0	0.74	10.4	0.18	17.3	0.10	0.50	2/15/80	19.5
OK-108	1	320	310 - 320	Carrizo	-13.8	9,530 ± 110	6,558	23.6	67	0.0	7.2	217.1	60.2	72.7	38.4	171.0	7.5	0.7	14.3	0.07	17.4	0.10	0.1	2/25/80	1.0
OK-105	1	88	78 - 88	Carrizo				20.2	49	0.0	6.0	16.1	5.5	2.9	10.6	2.7	4.2	0.6	1.2	0.04	15.8	0.43	0.4	2/26/80	15.0
	2				-21.3	1,760 ± 90	1,760	20.6	49	0.0	6.0	18.1	5.5	3.1	19.6	1.9	4.4	0.6	0.7	0.04	15.1	0.32	0.3	2/26/80	21.0
OK-102	1	148	138 - 148	Carrizo				22.0	53	0.0	6.1	22.1	8.2	2.0	13.2	4.4	2.0	0.1	1.7	0.03	12.8	0.07	0.1	3/5/80	1.5
	2				-19.2	2,130 ± 110	1,808	21.6	53	0.0	5.9	20.1	7.9	2.0	11.1	9.6	2.0	0.1	1.0	0.1	13.1	0.07	0.1	3/5/80	8.5
OK-115	1	405	385 - 405	Carrizo	—	—	—	—	—	—	7.2	78.5	25.3	32.0	20.9	84.2	7.5	0.1	5.3	0.1	13.1	0.05	0.1	3/12/80	

*All chemical analyses measured in mg/L.

154
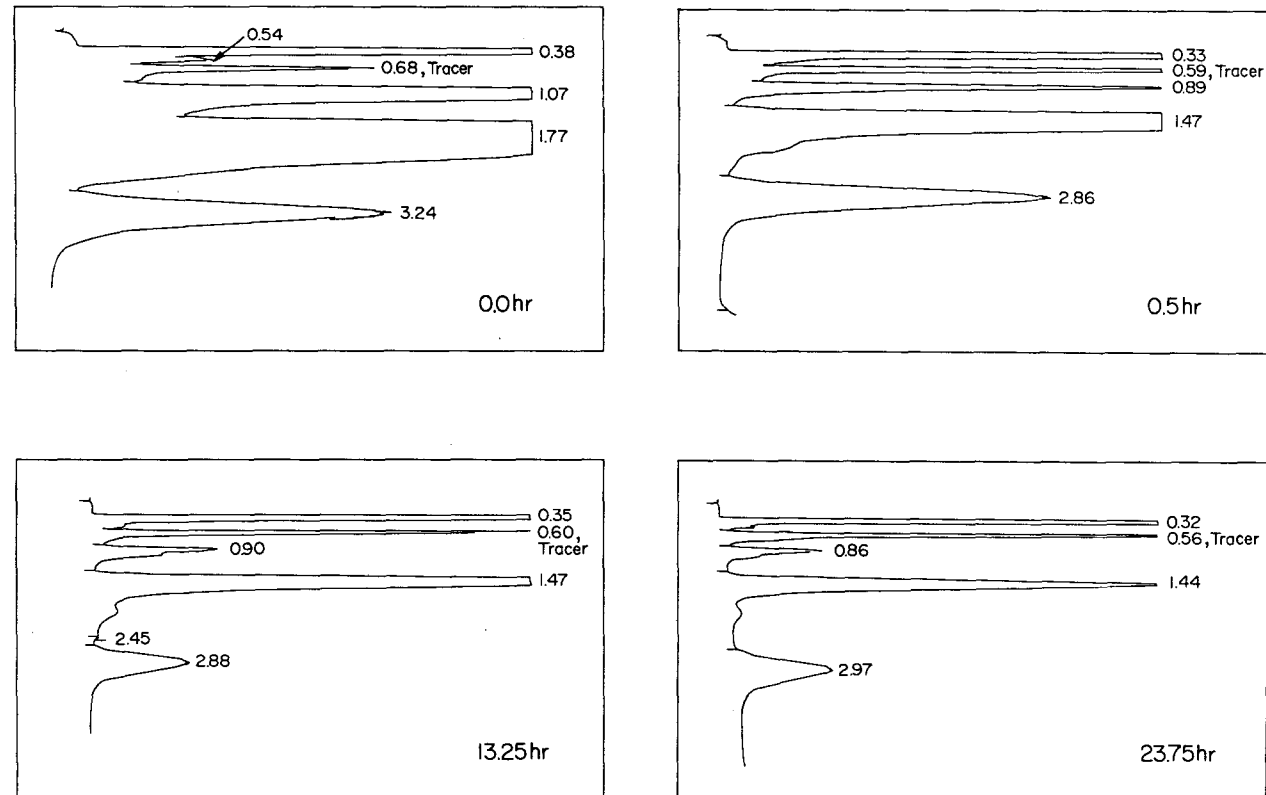
Figure 94. Gas-chromatograph traces of organic material in water samples from monitoring well TOH-5, Oakwood Dome area, Texas. Sampling occurred four different times during pump test. An artificial tracer, the fluorocarbon chlorobromodifluoro-methane, was injected into drilling mud during the drilling of well TOH-5. Gas-chromatograph trace at 0.5 to 0.7 minutes is peak of tracer. Tracer is evident in well water during and after 24 hours of production at a yield of approximately 280 gpm.
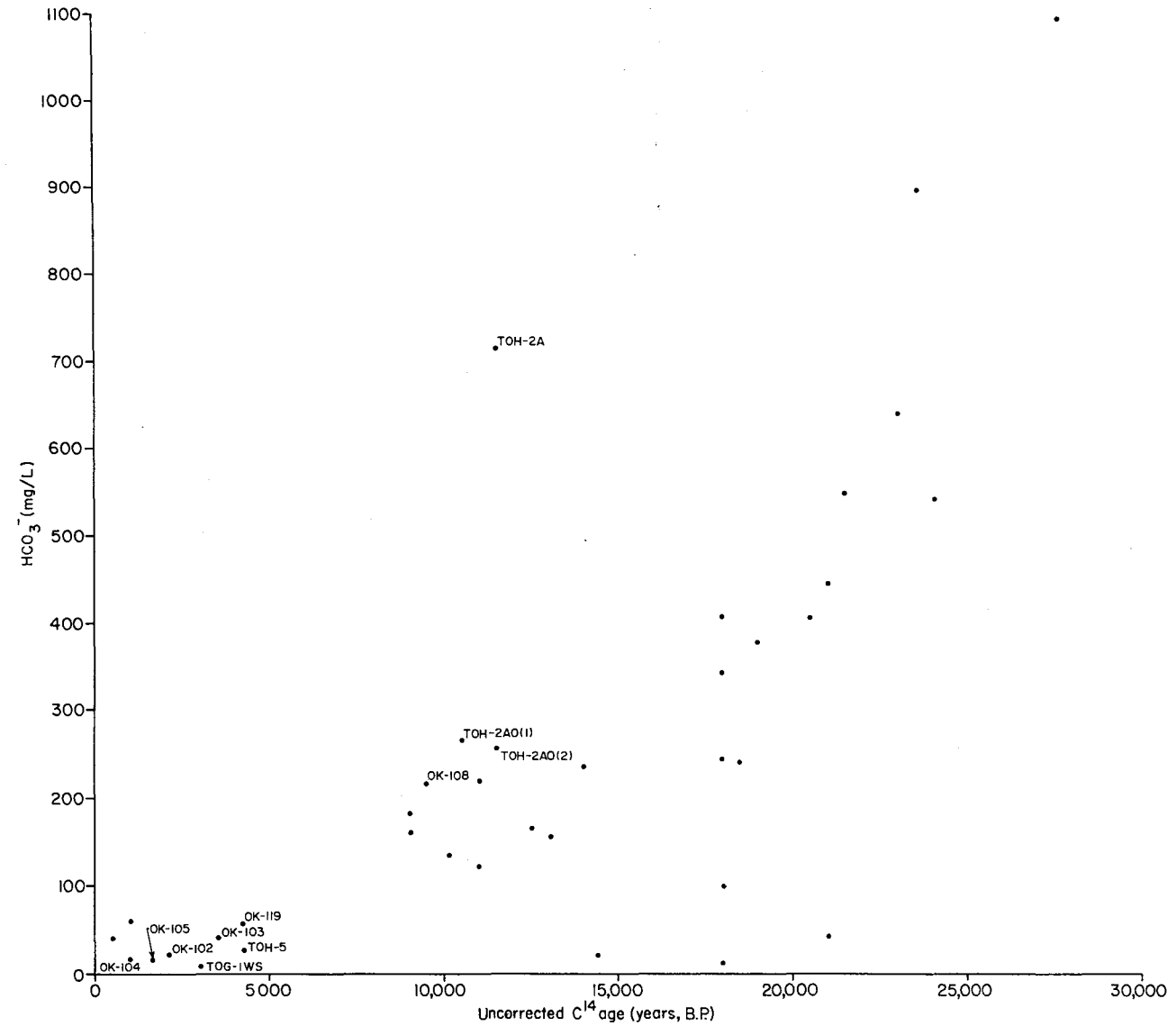
Figure 95. Uncorrected carbon-14 ages versus HCO_3^- concentrations for ground waters in Carrizo and Wilcox aquifers, East Texas Basin. Note that well TOH-2A is significantly off trend, indicating a probable error in analysis.

CARBON-14 DATING OF GROUND WATER NEAR OAKWOOD DOME, EAST TEXAS

Charles W. Kreitler and H. Victor Wuerch

Carbon-14 ages of ground waters near Oakwood Dome increase down the hydraulic gradient from the outcrop recharge area toward the Trinity River. Carbon-14 ages also increase as the water chemistry evolves from a Ca-Mg, Cl-SO_4 water to a Na-HCO_3 water. Waters in the shallow Carrizo are younger than waters in the deeper Wilcox aquifer.

Chemical composition, δC^{13} values, and carbon-14 ages of ground water in the Wilcox, Carrizo, and Queen City aquifers near Oakwood Dome indicate that ground water flows from outcrop down the hydraulic gradient toward the Trinity River; possible discharge occurs into Upper Keechi Creek, a tributary of the Trinity River. Ground-water ages increase from approximately 1,000 to 4,000 years old in the Carrizo aquifer over Oakwood Dome to 7,000 to 8,000 years old in the Wilcox and Carrizo aquifers at greater depths, and to approximately 15,000 years old in the vicinity of Upper Keechi Creek (fig. 96; table 12). Water in sample 4 (fig. 96; table 12) from a shallow water well in the Queen City aquifer near Upper Keechi Creek is 15,000 years old. The age of this shallow Queen City water results from the well's location in a regional discharge zone.

Evolution of the ground-water chemistry from a Ca-Mg, Cl-SO_4 water (recharge water) to a Na-HCO_3 water coincides with increased carbon-14 age of the samples. Figure 97 shows this linear relation between water chemistry and carbon-14 ages. A plot of HCO_3 values versus corrected ages also shows a linear relation (fig. 98).

Carbon-14 ages must be corrected to account for additional dead carbon from the dissolution of carbonate minerals. For this, correction factor (P) described by Ingerson and Pearson (1964) is used:

$$P = \frac{\delta C^{13} \text{ (sample)} - \delta C^{13} \text{ (limestone)}}{\delta C^{13} \text{ (soil } CO_2) - \delta C^{13} \text{ (limestone)}}$$

The δC^{13} value for limestone is assumed to be 0 °/oo on the basis of the average value of six whole rock samples taken from the Wilcox core, and the δC^{13} value for soil gas is assumed to be -20.0 °/oo, on the basis of values plotted in figure 99. Low

HCO_3 concentrations occur in shallow ground water and are assumed to be composed predominantly of soil gas carbon dioxide with a δC^{13} of -20.00 ‰.

Carbon-14 ages of bicarbonate in ground water at the Oakwood Dome help confirm directions and rates of ground-water flow previously determined by hydraulic head data. The carbon-14 ages also establish a rate for the chemical evolution of the ground water. Both rates of flow and rates of chemical change are needed to assess radionuclide migration away from a salt dome.

Table 12. Carbon-14 ages of bicarbonate ion
in ground waters near Oakwood Dome,
East Texas.*

	Well Number on Figure 96				
	1	2	3	4	5
Sample no.	3601	3666	3665	3593	3598
Screened Interval [ft]	350-371 601-678	400-482	—	—	340-380
Depth [ft]	691	482	640	190	380
δC^{13}	-7.2	-15.5	-6.3	-15.1	-18.6
C^{14} age	22,960 ± 460	8,920 ± 220	21,550 ± 400	18,840 ± 340	3,160 ± 90
Corrected C^{14} age	14,670	6,890	12,200	14,820	2,582
pH	8.8	7.4	8.3	8.6	5.5
Temp. [°C]	26.2	26.7	24.0	28.0	23.0
Ca^{+2}	6.1	27.2	5.5	30.8	5.2
Na^+	297.8	46.5	179.6	72.2	9.7
Mg^{+2}	0.53	9.88	1.05	7.83	2.2
K^+	3.1	7.0	4.0	7.1	4.2
Cl^-	38.5	34.6	27.0	45.0	12.6
SO_4^{-2}	3.0	36.0	5.0	16.5	13.0
HCO_3^-	640.0	181.0	540.0	236.0	34.0
Br^-	0.76	1.42	1.27	1.41	<0.1
F^-	0.68	<0.01	0.21	0.19	<0.1
SiO_2	13.6	19.5	13.6	13.0	36.7
Fe	0.01	0.39	0.17	0.03	<0.6
Sr	—	—	—	—	—
H_2S	<0.02	<0.02	<0.02	<0.02	—
I^-	—	—	—	—	—
Mn	<0.01	0.03	0.01	<0.01	<0.02

*All chemical analyses measured in mg/L
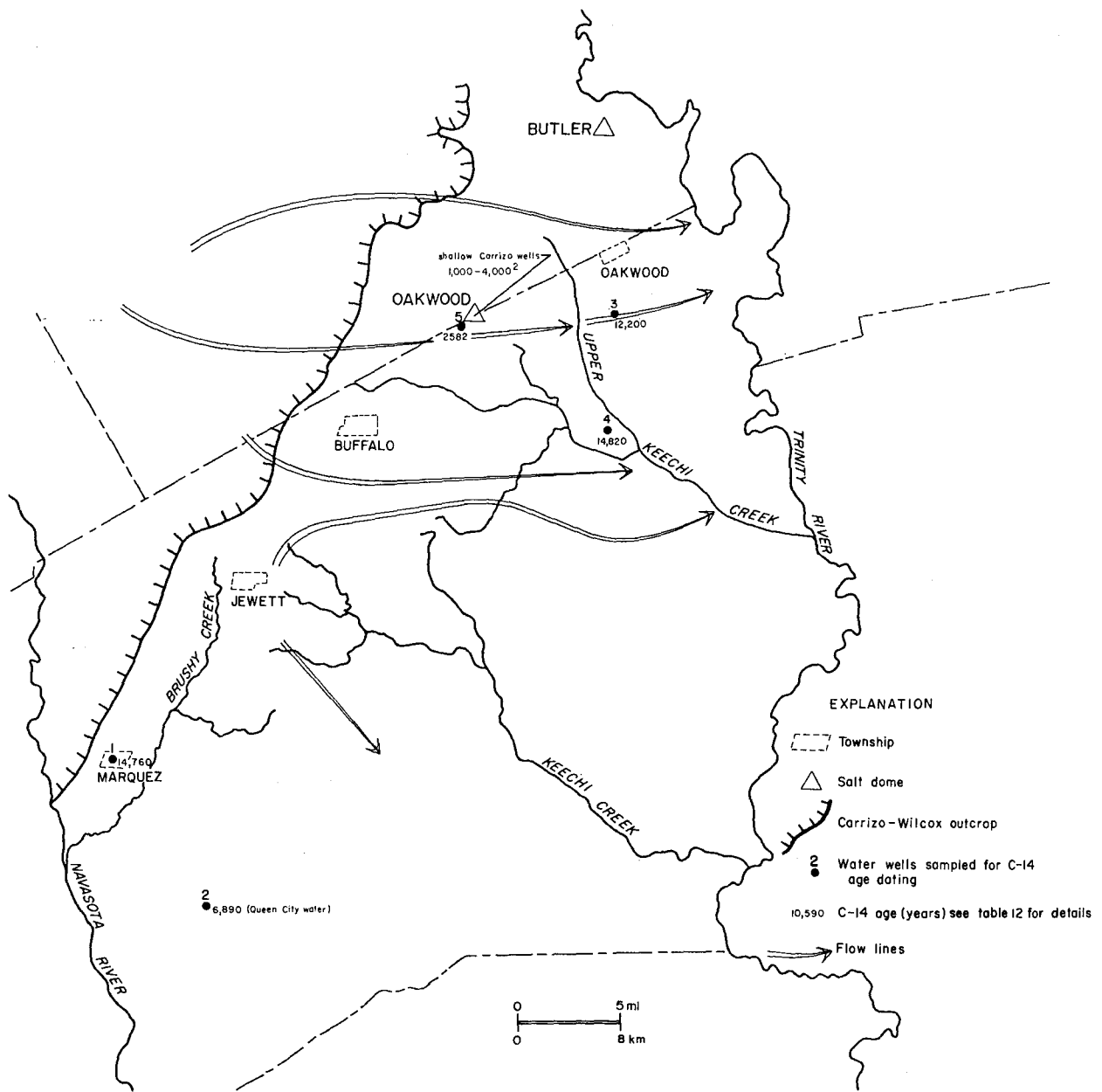
Figure 96. Carbon-14 ages of HCO_3^- ion in ground water in Oakwood Dome area, East Texas. There is a general increase in age from outcrop-recharge area to downdip artesian parts of Carrizo and Wilcox aquifers.

158
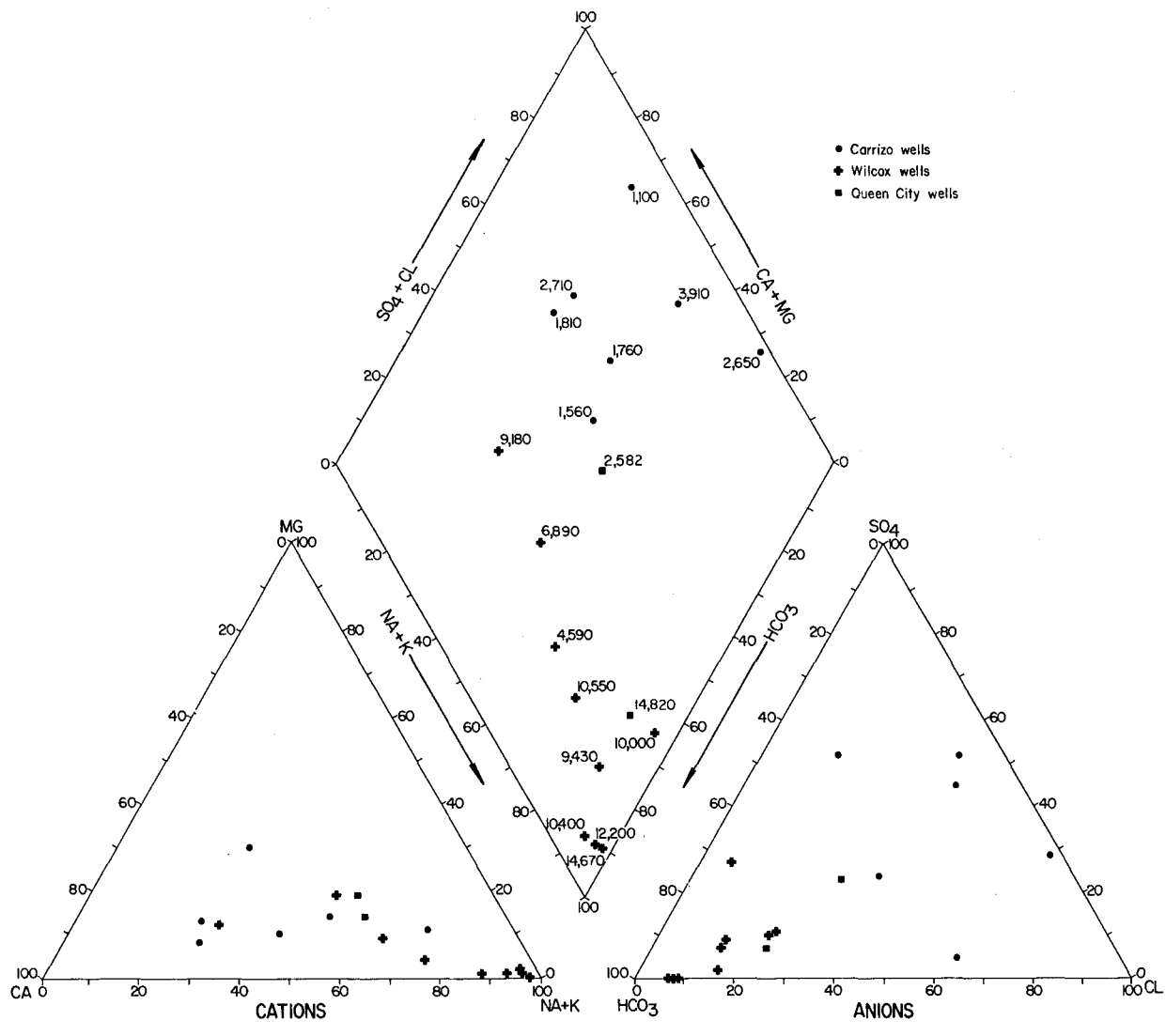
Figure 97. Piper diagram of water samples selected for carbon-14 age dating, Oakwood Dome area, East Texas. Corrected carbon-14 ages increase as water chemistry evolves from a Ca-Mg, Cl-SO$_4$ water in the shallow Carrizo to a Na-HCO$_3$ water in the deep Wilcox.

159
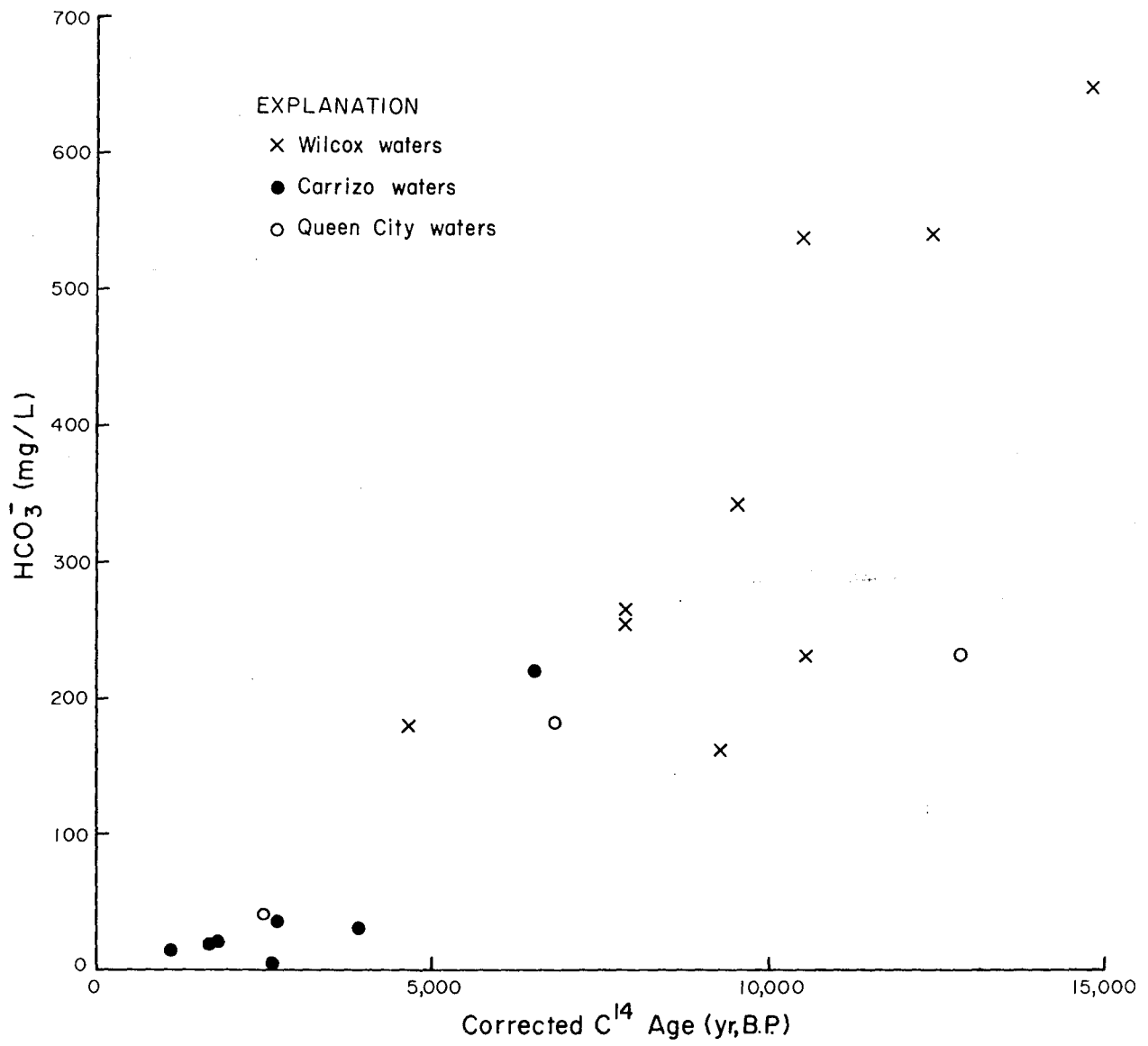
Figure 98. Corrected carbon-14 ages versus HCO_3^- for Carrizo, Wilcox, and Queen City waters near Oakwood Dome, East Texas.

160
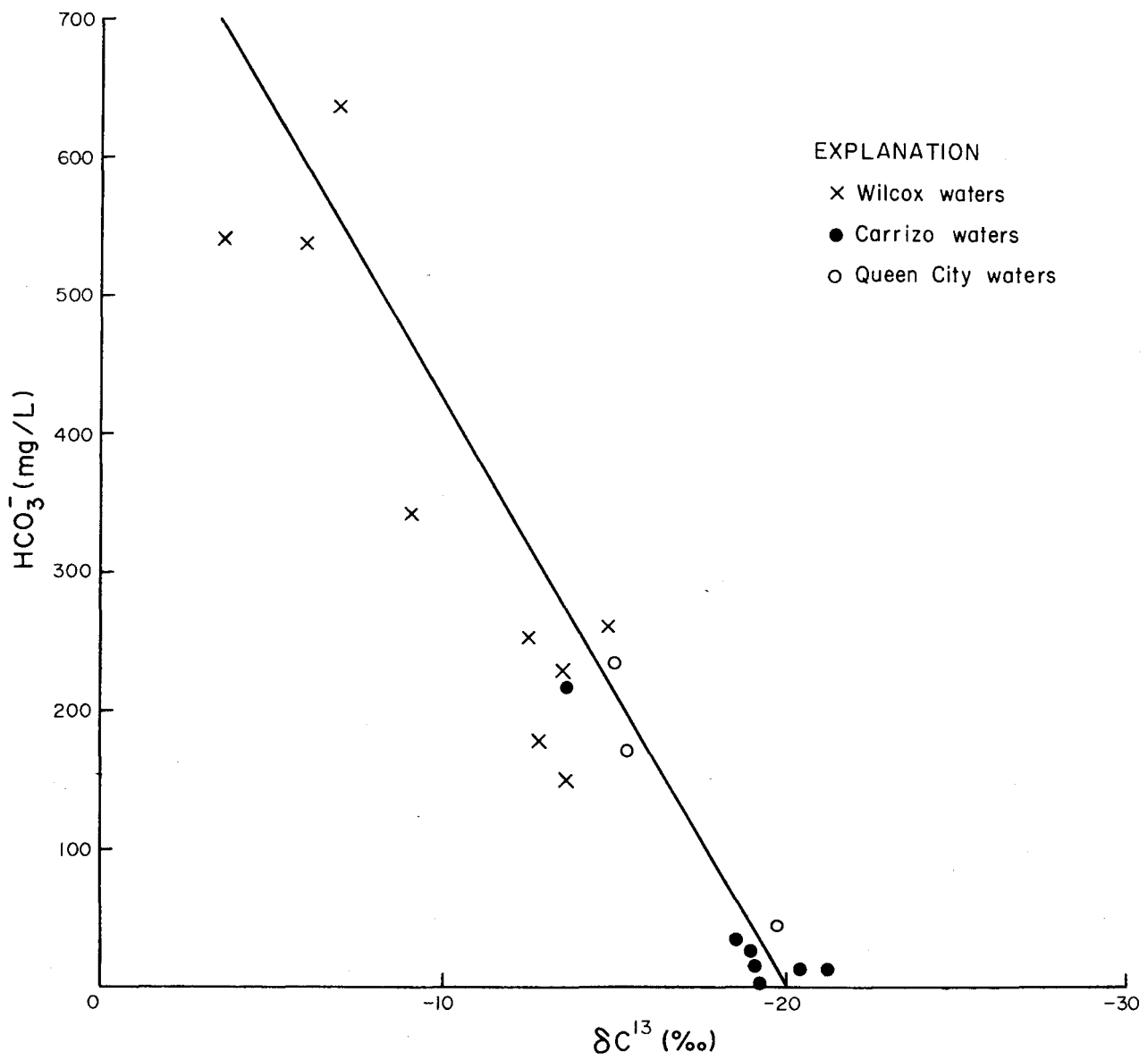
Figure 99. Relation of δC^{13} versus HCO_3^- concentration, Oakwood Dome area, East Texas. A linear relation exists between HCO_3^- concentration and its δC^{13} value. Shallow ground waters in Wilcox-Carrizo aquifers typically are low in bicarbonate, whereas deep waters have much higher concentration. Extrapolation of this trend to 0.0 bicarbonate concentration provides an estimate of the initial δC^{13}.

CAP-ROCK STUDIES OF OAKWOOD DOME

Shirley P. Dutton and Charles W. Kreitler

Cap rock at Oakwood Dome consists of low-permeability anhydrite resting in sharp contact with the underlying salt. A more porous calcite section overlies the anhydrite. The cap rock seems to be an effective seal that prevents dome dissolution.

Cap rock on top of Oakwood Salt Dome is 450 ft (137 m) thick in the LETCO TOG no. 1 well, Freestone County. The cap rock consists of an upper calcite zone (713 to 902 ft [217 to 275 m]) and a lower anhydrite zone (908 to 1,163 ft [277 to 354 m]), separated by a narrow transition zone (fig. 100).

The salt/cap-rock contact is sharp, and no cavity is present. A band of salt-cemented anhydrite grains 1 to 2 mm wide separates the salt stock from the tightly compacted anhydrite cap rock. Interpenetration of anhydrite grains of the cap rock was probably caused by deformation, which has resulted in a tight grain fabric with very low porosity (0.7 to 3.3 percent; fig. 101) and permeability (less than 0.01 to 0.02 md).

Between 907 and 902 ft (276.5 and 274.9 m), the cap rock changes upward from predominantly anhydrite to predominantly calcite (fig. 100). Fine-grained calcite crystals (0.03 to 0.15 mm) first appear at 926 ft (282 m), where they surround and corrode anhydrite grains. At 907 ft (276.5 m), part of the cap rock consists of a very porous, open network of fine-grained calcite, pyrite, and sulfur (fig. 101). Where anhydrite remains, it is commonly surrounded by calcite or gypsum. By 905 ft (275.8 m), much of the porosity has been occluded by precipitation of fine-grained calcite. Above this depth, no anhydrite or gypsum remains.

The calcite zone of the cap rock consists of horizontal bands of dark-gray, fine-grained calcite (0.03 to 0.25 mm) separated by layers of coarse-grained calcite (crystals are 1.5 to 5.0 mm). The coarse calcite appears to have grown into open pores and formed later than the fine-grained calcite. Porosity as high as 22.5 percent (fig. 101), and permeability up to 43 md have been measured in the calcite cap rock.

The cap rock has undergone several diagenetic processes. The first was the original formation of anhydrite cap rock through dissolution of salt by non-meteoric water and subsequent accumulation of residual anhydrite crystals. Deformation of the

anhydrite grains probably occurred at depth and was due to high confining pressures and high temperatures.

The second diagenetic process was formation of dark, fine-grained calcite by reduction of anhydrite; this reaction may have involved the sulfur-reducing bacteria, Desulfrovibrio desulfuricans (Feely and Kulp, 1957). Reduction of calcium sulfate presumably occurred as reducing, organic-rich, saline formation waters migrated out of the basin. Very light values of δC^{13} were measured in the fine-grained calcite (fig. 102), which indicates that there was an organic source of carbon for the calcite.

The final diagenetic reaction involves formation of the white, coarse-grained calcite, which is considered a later diagenetic mineral. Similarity of δC^{13} values in dark and white calcite at a given depth (fig. 102) suggests that white calcite formed by solution and reprecipitation of dark calcite. Different trace-element concentrations in the light calcite compared with concentrations in dark calcite indicate that different fluids were present in the cap rock when the light calcite precipitated.

The presence of cap rock on a salt dome implies that salt dissolution has occurred. However, the cap rock at Oakwood Dome appears to have formed in saline aquifers at depth and not in the present shallow meteoric system. The tight salt/cap-rock contact and impermeable anhydrite texture indicate that the Oakwood cap rock is a barrier to further dome dissolution.
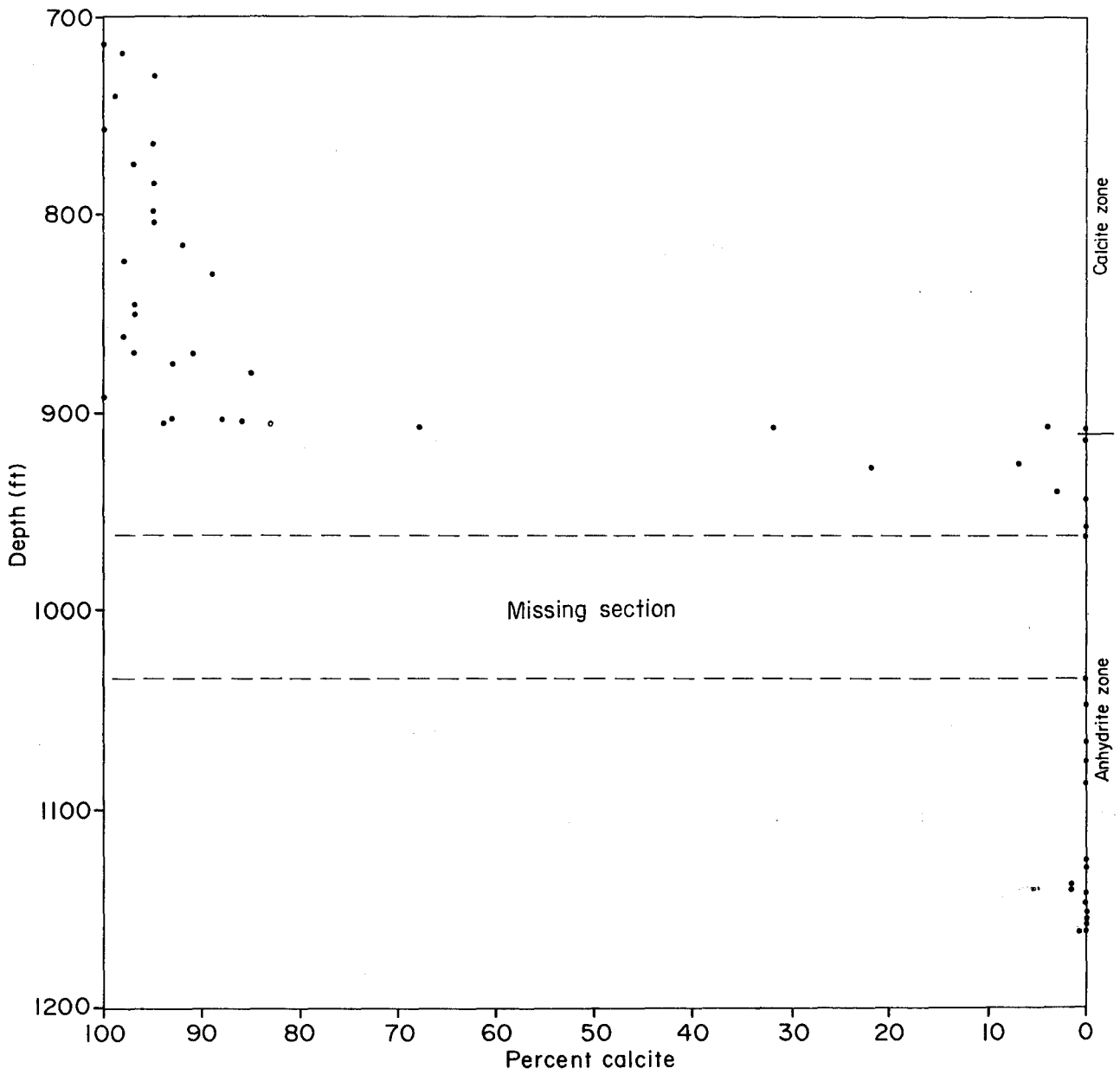
Figure 100. Percentage of calcite versus depth in Oakwood cap rock, East Texas. Below 905 ft (276 m) the cap rock consists of anhydrite.

164

Figure 101. Percentage of porosity versus depth in Oakwood cap rock, East Texas.
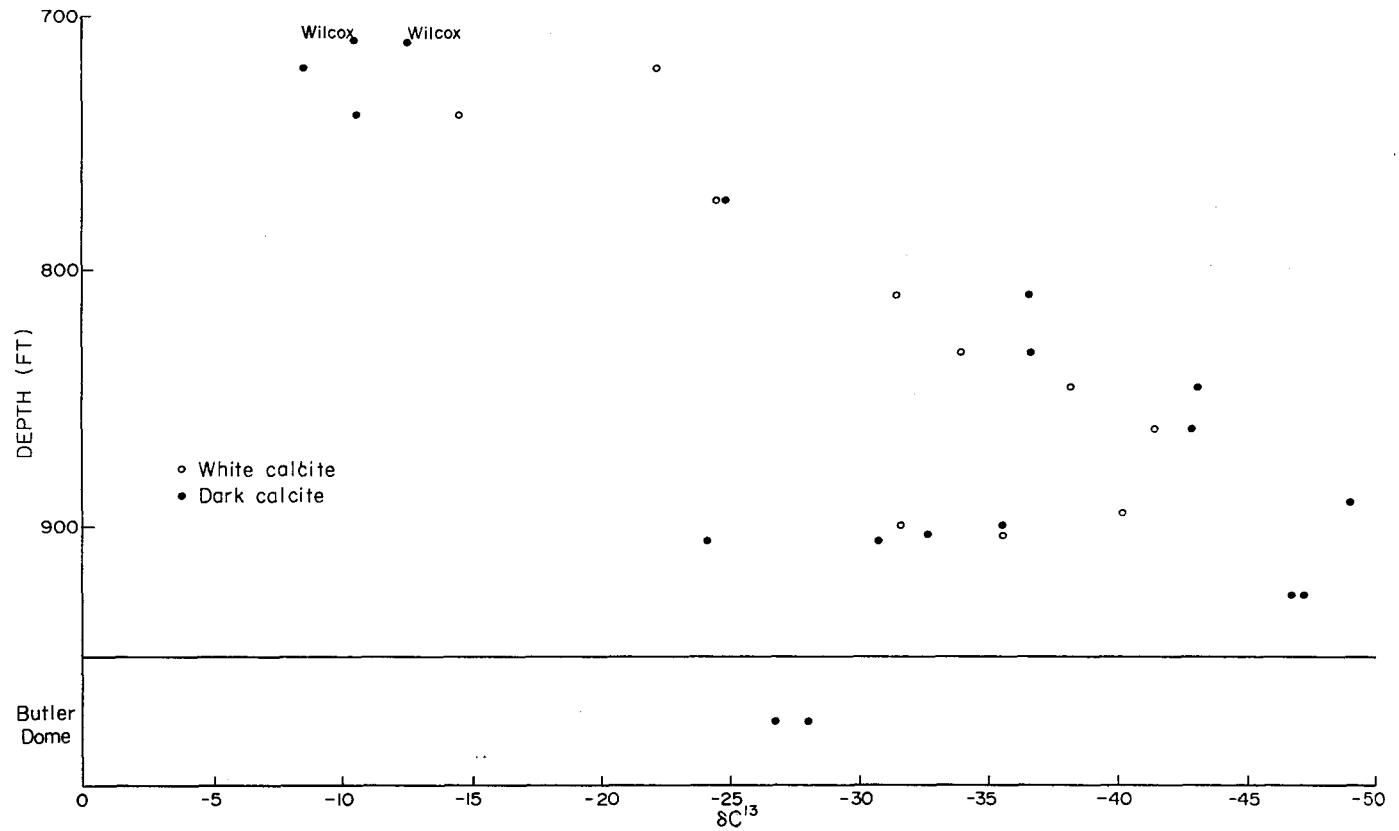
165

Figure 102. Values of δC^{13} versus depth in calcite zone of Oakwood cap rock, East Texas. Samples of false cap rock from Butler Dome and calcite-cemented Wilcox sandstone are shown for comparison.

GEOCHEMISTRY OF GROUND WATER AND CAP ROCK FROM GYP HILL SALT DOME, SOUTH TEXAS

Charles W. Kreitler, Shirley P. Dutton, and Graham E. Fogg

Saline water in the shallow gypsum cap rock at Gyp Hill Salt Dome results from a phase change from anhydrite to gypsum and subsequent expulsion of trace elements from the gypsum crystals rather than diffusion of the trace elements from the salt through the impermeable anhydrite zone. This conclusion is important in judging the adequacy of impermeable cap rock to isolate radionuclides.

Shallow ground water in the gypsum zone of the gypsum-anhydrite cap rock at Gyp Hill, Brooks County (fig. 103; table 13), is saline, even though the salt/cap-rock interface is at least 700 ft (210 m) below these waters. The origin of this shallow saline water is important because of its implications to the hydrologic integrity of salt-dome cap rock. Manheim and Bischoff (1969) identified a chloride halo in the slope deposits in the Gulf of Mexico, overlying a shallow salt diapir. They attributed this anomalous chlorinity to ionic diffusion from the diapir. If a similar mechanism is operating between the salt and the overlying cap rock of salt domes in the Gulf Coast Interior Basin, this mechanism would provide a pathway for radionuclides to migrate from a salt repository to the biosphere.

Hydraulic-head data gathered at Gyp Hill during coring of the cap rock indicate decreasing hydraulic potentials with depth and, therefore, a downward direction of ground-water flow. Consequently, advection should not carry saline waters from the salt dome into the shallow cap rock.

Ionic diffusion is another mechanism by which trace elements can be transported through the cap rock. To test this hypothesis, samples of the cap rock were analyzed to determine if concentration gradients for trace elements decrease away from the salt, which would imply diffusion. Strontium, sodium, magnesium, and chloride do not show a linear decrease in concentration through the caprock, but do show a sharp decrease in the transition zone between anhydrite and gypsum (fig. 104). Recrystallization during the phase change from anhydrite to gypsum apparently has purged trace elements from the anhydrite. For example, in the anhydrite zone, Sr concentrations are approximately 900 μg/g, whereas in the gypsum zone, Sr concentrations are approximately 400 μg/g. Because of the phase change from anhydrite to gypsum, 50 percent of the Sr has been released. Strontium concentrations in gypsum and

167

anhydrite are within ranges observed for these two minerals in marine evaporites (Butler, 1973, table 4). Butler found that anhydrite can incorporate twice as much Sr as can gypsum, and he calculated a partition coefficient* of approximately 0.4 for anhydrite and approximately 0.2 for gypsum. Similar partitioning also appears to exist for other trace elements found in $CaSO_4$ minerals (fig. 104, a through d), but no data are available to quantify partition coefficients. The trace elements purged from gypsum would migrate into the ground water. This mechanism may explain the presence of saline water at shallow depths in the Gyp Hill cap rock.

Linear decreases in ionic concentrations from the bottom to the top of the cap rock were not observed, and therefore, diffusion is not considered to be an important mechanism.

The general occurrence of celestite in cap rock probably results from expulsion of Sr from $CaSO_4$ minerals. Excessive Sr oversaturates the ground water with respect to celestite and results in precipitation of celestite.

The saline water found in the shallow cap rock of Gyp Hill salt dome appears to result from the expulsion of trace elements during the hydration of anhydrite to gypsum rather than from ionic diffusion. Impermeable cap rock appears to be an effective barrier to radionuclide migration by diffusion.

---

*Partition coefficient = $\dfrac{\dfrac{\text{concentration trace element in solid}}{\text{concentration major element in solid}}}{\dfrac{\text{concentration trace element in solution}}{\text{concentration major element in solution}}}$

Table 13. Results of water chemistry analyses from shallow water wells located in gypsum zone, Gyp Hill cap rock, Brooks County, Texas.

			Chemistry (mg/L)														Comments
Well no.	Well depth (m)	Sample date	Na	K	Ca	Mg	Cl	SO_4	F	HCO_3	SiO_2	Mn	Fe	Sr	Br	I	
78-25	48	1/26/79	1,351	44.0	791	47.4	2,233	2,130	1.2	176	34.3	0.7	0.18	3.86	10.5	0.25	Pump test started
78-25	48	1/28/79	1,419	46.1	817	59.9	2,570	2,190	1.6	63	47.5	0.88	0.20	4.18	20.0	0.25	1/25/79
78-25	48	1/29/79	1,426	45.8	817	60.5	2,640	2,170	1.7	66.2	49.8	0.91	0.19	4.18	21.5	0.25	
78-18	43	2/16/79	5,518	143	1204	99.4	8,690	2,880	1.2	207	28.5	0.37	0.50	9.8	77	2.0	Pump test started
78-18	43	2/17/79	5,363	144	1206	104	8,640	2,987	1.1	175	28.0	0.34	0.53	10.0	67	0.5	2/15/79
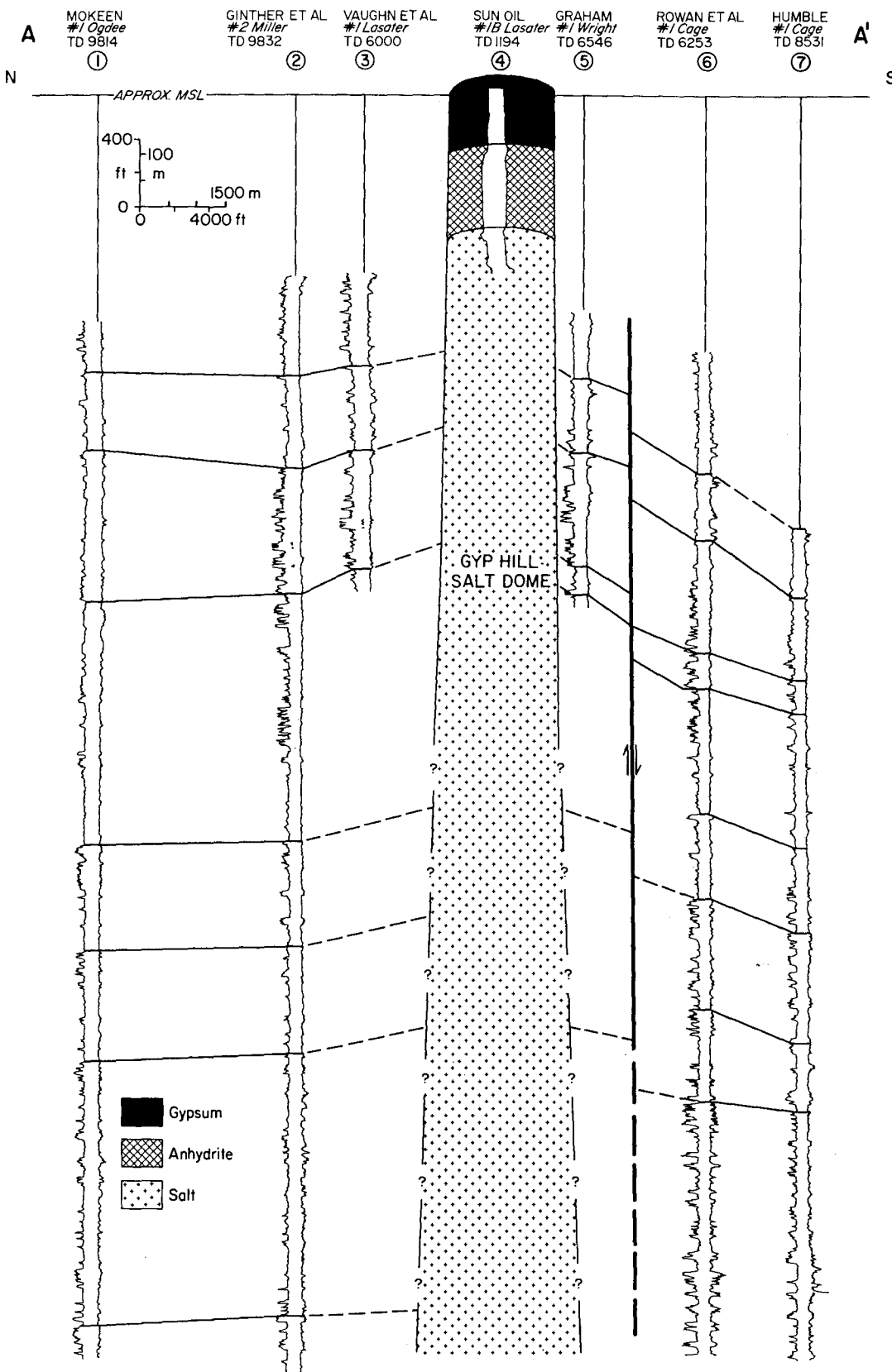
Figure 103. Cross section of Gyp Hill Salt Dome, East Texas Basin. Note gypsum and anhydrite zones of cap rock.
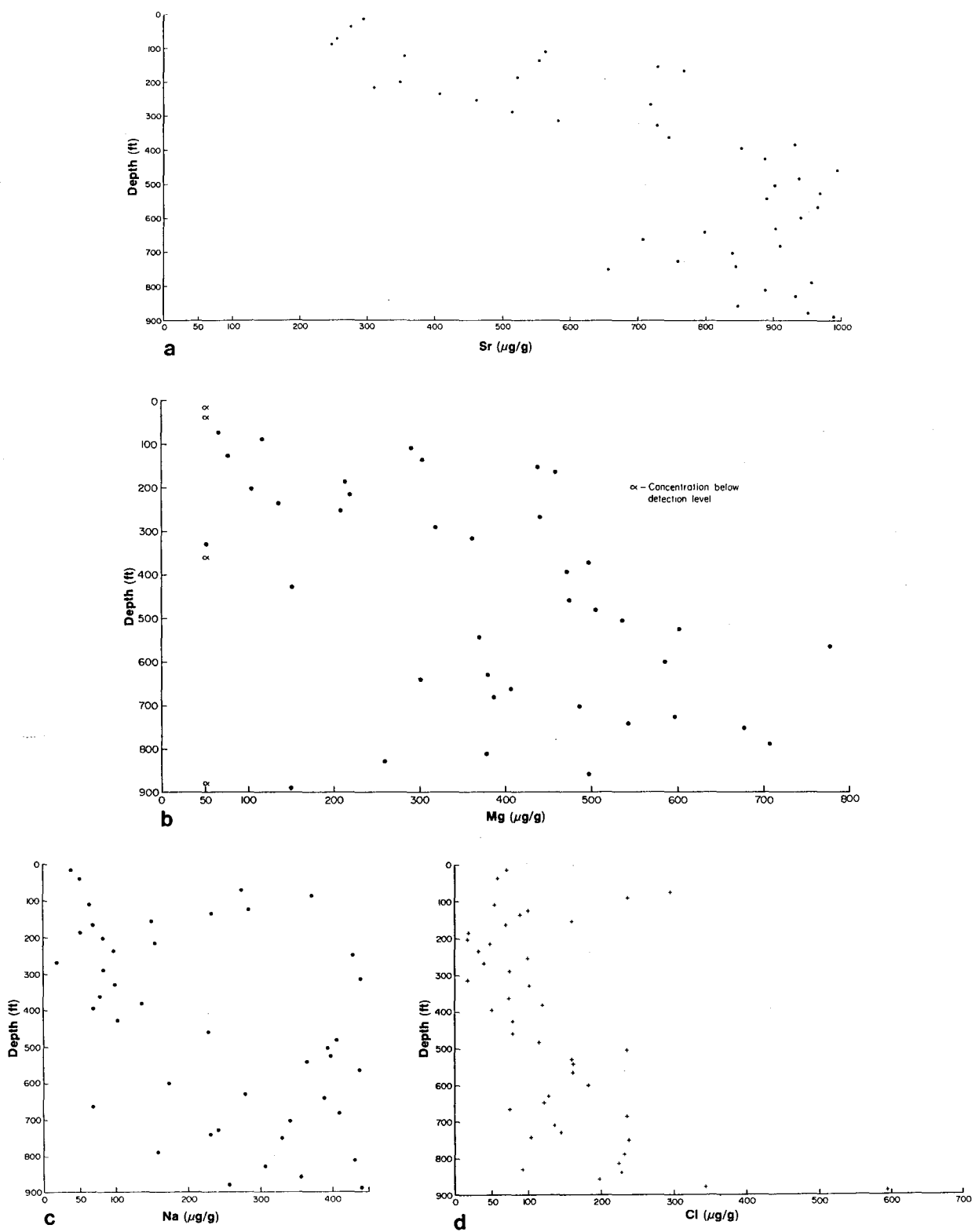
170

Figure 104. Results of chemical analyses of trace elements, (a) Sr, (b) Mg, (c) Na, and (d) Cl, in anhydrite and gypsum of Gyp Hill cap rock, Brooks County, Texas. Transition from anhydrite to gypsum occurs at a depth between 400 to 500 ft (125 to 150 m). Note lower concentrations of trace elements in gypsum relative to anhydrite.

171

LITHOLOGY OF THE OAKWOOD SALT CORE

Owen R. Dix and M. P. A. Jackson

Salt core from Oakwood Dome is greater than 98 percent pure, and displays evidence of two distinct periods of recrystallization. Deformation and recrystallization during diapir growth produced a penetrative schistosity. Later recrystallization of the upper 2 m of salt in the presence of ground water under conditions of low differential stress has produced a granoblastic fabric.

Fifty-seven meters of rock salt were cored from immediately below the Oakwood Dome cap rock: the lower 55 m is characterized by a strong penetrative schistosity; in the upper 2 m the schistosity is replaced by an unfoliated granoblastic texture.

The foliated rock salt consists of zones of pure halite (less than 1 percent anhydrite) 2 to 600 cm thick, which alternate with disseminated anhydrite (5 to 15 percent) layers 1 to 10 cm thick. Anhydrite-rich layering (greater than 40 percent anhydrite) is present in one part of the core. It comprises a 90-cm thick zone of microfolded and boudinaged anhydrite layers 2 cm to 10 cm thick surrounded by pure halite (fig. 105). Results of analysis of 38 samples taken at intervals of approximately 1.5 m indicate that the mean anhydrite content for the entire section of salt core (57 m) is 1.3 ± 0.7 percent at the $2\,\sigma$ level of confidence.

Halite crystals are disc-like, ranging in size from 7 by 15 mm (in the XZ and YZ principal planes of strain) in zones containing disseminated anhydrite, to greater than 10 by 30 mm in zones of pure halite (fig. 106). This difference in halite grain size between pure rock salt and anhydrite-bearing rock salt could be primary, but is more likely to have resulted from the immobilization of halite grain boundaries by anhydrite grains that prevented significant grain growth during secondary recrystallization at depth. Anhydrite forms prismatic crystals with a mean grain size of about 0.5 mm. The grains are generally scattered through the halite crystals as poikiloblastic inclusions, but in places are concentrated along halite grain boundaries. In contradistinction to halite, preferred orientation of anhydrite is not prominent except in the anhydrite-rich layers; here the mineral is generally subidioblastic and moderate to strong parallelism of the long axes define a schistosity that has been deformed by microfolding.

172

The contact between the foliated and unfoliated rock salt is parallel to the foliation and has a dip of 20°. The transition 2 m below the cap rock is defined by an abrupt change in fabric from schistose to granoblastic halite over a distance of about 2 cm. Halite in the unfoliated section is generally equant with little or no evidence of an anisotropic fabric. The unfoliated rock salt comprises two distinct zones: the lower 140 cm consists of medium-grained granoblastic halite with a mean grain size of 5 mm to 10 mm; the upper 60 cm consists of coarse-grained granoblastic halite with a maximum diameter of 50 mm. The presence of a microscale transposed anhydrite-bearing layer in the medium-grained unfoliated rock salt (fig. 107) indicates (1) that a strong foliation had previously existed before recrystallization of the halite under stable conditions of low differential stress and (2) that recrystallization was a solid-state, in-place process that did not involve dissolution and reprecipitation. The presence of disseminated anhydrite layers in the coarse-grained interval indicates that the large size of halite in this rock salt is due to more-advanced recrystallization of the medium-grained halite rather than to precipitation from solution.

The contact between cap rock and the coarse-grained granoblastic rock salt is sharp and has no cavity (fig. 108). Horizontal laminae in the cap rock have been truncated, suggesting that brines at the contact locally eroded or dissolved anhydrite at some earlier stage. Vertical extension fractures in the cap rock have been filled by halite. The presence of an anhydrite-rich layer across the fracture openings at the cap-rock contact indicates that anhydrite may have accreted on the base of the cap rock after fracturing and dilation.

Intracrystalline brine inclusions in cuboid negative crystals and as fillets (bridges connecting anhydrite crystals) are abundant within halite of the coarse-grained granoblastic zone, but have not been identified lower in the rock salt. The cuboid inclusions range in size from less than 0.02 mm to more than 1.0 mm. The upper 25 cm of rock salt contain a mean of 20 cuboid inclusions per cm^3, whereas the lower 35 cm contain only 2 per cm^3. All but some of the smallest inclusions contain a gas bubble, which underwent an eightfold average increase in volume on breaching of the inclusions by experimental dissolution at room temperature. Roedder and Belkin (1979) attributed this expansion to the presence of pressurized gas (probably CO_2 or CH_4) within the bubbles.

Halite within 2 m of the cap-rock contact has recrystallized largely in place, probably in the presence of intercrystalline brine that migrated downward from the contact. The lack of a strong fabric in the uppermost rock salt suggests that uplift of

173

rock salt relative to cap rock in this part of the diapir has been minimal since recrystallization. Rock salt is not being dissolved at this location, as evidenced by the absence of a cavity at the rock-salt/cap-rock contact. Intracrystalline brine inclusions have not been identified within the foliated rock salt. Even where these inclusions are abundant, directly below the cap-rock contact, for instance, modal analysis indicates that the total amount of fluid present is very small (about 0.05 percent).

This study indicates that although brines were undoubtedly present just below the cap rock during recrystallization of the rock salt, these brines could have been concentrated from former sites along grain boundaries of foliated rock salt or introduced from outside the salt stock, probably along the cap-rock contact. Only minute amounts of brine have been trapped, but the presence of truncation features suggestive of erosion indicates that fluids may have formerly been more abundant. The tight seal of the contact and low strains in the rock salt immediately below indicate that where intersected by the borehole Oakwood Dome is now structurally and hydrologically stable. However, textural relations in the contact zone suggest that dissolution, recrystallization, and cavity formation are cyclic.
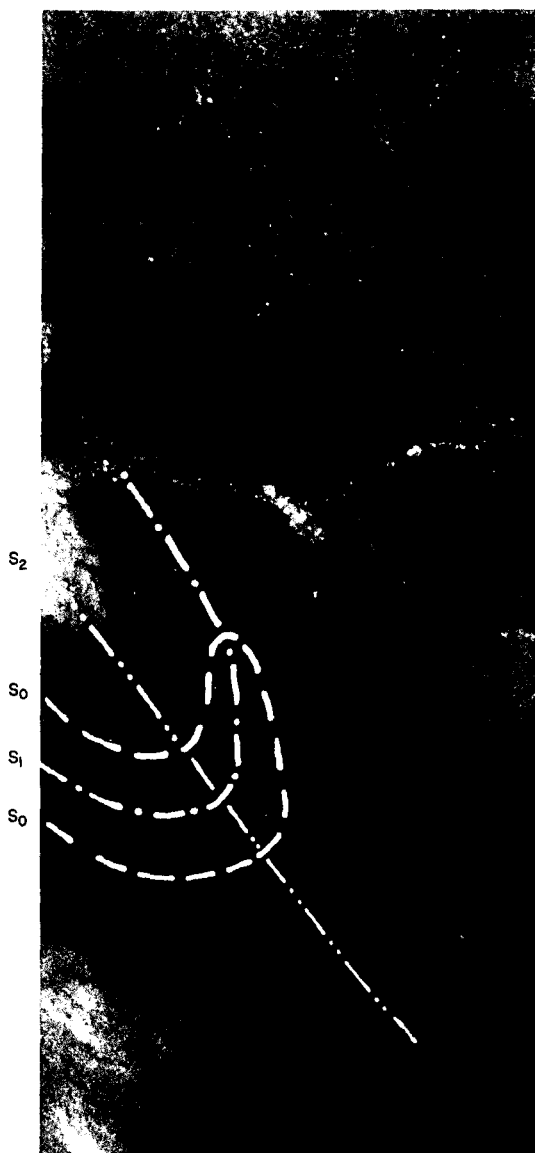
Figure 105. Refolding of anhydrite-rich layering in foliated rock salt, Oakwood Dome, East Texas. "S_0" represents layering; "S_1" represents axial plane of early fold; "S_2" represents axial-plane schistosity formed by later deformation. Slabbed core, transmitted and reflected light, depth 387.1 m.

Figure 106. Schistosity (S_2) dipping to left in foliated salt, Oakwood Dome, East Texas. Coarser salt at right is pure; finer grained salt on left contains disseminated anhydrite. Thick section, transmitted light, depth 374.6 m.
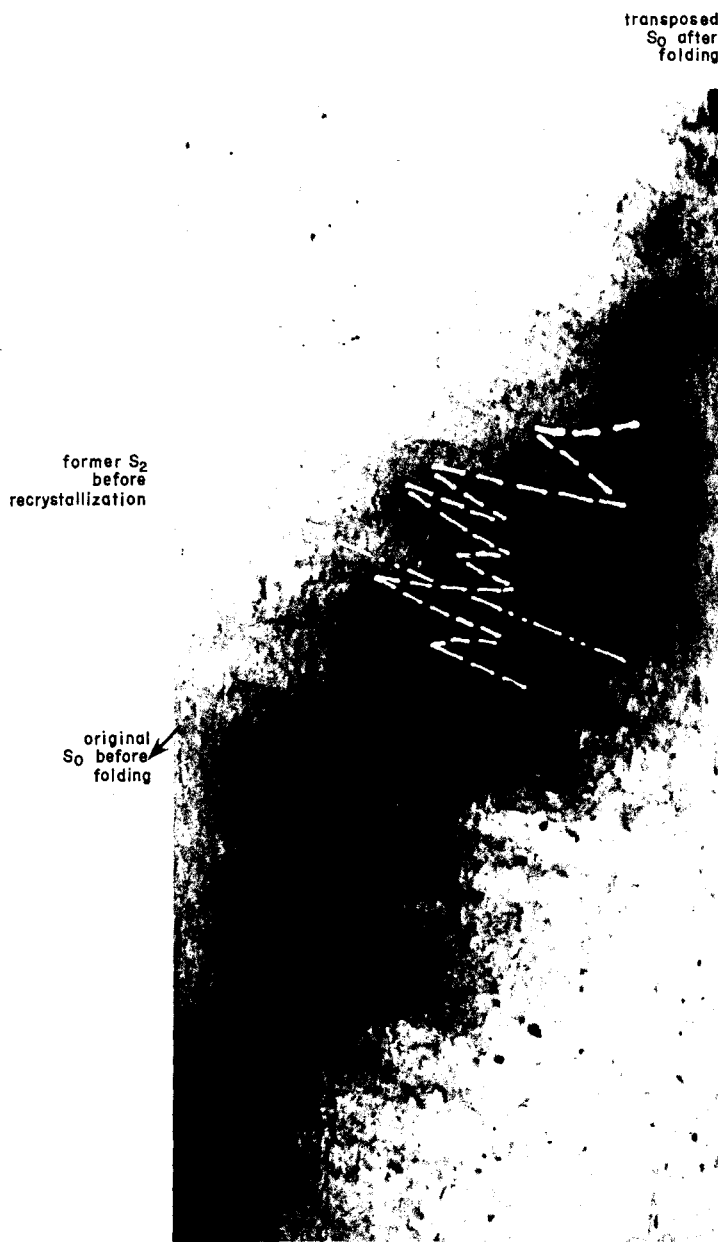
Figure 107. Transposed anhydrite-bearing layer in recrystallized, unfoliated rock salt, Oakwood Dome, East Texas. Unslabbed core, transmitted light, depth 347.5 m.
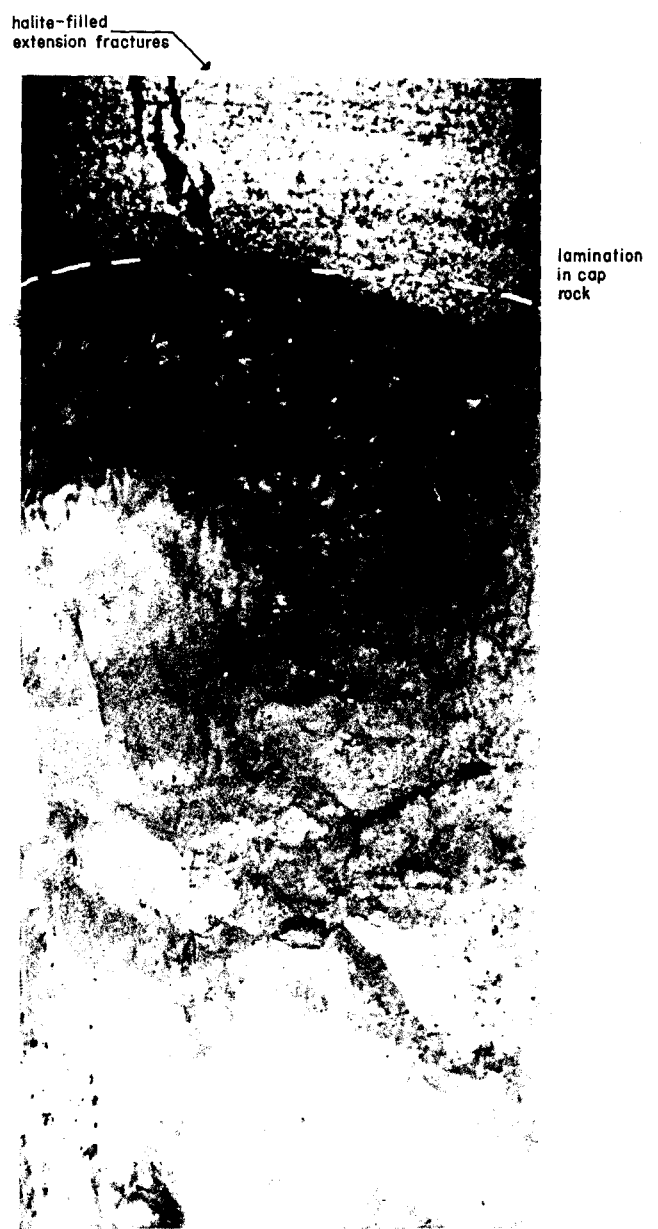
Figure 108. Contact between unfoliated rock salt and cap rock, Oakwood Dome, East Texas. Dark appearance of halite at the contact is produced by internal reflection. Laminae in cap rock have been truncated at the contact and replaced by recrystallized halite. Unslabbed core, transmitted and reflected light, depth 345.0 m.

176

GEOMETRIC ANALYSIS OF MACROSCOPIC STRUCTURES IN OAKWOOD SALT CORE

M. P. A. Jackson and Owen R. Dix

Analysis of the orientation of anhydrite layering and schistosity in the Oakwood core suggests that the core has penetrated the hinge zone and lower part of a large inclined overthrust antiform representing one of the highest and youngest of a series of salt tongues that fed the spreading diapir cap. The fold geometry also suggests that tens or hundreds of meters of overlying salt have been truncated from the top of the diapir, most probably by ground-water dissolution.

Geometric synthesis of mesoscopic structures in the Oakwood salt core is necessary to determine the form and orientation of the macroscopic structures intersected by the vertical drill core. Nongraded layering, defined by disseminated anhydrite inclusions in poikiloblastic halite grains, and a tectonite fabric constitute the basic structural elements. The fabric has a strong planar component in the form of a schistosity defined by the preferred orientation of disc-like halite grains within planes; it also has a weak linear component in the form of a mineral lineation defined by the preferred orientation of the major axes of halite grains within the plane of schistosity.

The orientation of layering and schistosity down the length of salt core is shown in figure 109. The borehole is vertical to within $2°$ throughout its length, but the core itself is nonoriented. However, the dip of the schistosity is remarkably consistent, with an average of $35°$. It is conceivable that the direction of dip could vary while the dip remains constant, but the resulting helical pattern of the foliation would be most unlikely. Thus, the direction of dip of the schistosity can be assumed to be constant, and the dip of the layering, which is highly variable, is measured relative to this. The structures have been extrapolated to zones adjacent to the core by assuming similar-type shear folding (Ramsay, 1967) as recorded by Balk (1949, 1953), Muehlberger (1959), and Kupfer (1968) in other Gulf Coast salt domes. The schistosity is axial planar to a series of late major folds that jointly define the lower part of a large inclined anticlinorium. The late major folds refold early minor isoclines, which are transected by the fabric.

Two important inferences may be drawn from the geometry described above. First, the core has penetrated only the lower part of a large fold, now directly overlain by cap rock. The upper part of this structure must therefore have been removed after

its formation, most likely by ground-water dissolution. The degree of truncation can be inferred by estimating the form of the original anticlinorium (fig. 110). A high degree of discordance between layering in rock salt and the cap-rock contact has also been reported from Tatum Dome in Mississippi (Eargle, 1962a), and Rayburn's and Vacherie Domes in Louisiana (Nance and Wilcox, 1979; Nance and others, 1979). This suggests that structural evidence for truncation of diapiric crests may be more common than previously thought.

A second inference is that of the flow pattern of salt during diapiric emplacement. Figure 111 illustrates a simple model for salt flow within a diapir cap of similar shape to Oakwood, in which salt spreads centrifugally as a single circular lobe. This geometry has been modeled experimentally (for example, Ramberg, 1973; Dixon, 1975) but fails to account for the opposed dip of the layering and schistosity in the centrally situated Oakwood core. Figure 112 shows a more complex and realistic model of multiple emplacement of salt tongues (compare Lotze, 1957; Muehlberger, 1959; Kupfer, 1968). The tongues emerge from the stem of the diapir as vertically plunging folds and become progressively refolded by lateral flow to form recumbent overthrust folds. The geometry of the Oakwood salt core suggests that it passed through the hinge zone of one of the younger, higher overthrust anticlinoria within the dome.

The present study demonstrates that it is possible to delineate the form of major structures in salt stocks on the basis of a single core, despite the absence of stratigraphic criteria. The form of these folds provides evidence for inhomogeneous flow of rock salt. In view of this, similar studies will be required for a thorough understanding of the internal structure of any salt stock considered for disposal of nuclear wastes.
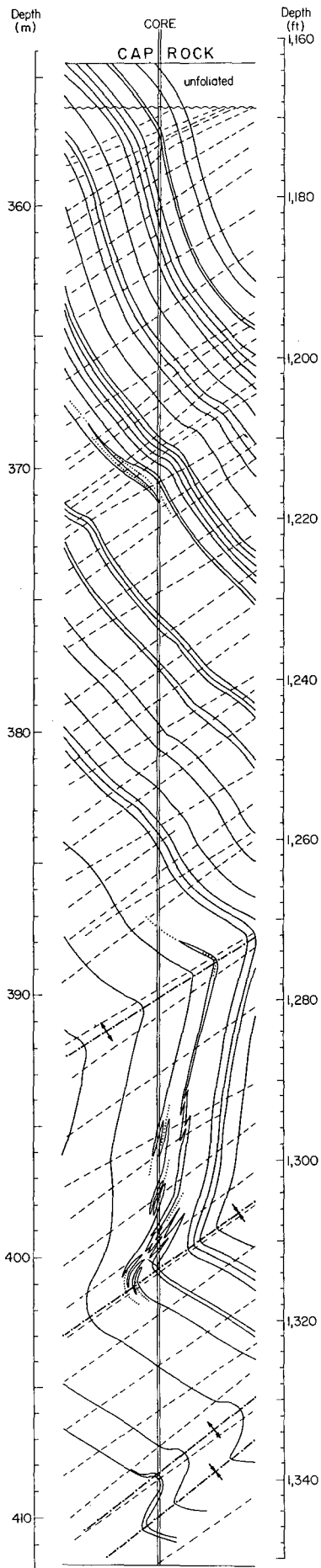
Figure 109. Structural section along vertical halite core, Oakwood Dome, East Texas. On the basis of measurements of orientation of layering and schistosity, the section was constructed to scale by projecting the layering orientations outward from the core along cleavage traces, which represent directions of maximum orientation stability. Arrows indicate synforms and antiforms.

179
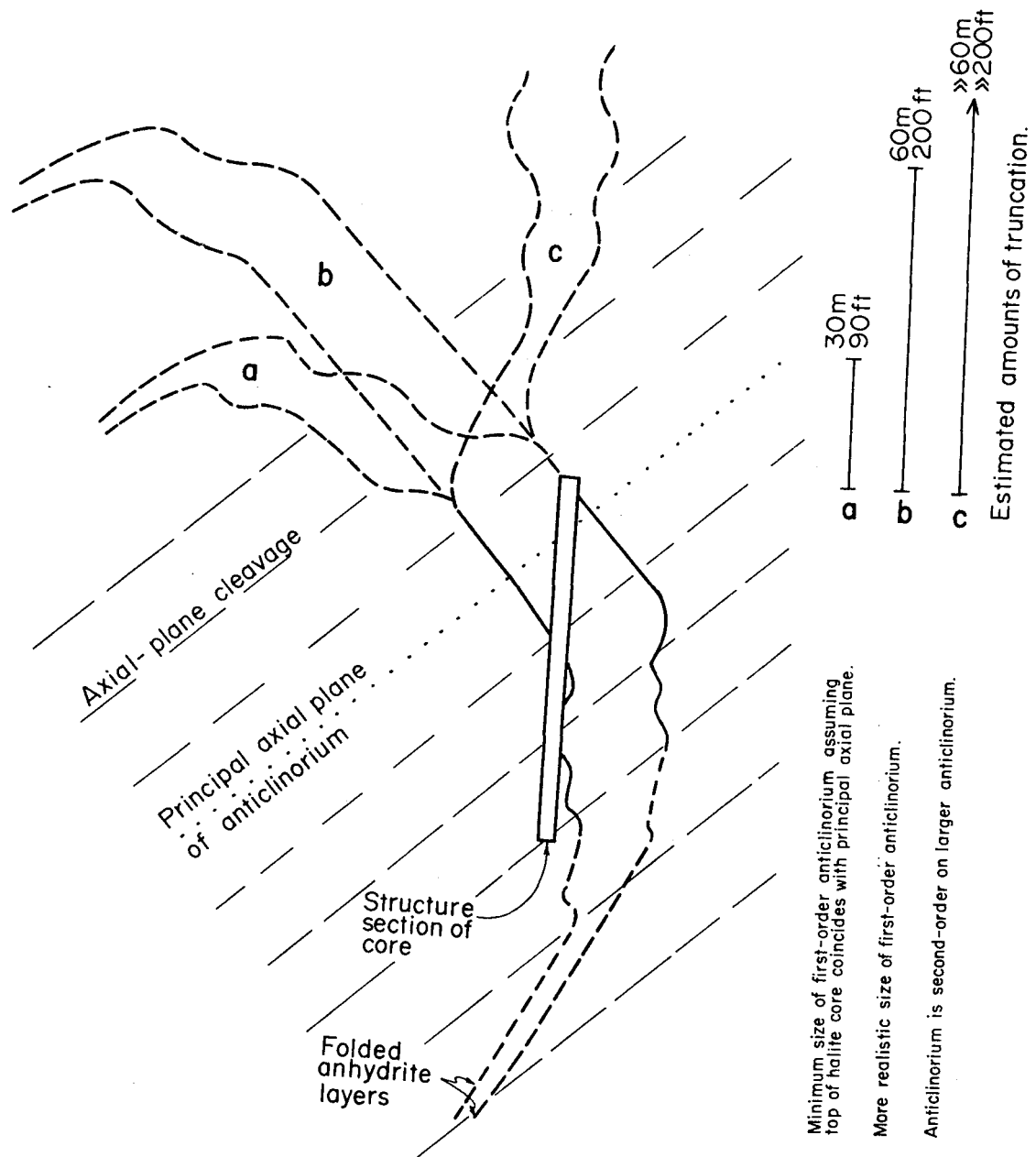
Figure 110. Position of salt core and geometric relations within the inferred anticlinorium, Oakwood Dome, East Texas.
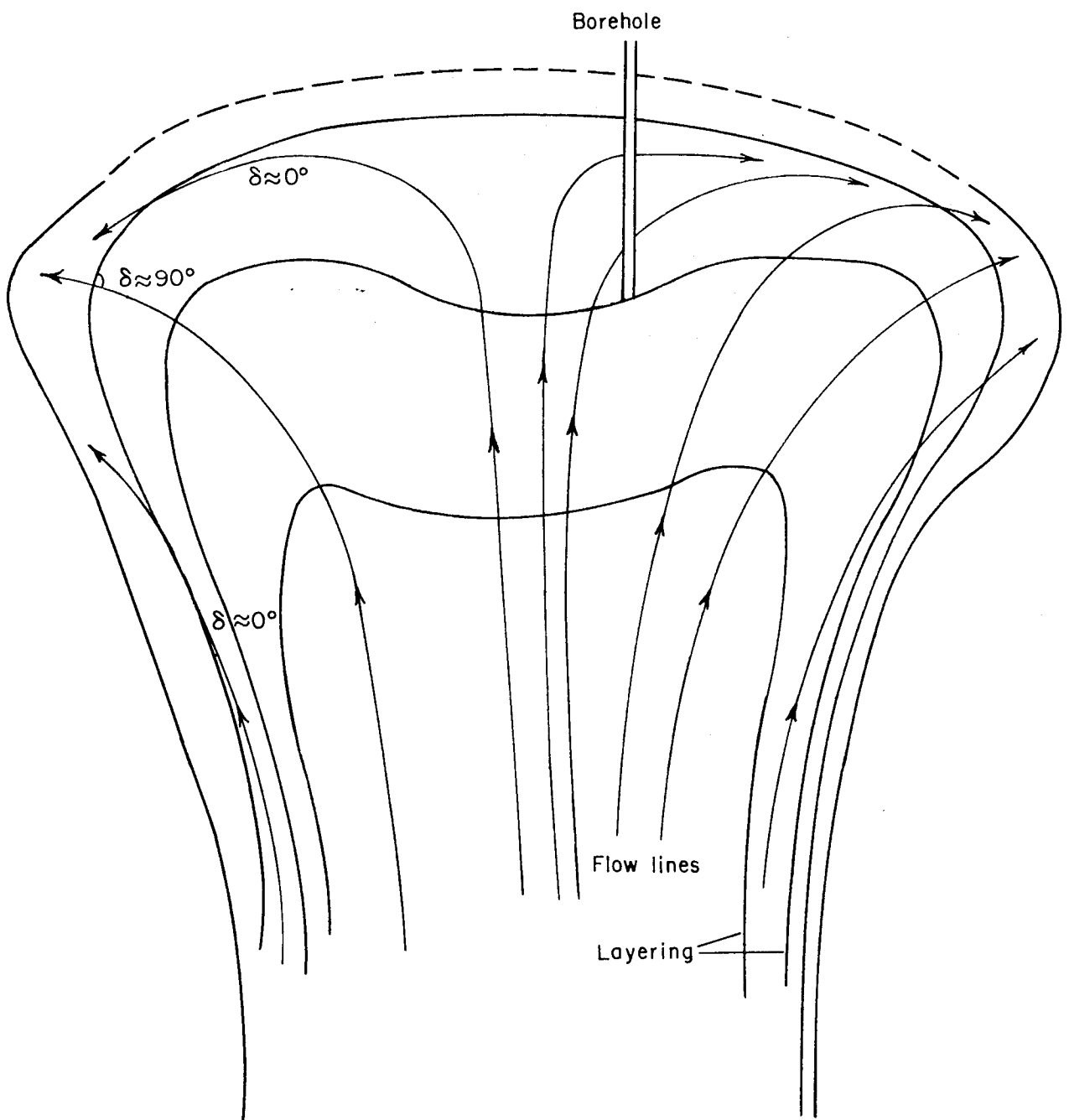
Figure 111. Flow patterns within a single lobe of centrifugally spreading salt, Oakwood Dome, East Texas. δ refers to dihedral angle between schistosity and layering.

181
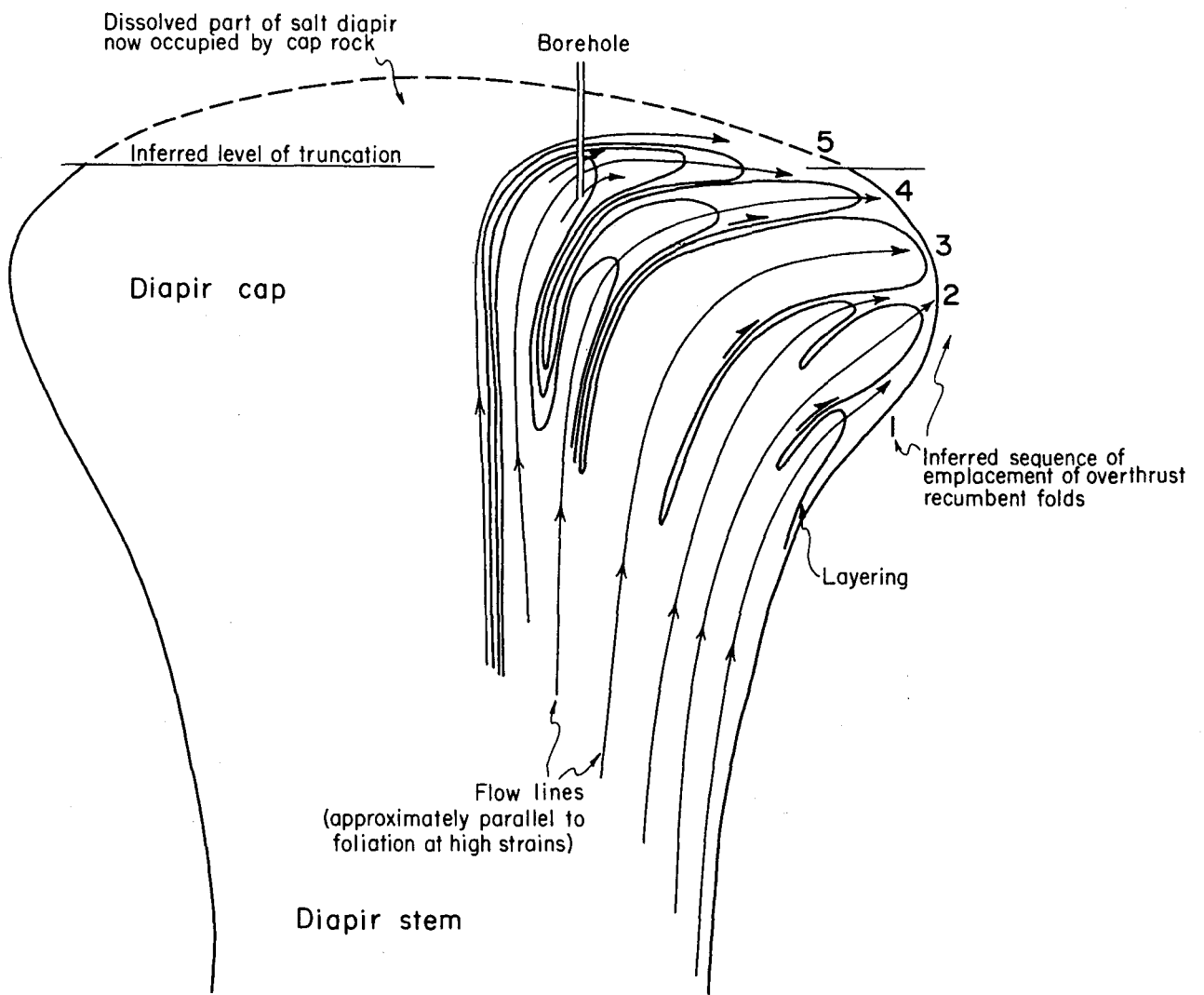
Figure 112. Inferred flow patterns within a laterally spreading, rising diapir fed by multiple emplacement of salt tongues as overthrust folds, Oakwood Dome, East Texas. Numbers refer to inferred sequence of emplacement of salt tongues.

STRAIN ANALYSIS OF HALITE IN THE OAKWOOD CORE

M. P. A. Jackson

Methods of strain analysis, developed for use on elliptical particles in random or preferred orientation before deformation, are used to analyze the internal structure of the Oakwood salt diapir by studying the present distribution of strain in halite and computing the nature of the initial fabric in the undeformed state.

Strain analysis, or the determination of the magnitude, orientation, or type of strains in a given sample, has progressed so that virtually any rock, including ice, may be investigated. Petrofabric studies, which represent a microscopic approach to geometric analysis, have been carried out on halite (for example, Balk, 1949; Schwerdtner, 1967; Muehlberger and Clabaugh, 1968), but these studies did not attempt to quantify strains. This study is designed to determine the strains at selected points along a vertical core drilled in the center of the Oakwood Salt Dome, to evaluate the nature of the initial fabric before deformation, to predict possible future flow paths for the salt, and to confirm or refine estimates of the degree of diapir truncation indicated by geometric analysis.

Results of critical examination of unstrained natural fabrics in sedimentary rocks have stressed that not only are spheroidal or near-spheroidal clasts extremely rare (even in oolitic limestones), but that most fabrics are slightly anisotropic even before deformation. This anisotropy commonly takes the form of linear or planar preferred orientation caused by depositional currents or compaction. Strain analysis of deformed sedimentary rocks must therefore deal with initially elliptical particles with variable initial axial ratios and orientations (fig. 113). After homogeneous strain each particle takes up a new shape and orientation depending on its initial shape and orientation (fig. 114); some clasts, such as the "pre-circle broad" category, became more rounded with increasing strain, whereas others, such as the "narrow" category, become more elliptical. The fluctuation, or range of ϕ angles (fig. 114), invariably decreases with increasing strain, a characteristic made use of by some methods of strain analysis.

During its transformation from flat-lying beds to the crest of a mature diapir like Oakwood, the salt passes through two main deformation phases. First, strong constriction involving centripetal lateral shortening and vertical extension characterizes diapiric necks (Balk, 1949, 1953; Dixon, 1975). Second, flattening by progressive

183

simple shear is superimposed on these fabrics as the salt reaches the upper levels of the diapir and spreads laterally (Dixon, 1975). The total strain recorded in the rock depends on its position in the diapir, the degree of maturity of the diapir, and the gross internal structure of the diapir.

Of the methods of strain analysis listed in table 14, three are routinely used in this project: the harmonic mean, the shape factor grid, and the theta-curve method; the method of random-point distributions is used occasionally to verify the other methods. Comparative examples of each of the four methods used are shown in figure 115 for principal sections showing the maximum (XZ plane) and minimum (XY plane) strains in a single specimen from the Oakwood salt core. Three mutually perpendicular sections, parallel to the XY, XZ, and YZ principal planes of strain, are cut for each specimen. The three planes are analyzed separately by the methods referred to above and the results integrated into a three-dimensional strain estimate, a procedure that also serves as an internal check for consistency.

On the basis of measurements of R_f and ϕ in 2,400 halite grains, strain has been analyzed at eight points along the core. The mean percentage shortening parallel to Z (the principal axis of shortening) decreases significantly from 50 (depth 408.1 m) to 39 (depth 359.0 m). The mean shortening further declines to 15 percent in the recrystallized upper 2 m of unfoliated rock salt (depth 355.4 m). This upward decrease in strain is compatible with petrographic observations of the core in an accompanying report (see "Lithology of the Oakwood Salt Core"). Mathematical and graphical unstraining of the fabrics suggests that before the deformation recorded in these rocks, their fabrics were isotropic. The present fabrics represent the finite result of repeated episodes of strain and recrystallization during diapirism; accordingly, estimates of the fabric in the original bedded rock salt would not be reliable. The $\underline{k}$ values ($\underline{k}=\ln\underline{a}/\ln\underline{b}$) of finite strain in the foliated rock salt vary from 0.1 to 0.5, which indicate the dominance of flattening over constriction; a similar strain state has been reported in experimentally modeled diapirs (Dixon, 1975; Schwerdtner and others, 1978). In the recrystallized rock salt just below the cap rock, the strain is completely oblate ($\underline{k}\approx0$), which suggests that some time after recrystallization this zone was subjected to weak uniaxial compression along a subvertical axis. The most likely agent for this compression is an upward force from the rising diapir, which may have contributed to the tight seal of the cap-rock contact where drilled. In-place stress measurements would be required to determine if this postulated force exists today.

184

Table 14. Some methods of strain analysis applied to elliptical particles.

Methods	Principles	Advantages	Disadvantages	References
Harmonic mean (H)	$$H = \dfrac{n}{\sum \frac{1}{R_f}}$$	Fast, simple, objective. Accurate to within 10% with $R_s > 2.5$. Accuracy increases at high strains and low fluctuation. Measurements of ϕ not required.	Valid only for isotropic initial fabrics. Greatly overestimates R_s in cases of low R_s or high R_i.	Lisle (1977b) Lisle (1979)
Shape factor grid	Polar graph of 2ϕ against $\frac{1}{2} \log_e R_f$. Qualitative identification of initial fabric from Mellis contoured pattern on graph. Strain estimate based on identification of initial circle point (ICP).	Suitable for isotropic, bedding-parallel, or imbricate initial fabrics. Does not require bedding or cleavage trace.	Serious errors result from misidentification of initial fabric. Less accurate at high R_s and low ϕ.	Elliott (1970) Boulter (1976)
Theta curve (θ)	Rectangular graph of ϕ against $\log R_f$ compared with sets of θ curves, which are loci of equal initial orientation, for different R_s values. Set resulting in most uniform distribution is taken as actual R_s. Computerized method provides unstraining facilities, χ^2 tests for goodness of fit.	Objective. Can test data for anisotropy in initial fabrics. Checks for ductility contrast or pressure solution. Does not require bedding or cleavage trace.	Valid only for isotropic initial fabrics. Less accurate at high R_s and low ϕ.	Lisle (1977a) Peach and Lisle (1979)
R_f/ϕ	Rectangular graph of ϕ against $\log_{10} R_f$ compared with sets of R_f/ϕ curves and "50% of data" curves. Computerized methods check symmetry.	Enables R_s estimates to be made from initially anisotropic fabrics in some cases. Valid for non-coaxial strain.	Later versions designed for some anistropic initial fabrics, but not necessarily valid. Matching of R_f/ϕ curves is subjective. Data are not used to test method. Less accurate at high R_s and low ϕ. Most versions require bedding or cleavage trace.	Ramsay (1967) Dunnett (1969) Dunnett and Siddans (1971) Roberts and Siddans (1971) Le Theoff (1979) De Paor (1980) Siddans (1980)
Random-point distributions	Produces "all-object-separations" plot corresponding to strain ellipse. Computerized or entirely graphical methods available.	Records total strain in rock. Method unaffected by pressure solution. Does not require bedding or cleavage trace.	Not suitable for Poisson, or truly random, initial distributions. Valid only for isotropic initial distributions.	Fry (1979) Hanna and Fry (1979)

185
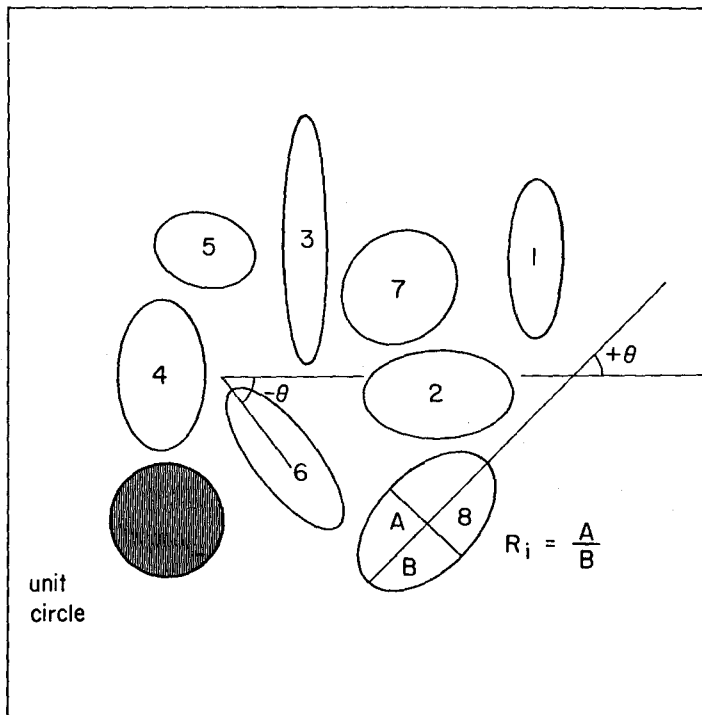
Figure 113. Unstrained elliptical particles, having arbitrary numbers, and a unit circle, showing initial axial ratios (R_i) and θ angles.
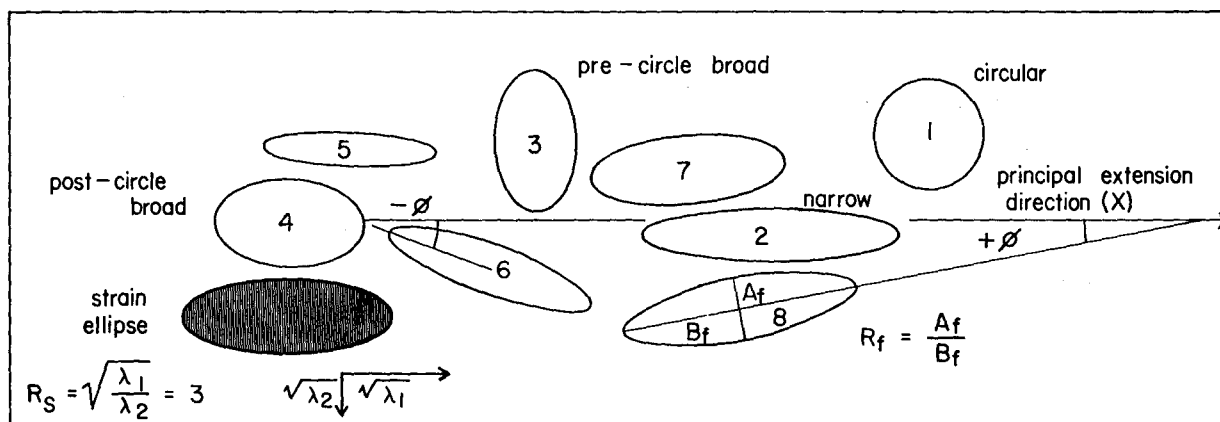
Figure 114. The particles of figure 113 after homogeneous strain illustrated by strain ellipse (R_s = 3), showing finite axial ratios (R_f) and modified ϕ_f angles. Most particles have become more elliptical and have rotated toward X direction, but particle 3 has become less elliptical, particle 1 has become circular, and particle 4 is little changed in shape (broad-narrow terminology from Elliott [1970]).

186
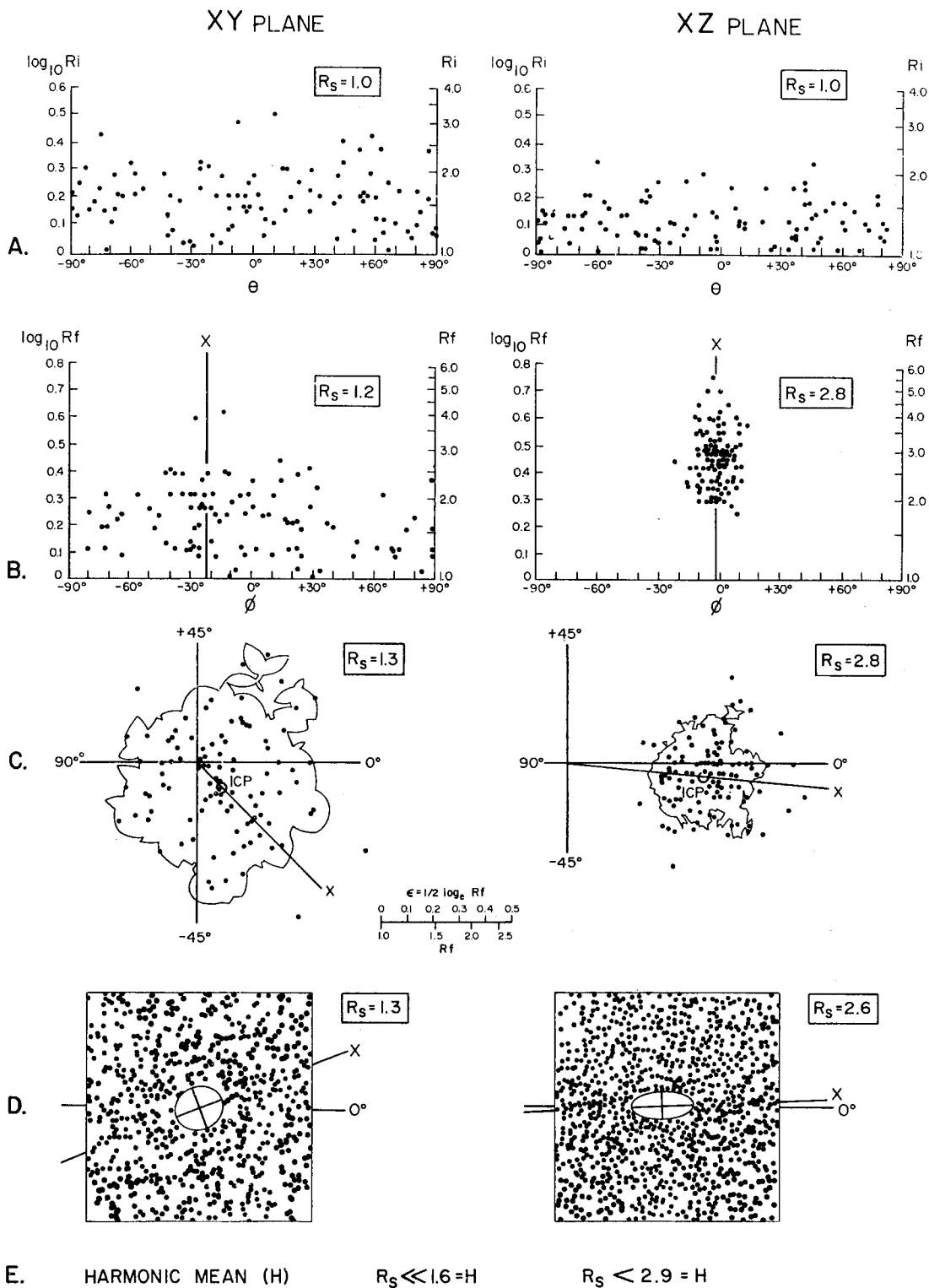
Figure 115. Comparative methods of strain analysis using perpendicular sections from the same specimen of rock salt in core from Oakwood Dome, East Texas, showing maximum strain (XZ plane) and minimum strain (XY plane). (A) 100 mathematically unstrained grains on a θ-curve plot showing estimated initial fabric in salt before deformation. (B) 100 strained grains on a θ-curve plot. (C) 100 strained grains on the shape-factor grid. The ICP (initial circle point) lies on the X direction and defines the strain. (D) Random-point distributions defining ellipses representing whole-rock strain. (E) Harmonic means, which provide more-accurate estimates at higher strains than lower strains.

187

GEOCHEMICAL ANALYSES OF SALT, GRAND SALINE DOME, EAST TEXAS

Charles W. Kreitler and William R. Muehlberger*

Salt in the Kleer Mine, Grand Saline Dome, varies from an anhydrite-rich halite near the center of the dome to a potassium-magnesium-rich halite on the margin of the dome. These variations may represent original geochemical evaporite facies.

The use of dome salt for the long-term storage of nuclear waste requires a better understanding of the salt chemistry and the possible chemical variations to be expected in a salt dome. Most previous analyses of salt have been from vertical, continuous cores. However, these cores pass through a limited number of different salt beds because most banding (bedding?) in salt domes is nearly vertical (for example, Nance and Wilcox, 1979). A suite of salt samples from a horizontal traverse through the Kleer Mine, Grand Saline Dome, East Texas (fig. 116), was analyzed to determine geochemical variations and to ascertain if stratigraphic relationships observed by Muehlberger (1979) correlated with geochemical changes. The following observations were made.

Samples are predominantly halite, and the principal secondary mineral is anhydrite. Maximum anhydrite (25 percent) was measured in a black band known as "superblack"; minimum anhydrite concentration detected is 0.02 percent (table 15). Sylvite occurs in the mine nearest to the dome margin (fig. 116).

Anhydrite content decreases from the center to the margin of the dome. In mine workings nearest to the edge of the dome, K and Mg concentrations are high (the maximum K is 6.3 w%; the maximum Mg is 2,770 ppm) (fig. 117). The trace elements Sr and Mg are concentrated in the anhydrite and not in the halite matrix. A plot of $CaSO_4$ (w%) versus Sr (ppm) (fig. 118) displays a linear correlation; the Sr concentration coincides with the $CaSO_4$ concentration. The Sr appears to occur entirely in the anhydrite. A similar relation exists for concentrations of Mg versus $CaSO_4$ (fig. 119) except that the curve intercepts the $CaSO_4$ weight percent at 80 ppm of Mg. Therefore, magnesium is present in both the halite and the anhydrite.

In the potassium-rich samples from the edge of the dome, the concentration of Mg does not correlate with $CaSO_4$ weight percent. The Mg occurs either in the halite or in sylvite. The high K content results from the occurrence of sylvite as determined by X-ray analysis.

*Department of Geological Sciences, The University of Texas at Austin.

Because of the continuity of specific anhydrite beds (for example, "superblack" and "double black") and the ability to determine stratigraphic tops and bottoms on anhydrite-rich salt beds, Muehlberger (1979) has shown that a traverse from the inner part of the mine to the edge of the dome rises up the stratigraphic section from older to younger Louann evaporites (fig. 117). This stratigraphic relation correlates with geochemical data (table 15): (1) Toward the center of the dome, and therefore lower in the section, the salt is more $CaSO_4$-rich than higher in the section; and (2) at the highest position of the section, which is exposed in the Kleer Mine nearest to the dome edge, there are potassium-rich and magnesium-rich salts. This geochemical sequence suggests that more evaporitic conditions existed during precipitation of the younger salt. The potassium-rich salts may represent later (or last) salts to be deposited during Louann time.

Some interesting implications can be drawn if the stratigraphic and geochemical interpretations are correct. (1) Even after significant deformation by differential flowage in Grand Saline Dome (Muehlberger, 1968), the integrity of the original Louann evaporite facies has been maintained. The parlor-room model of pulling a napkin through a napkin ring and creating large vertical pleated folds (Kupfer, 1970) appears analogous to the structures observed in Grand Saline. If the analogy is expanded, even the upper surface of the "napkin" (the upper Louann) is in its proper position near the edge of the dome. (2) If potassium-rich salts represent the upper Louann, then there has been minimal solution of the flanks of the dome since its original emplacement as a diapir (probably during Late Jurassic or Early Cretaceous). The very soluble potassium salts still remain in the margin of the dome. If there had been significant dissolution of the dome, the potassium salts would not have remained on the dome flanks.

Table 15. Results of chemical analyses of salt, Kleer Mine, Grand Saline Salt Dome, East Texas.

Loc. No.	K (w%)	Ca (w%)	Mg (ppm)	Fe (ppm)	Mn (ppm)	Sr (ppm)	Br (w%)	I (ppm)	SO_4^{-2} (w%)	$CaSO_4$ (w%)	Comments
1	0.03	0.01	77.2	9.2	<2.5	5.0	0.023	2.9	0.02	0.02	
2	0.03	1.48	122.0	20.2	<2.5	50.0	0.025	3.3	3.24	4.60	Dark band
3	0.02	0.49	76.4	14.7	<2.5	20.0	0.023	4.3	0.97	1.37	
4	0.03	2.29	85.0	20.2	<2.5	75.0	0.032	2.2	4.80	6.81	Dark band
5	0.02	0.05	83.4	15.9	<2.5	7.5	0.013	0.7	0.06	0.86	
6	0.03	10.60	176.0	40.3	11.4	294.0	0.008	4.5	17.42	24.74	"Super black"
7	0.03	0.01	90.9	14.1	<2.5	5.0	0.024	4.9	0.006	0.009	
8	0.03	0.37	103.0	15.3	<2.5	15.0	0.026	2.0	0.79	1.12	
9	0.02	5.50	174.0	25.1	11.2	165.0	0.008	4.0	9.34	13.26	Dark band
11	0.03	5.65	145.0	14.7	5.0	175.0	0.009	1.6	16.51	23.45	Dark band
12	0.03	0.07	87.0	14.7	<2.5	5.0	0.002	4.4	0.06	0.09	
14	0.02	0.33	67.1	13.2	<2.5	15.0	0.006	1.4	0.76	1.07	
15	0.02	0.21	71.0	<0.5	<2.5	10.0	0.021	3.2	0.41	0.58	
16	0.03	0.92	101.0	15.9	2.9	35.0	0.002	2.0	2.07	2.95	Dark band
17	0.03	0.38	85.0	13.2	<2.5	15.0	0.002	1.6	0.73	1.03	
18	0.02	0.17	86.2	12.9	<2.5	15.0	0.012	1.6	0.22	0.31	
19	0.02	4.51	195.0	22.0	7.7	138.0	0.023	2.8	10.24	14.59	Double black
20	0.02	0.25	80.3	11.6	<2.5	10.0	0.018	6.9	0.37	0.50	
21	0.03	3.24	194.0	15.9	6.9	105.0	0.020	1.6	7.31	10.37	Double black
22	0.03	0.35	85.0	15.0	<2.5	15.0	0.025	5.6	0.67	0.95	
23	0.02	0.04	85.0	12.3	<2.5	5.0	0.021	0.6	0.004	0.00	
24	0.02	2.65	905.0	18.7	4.2	83.0	0.014	1.2	6.14	8.72	Double black
25	0.03	0.17	97.9	15.9	<2.5	7.5	0.028	4.0	0.23	0.33	
26	0.03	4.77	167.0	56.2	5.7	143.0	0.016	1.6	11.24	15.96	Double black
27	0.02	0.33	69.8	13.8	<2.5	15.0	0.024	2.7	0.90	1.28	

Table 15   (con.)

| Loc. No.	K (w%)	Ca (w%)	Mg (ppm)	Fe (ppm)	Mn (ppm)	Sr (ppm)	Br (w%)	I (ppm)	SO_4^{-2} (w%)	$CaSO_4$ (w%)	Comments
28	0.02	0.25	72.5	24.2	<2.5	10.0	0.009	5.2	0.33	0.47	
29	0.02	0.29	72.9	16.8	<2.5	10.0	0.015	0.3	0.53	0.76	
30	0.02	2.63	90.1	13.2	<2.5	85.0	0.023	2.4	6.05	8.59	Dark band
31	0.03	0.26	85.4	13.5	<2.5	10.0	0.018	0.6	0.37	0.52	
32	0.02	1.07	87.7	13.8	<2.5	40.0	0.014	1.1	2.11	3.00	Dark band
33	0.02	0.26	68.6	13.2	<2.5	13.0	0.011	0.1	0.40	0.57	
34	0.03	0.24	87.4	15.6	<2.5	10.0	0.015	2.1	0.38	0.55	
35	0.02	<0.001	79.6	16.5	<2.5	23.0	0.020	1.8	1.24	1.76	Dark band
36	0.02	0.37	75.3	14.4	<2.5	15.0	0.215	1.2	0.27	0.38	
37	0.03	1.50	84.2	18.7	<2.5	55.0	0.022	1.0	3.10	4.40	
38	0.02	0.36	76.4	15.3	<2.5	15.0	0.017	0.7	0.61	0.86	
39	0.05	0.33	204.0	33.0	<2.5	15.0	0.026	1.2	0.47	0.67	
40	0.08	0.02	448.0	23.9	<2.5	30.0	0.023	0.1	1.13	1.61	
41	2.38	0.15	1000.0	41.9	<2.5	10.0	0.039	2.2	0.10	0.14	
42	0.05	0.27	102.0	16.5	<2.5	15.0	0.017	1.1	0.38	0.53	
43	0.72	0.43	350.0	12.0	<2.5	25.0	0.009	0.6	0.76	1.08	
44	0.02	0.37	83.5	10.4	<2.5	15.0	0.016	1.8	0.67	0.95	
45	0.69	0.21	790.0	19.6	<2.5	15.0	0.028	4.9	0.33	0.47	Edge of dome
46	2.54	0.20	650.0	13.2	<2.5	10.0	0.019	1.1	0.31	0.44	
47	2.70	0.18	2350.0	66.6	<2.5	13.0	0.041	3.4	0.25	0.35	
48	0.05	0.30	632.0	17.4	<2.5	15.0	0.002	1.9	0.46	0.65	
49	0.54	0.38	1230.0	29.1	<2.5	18.0	0.011	2.5	0.62	0.88	
50	0.05	<0.001	184.0	138.0	<2.5	25.0	0.007	0.3	1.10	1.57	
51	0.08	2.31	259.0	17.4	<2.5	90.0	0.006	0.1	5.66	8.04	
52	6.33	0.21	2770.0	50.1	<2.5	10.0	0.033	9.1	0.29	0.41	
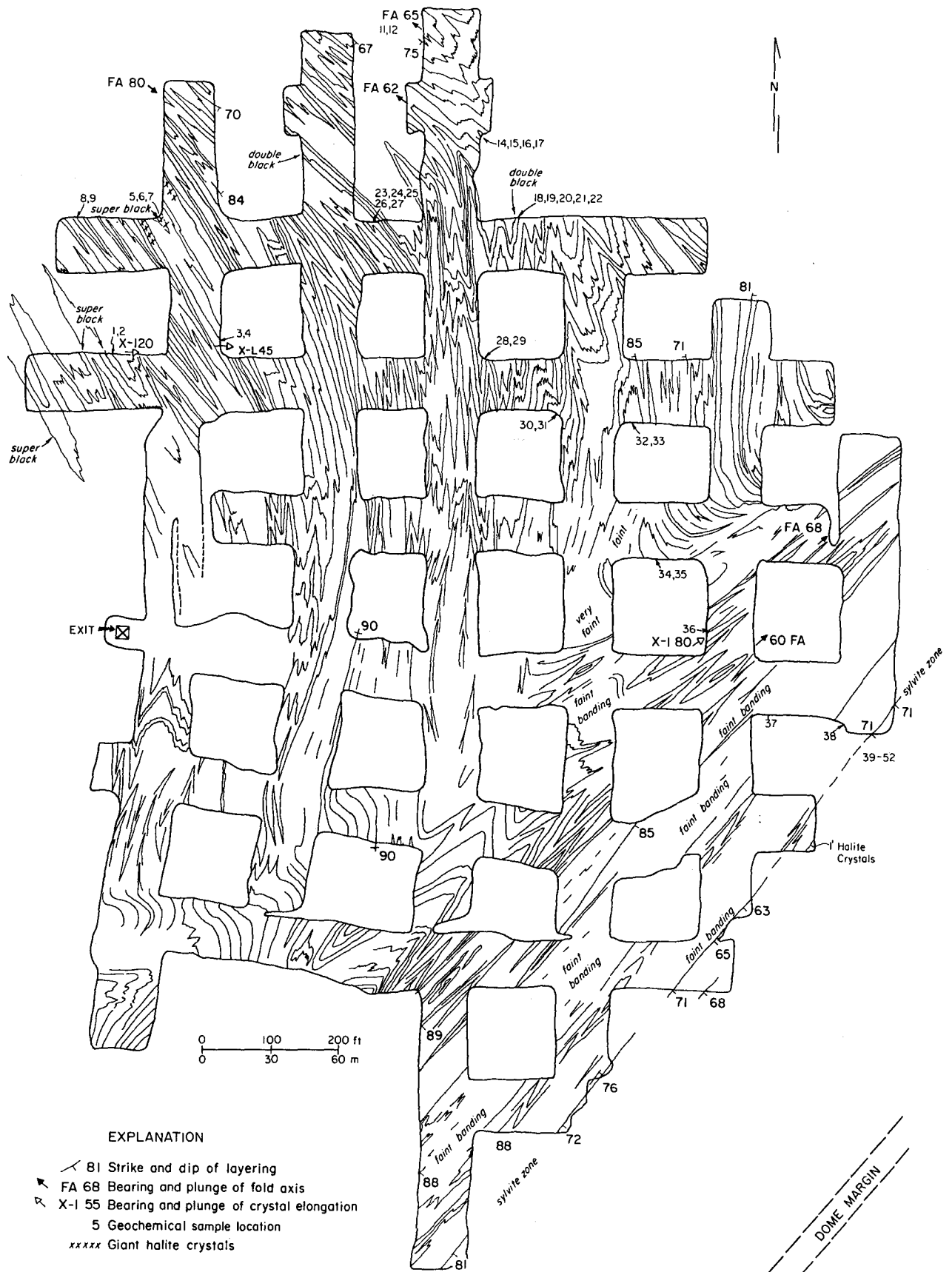
Figure 116. Location of salt samples from southeast section of the Kleer Mine, Grand Saline Salt Dome, East Texas. Geologic base map from Muehlberger (1979).
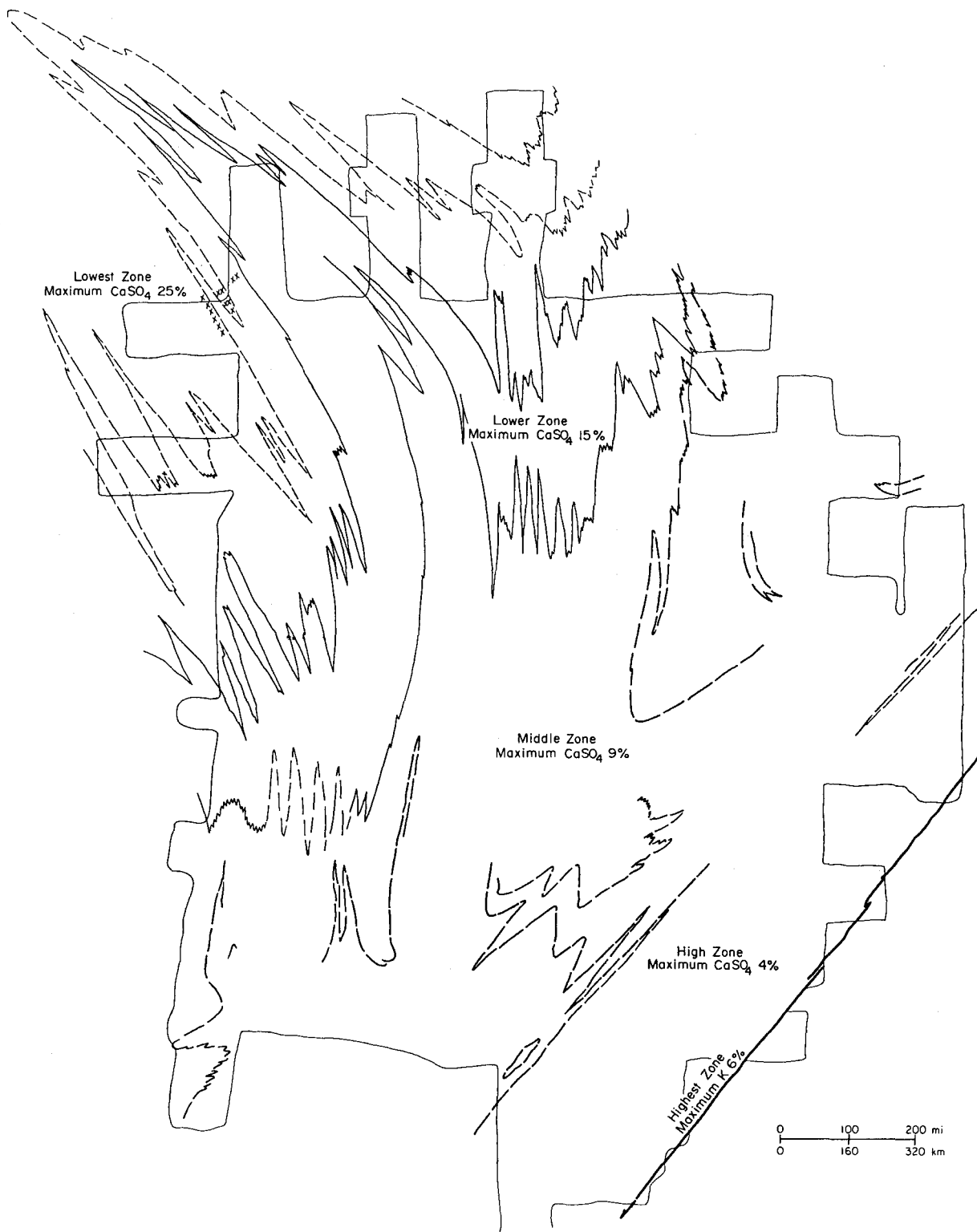
192

Figure 117. Interpretation of evaporite stratigraphy from Kleer Mine, Grand Saline Dome, East Texas. Salt beds near center of dome are older than beds near edge of dome. There is a general decrease in $CaSO_4$ concentrations from older salt to younger salt; an abrupt increase in K and Mg near edge of dome suggests that more restricted evaporitic conditions existed higher in the section and caused precipitation of bittern (K and Mg) salts. See figure 116 for location and scale.
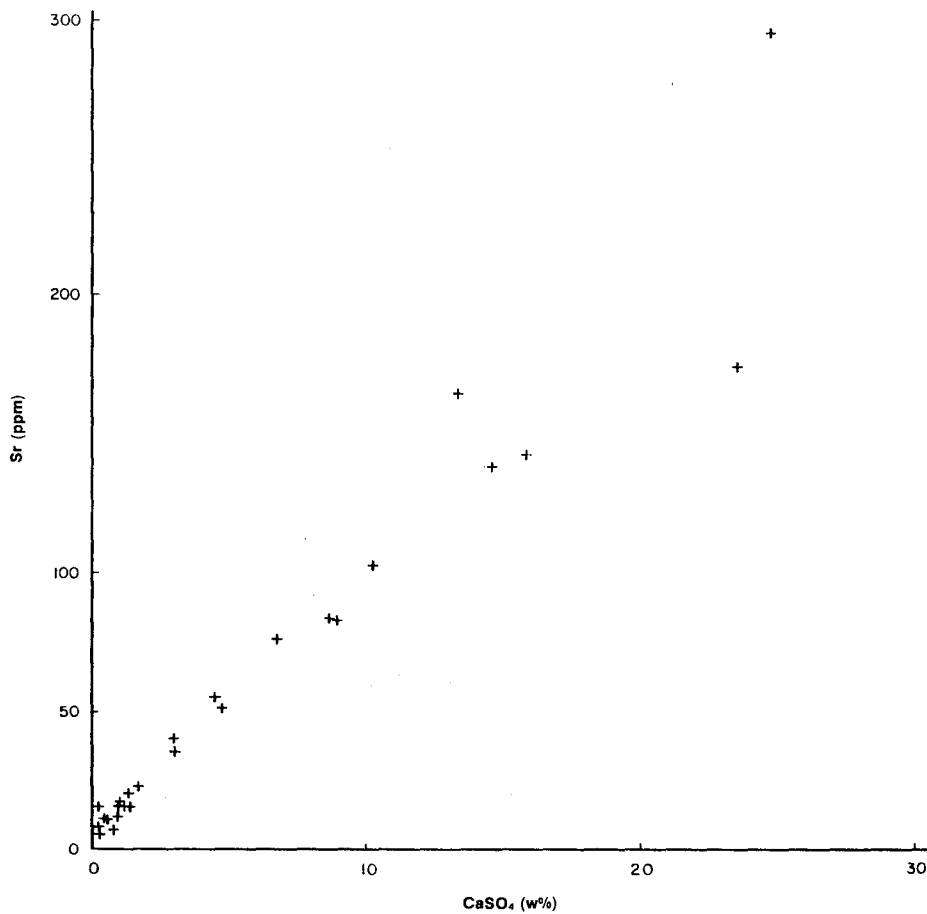
193

Figure 118. Graph showing Sr (ppm) versus CaSO$_4$ (w%) in salt samples, Kleer Mine, Grand Saline Dome, East Texas. For geochemical data, see table 15. Sr is concentrated in anhydrite but not in halite.
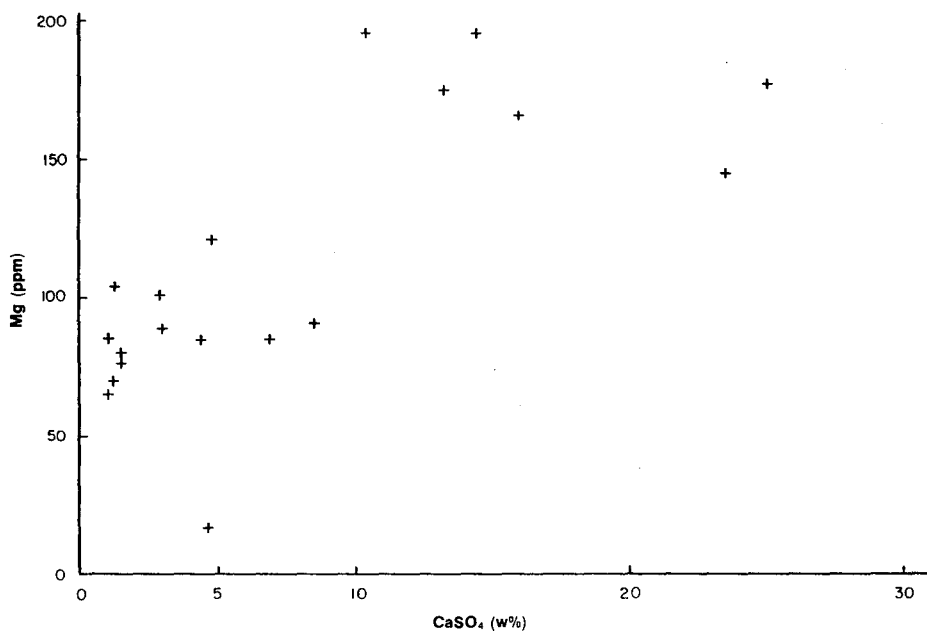

Figure 119. Graph showing Mg (ppm) versus CaSO$_4$ (w%) in salt samples, Kleer Mine, Grand Saline Dome, East Texas. For geochemical data, see table 15. High Mg concentrations from potassium-rich salts are not included in plot. Mg occurs in both anhydrite and halite.

194

HANDLING PROCEDURES FOR WILCOX CORE FROM LETCO TOH-2AO NEAR OAKWOOD DOME, EAST TEXAS BASIN

E. Dow Davidson, G. Donaldson, and S. J. Seni

Technical problems associated with recovery and slabbing of unconsolidated sediment cored from the Wilcox Group south of Oakwood Salt Dome were solved by special freezing and cutting techniques.

The unconsolidated nature of the core from the Wilcox Group and research requirements for the core required development of special core retrieval, handling, and slabbing techniques. Christiansen-Diamond rubber-core barrel liners were used to retrieve unconsolidated Wilcox sands and muds. Approximately 75 percent of the Wilcox section was recovered using this technique.

Special core slabbing and handling techniques overcame problems associated with water-saturated sands, random tightly cemented zones, plastic muds, and lignites. Five-foot (1.5-m) lengths of core in rubber-core barrel sleeves were frozen overnight and stored. Freezing permitted uniform cutting of the diverse rock types. Frozen 5-ft (1.5-m) sections were cut into 1-ft (0.3-m) sections on a 10-inch radial-arm saw equipped with a tungsten-carbide blade. Two lengthwise cuts $180°$ apart were made through the rubber sleeve with a razor knife to reduce friction before the sections were cut by a diamond-bladed rock saw. Two equal-sized sections remained in the respective rubber sleeves. Sections were placed in separate 9-ft- (3-m-) capacity flat core boxes. Split PVC pipe supported the core within each box. Polyethylene tubing was used to seal the core to prevent loss of formation waters.

ACKNOWLEDGMENTS

REFERENCES

Adey, E. A., and Cook, H. M., 1964, Suspended-sediment load of Texas streams, compilation report, October 1959-September 1961: Texas Water Commission Bulletin 6410, 56 p.

Anderson, T. H., and Schmidt, V. A., 1980, The evolution of Middle America and the Gulf of Mexico--Caribbean Sea region during Mesozoic time (abs.), in Symposium on the origin of the Gulf of Mexico and the early opening of the central North Atlantic Ocean: Baton Rouge, Louisiana State University, School of Geoscience, p. 99-100.

Baldwin, B., Coney, P. J., and Dickinson, W. R., 1974, Dilemma of a Cretaceous time scale and rates of seafloor spreading: Geology, v. 2, no. 1, p. 267-270.

Balk, R., 1949, Structure of Grand Saline Salt Dome, Van Zandt County, Texas: American Association of Petroleum Geologists Bulletin, v. 33, no. 11, p. 1791-1829.

_____ 1953, Salt structure of Jefferson Island Salt Dome, Iberia and Vermilion Parishes, Louisiana: American Association of Petroleum Geologists Bulletin, v. 37, no. 11, p. 2455-2474.

Barnes, V. E., 1967, Palestine sheet: The University of Texas at Austin, Bureau of Economic Geology, Geologic Atlas of Texas, scale 1:250,000.

_____ 1979, Waco sheet: The University of Texas at Austin, Bureau of Economic Geology, Geologic Atlas of Texas, scale 1:250,000.

Bassett, R. L., Weeks, E. P., Ceazan, M. L., Perkins, S. G., Signor, D. C., Redinger, D. L., Malcolm, R. L., Aiken, G. R., Thurman, E. M., Avery, P. A., Wood, W. W., Thompson, G. M., and Stiles, G. K., 1981, Preliminary data from a series of artificial recharge experiments at Stanton, Texas: U.S. Geological Survey, Open-File Report 81-149, 235 p.

Berryhill, R. A., Champion, W. L., Meyerhoff, A. A., Sigler, C. G., Cook, D. S., Laird, J. D., Skillern, I. E., Spooner, H. V., Jr., Wisdom, C. F., Beebe, B. W., and Spillers, J. P., 1968, Stratigraphy and selected gas-field studies of North Louisiana, in Beebe, B. W., and Curtis, B. F., eds., Natural gases of North

America: American Association of Petroleum Geologists Memoir 9, v. 1, p. 1103-1137.

Boulter, C. A., 1976, Sedimentary fabrics and their relation to strain-analysis methods: Geology, v. 4, no. 3, p. 141-146.

Brunton, G. D., and McClain, W. C., 1977, Geologic criteria for radioactive waste repositories: Oak Ridge National Laboratories, Y/OWL/TM-47, 12 p.

Buffler, R. T., Watkins, J. S., Schaub, F. J., and Worzel, J. L., 1980, Structure and early geologic history of the deep central Gulf of Mexico basin, in Proceedings, Symposium on the origin of the Gulf of Mexico and the early opening of the central North Atlantic Ocean: Baton Rouge, Louisiana State University, School of Geoscience, p. 3-16.

Burke, K., 1976, Development of graben associated with the initial ruptures of the Atlantic Ocean, in Bott, M. H. P., ed., Sedimentary basins of continental margins and cratons: Tectonophysics, v. 36, no. 1-3, p. 93-112.

Butler, G. P., 1973, Strontium geochemistry of modern and ancient calcium sulphate minerals, in Purser, B. H., ed., The Persian Gulf: New York, Springer-Verlag, p. 423-452.

Casey, R., 1964, The Cretaceous Period, in The Phanerozoic time scale: Geologic Society of London Quarterly Journal, v. 120, supplement, p. 193-202.

Collins, E. W., and Hobday, D. K., 1980, Surface geology and shallow borehole investigations of Oakwood Dome--preliminary studies, in Kreitler, C. W., and others, Geology and geohydrology of the East Texas Basin: a report on the progress of nuclear waste isolation feasibility studies (1979): The University of Texas at Austin, Bureau of Economic Geology Geological Circular 80-12, p. 88-94.

Collins, E. W., Hobday, D. K., and Kreitler, C. W., 1980, Quaternary faulting in East Texas: The University of Texas at Austin, Bureau of Economic Geology Geological Circular 80-1, 20 p.

Cook, H. M., 1970, Suspended-sediment load of Texas streams, compilation report, October 1963-September 1965: Texas Water Development Board Report 106, 61 p.

Cooper, H. H., Jr., and Jacob, C. E., 1946, A generalized graphical method for evaluating formation constants and summarizing well-field history: Transactions, American Geophysical Union, v. 27, p. 526-534.

De Paor, D. G., 1980, Some limitations of the $R_f/\emptyset$ technique of strain analysis: Tectonophysics, v. 64, no. 1, p. T29-T31.

Dickinson, W. R., and Coney, P. J., 1980, Plate tectonic constraints on the origin of the Gulf of Mexico, in Proceedings, Symposium on the origin of the Gulf of Mexico and the early opening of the central North Atlantic Ocean: Baton Rouge, Louisiana State University, School of Geoscience, p. 27-36.

Dix, Owen R., 1979, Drainage patterns over East Texas salt domes as indicators of dome movement (abs.): Geological Society of America, Abstracts with Programs, v. 11, no. 7, p. 413.

Dixon, J. M., 1975, Finite strain and progressive deformation in models of diapiric structures: Tectonophysics, v. 28, no. 1/2, p. 89-124.

Dougherty, John P., 1979, Suspended-sediment load of Texas streams, compilation report, October 1971-September 1975: Texas Department of Water Resources Report 233, 82 p.

Dunnet, D., 1969, A technique of finite strain analysis using elliptical particles: Tectonophysics, v. 7, no. 2, p. 117-136.

Dunnet, D., and Siddans, A. W. B., 1971, Non-random sedimentary fabrics and their modification by strain: Tectonophysics, v. 12, no. 4, p. 307-325.

Eargle, D. H., 1962a, Geology of core hole WP-1 Tatum Dome, Lamar County, Mississippi: U.S. Geological Survey Technical Letter Dribble-15, Open-File Report 474-278, 46 p.

_____ 1962b, Geology of core hole WP-4 Tatum Dome, Lamar County, Mississippi: U.S. Geological Survey Technical Letter Dribble-19, Open-File Report 474-282, 45 p.

Ebanks, G. K., 1965, Structural geology of Keechi Salt Dome, Anderson County, Texas: University of Texas, Austin, Master's thesis, 85 p.

Elliott, D., 1970, Determination of finite strain and initial shape from deformed elliptical objects: Geological Society of America Bulletin, v. 81, no. 8, p. 2221-2236.

Evans, J. C., and Bramblett, H. L., 1960, Report on sedimentation of Lake Cherokee, Gregg and Rusk Counties, Texas: U.S. Department of Agriculture, Soil Conservation Service, 12 p.

Exploration Techniques, Inc., 1979, Gravity models of Oakwood and Keechi Domes: Unpublished report prepared for Law Engineering Testing Company, Marietta, Georgia.

199

Falvey, D. A., 1974, The development of continental margins in plate tectonic theory: Australian Petroleum Exploration Association Journal, v. 14, no. 1, p. 95-106.

Feely, H. W., and Kulp, J. L., 1957, Origin of the Gulf Coast salt dome sulfur deposits: American Association of Petroleum Geologists Bulletin, v. 41, no. 8, p. 1802-1853.

Fisher, W. L., and McGowen, J. H., 1967, Depositional systems in the Wilcox Group of Texas and their relationship to occurrence of oil and gas: Gulf Coast Association of Geological Societies Transactions, v. 17, p. 105-125.

Fisk, H. N., McFarlan, E., Jr., Kolb, C. R., and Wilbert, L. J., Jr., 1954, Sedimentary framework of the modern Mississippi delta: Journal of Sedimentary Petrology, v. 24, p. 76-99.

Fogg, G. E., 1980a, Aquifer modeling at Oakwood Dome, in Kreitler, C. W., and others, Geology and geohydrology of the East Texas Basin: a report on the progress of nuclear waste isolation feasibility studies (1979): The University of Texas at Austin, Bureau of Economic Geology Geological Circular 80-12, p. 35-40.

_____ 1980b, Regional aquifer hydraulics, East Texas Basin, in Kreitler, C. W., and others, Geology and geohydrology of the East Texas Basin: a report on the progress of nuclear waste isolation feasibility studies (1979): The University of Texas at Austin, Bureau of Economic Geology Geological Circular 80-12, p. 55-67.

_____ 1980c, Salinity of formation waters, in Kreitler, C. W., and others, Geology and geohydrology of the East Texas Basin: a report on the progress of nuclear waste isolation feasibility studies (1979): The University of Texas at Austin, Bureau of Economic Geology Geological Circular 80-12, p. 68-72.

Fogg, G. E., and Kreitler, C. W., in preparation, Ground-water hydraulics and hydrochemical facies in Eocene aquifers of the East Texas Basin: The University of Texas at Austin, Bureau of Economic Geology.

Fogg, G. E., Kreitler, C. W., and Dutton, S. P., 1980, Hydrologic stability of Oakwood Dome, in Kreitler, C. W., and others, Geology and geohydrology of the East Texas Basin: a report on the progress of nuclear waste isolation feasibility study: The University of Texas at Austin, Bureau of Economic Geology Geological Circular 80-12, p. 30-32.

Freeze, R. A., and Cherry, J. A., 1979, Groundwater: New Jersey, Prentice-Hall, 604 p.

Fry, N., 1979, Random point distributions and strain measurement in rocks: Tectono-physics, v. 60, no. 1/2, p. 89-105.

Galloway, W. E., 1968, Depositional systems of the Lower Wilcox Group, north-central Gulf Coast Basin: Gulf Coast Association of Geological Societies Transactions, v. 18, p. 275-289.

Geomap Company, 1980, Executive's geologic atlas for East Texas: Dallas, 240 maps, scale 1"=4,000'.

Giles, A. B., 1980, Evolution of East Texas salt domes, in Kreitler, C. W., and others, Geology and geohydrology of the East Texas Basin: a report on the progress of nuclear waste isolation feasibility studies (1979): The University of Texas at Austin, Bureau of Economic Geology Geological Circular 80-12, p. 20-29.

Giles, A. B., and Wood, D. H., in preparation, Oakwood Salt Dome, East Texas geologic framework and growth history: The University of Texas at Austin, Bureau of Economic Geology.

Gose, W. A., Scott, G. R., and Swartz, D. K., 1980, The aggregation of Mesoamerica: paleomagnetic evidence, in Proceedings, Symposium on the origin of the Gulf of Mexico and the early opening of the central North Atlantic Ocean: Baton Rouge, Louisiana State University, School of Geoscience, p. 51-54.

Gundersen, W. C., Matzke, R. H., and Moore, W. E., 1969, Gulf of Mexico--generalized correlation chart (Mesozoic): unpublished chart prepared by Cretaceous Study Group, Exxon Production Research Co.

Hanna, S. S., and Fry, N., 1979, A comparison of methods of strain determination in rocks from southwest Dyfed (Pembrokeshire) and adjacent areas: Journal of Structural Geology, v. 1, no. 2, p. 155-162.

Harding, T. P., and Lowell, J. D., 1979, Structural styles, their plate-tectonic habitats, and hydrocarbon traps in petroleum provinces: American Association of Petroleum Geologists Bulletin, v. 63, no. 7, p. 1016-1058.

Heede, B. H., 1974, Stages of development of gullies in Western United States of America: Zeitschrift für Geomorphologie, v. 18, no. 1, p. 260-271.

Hightower, M. L., 1958, Structural geology of the Palestine Salt Dome, Texas: University of Texas at Austin, Master's thesis, 83 p.

Hsu, K. J., 1965, Isostasy, crustal thinning, mantle changes, and the disappearance of ancient land masses: American Journal of Science, v. 263, no. 2, p. 97-109.

Ibrahim, A. K., Carye, J., Latham, G., and Buffler, R., 1980, Crustal structure of the Gulf of Mexico from O.B.S. refraction and multichannel reflection data (abs.), in

Proceedings, Symposium on the origin of the Gulf of Mexico and the early opening of the central North Atlantic Ocean: Baton Rouge, Louisiana State University, School of Geoscience, p. 100.

Ingerson, E., and Pearson, F. J., Jr., 1964, Estimation of age and rate of motion of ground-water by the carbon-14 method, in Recent research in the fields of hydrosphere, atmosphere and nuclear geochemistry: Tokyo, p. 263-283.

International Oil Scouts Association, 1978, Texas oil and gas development, Texas yearbook 1978 (Review of 1977), v. 6, 359 pp.

Kaiser, W. R., Johnston, J. E., and Bach, W. N., 1978, Sand-body geometry and the occurrence of lignite in the Eocene of Texas: The University of Texas at Austin, Bureau of Economic Geology Geological Circular 78-4, 19 p.

Kehle, R. O., 1971, Origin of the Gulf of Mexico: unpaginated manuscript on file at The University of Texas at Austin, Geology Library.

Kinsman, D. J. J., 1975, Rift valley basins and sedimentary history of trailing continental margins, in Fischer, A. G., and Judson, S., eds., Petroleum and global tectonics: Princeton, Princeton University Press, p. 84-125.

Klitgord, K. D., 1980, Mesozoic evolution of the Atlantic, Caribbean, and Gulf of Mexico (abs.), in Proceedings, Symposium on the origin of the Gulf of Mexico and the early opening of the central North Atlantic Ocean: Baton Rouge, Louisiana State University, School of Geoscience, p. 100-101.

Kreitler, C. W., Agagu, O. K., Basciano, J. M., Collins, E. W., Dix, O., Dutton, S. P., Fogg, G. E., Giles, A. B., Guevara, E. H., Harris, D. W., Hobday, D. K., McGowen, M. K., Pass, D., and Wood, D. H., 1980, Geology and geohydrology of the East Texas Basin: a report on the progress of nuclear waste isolation feasibility studies (1979): The University of Texas at Austin, Bureau of Economic Geology Geological Circular 80-12, 112 p.

Kupfer, D. H., 1968, Relationship of internal to external structure of salt domes: American Association of Petroleum Geologists Memoir 8, p. 79-89.

_____ 1970, Mechanism of intrusion of Gulf Coast salt, in The geology and technology of Gulf Coast salt, a symposium: Baton Rouge, Louisiana State University, School of Geoscience, p. 25-66.

Law Engineering Testing Company, 1978, Geology and growth history of Minden Salt Dome, Webster Parish, Louisiana: Marietta, Georgia, 69 p.

_____ 1980, Area characterization report--Gulf Coast salt domes project, v. II, East Texas study area: Report prepared for Battelle Memorial Institute, Office of Nuclear Waste Isolation, unpaginated.

Le Theoff, B., 1979, Non-coaxial deformation of elliptical particles: Tectonophysics, v. 53, no. 1/2, p. T7-T13.

Lisle, R. J., 1977a, Clastic grain shape and orientation in relation to cleavage from the Aberystwyth Grits, Wales: Tectonophysics, v. 39, nos. 1-3, p. 381-395.

_____ 1977b, Estimation of the tectonic strain ratio from the mean shape of deformed elliptical markers: Geologie en Mijnbouw, v. 56, no. 2, p. 140-144.

_____ 1979, Strain analysis using deformed pebbles: the influence of initial pebble shape: Tectonophysics, v. 60, no. 3/4, p. 263-277.

Livingstone, Daniel A., 1963, Chemical composition of rivers and lakes, chapter G, in Data of geochemistry (6th ed.): U.S. Geological Survey Professional Paper 440-G, 64 p.

Loocke, J. E., 1978, Growth history of the Hainesville Salt Dome, Wood County, Texas: The University of Texas at Austin, Master's thesis, 95 p.

Lotze, F., 1957, Steinsalz und Kalisalze, Pt. I: Berlin, Gebrüder Borntraeger, 466 p.

Manheim, F. T., and Bischoff, J. L., 1969, Geochemistry of pore waters from Shell Oil Company drill holes on the continental slope of the northern Gulf of Mexico: Chemical Geology, v. 4, p. 63-82.

Martinez, J. D., Thoms, R. L., Kupfer, D. H., Smith, C. G., Jr., Kolb, C. R., Newchurch, E. J., Wilcox, R. E., Manning, T. A., Jr., Romberg, M., Lewis, A. J., and Rouik, J. E., 1976, An investigation of the utility of Gulf Coast salt domes for the storage or disposal of radioactive wastes: Baton Rouge, Louisiana State University, Institute for Environmental Studies, Report prepared for the Office of Waste Isolation, Union Carbide Corporation, 329 p.

Masch, F. D., and Denny, K. J., 1966, Grain-size distribution and its effect on the permeability of unconsolidated sands: Water Resources Research, v. 2, no. 4, p. 665-677.

McKenzie, D., 1978, Some remarks on the development of sedimentary basins: Earth and Planetary Science Letters, v. 40, p. 25-32.

Mirabal, James, 1974, Suspended-sediment load of Texas streams, compilation report, October 1965-September 1971: Texas Water Development Board Report 184, 117 p.

Muehlberger, W. R., 1959, Internal structure of the Grand Saline Salt Dome, Van Zandt County, Texas: University of Texas, Austin, Bureau of Economic Geology Report of Investigations No. 38, 22 p.

_____ 1968, Internal structures and mode of uplift of Texas and Louisiana salt domes: Geological Society of America Special Paper 88, 6 p.

_____ 1979, Grand Saline Salt Dome, Van Zandt County, Texas: Unpublished report prepared for Law Engineering Testing Company.

Muehlberger, W. R., and Clabaugh, P. S., 1968, Internal structure and petrofabrics of Gulf Coast salt domes: American Association of Petroleum Geologists Memoir 8, p. 90-98.

Nance, D., Rovik, J., and Wilcox, R. E., 1979, Lithology of the Vacherie Salt Dome core: Baton Rouge, Louisiana State University, Institute of Environmental Studies Topical Report, 343 p.

Nance, D., and Wilcox, R. E., 1979, Lithology of the Rayburn's Dome salt core: Baton Rouge, Louisiana State University, Institute of Environmental Studies Topical Report, 307 p.

Nance, R. L., 1962, Oakwood Dome Field, in Eaton, R. W., and Nichols, P. H., eds., Occurrence of oil and gas in northeast Texas: East Texas Geological Society, Publication 5, v. 1, p. 45-50.

Netherland, Sewell and Associates, Inc., 1976, Geologic study of the interior salt domes of northeast Texas salt-dome basin to investigate their suitability for possible storage of radioactive waste material as of May, 1976: Report prepared for Office of Waste Isolation, Union Carbide Corporation, Nuclear Division, 57 p.

Nichols, R. H., Peterson, G. E., and Wuerstner, C. E., 1968, Summary of subsurface geology of northeast Texas, in Beebe, B. W., and Curtis, B. F., eds., Natural gases of North America: American Association of Petroleum Geologists Memoir 9, v. 2, p. 982-1004.

Parsons, B., and Sclater, J. G., 1977, An analysis of the variation of ocean floor bathymetry and heat flow with age: Journal of Geophysical Research, v. 62, p. 803-825.

Peach, C. J., and Lisle, R. J., 1979, A Fortran IV program for the analysis of tectonic strain using deformed elliptical markers: Computers and Geosciences, v. 5, no. 3/4, p. 325-334.

Peters, J. W., and Dugan, A. F., 1945, Gravity and magnetic investigations at the Grand Saline Salt Dome, Van Zandt County, Texas: Geophysics, v. 10, no. 3, p. 376-391.

Pilger, R. H., Jr., 1978, A closed Gulf of Mexico, pre-Atlantic Ocean plate reconstruction and the early rift history of the Gulf and North Atlantic: Gulf Coast Association of Geological Societies Transactions, v. 28, p. 385-393.

Powers, S., 1926, Interior salt domes of Texas: American Association of Petroleum Geologists Bulletin, v. 10, no. 1, p. 1-60.

Ramberg, H., 1973, Model studies of gravity-controlled tectonics by the centrifuge technique, in De Jong, K. A., and Scholten, R., eds., Gravity and tectonics: New York, Wiley, p. 49-69.

Ramsay, J. G., 1967, Folding and fracturing of rocks: New York, McGraw-Hill, 568 p.

Relyea, S. F., Ames, L. L., Serne, R. J., Fulton, R. W., and Washburne, C. D., 1978, Batch KD determinations with common minerals and representative ground waters: Proceedings, Task 4 Waste Isolation Safety Assessment Program, Battelle Pacific Northwest Laboratories, Second Contractors Information Meeting, PNL-SA-7352, v. 2, p. 259-330.

Renick, B. C., 1928, Recently discovered salt domes in East Texas: American Association of Petroleum Geologists Bulletin, v. 12, no. 5, p. 527-547.

Ringwood, A. E., 1969, Composition and evolution of the upper mantle, in Hart, P. J., ed., The Earth's crust and upper mantle: American Geophysical Union Geophysical Monograph 13, p. 1-17.

Roberts, B., and Siddans, A. W. B., 1971, Fabric studies in the Llwyd Mawr Ignimbrite, Caernarvonshire, North Wales: Tectonophysics, v. 12, no. 4, p. 283-306.

Roedder, E., and Belkin, H. E., 1979, Fluid inclusions in salt from the Rayburn and Vacherie Domes, Louisiana: U.S. Geological Survey Open-File Report, no. 79-1675, 25 p.

Royden, L., Sclater, J. G., and Von Herzen, R. P., 1980, Continental margin subsidence and heat flow: important parameters in formation of petroleum hydrocarbons: American Association of Petroleum Geologists Bulletin, v. 64, no. 2, p. 173-187.

Salvador, A., and Green, A. R., 1980, Opening of the Caribbean Tethys (origin and development of the Caribbean and the Gulf of Mexico), in Colloque C5: Géologie de chaînes alpines issues de la Téthys: Bureau de Recherches Géologiques et Minières, Mémoire 115, p. 224-229.

Schwerdtner, W. M., 1967, Intragranular gliding in domal salt: Tectonophysics, v. 5, no. 5, p. 353-380.

Schwerdtner, W. M., Sutcliff, R. H., and Tröeng, B., 1978, Patterns of total strain in the crestal region of immature diapirs: Canadian Journal of Earth Sciences, v. 15, no. 9, p. 1437-1447.

Sclater, J. G., and Christie, P. A. F., 1980, Continental stretching: an explanation of the post-mid-Cretaceous subsidence of the Central North Sea Basin: Journal of Geophysical Research, v. 85, p. 3711-3739.

Sedimentation Committee of Water Resources Council, 1975, Sediment deposition in United States' reservoirs--summary of data reported through 1975 (supplement): U.S. Department of Agriculture Miscellaneous Publication No. 1362.

Shaub, F. J., Buffler, R. T., and Worzel, J. L., 1980, Basement structural trends in the deep Gulf of Mexico (abs.), in Proceedings, Symposium on the origin of the Gulf of Mexico and the early opening of the central North Atlantic Ocean: Baton Rouge, Louisiana State University, School of Geoscience, p. 101-102.

Siddans, A. W. B., 1980, Analysis of three-dimensional, homogeneous, finite strain using ellipsoidal objects: Tectonophysics, v. 64, no. 1, p. 1-16.

Sleep, N. H., 1971, Thermal effects of the formation of Atlantic continental margins by continental breakup: Geophysical Journal of the Royal Astronomical Society, v. 24, no. 4, p. 325-350.

Stout, I. M., Bentz, L. C., and Ingram, H. W., 1961, Silt load of Texas streams, a compilation report, June 1889-September 1959: Texas Board of Water Engineers Bulletin 6108, 236 p.

Texas Railroad Commission, 1978, Annual report of the Oil and Gas Division, 1978: Austin, 613 p.

Theis, C. V., 1935, The relation between the lowering of the piezometric surface and the rate and duration of discharge of a well using ground-water storage: Transactions, American Geophysical Union, v. 2, p. 519-524.

Tóth, J., 1978, Gravity-induced cross-formational flow of formation fluids, Red Earth Region, Alberta, Canada: analysis, patterns, and evolution: Water Resources Research, v. 14, no. 5, p. 805-843.

Trusheim, F., 1960, Mechanism of salt migration in northern Germany: American Association of Petroleum Geologists Bulletin, v. 44, no. 9, p. 1519-1540.

U.S. Army Corps of Engineers, 1960, Report of sedimentation resurvey, Dam B reservoir, Neches River, Texas: Fort Worth Engineering District, 21 p.

U.S. Coast and Geodetic Survey, 1957, United States earthquakes: Washington, D.C., p. 16-18.

Vail, P. R., Mitchum, R. M., and Thompson, S., III, 1977, Seismic stratigraphy and global sea level, Part 4: Global cycles of relative changes in sea level, in Payton, C. E., ed., Seismic stratigraphy--applications to hydrocarbon exploration: American Association of Petroleum Geologists Memoir 26, p. 83-97.

Van Hinte, J. E., 1976a, A Cretaceous time scale: American Association of Petroleum Geologists Bulletin, v. 60, no. 4, p. 498-516.

_____ 1976b, A Jurassic time scale: American Association of Petroleum Geologists Bulletin, v. 60, no. 4, p. 489-497.

Weres, O., and Schroeder, R. C., 1978, Documentation for program OGRE: University of California, Lawrence Berkeley Laboratory, report no. LBL-7060, prepared for U.S. Department of Energy under contract W-7405-ENG-48, 58 p.

Winker, C. D., 1979, Late Pleistocene fluvial-deltaic deposition, Texas coastal plain and shelf: The University of Texas at Austin, Master's thesis, 187 p.

Wood, D. H., and Guevara, E. H., 1981, Regional structural cross sections and general stratigraphy, East Texas Basin: The University of Texas at Austin, Bureau of Economic Geology Cross Section Report, 22 p.